Emergent phenomena in spatially and energetically inhomogeneous strongly correlated model electron systems

A Thesis
Submitted For the Degree of
Doctor of Philosophy
in the Faculty of Science

by

Sudeshna Sen

Chemistry and Physics of Materials Unit
Jawaharlal Nehru Centre for Advanced Scientific Research
Bangalore – 560 064

MARCH 2016

To My Parents

Declaration

I hereby declare that the matter embodied in the thesis entitled "**Emergent phenomena in spatially and energetically inhomogeneous strongly correlated model electron systems** " is the result of investigations carried out by me at the Chemistry and Physics of Materials Unit, Jawaharlal Nehru Centre for Advanced Scientific Research, Bangalore, India under the supervision of Prof. N. S. Vidhyadhiraja and that it has not been submitted elsewhere for the award of any degree or diploma.

In keeping with the general practice in reporting scientific observations, due acknowledgement has been made whenever the work described is based on the findings of other investigators.

Sudeshna Sen

Certificate

I hereby certify that the matter embodied in this thesis entitled "**Emergent phenomena in spatially and energetically inhomogeneous strongly correlated model electron systems**" has been carried out by Ms. Sudeshna Sen at the Chemistry and Physics of Materials Unit, Jawaharlal Nehru Centre for Advanced Scientific Research, Bangalore, India under my supervision and that it has not been submitted elsewhere for the award of any degree or diploma.

Prof. N. S. Vidhyadhiraja
(Research Supervisor)

Acknowledgements

I would first like to thank my supervisor, Prof. N. S. Vidhyadhiraja, for all his support, encouragement, patience and most importantly academic ideas. While I was always interested in condensed matter physics, it is he who introduced me to the world of many-body physics. His wonderful thought process and unique way of looking into problems is certainly *something* that has improved my understanding of physics. Discussions with him has not only helped me improve my concepts in physics but also learn several computational and technical skills that have proven to be extremely important. He is the best teacher to learn from. I have always found him encouraging my ideas and perspectives on a problem.

During my PhD, I have had the great opportunity of visiting Prof. Mark Jarrell and Prof. Juana Moreno from Louisiana State University. Collaborating with Mark, Juana and their students is a wonderful learning experience. I find myself privileged to work with Mark and Juana. Especially, Mark's enthusiasm for physics helped me enjoy and learn during the most academically demanding part of my PhD tenure. I will always admire his way of tackling diverse physical problems from different perspectives with extraordinary ideas. I must mention that when at times, Mark's ideas appeared difficult, it was Raja who made it simple enough for me to understand. I am very grateful to Raja, Mark and Juana for their tremendous support at various stages of my academic career.

I am especially thankful to Prof. Balasubramanian Sundaram and Prof. Shobhana Narasimhan for providing their support on various occasions. I thank all my course instructors in JNC and IISc: Prof. Balasubramanian Sundaram, Prof. Sundaresan, Prof. Chandrabhas Narayana, Prof. G. U. Kulkarni, Prof. T. K. Maji, Prof. Eswaramoorthy, Prof. Waghmare, Prof. Shobhana Narasimhan, Prof. Subir Das, Prof. Swapan K. Pati, Prof. Subroto Mukerjee. I enjoyed several fruitful discussions with Dr. Subhro Bhattacharya from ICTS, Prof. Vikram Tripathi from TIFR, Prof. H. R. Krishnamurthy from IISc and Prof. R. C. Budhani from IIT, Kanpur. I would also like to thank Prof. Timothy Fisher and his student Robert

Sayer from Purdue University for several discussions during our collaboration.

I thank my collaborators, Dr. Chinedu Ekuma, Dr. Hanna Terletska, Dr. Shuxiang Yang, Dr. Kiran Nair, Dr. Ka Ming Tam, Elisha for being very supportive during my stay in the US. I also extend my gratitude to my past and current group members Himadri, Abhay, Pramod, Naushad, Dasari, Rukhsan, Wasim, Debsankar and Anirudh. I thank the essential back-up team of friends at JNCASR especially those who have been by my side over the last one year. While the list goes on, special mention goes to my juniors Sisir, Somnath, Arpan, Abhijit, Subhajit, Jiarul, Saikat, Chandan. I found them to be very talented guys with a great sense of humour. I would also specially thank Arkamita, Dibyajyoti, Koushik, Debdipto and Rajib for helping me realize the lighter side of several harsh moments. Special thanks to Arkamita and Anirudh for proofreading several parts of my thesis. I thank all my integrated PhD batch mates with whom I had started my journey in JNC. I also extend my gratitude to all my juniors and seniors in the theoretical sciences unit of JNC. Special thanks to Dr. Somesh from JNC, Dr. Kusum and Dr. Prithvi from ICTS for various advices. I thank Dr. Pralok, who have always proven to be a great friend, a person you can always rely on. I also thank our 'Yoga' group at JNC and Mrs. Rajashree. Here, I enjoyed several relaxing sessions and found a platform for pursuing one of my interests.

At various stages of my life I had the opportunity of being guided by some excellent teachers. I would like to take this opportunity to mention their names. They are, Mrs. Sanjukta Sen, Mrs. Tandra Bhattacharya, Mr. Nazir Hossain. They inspired me to pursue this career and to never lose heart but be confident no matter what the situation is. They helped me to be deeper and deeper and try to find the roots of any subject, be it literature or science.

Finally, I thank my parents, to whom I dedicate this thesis. My father is a role model, a person whom I will always try to emulate. He has taught me the necessities of survival: perseverance, discipline, hard-work and confidence. He is my friend, philosopher and guide. While a great fan of my successes and a great critic of my failures, he has always seen a brighter side even in my worst performances.

My mother has taught me to be strong and deep in whatever I am achieving. I thank my brother, my elder sister and her family, especially my niece, Agnimitra. They have and will always put up with my nuisances with a smiling face. Over the last few years, I have found a wonderful person in my life who has been both my best friend and my greatest academic critic. Thank you, Nilay, for putting up with me through all the ups and downs in our lives. Like my family, he too has seen my best and my worst, and provided the support, hugs, and energy in this journey that have helped me focus more, no matter how far we are. Thank you all for your unconditional love and support.

Synopsis

In this thesis we have explored novel quantum phenomena that we have found to emerge due to an interplay of inhomogeneities and electronic correlations. The inhomogeneities looked into in this thesis were of two kinds: In one kind we considered spatially heterogeneous lattices like heterostructures where translation invariance is broken in one direction; in the other kind we considered energetically disordered lattices with broken translational invariance in all directions.

Combining the inhomogeneous dynamical mean field theory (IDMFT) for layered structures, and coherent potential approximation (CPA) for disorder we proposed a novel framework to investigate disordered interfaces in correlated electron systems. The local moment approach (LMA) (Logan *et al.* , JPCM, **10**, 2673 (1998)) was used as the impurity solver within the framework of IDMFT. In particular, we considered a single substitutionally disordered Kondo-insulator layer at the boundary of several clean layers. Such a situation could occur in heavy fermion heterostructures where the magnetic sites of the heavy fermion layers are substituted by non-magnetic impurities diffusing from the metallic layers. Three distinct types of clean adjacent layers were considered, namely, (a) non-interacting metals, (b) non-interacting band insulators, and, (c) several clean Kondo insulators. We derived several analytical expressions for simpler scenarios like a bilayer or a trilayer system that helped us gain insight into the multilayered scenario. Subsequently, we explored the range and extent to which Kondo hole incoherence could penetrate into the adjacent layers. Before considering the treatment of disorder beyond CPA, we looked into a particularly intriguing unconventional phenomenon that we found serendipitously to emerge in a coupled Kondo-insulator-non-interacting metal bilayer system. Employing the framework of IDMFT, and using the LMA as the impurity solver, we found that this model system can exhibit a surface of interacting type, quantum critical points, that separate a Kondo screened, Fermi liquid phase from a local moment, Mott insulating phase. We propose that this model could serve as a paradigmatic theoretical model, that brings together three hallmarks of strong correlation physics, namely, Mott transition, quantum criticality, and heavy fermions. This bilayer model exhibits a novel scenario where the interlayer coupling represents a handle for tuning a quantum critical metal insulator transition.

In another aspect of this thesis, we explored quenched disordered lattices with onsite Coulomb interactions. It is known that the interplay of disorder and strong correlations can lead to non-Fermi liquid behaviour. The primary aim for such a study was to elucidate the microscopic origin for such an observation. In this regard, we first revisited the Anderson-Hubbard model, within the framework of a local theory. We employed the typical medium theory (TMT) for disorder in conjunction with a dynamical mean field theory treatment of the interactions with the LMA as the impurity solver. We find a qualitative agreement of our results with the earlier ones derived using the numerical renormalization group approach (NRG) (Byczuk *et al.* , PRL **94**, 056404 (2005)) or the slave boson mean field theory (SB) approach (Aguiar *et al.* , PRL **102**, 156402 (2009)). In addition to an analysis from the perspective of the density of states (DoS) we also demonstrated the behaviour of the distribution of the Kondo scales (T_K), namely, $P(T_K)$. We derived the phase diagram based on DoS and $P(T_K)$ and demonstrated its agreement with the known results, thus validating our method. Based on our self-energy (and spectral) analysis we predicted the existence of an underlying universal low energy scale, T_K^{peak}, to be identified as the peak of $P(T_K)$. Subsequently, we aimed at the development of a non-local theory that can capture the interplay of interactions and non-local, dynamical effects of disorder. We therefore employed the typical medium dynamical cluster approximation originally implemented for treating disorder in either non-interacting (Ekuma *et al.* , PRB **89**, 081107(R) (2014)) or weakly correlated systems (Ekuma *et al.* , PRB **92**, 014209 (2015)), for strongly interacting disordered systems. With this development, we showed that the systematic incorporation of short ranged effects of disorder could lead to a form of $P(T_K)$ that can lead to non-Fermi liquid behaviour. Indeed, our analysis of the local self-energy showed a clear emergence of a crossover from a Fermi liquid to non-Fermi liquid, with increasing disorder strength. This analysis helped us establish a critical boundary that separates the physics of the disorder induced non-Fermi liquid from a conventional Fermi liquid.

This thesis opens up several new directions. Some of these are discussed as future outlooks in Chapter 7, where we also summarize the thesis.

Publication List

Included in the thesis:

- **Sudeshna Sen**, Juana Moreno, Mark Jarrell, N. S. Vidhyadhiraja, “Spectral changes in layered f-electron systems induced by Kondo hole substitution in the boundary layer”, Physical Review B, **91**, 155146 (2015)
- **Sudeshna Sen**, N. S. Vidhyadhiraja, “Quantum critical Mott transitions in a bilayer Kondo insulator-metal model system” Physical Review B, **93**, 155136 (2016)
- **Sudeshna Sen**, Hanna Terletska, Juana Moreno, N. S. Vidhyadhiraja, Mark Jarrell, “A local theory for the Anderson Mott localization”, (To be submitted)
- **Sudeshna Sen**, Hanna Terletska, Juana Moreno, N. S. Vidhyadhiraja, Mark Jarrell, “Emergence of non-Fermi liquid dynamics due to non-local correlations in an interacting disordered electronic system”, (manuscript under preparation)

Not included in the thesis:

- R. A. Sayer, J. D. Engerer, **Sudeshna Sen**, N. S. Vidhyadhiraja and T. S. Fisher, “Low frequency electrical noise thermometry in micro- and nano-scale devices”, ASME International Mechanical Engineering Congress and Exposition (Denver, CO, 2011), pp. IMECE2011-63586
- **Sudeshna Sen**, N. S. Vidhyadhiraja, “ Protocols for Characterising Quantum Transport through Nano-structure”, Applied Physics Letters, **101**, 133106 (2012)

Contents

List of Figures

Chapter 1

Introduction

Contents

The work in this thesis aims at modelling strongly correlated electron systems (SCES) in presence of inhomogeneities. In SCES, the electron-electron interactions are comparable to or larger than the electronic kinetic energy [1]. Prominent examples of such systems are the family of high T_c superconductors, (*e.g.* $\mathrm{La}_{2-x}\mathrm{Sr}_x\mathrm{CuO}_4$), the transition metal oxides, (*e.g.* $\mathrm{V}_{2-x}\mathrm{Cr}_x\mathrm{O}_3$ family), colossal magnetoresistance materials, (*e.g.* $La_{1-x}Ca_xMnO_3$), heavy fermion materials, (*e.g.* $CeAl_3$, UPt_3) or organic charge transfer salts, (*e.g.*). SCES serve to be an interesting paradigm in condensed matter physics from both fundamental and technological aspects [1–3]. The interplay of charge, orbital and lattice degrees of freedom in these materials give rise to a plethora of interesting phenomena, like, high temperature superconductivity/superconductors (HTSCs), colossal thermodynamic responses etc.. Conventional bandstructure theory fails to predict the physical properties of SCES, for example, the case of Mott insulators [4–6]. These are purely interaction driven insulators which otherwise in a tight-binding (band theoretical) model would be deemed as a metal.

One of the recent trends in condensed matter physics is the study of strongly correlated heterostructures [2, 7]. Heterostructure geometries provide a fertile playground for tuning material properties. Especially, when the constituent materials are strongly correlated, they provide an even wider scope for realizing unconventional physics at hetero-interfaces. Recent experiments on such systems provide several novel scenarios opening possible directions for realizing tunable HTSCs [8] or SCES based ultrafast electronics [3], namely, Mottronics [9] or probing fundamental physics in heavy fermions [10, 11]. These systems are, however, spatially inhomogeneous owing to the hetero-structure geometry, or at most, quasi-periodic, as in superlattices. Moreover, the occurrence of a disordered interface is inevitable. While one of the works presented in this thesis deals with a novel prediction of an emergent quantum phase transition at such a hetero-interface, another work revolves around the implementation of a self-consistent theoretical framework that may be used to understand some aspects of such a disordered interface.

Another kind of inhomogeneity commonly present in solid state systems is the presence of quenched disorder, where the atoms sit in a random energetic landscape. In fact, as emphasized by the pioneering work by Anderson [12], in non-interacting systems, quenched disorder may lead to a disorder driven metal insulator transition, namely, the phenomenon of ‘Anderson localization’ [13–15]. This is again a purely quantum phenomenon driven by the interference of electronic wave-functions. Both interactions and energetic disorder can individually pave intricate ways for observing intriguing physics. Imagine, the novel but complex picture that would emerge when these two combine. Investigating this interplay also forms a part of this thesis.

In this chapter, we therefore, introduce some of the aspects of SCES and disordered electronic systems and subsequently interacting disordered electronic systems. Let us first briefly begin with the Landau Fermi liquid theory paradigm of SCES in section 1.1, followed by an introduction to strongly correlated heterostructures and physically relevant strongly correlated models (that have been utilized in this thesis) in section 1.2. Subsequently, in section 1.3, we will introduce the role of random energetic disorder in electronic systems and speculate on its role in SCES. Finally, in section 1.4, we will provide a brief summary and overview of the problems that we have studied in this thesis.

1.1 From Fermi gas to Fermi liquid

1.1.1 Ideal Fermi gas

The Drude theory of metals [16], formulated in 1900, by Drude, is the first model that attempted to describe conduction in metals. In this model a classical gas of conduction electrons move in a static background of positive ions. The electrons propagate freely between collisions with the ionic background. Each electron's collisions are typically separated by a mean scattering time τ and the velocities obey classical Maxwell-Boltzmann distribution. However, in experiments, there were apparent deviations from this classical theory, for example, the specific heat, c_v did not show the classically expected value of $\frac{3}{2}k_B$ per conduction electron.

With the advent of quantum theory, Sommerfeld rectified the above problem by the introduction of the Fermi-Dirac distribution function instead of the Maxwell-Boltzmann distribution function. Nevertheless, several mysteries still remained and most importantly, both the theories of Drude and Sommerfeld failed to explain why some solid-state materials are nonmetallic. It was necessary to treat the positive ions of Drude and Sommerfeld's theories more carefully. X-ray diffraction studies revealed that these ions are often arranged in periodic lattices, motivating the formulation of Bloch theory or band theory of solids, where the electrons move in a background periodic potential and satisfy the Bloch's theorem [16].

1.1.2 Fermi liquid

Several aspects still remained un-understood in regards to experiments on several metals that owed its origin to interactions between electrons. It was then Landau's phenomenological theory of interacting Fermi systems [17, 18] that served as the paradigm for the understanding of metallic behavior. At the heart of this theory is the idea that the low lying excitations of an interacting system have a one-to-one correspondence with the excitations of a free Fermi gas as illustrated in Fig. 1.1(a). Moreover Landau guessed that the interacting states can be labelled with roughly the same quantum numbers of the non-interacting ones. In other words, the elementary excitations of interacting fermions are described by almost independent fermionic quasiparticles. However, this hypothesis of adiabatic continuity or a one-to-one correspondence is in reality a strong constraint on the interaction. For example attractive interactions, even very weak, leading to the formation of composite objects should be excluded.

The excitation spectrum of the system is given by the poles of the single particle Green's function. A study of the analytic properties of the Green's function determines if the particular system is a Fermi liquid or not. The (retarded) Green's function for a free Fermi gas is given by,

$$G(\mathbf{k},\omega) = \frac{1}{\omega + i\eta - \epsilon_k + \mu} \quad \eta \to 0^+,$$

where, ϵ_k is the (band) energy for an electron of crystal momentum k, and μ is the chemical potential. For an interacting system, the effects of interactions are approximated by the self-energy, $\Sigma(\mathbf{k},\omega)$, such that the retarded Green's function is given by,

$$G(\mathbf{k},\omega) = \frac{1}{\omega + i\eta - \epsilon_k + \mu - \Sigma(\mathbf{k},\omega)}.$$

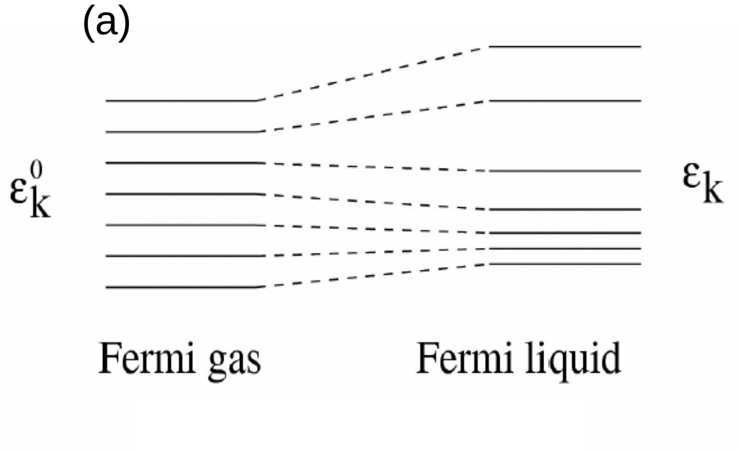

Figure 1.1: **Fermi liquid and adiabatic continuity:** States of a Landau Fermi liquid may be put in one-to-one correspondence with the non-interacting Fermi gas, by adiabatically turning on the interactions.

For a Fermi liquid (FL), the $\Sigma(\mathbf{k},\omega)$, for small ω and ϵ_k near μ can be expanded at temperature, $T = 0$ as, $\lim_{\omega\to 0}\Sigma(\mathbf{k},\omega) = \left(1 - \frac{1}{Z_{\mathbf{k}}}\right)\omega - iB_{\mathbf{k}}\omega^2$ The quantity $Z_{\mathbf{k}}$ is the quasi-particle mass renormalization factor given by, $Z_{\mathbf{k}}^{-1} = 1 - \frac{\partial \mathrm{Re}\,\Sigma(\mathbf{k},\omega)}{\partial\omega}$ and $B_{\mathbf{k}}$ represents the inverse of the quasi-particle relaxation time that becomes infinite on the Fermi surface as $\epsilon_k \to \mu$. Such a dependence essentially arises from the *Fermi golden rule* of scattering. If we inject an electron into a Fermi liquid with an energy ω above the Fermi energy, then, we expect the particle to experience an inelastic scattering, due to electron-electron interactions U which is proportional to ω^2. One factor of ω is due to energy conservation and the other due to momentum conservation with both constrained by the Pauli principle. That is, the inelastic scattering vanishes as $\omega \to 0$. Within a Fermi liquid theory, the role of interactions may be identified as the introduction of quasi-particles that carry the same charge and spin as an electron but with a renormalised effective mass, m_{eff}, that may be related to the quasi-particle renormalisation factor and the free electron mass, m, as, $m_{eff} = m/Z_k$, when the self-energy is momentum independent.

The above form of self-energy has important consequences on the low temperature transport and thermodynamic properties. For example, the resulting finite temperature (T) resistivity can be shown to have a quadratic form at low temperatures,

$$\rho(T) = \rho_0 + AT^2,$$

where ρ_0 is the residual resistivity due to static impurity scattering. Note that a non-zero resistivity requires both a decay time and energy loss mechanism either by umklapp or disorder scattering of electrons.

The electronic specific heat, C_{el} for a free Fermi gas is given by,

$$C_{el}(T) = \gamma_{free} T, \tag{1.1}$$

where, T is the temperature and $\gamma_{free} \propto \rho(\epsilon_f)$, with $\rho(\epsilon_f)$ being the density of states at the Fermi level, ϵ_f. For a FL, which is an interacting system, the same form of C_{el} holds (at reduced temperature scales), but with an enhanced linear coefficient, γ, where,

$$\frac{\gamma}{\gamma_{free}} = \left(\frac{1}{Z_k}\right)_{k=k_F}. \tag{1.2}$$

1.2 Strongly correlated electron systems (SCES)

SCES may show deviations from the conventional FL characteristics depending on the strength of interactions. For example, the family of transition metal oxide compounds, (*e.g.* $V_{2-x}Cr_xO_3$), exhibits a range of metal-insulator transitions (MITs) as a function of doping (x), temperature (T) and pressure (P), [3, 19]. The effect of pressure is basically to change the ratio of the electron-electron interaction, U, to the bandwidth, U/t^*, where t^* is the bandwidth. This behaviour has no analog in Landau FL theory. These interaction driven insulators are known as Mott insulators.

There is another class of SCES known as the heavy fermions [21], (*e.g.* $CeAl_3$, UPt_3). One specific characteristic of these systems is that the specific heat of these compounds show a strong renormalization as reflected by the coefficient of the linear term, γ. It is about 3 orders of magnitude larger than for Potassium, indicating

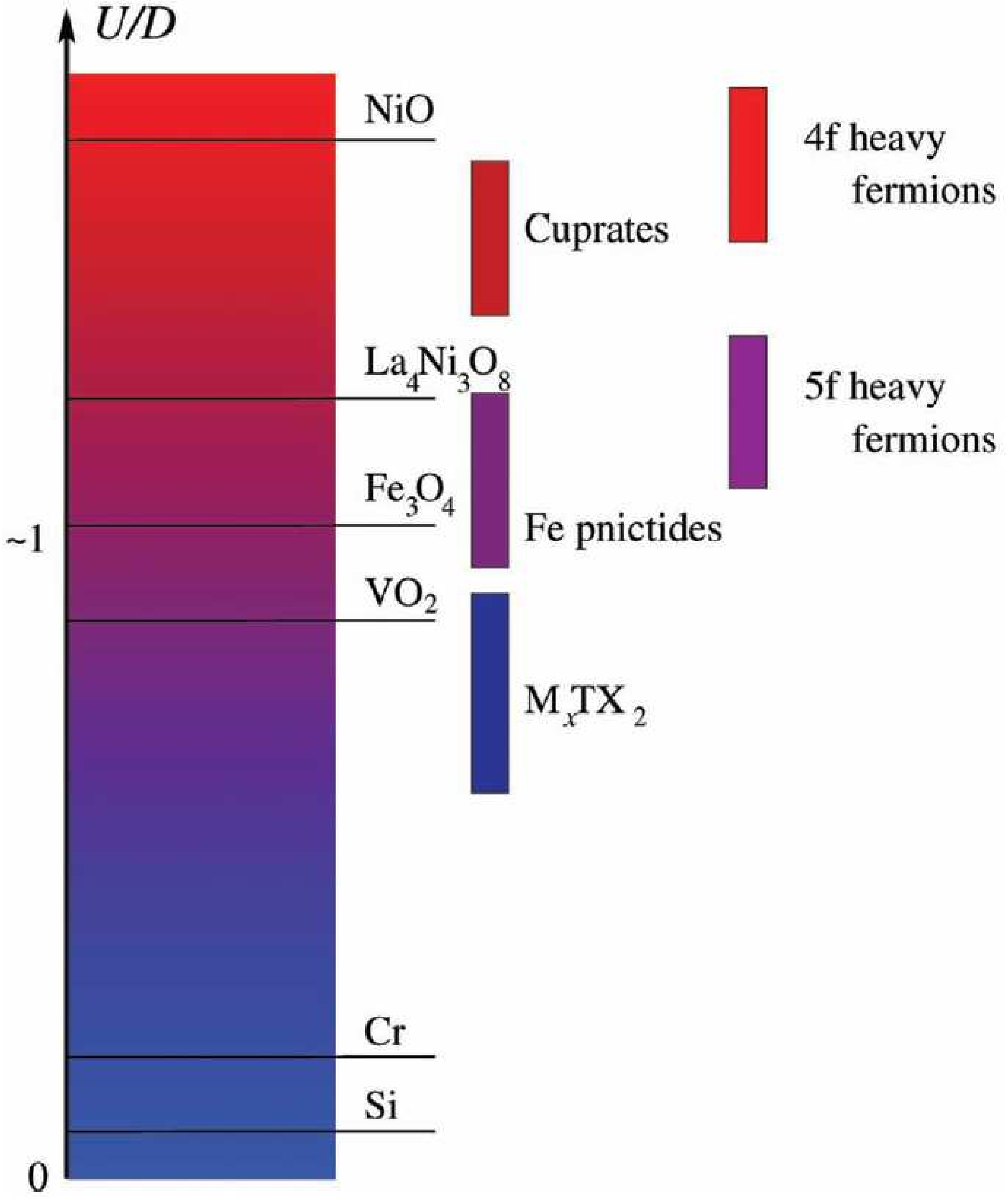

Figure 1.2: **A schematic chart of various strongly correlated materials**, plotted as a function of their correlation strengths, U, relative to the electron bandwidth, D. The displayed values should be considered semi-qualitative. The colour code serves as a rough guide of the interaction strength, increasing from blue (non-interacting) to red (very strongly interacting). Figure taken from [1] with permission.

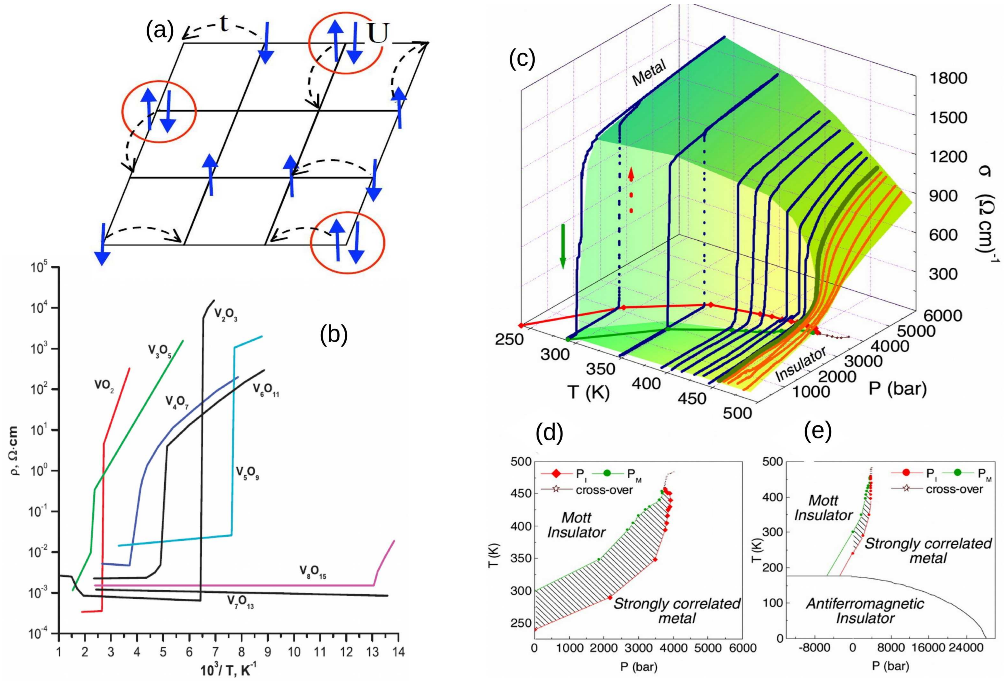

Figure 1.3: **Transition metal oxides:** (a) Schematic illustration of the single band Hubbard model, described in Eq. (1.3) where the competition between the hopping energy, t and the Coulomb repulsion energy, U can induce an interaction driven metal-insulator transition (MIT) in a half-filled lattice. Open d shell materials like the family of $V_{2-x}Cr_xO_3$ are known to demonstrate such MITs. (b) The Vanadium dioxide family has become like a laboratory prototype and as seen in this figure, about ten oxides of this family exhibit MITs at different temperatures, thus offering a potential arena for technological applications like in Mott transition field effect transistors. This figure is taken from [20] with permission. (c) As mentioned earlier, such transitions can also be induced by tuning the U/t ratio, that can be achieved by changing the pressure. In this plot, conductivity is shown as a function of decreasing pressure for a range of temperatures. In most cases these are first order in nature, as depicted by the hysteresis cycle shown for $T = 290$ K and $T = 348$ K. (d) Phase diagram of $(V_{1-x}Cr_x)_2O_3$ as a function of pressure and temperature is shown. The pressure can be thought of as a parameter for changing the U; (e) the global phase diagram of the same material. Figures presented in (c), (d) and (e) have been taken from [19] with permission.

that the quasiparticle effective mass is about 1000 times more than the free electron value, and, thus the origin of the name *heavy fermions*. Figure 1.2 lists some of these materials and grades them as a function of the interaction strength.

Theoretically, SCES have been conventionally modelled by simplified "effective" low energy Hamiltonians such as the Hubbard model(HM) and the periodic Anderson model(PAM). In these model scenarios, one neglects realistic factors like band-structure, disorder etc. We give brief descriptions of these models below. The single-band HM (shown as a schematic in Fig. 1.3(a)), is given by,

$$H = -t \sum_{\langle ij \rangle, \sigma} \left(c^{\dagger}_{i\sigma} c_{j\sigma} + H.c. \right) + \sum_{i} \ \epsilon_c \hat{n}_i + U \sum_{i} n_{i\uparrow} n_{i\downarrow}, \tag{1.3}$$

where, t is the hopping amplitude also related to the kinetic energy of the electrons; $c^{\dagger}_i (c_i)$ creates (annihilates) an electron with spin σ at site i and $\hat{n}_i$ is the electron number operator; ϵ_c is on-site energy minus the chemical potential. In the half-filled Hubbard model, for which, $\epsilon_c = -U/2$, the single-band HM shows a metal-insulator transition as a function of U/t^*, where t^* is related to the band-width of the electronic density of states. So it is thought to provide a good zeroth order description of the physics of transition metal oxides.

As mentioned earlier, another class of SCES are the heavy fermions, where, each unit cell of the lattice consists of one rare earth atom (*e.g.* Ce, U) having partially filled 4-f or 5-f shells and one or more metal ions having partially filled s, p, or, d shells. A list of such materials is shown in Fig. 1.4. The f shells are highly localized and unlike the conduction electrons, can hardly form a band. Hence, as a minimal description, such systems may be represented as what is known as the periodic Anderson model (PAM) (shown as a schematic in Fig. 1.5(a)), given by,

$$\begin{aligned} \mathcal{H} = & - \sum_{ij\sigma} t_{ij} \left(c^{\dagger}_{i\sigma} c_{j\sigma} + h.c. \right) + \sum_{i\sigma} V \ \left(f^{\dagger}_{i\sigma} c_{i\sigma} + h.c. \right) \\ & + \sum_{i\sigma} \left(\epsilon_c c^{\dagger}_{i\sigma} c_{i\sigma} + \epsilon_f f^{\dagger}_{i\sigma} f_{i\sigma} \right) + + \sum_{i} U n_{fi\uparrow} n_{fi\downarrow}, \end{aligned} \tag{1.4}$$

where, t_{ij} represents the hopping between the conduction band (c-electron) orbitals

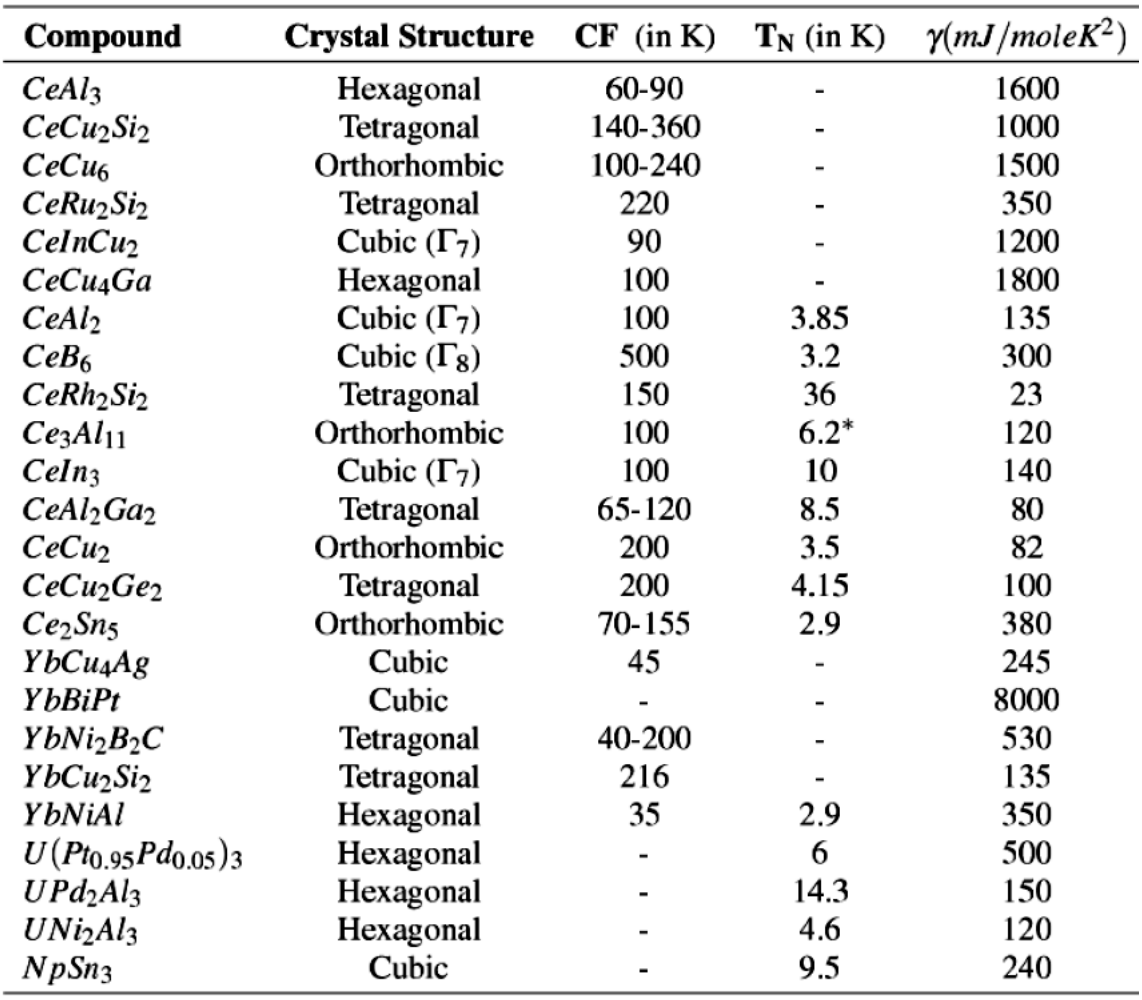

Compound	Crystal Structure	CF (in K)	T_N (in K)	$\gamma (mJ/moleK^2)$
$CeAl_3$	Hexagonal	60-90	-	1600
$CeCu_2Si_2$	Tetragonal	140-360	-	1000
$CeCu_6$	Orthorhombic	100-240	-	1500
$CeRu_2Si_2$	Tetragonal	220	-	350
$CeInCu_2$	Cubic (Γ_7)	90	-	1200
$CeCu_4Ga$	Hexagonal	100	-	1800
$CeAl_2$	Cubic (Γ_7)	100	3.85	135
CeB_6	Cubic (Γ_8)	500	3.2	300
$CeRh_2Si_2$	Tetragonal	150	36	23
Ce_3Al_{11}	Orthorhombic	100	6.2*	120
$CeIn_3$	Cubic (Γ_7)	100	10	140
$CeAl_2Ga_2$	Tetragonal	65-120	8.5	80
$CeCu_2$	Orthorhombic	200	3.5	82
$CeCu_2Ge_2$	Tetragonal	200	4.15	100
Ce_2Sn_5	Orthorhombic	70-155	2.9	380
$YbCu_4Ag$	Cubic	45	-	245
$YbBiPt$	Cubic	-	-	8000
$YbNi_2B_2C$	Tetragonal	40-200	-	530
$YbCu_2Si_2$	Tetragonal	216	-	135
$YbNiAl$	Hexagonal	35	2.9	350
$U(Pt_{0.95}Pd_{0.05})_3$	Hexagonal	-	6	500
UPd_2Al_3	Hexagonal	-	14.3	150
UNi_2Al_3	Hexagonal	-	4.6	120
$NpSn_3$	Cubic	-	9.5	240

Figure 1.4: **Examples of heavy fermion compounds:** For each entry the crystal structure (2nd column), crystalline field (3rd), Nèel temperature for magnetic ordering (4th) and Sommerfeld specific heat constant, (the coefficient of the linear term) (5th) has been reported. The Sommerfeld specific heat constant is seen to be ~ 3 orders of magnitude higher than the free electron value, and hence the name *heavy fermions*. This figure is taken from [21] with permission.

at sites i and j; ϵ_c and ϵ_f are the onsite energies of the c- and f-electrons, respectively; V is the hybridization between the heavy f-electrons and the c-electrons; U is the onsite Coulomb repulsion between two electrons occupying an f orbital.

Such models, although approximate, are physically motivated and when solved within a framework that can handle the non-perturbative nature of U, can suc-

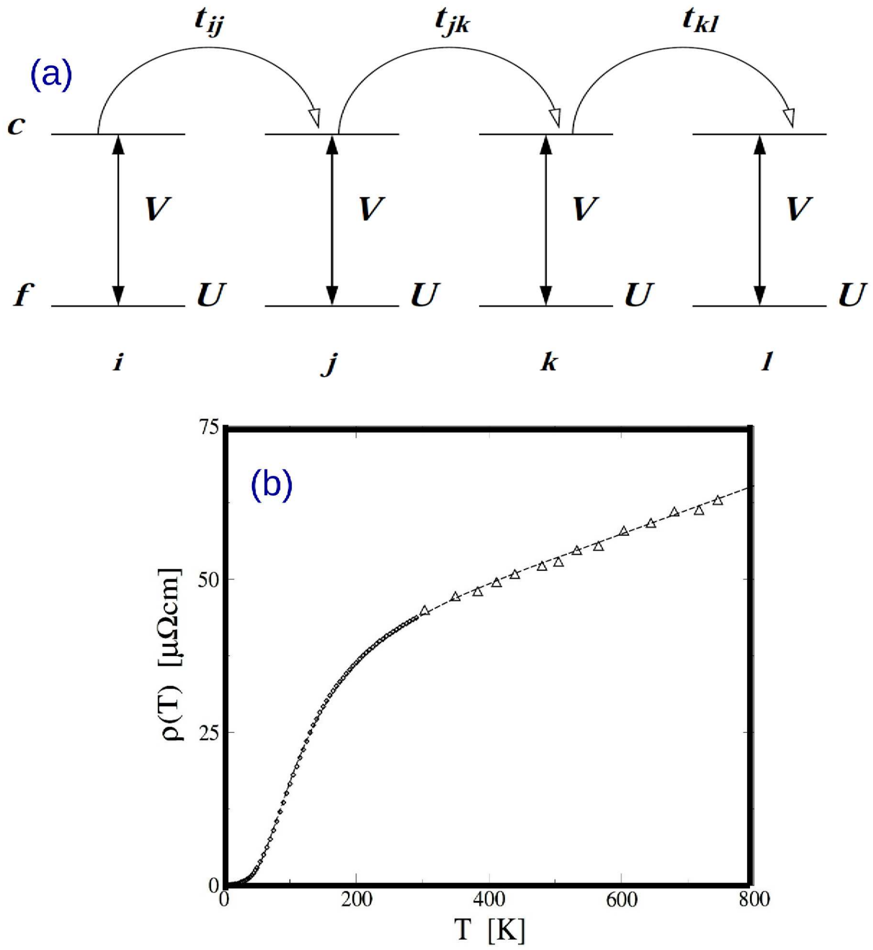

Figure 1.5: **Heavy fermion systems:** (a) Schematic illustration of the periodic Anderson model (PAM) as described in Eq. (1.4); here a highly localised orbital, like the f orbitals of heavy fermion materials, hybridises locally with a non-interacting conduction band orbital (c-orbital) *via* an energy V. Interactions enter *via* the on-site Coulomb repulsion U and neighbouring conduction orbitals are connected through a one-electron hopping matrix element, t_{ij}. (b) Theoretical resistivity ($\rho(T)$) for $YbAl_3$ (dashed line) is compared to the experimental results. This figure is taken from [22]. In this work [22], the PAM was solved within the framework of dynamical mean field theory and the excellent agreement between the theory and experiment is well evident.

cessfully explain various experimental scenarios [19, 22]. The dynamical mean field theory (DMFT) [23] is one such framework that can indeed capture the non-perturbative effects of U and is also thermodynamically consistent, being exact in several limits. The DMFT has been very successful and yields much insight into the behaviour of SCES, despite its drastic simplifications. Within DMFT, the details of which are given in Chapter 2, one self-consistently maps the many body lattice problem onto an impurity model like the single impurity Anderson model (SIAM). Therefore, one needs efficient solvers for investigating the impurity problem. There exist several such perturbative and non-perturbative methods. Each of these methods have their own advantages and disadvantages. For example, one of the numerically exact methods, namely, the Hirsch-Fye quantum Monte Carlo [24–26], the continuous time quantum Monte carlo (CTQMC) [27, 28], encounter, what is known as the fermionic sign problem at very low temperatures and hence cannot exactly describe low T or $T = 0$ properties. The numerical renormalization group (NRG) approach [29–31] is another highly efficient method that can capture the impurity Kondo effect. Although numerically exact, these highly accurate methods are computationally expensive. Semi-analytical methods like the iterated perturbation theory (IPT) [32] or the local moment approach (LMA) [33] on the other hand are approximate but cheap. While IPT fails to capture the Kondo effect correctly, it does predict a Mott MIT in the HM as a function of U. The LMA [33] on the other hand, captures all aspects of the strong coupling physics of these models, but, for the HM predicts a relatively smaller coexistence regime unlike the other methods [34]. Nevertheless, it captures the correct spectral lineshapes at all energies. This thesis uses the LMA as the solver and utilizes several extensions of DMFT depending on the nature of the problem or the model being looked at. These frameworks are discussed in detail in Chapter 2, including a section on the LMA.

The above models and frameworks can be easily utilized/modified in order to explore certain spatially and energetically inhomogeneous scenarios of the above clean models. Indeed, exploring these physical scenarios, forms the main subject of interest in this thesis. We, therefore, now discuss, the inhomogeneous extensions of the above models that are particularly relevant to this thesis.

1.3 Inhomogeneous scenarios in SCES

1.3.1 Strongly correlated heterostructures: Spatial inhomogeneity

Current state-of-art experimental techniques in fabrication processes of layered structures [10, 11, 35] has led to a fascinating new research field: artificial structures of complex materials with strongly correlated electron systems [2, 7, 36]. Such artificial structures offer new playgrounds to control the material properties and it is possible to reach regimes which are not accessible in bulk. Moreover, materials with strongly correlated electron systems show a rich variety of electronic and magnetic states. Therefore, their phase diagrams are considerably richer compared to semiconductors and standard metals. One of the main interests in these geometries is the possibility of stabilizing new/unconventional phases at a hetero-interface. Over the past few years, several experiments have been conducted on this front. Heterostructures involving manganites [36] have been extensively studied.

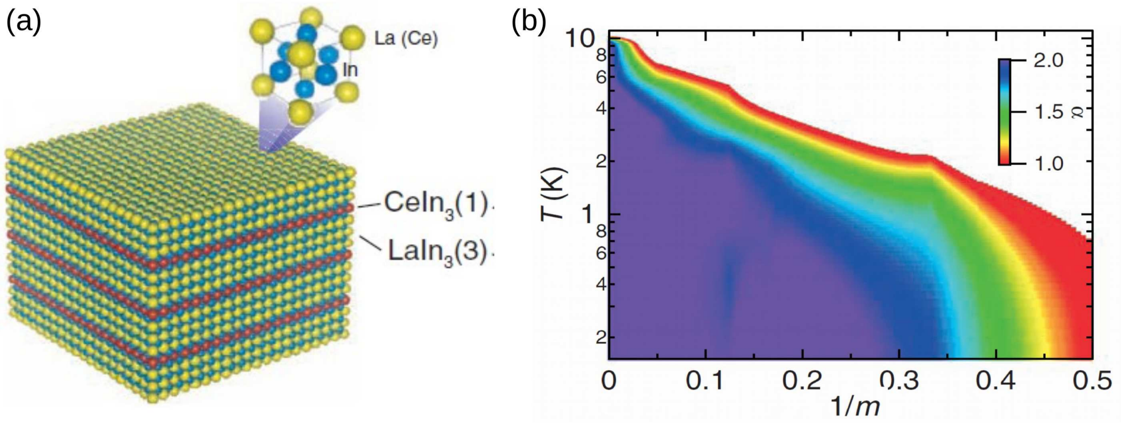

Figure 1.6: **Experimental realization of a heavy fermion heterostructure:** (a) Schematic illustration of an artificial superlattice $(m : n)$ composed of m unit cell-thick layers of heavy fermion (HF) CeIn$_3$ and n unit cell-thick layers of non-interacting LaIn$_3$. (b) Evolution of the exponent α in resistivity, $\rho(T) = \rho_0 + AT^{\alpha}$, as a function of the number of HF layers, m, displaying deviations from the standard Fermi liquid low-temperature electronic properties as m is reduced. This figure is taken from [10] with permission.

For example experiments on manganites have demonstrated unique realizations of interfacial magnetism. Recently an inverse spin switch behaviour was observed in layered systems involving $La_{1-x}Ca_xMnO_3$ and $Y_2Ba_3CuO_{7-\delta}$ [37]. Such effects can be useful for spintronic applications.

The heterostructure geometry naturally leads to a physical situation where one encounters a disordered interface. Particularly, a hetero-interface may lead to a natural *electronic doping* scenario, as opposed to *chemical doping*; and *electronic doping* creates a *quenched disorder* scenario, (a situation that will be discussed in the next section,) unlike chemical doping that has a tendency to induce structural and Coulombic defects in the material [38]. Thus, detailed studies on heterostructure geometries opens up new possibilities for realizing unconventional phases originating due to an interplay of disorder and electronic correlations that is otherwise not realizable in chemically doped bulk materials. Such concepts of interface engineering may also help unveil the true phase diagram of high temperature superconductors. For example, in the phenomenological calculations by Alvarez *et al.* in Ref.[39], they showed that the true experimentally observed phase diagram of $La_{2-x}Sr_xCuO_4$ (LSCO) can in fact be obtained from the clean limit theoretical phase diagram by merely adding quenched disorder in the theoretical model. In this connection, Cu-oxide multilayers provide a possible path of naturally realizing quenched disorder and reveal the *real clean limit* phase diagram, which, may be currently distorted by the chemical doping procedure.

Experiments on heavy fermion layers have reported dimensional confinement of the heavy f electrons [10]. These dimensionally confined systems then displayed non-FL properties that manifested as a linear temperature dependence in resistivity, $\rho_{xx} \sim T$, with a T^2 behavior recovered on increasing the number of $CeIn_3$ layers. Among several other questions, lie, the effects of this reduced translational symmetry on the excitation spectrum of the single particle quantities. This report is also shown in Fig. 1.6 as an example.

Theoretically, the reduced translation symmetry in such surface/heterostructure geometries complicate the situation, in addition, to the challenges involved in treating the many body problem. From a model context, such strongly correlated heterostructures may be described by including interlayer coupling/hybridization terms in the conventional Hubbard or the periodic Anderson model, depending on the relevant physical scenario.

1.3.2 Energetic disorder in electronic systems

Over the years physicists have studied crystalline materials in great detail since the beginning of quantum mechanics. A perfectly crystalline material is periodic in structure and hence permits the classification of electronic wave functions as Bloch waves [16]. This makes life much simpler and allows the calculation of band structures. However, in real life, disorder exists in varying degree. It can range from a few impurities or interstitials in an otherwise perfect host or may manifest as alloy disorder or as glassy amorphous solids. In a crystalline metal, in the weak disorder limit, it was traditionally thought that Bloch waves get scattered off impurities leading to a diffusive transport with the low temperature resistivity of the form, $\rho(T) = \rho_0 + AT^n$, where, T is the temperature of the system and ρ_0 denotes the residual resistivity. Here, $A > 0$ and $n \geq 2$ ($n = 2$, if electron-electron scattering dominates). On the other hand, in the strong disorder limit, the traditional approach was to embed the system into an effective mean field medium and force some average periodicity on the system, so that the traditional concepts of ordered lattices may be employed.

Numerous studies over the past few years led to a common understanding that disorder may not be treated in a mean field fashion [14]. In real-life systems two different aspects would arise. The first is the concept of Anderson localization, to which we shall come shortly and the second aspect deals with the physics due to the Coulomb interactions between the electrons. The Fermi liquid quasi-particles are now diffusive, in presence of the random disorder potentials. This leads to profound modifications in the physics of the system.

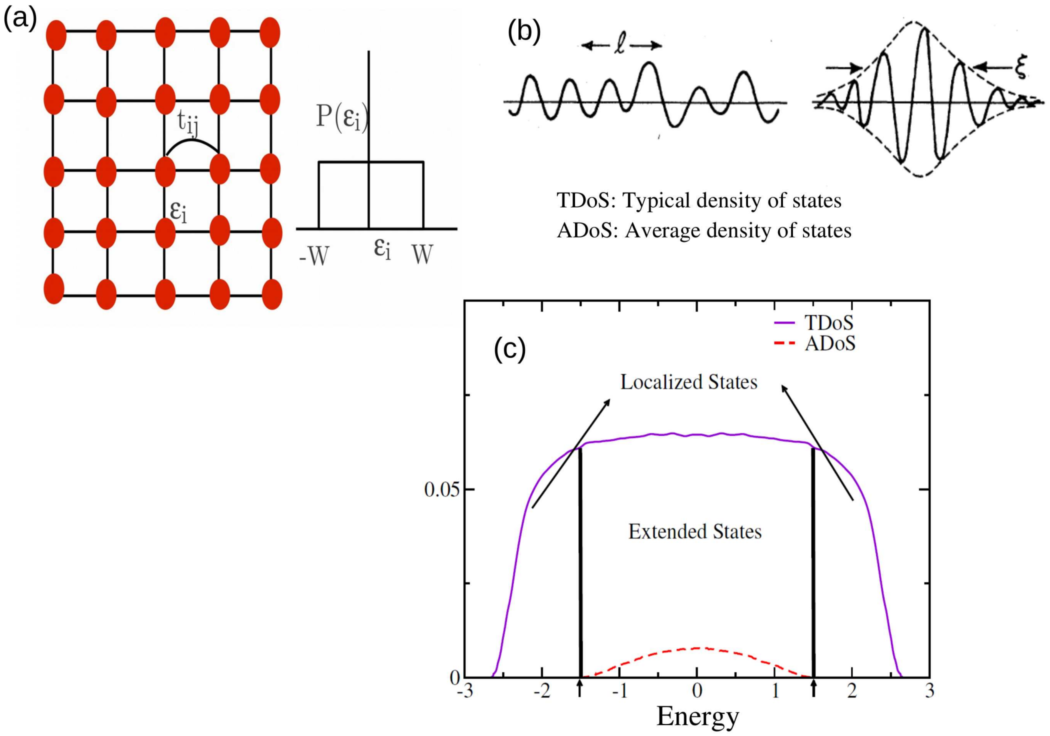

Figure 1.7: **Quenched disorder in non-interacting systems:** (a) Schematic illustration of the Anderson model, in which an electron hops around a disordered lattice background, with kinetic energy, t_{ij}, where the disorder is experienced through the random on-site potential energy (ϵ_i) landscape, thus breaking the original lattice translation symmetry. The ϵ_i's follow a probability distribution which may be represented as a box (shown in figure) or binary, or gaussian etc. (b) When an electron moves around a disordered lattice, unlike a Bloch lattice, it acquires a mean free path, l, as shown in the figure, that measures the average distance travelled by the electron between two successive scattering events. The disordered metallic state will thus be represented as an extended state with a finite l in real space. This schematic is taken from [13] with permission. There would also be localized states centred around the strong scattering centres, and the wavefunction of a localized electron would be characterised by a localization length, ξ as shown in the figure. (c) The same picture in the energy space, where the (arithmetically) disorder averaged density of states (ADoS) will comprise extended and localised states. The band-edge of geometrically averaged (typical) density of states (TDoS) represents the mobility edge.

Anderson localization in non-interacting systems

In his seminal paper [12] called "Absence of diffusion in certain random lattices", Anderson presented a simple model to show that, in a disordered lattice, i.e. a lattice with random site energies, particle diffusion may be suppressed or absent. The Anderson Hamiltonian (schematically represented in Fig. 1.7(a)) is given by,

$$H = -t \sum_{\langle ij \rangle, \sigma} \left(c^{\dagger}_{i\sigma} c_{j\sigma} + H.c. \right) + \sum_{i} \ \epsilon_i \hat{n}_i \tag{1.5}$$

where, t is the hopping amplitude; $c^{\dagger}_i (c_i)$ creates (annihilates) an electron with spin σ at site i and $\hat{n}_i$ is the electron number operator; ϵ_i's are the random site energies distributed according to some distribution function characterized by width D. For $D \ll t$, Bloch waves lose phase coherence on a length of the order of the mean free path l; hence between two successive scattering events, electrons move ballistically and one recovers the conventional resistive behaviour. This idea is shown in Fig. 1.7(b).

When $D \gg t$, Eq. (1.5) physically describes electrons moving in random potential wells where some of these wells are very deep compared to the kinetic energies. Anderson pointed out that in such a scenario, the electron's wave function, $\psi_n(r)$ would decay exponentially from some point r_0 to r in space, as, $\psi_n(r) \approx \mathrm{e}^{-\frac{r-r_0}{\xi}}$, where, ξ is the localization length. This is also shown in Fig. 1.7(b). If the disorder is strong enough or the potential well is deep enough there exists a possibility of exponential localization of an electronic state depending on the energy of the state. As, illustrated in Fig. 1.7(c), the electronic local density of states thus consists of extended and localized states that hybridize and give rise to the global density of states, such that the localized states manifest themselves as tails and the extended states occur around the band center of the global density of states. It was Mott's reasoning that the extended states would exist near the center of the band while the localized states would be confined in the tails. With an increase in the disorder strength, the mobility edge separating the extended and localized states start moving towards the band center and at the Anderson localization transition (ALT) all the localized states reach the band center. Hence, the states at the Fermi level change their nature from being macroscopically extended to being exponentially localized, leading to a metal insulator transition.

Experimental observations of disorder induced metal-insulator transitions

One of the earliest experimental observations of disorder induced metal-insulator transition, namely, the ALT is on the amorphous semiconductors [14]. In the electron localized regime, the temperature (T) dependent conductivity, $\sigma(T)$, is due to electron-phonon coupling and is observed to follow Mott's *variable range hopping* [40, 41], *i.e.*, a thermally activated conductivity [42],

$$\sigma(T) \sim \exp\left(-\left(\frac{T}{T_0}\right)^{\frac{1}{d+1}}\right) \tag{1.6}$$

where d is the dimension. Efros and Shklovskii [43], showed that in 3-dimensions, the exponent in Eq. (1.6) changes from 1/4 to 1/2 when Coulomb interactions between the localized electrons are taken into account.

One of the most studied systems exploring electron localization is the heavily doped semiconductor like the Si:P and Si:B [44–46]. Some of the predictions of the single parameter scaling theory [47] were experimentally tested in these experiments. However, for several data sets, there exists an apparent discrepancy between the scaling theory and experimental observations [15, 48, 49]. Electron-electron interactions, ignored in the scaling theory have been speculated to be an important ingredient for understanding the precise nature of the metal-insulator transitions in these compounds [50–53].

Interactions and random energetic disorder

We now realize that in fermionic systems there are two basic routes to electron localization, namely, the disorder driven [12] or the interaction driven [54, 55]. Naively, this may lead us to think that both these ingredients would favor insulating behaviour. However, this prejudice underestimates the considerable richness of the disordered many-body problem. Each of these fundamental phenomena, electron correlations and disorder, on its own gives rise to both experimental and theoretical challenges. It is still a subject of current investigations and this interplay is of central interest within present day solid state physics research. Disorder and (a certain amount of) interactions being ubiquitous in nature, the realistic modeling of materials requires the simultaneous consideration of both effects. It is now well established that both these phenomena individually and in combination, modify the transport properties of solids [19, 56–59] (leading to metal-insulator phase transitions), the precise nature of which is a challenging question to answer. The physics due to the combined effects of disorder and electron correlations [60, 61] undoubtedly lead to unconventional physics and investigating one such aspect serves to be one of the purposes of this thesis.

Although both interactions and disorder tend to localize the electrons, their combined effect is not always cooperative. There occurs non-trivial renormalization of the electron trajectories such that the mobility edges and the critical parameters like the critical disorder strengths may be different from those of the pure Anderson MIT. A minimal model to explore these issues is the Anderson-Hubbard model (shown as a schematic in Fig. 1.8(a)), given by,

$$\mathcal{H} = \sum_{ij,\sigma} t_{ij} c^{\dagger}_{i\sigma} c_{j\sigma} + \sum_{i,\sigma} (\epsilon_i - \mu) \hat{n}_{i\sigma} + U \sum_{i} \hat{n}_{i\uparrow} \hat{n}_{i\downarrow}, \tag{1.7}$$

where, $c^{\dagger}_{i\sigma}$ ($c_{i\sigma}$) is the fermionic creation (annihilation) operator for an electron with spin σ at site i, and $\hat{n}_{i\sigma} = c^{\dagger}_{i\sigma} c_{i\sigma}$, t_{ij} is the site to site hopping amplitude, U is the onsite Coulomb interaction energy. The random onsite energy, ϵ_i is considered to follow a box distribution $P(\epsilon_i)$ of width W. In the limit $W = 0$ this model reduces to the conventional single band Hubbard model which at half-filling exhibits an interaction driven metal-insulator transition [23] as schematically shown in Fig. 1.8(b). In the other limit when, $U = 0$, a disorder driven metal-insulator transition is observed as shown in Fig. 1.8(c). Let us now, very briefly, look at certain interesting consequences of this interplay, that have been reported in the literature:

Single particle spectra:

Several, recent studies have reported the phase diagram of the above model in the W-U plane [62, 63]. These studies support the fact that for moderate interaction strengths, the critical disorder strength for localization, increases with an increase

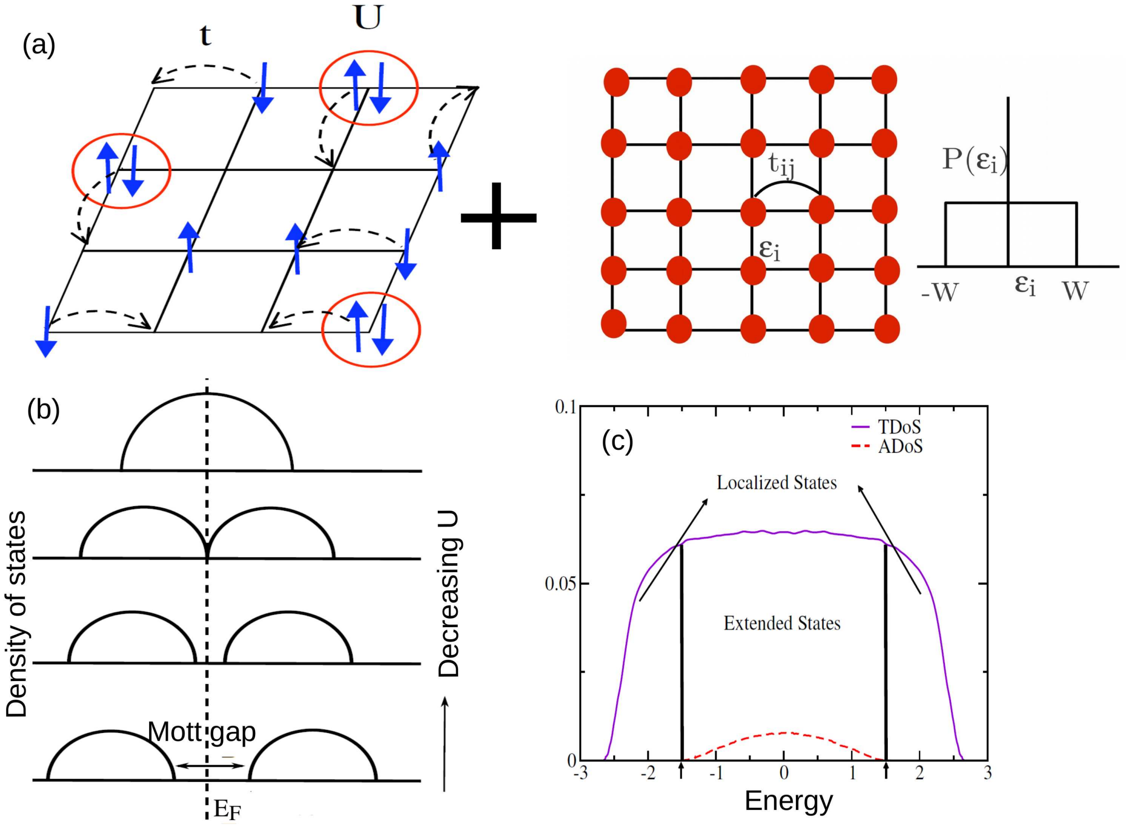

Figure 1.8: **Interactions and disorder:** (a) Schematic illustration of the Anderson-Hubbard model for treating the interplay of quenched disorder and interactions. (b) Schematic of interaction driven Mott metal-insulator transition in a clean Hubbard model and (c) disorder driven metal-insulator transition in an Anderson model.

in U. A particular recent study [64] on the *effects of weak interactions* on the single-particle mobility edge, in presence of disorder, $W < W_c^{U=0}$, where, $W_c^{U=0}$ is the critical disorder strength for the ALT in a non-interacting system, revealed that for $\mu < \omega_\epsilon$, (where, ω_ϵ is the mobility edge energy in absence of interactions,) arbitrary small interactions lead to the masking of a sharp mobility edge, that separates the localized and extended states in the non-interacting case. However, when, $\mu > \omega_\epsilon$, the well defined localization edge is restored.

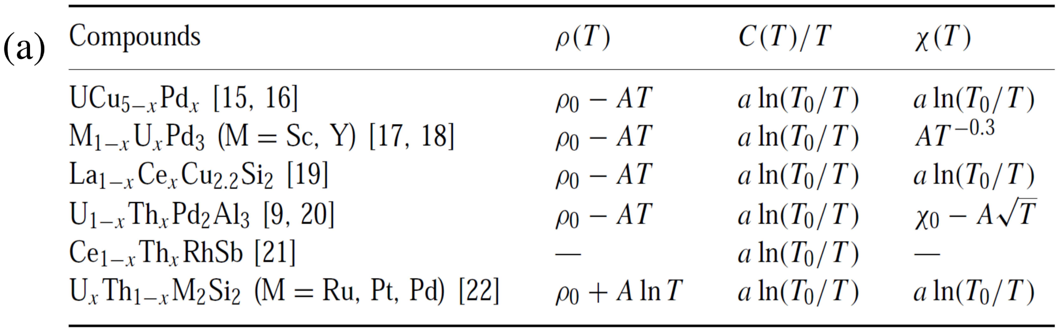
(a)

Compounds	$\rho(T)$	$C(T)/T$	$\chi(T)$
$UCu_{5-x}Pd_x$ [15, 16]	$\rho_0 - AT$	$a\ln(T_0/T)$	$a\ln(T_0/T)$
$M_{1-x}U_xPd_3$ (M = Sc, Y) [17, 18]	$\rho_0 - AT$	$a\ln(T_0/T)$	$AT^{-0.3}$
$La_{1-x}Ce_xCu_{2.2}Si_2$ [19]	$\rho_0 - AT$	$a\ln(T_0/T)$	$a\ln(T_0/T)$
$U_{1-x}Th_xPd_2Al_3$ [9, 20]	$\rho_0 - AT$	$a\ln(T_0/T)$	$\chi_0 - A\sqrt{T}$
$Ce_{1-x}Th_xRhSb$ [21]	—	$a\ln(T_0/T)$	—
$U_xTh_{1-x}M_2Si_2$ (M = Ru, Pt, Pd) [22]	$\rho_0 + A\ln T$	$a\ln(T_0/T)$	$a\ln(T_0/T)$

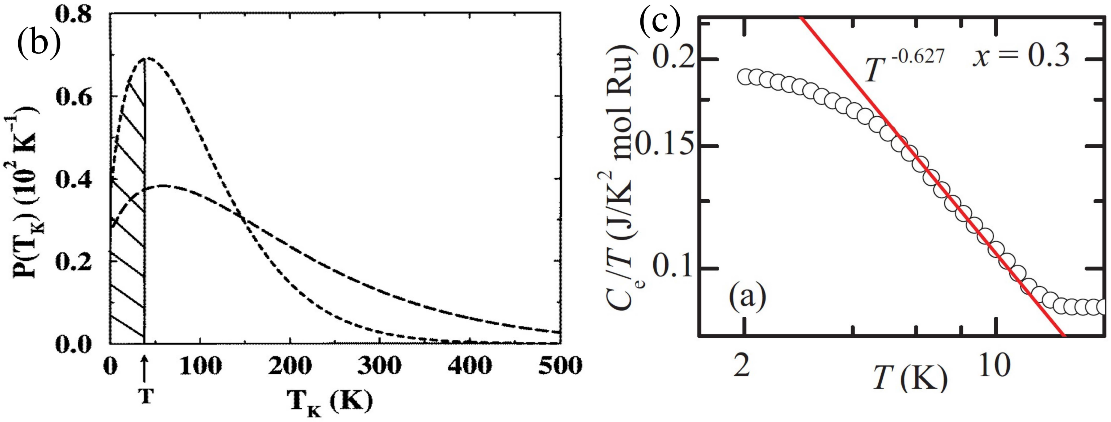

Figure 1.9: **Disorder induced non-Fermi liquid:** (a) Heavy-fermion alloys which exhibit non-Fermi-liquid behaviour as demonstrated by their anomalous thermodynamic response. Here, $\rho(T)$ is the DC resistivity, $C(T)$ is the specific heat, $\chi(T)$ is the magnetic susceptibility. (b) Schematic illustration of a distribution of Kondo scales expected to originate in a disordered interacting system, such that some sites with very small Kondo temperatures are *unquenched* at low temperatures (shaded region) dominating the thermodynamics and transport. Figures (a), (b) are taken from [59] (c) Similar signatures in doped ruthenates. This is taken from [58] with permission.

Disorder induced non-Fermi liquid:

Another interesting effect of this interplay is the realization of disorder induced non-Fermi liquids that have been observed in experiments [21, 61]. Several, alloy/doped materials have exhibited singular thermodynamic responses as a function of increasing doping concentration. Fig. 1.9(a) lists out some of these experimental observations. Microscopic disorder has been speculated to be the prime reason behind such non-Fermi liquid responses, the central idea being the emergence of a broad distribution of Kondo scales, $P(T_K)$ such that, a few local sites with very small Kondo temperatures are unquenched at low temperatures and transport and thermodynamics is dominated by these local moments. Such a distribution is shown in Fig. 1.9(b). In Fig. 1.9(c), we show the work of Qu *et al.* [58] where non-Fermi liquid signatures were observed in doped ruthenates. Several, theoretical calculations [61, 65, 66] based on statistical-DMFT [67] and slave-boson mean-field theory [68–70] derived $P(T_K)$ of the form $P(T_K) \sim T_K^{\alpha-1}$, where the exponent α was found to be a continuously varying function of the disorder strength, W. When, $\alpha < 1$ nFL behaviour is expected to be observed in the response functions. These are important observations and a large section of this thesis is devoted to investigations od nFL behaviour in these systems.

1.4 Outline of the thesis

1.4.1 Theoretical Frameworks

In **Chapter 2** of this thesis, we begin with a discussion of the dynamical mean field theory (DMFT) [23] and the dynamical cluster approximation (DCA) [71] in sufficient detail thus building the introductory basis for adapting these to inhomogeneous situations. We also provide a description of the local moment approach (LMA) [33] that we have used throughout this thesis, for looking into the interacting problem.

Subsequently, we discuss the inhomogeneous DMFT (IDMFT) [72, 73] for looking into heterostructures thus setting up the stage for also looking at emergent physics at disordered interfaces and heterojunctions that serves to be the basic theoretical framework for Chapter 3 and Chapter 4.

We provide a very brief overview of the various effective medium theories for investigating quenched disorder scenarios in electronic systems. Specifically, we mention the drawbacks of the theories like coherent potential approximation, DMFT and DCA for energetically disordered systems [60, 74–76] and highlight the need for their refinements so that disorder induced quantum critical physics may be observed in both non-interacting and interacting electronic systems. We discuss the typical medium theory [60, 77] and how it may be embedded within DMFT [62, 63], for looking into interacting disordered electronic systems, at a *site local* level. This happens to be the framework for Chapter 5. We follow this up with an introduction to the typical medium DCA [76] that has been recently developed and proved to be a both qualitatively and quantitatively successful theory for exploring Anderson localization physics in non-interacting systems. This framework may be viewed as a first systematic cluster extension of the local TMT. The efficiency and versatility of this framework offers possibilities of extensions to interacting systems. And this development and implementation serves to be one of the main ingredients of Chapter 6.

1.4.2 Problems treated in this thesis:

Proximity effects of substitutional disorder in heavy fermion multilayers

In **Chapter 3**, we explore model heavy fermion heterostructure geometries, where, a single Kondo insulator may be coupled to several other Kondo insulators or metallic layers or band insulating layers. In particular, we mimic a disordered interface by doping the boundary Kondo insulator with Kondo holes. We implement a self-consistent scheme within the IDMFT framework, and combine it with a coherent potential approximation for exploring such a substitutional disordered interface. Although, we used it for a particular heterostructure model comprising of heavy-fermion layers, it may well be adapted for other strongly correlated disordered interfaces. Moreover, this framework may easily be used to explore multiple disordered interfaces. With this implementation, we investigate the effect of disorder on the dynamical spectrum of layered f-electron systems. With random dilution of f sites in a single Kondo insulating layer, we explore the range and extent to which Kondo hole incoherence can penetrate into adjacent layers. We also discuss the possibility of a crossover from non-Fermi-liquid to Fermi-liquid behavior upon increasing the ratio of clean to disordered layers in particle-hole asymmetric systems.

Quantum critical Mott transitions in a Kondo insulator-metal heterojunction

As already discussed in the introduction, heterostructure/hetrojunction geometries offer an interesting playground for realizing and stabilizing unconventional quantum phases which may otherwise not be realizable in the bulk scenario. In **Chapter 4**, we investigate a bilayer Kondo-insulator-metal model system, where only the conduction electrons of each layer are mutually coupled, via, an interlayer coupling, $t_\perp$. Our preliminary study on such a bilayer system in the previous chapter, showed the emergence of a metallic character in the otherwise localized f-electrons when they are indirectly coupled to a non-interacting metallic layer. Guided by this *emergent* similarity of the f e^- density of states (DoS) to paramagnetic DoS of rare-earth materials, we ask if a Mott transition can be induced in this model, and, if so, then what would be the nature of the Mott transition of the f e^-s. We first set the stage by providing some physical insights using our low frequency analysis, and then provide the entire phase diagram of the Mott transitions in the interlayer coupling-interaction plane. Guided by the spectral lineshape and the behaviour of the low energy scales of the problem, we predict the existence of an entire surface of *quantum critical* Mott transitions in this model.

A local theory for the Anderson-Mott localization

In **Chapter 5**, we shift our focus from spatially inhomogeneous geometries to energetically inhomogeneous situations. In this chapter, we revisit the Anderson-Hubbard model (AHM), on a 3D cubic lattice, within the local framework of TMT-DMFT, but with the LMA. It is to be noted that the TMT-DMFT framework requires one to use a real frequency impurity solver. The importance of this work is two fold:

(1) Earlier investigations of the AHM within the TMT-DMFT framework were performed using the numerical renormalization group method (NRG) [62] and mean field slave-boson (SB) based methods [63]. The work by Byczuk *et al.* [62], using NRG, however did not explore the evolution of the low energy Kondo scales as a

function of disorder. This was subsequently, explored using the mean-field SB based calculations [63]. However, it is well known that SB based methods fail to account for inelastic scatterings thus failing to predict the correct spectral lineshape. The LMA on the other hand has been extensively benchmarked with NRG for impurity models [78] and has successfully described several aspects of interacting lattice models like the PAM [22, 79] or the HM [34], when utilized within the framework of DMFT. It is known to capture both the high and low energy features efficiently. This motivates the use of LMA for justifying its applicability for disordered interacting systems. The earlier works focused on the Bethe lattice, while our calculations are obtained for a 3-dimensional cubic lattice DoS. Therefore, while an extensively quantitative benchmark is not possible, we however obtain the same qualitative physics in agreement with the other methods. Our numerics successfully capture the high energy Hubbard bands simultaneously providing access to the low energy scales. Additionally this implementation helps us look into several new aspects of the AHM predicatble within the local theory. We explored the distribution of Kondo scales and the disorder averaged self-energy demonstrating the existence of *universal* single particle dynamics even in an interacting disordered system.

(2) This successful implementation opens up a possibility of exploring short range correlation effects of disorder within the TMDCA. This development paves way for the work presented in Chapter 6 of this thesis.

Emergence of non-Fermi liquid dynamics through non-local correlations in an interacting disordered system

In **Chapter 6** we develop a cluster extension of the TMDCA for interacting disordered systems with the aim of investigating low energy physics due to short range correlation effects of disorder and its interplay with interactions. Within this framework, we self-consistently embed a real space cluster in a *appropriately* disorder averaged hybridizing medium with non-local spatial fluctuations built in. The interaction self-energy is however approximated to be local, in similar spirit, as in statistical DMFT. Guided by the studies of the Anderson model, we ensured that a proper ansatz for the typical density of states was considered so that the theory did not suffer from any self-averaging issues, a crucial criterion to eliminate, for looking at Anderson localization physics within an effective medium theory.

We first outline the above numerical implementation, subsequently, (1) we explore the precise evolution of the disorder averaged scattering dynamics and the associated distribution of Kondo scales; (2) we predict the emergence of a disorder induced non-Fermi liquid (nFL) dynamics and a unique disorder dependent FL to nFL crossover scale; (3) and we also contrast the non-local physics of disorder with that obtained from TMT-DMFT. In particular, we show that indeed the systematic inclusion of non-local, dynamical correlations due to disorder render a broad distribution of Kondo scales with a lower T_K tail that is responsible for the emergent non-Fermi liquid scale in the self-energy of the electrons. Our precise calculations, also suggest, that this phenomenon is not limited to any specific regime of interaction strengths in the AHM, but may be observed generically as a function of disorder, even for a low/moderate interaction strength. The emergent non-FL dynamics also provides insight into the generic quantum critical phenomenon of the disorder driven transition in an interacting system.

Summary and future outlook

In **Chapter 7** we summarize the thesis, highlighting the significance of the works presented in Chapters 3, 4, 5 and 6. This thesis opens up several new directions to be further explored and in this chapter we also outline some of these.

Bibliography

[1] E. Morosan, D. Natelson, A. H. Nevidomskyy, and Q. Si, Advanced Materials **24**, 4896 (2012).

[2] E. Dagotto, Science **318**, 1076 (2007).

[3] Z. Yang, C. Ko, and S. Ramanathan, Ann. Rev. Mater. Res. **41**, 337 (2011).

[4] N. F. Mott, *Metal-Insulator transitions* (Taylor and Francis, 1990).

[5] J. Hubbard, Proceedings of the Royal Society of London A: Mathematical, Physical and Engineering Sciences **276**, 238 (1963).

[6] J. Hubbard, Proceedings of the Royal Society of London A: Mathematical, Physical and Engineering Sciences **281**, 401 (1964), ISSN 0080-4630.

[7] P. Zubko, S. Gariglio, M. Gabay, P. Ghosez, and J.-M. Triscone, Ann. Rev. Condens. Matter Phys. **2**, 141 (2011).

[8] F. Baiutti, G. Logvenov, G. Gregori, G. Cristiani, Y. Wang, W. Sigle, P. van Aken, and J. Maier, Nature communications **6** (2015).

[9] S. Hormoz and S. Ramanathan, Solid-State Electronics **54**, 654 (2010).

[10] H. Shishido, T. Shibauchi, K. Yasu, T. Kato, H. Kontani, T. Terashima, and Y. Matsuda, Science **327**, 980 (2010).

[11] M. Shimozawa, T. Watashige, S. Yasumoto, Y. Mizukami, M. Nakamura, H. Shishido, S. K. Goh, T. Terashima, T. Shibauchi, and Y. Matsuda, Phys. Rev. B **86**, 144526 (2012).

[12] P. W. Anderson, Phys. Rev. **109**, 1492 (1958).

[13] P. A. Lee and T. V. Ramakrishnan, Rev. Mod. Phys. **57**, 287 (1985).

[14] B. Kramer and A. Mackinnon, Rev. Prog. Phys. **56**, 1469 (1993).

[15] F. Evers and A. D. Mirlin, Rev. Mod. Phys. **80**, 1355 (2008).

[16] N. Ashcroft and N. Mermin, *Solid State Physics* (Thomson, 2007).

[17] L. Landau, Soviet Physics Jetp-Ussr **3**, 920 (1957).

[18] P. Nozières and D. Pines, *The Theory of Quantum Liquids* (Westview Press, Boulder, CO, 1999).

[19] P. Limelette, A. Georges, D. Jérome, P. Wzietek, P. Metcalf, and J. M. Honig, Science **302**, 89 (2003), ISSN 0036-8075.

[20] A. Pergament, G. Stefanovich, and A. Velichko, Journal on Selected Topics in Nano Electronics and Computing **1**, 24 (2013).

[21] Z. Fisk, D. W. Hess, C. J. Pethick, D. Pines, J. L. Smith, J. D. Thompson, and J. O. Willis, Science **239**, 33 (1988), ISSN 0036-8075.

[22] N. S. Vidhyadhiraja and D. E. Logan, Journal of Physics: Condensed Matter **17**, 2959 (2005).

[23] A. Georges, G. Kotliar, W. Krauth, and M. J. Rozenberg, Rev. Mod. Phys. **68**, 13 (1996).

[24] J. E. Hirsch and R. M. Fye, Phys. Rev. Lett. **56**, 2521 (1986).

[25] N. Blümer, Phys. Rev. B **76**, 205120 (2007).

[26] M. Jarrell, Phys. Rev. Lett. **69**, 168 (1992).

[27] P. Werner, A. Comanac, L. de' Medici, M. Troyer, and A. J. Millis, Phys. Rev. Lett. **97**, 076405 (2006).

[28] A. N. Rubtsov, V. V. Savkin, and A. I. Lichtenstein, Phys. Rev. B **72**, 035122 (2005).

[29] H. R. Krishna-murthy, J. W. Wilkins, and K. G. Wilson, Phys. Rev. B **21**, 1003 (1980).

[30] H. R. Krishna-murthy, J. W. Wilkins, and K. G. Wilson, Phys. Rev. B **21**, 1044 (1980).

[31] R. Bulla, A. C. Hewson, and T. Pruschke, Journal of Physics: Condensed Matter **10**, 8365 (1998).

[32] G. Kotliar and H. Kajueter, Phys. Rev. B **54**, R14221 (1996).

[33] D. E. Logan, M. P. Eastwood, and M. A. Tusch, Journal of Physics: Condensed Matter **10**, 2673 (1998).

[34] D. E. Logan, M. P. Eastwood, and M. A. Tusch, Journal of Physics: Condensed Matter **9**, 4211 (1997).

[35] A. Ohtomo, D. Muller, J. Grazul, and H. Hwang, Nature **419**, 378 (2002).

[36] S. Okamoto, *Multifunctional Oxide Heterostructures* (Oxford University Press, 2012).

[37] N. M. Nemes, M. García-Hernández, S. G. E. te Velthuis, A. Hoffmann, C. Visani, J. Garcia-Barriocanal, V. Peña, D. Arias, Z. Sefrioui, C. Leon, et al., Phys. Rev. B **78**, 094515 (2008).

[38] I. González, S. Okamoto, S. Yunoki, A. Moreo, and E. Dagotto, Journal of Physics: Condensed Matter **20**, 264002 (2008).

[39] G. Alvarez, M. Mayr, A. Moreo, and E. Dagotto, Phys. Rev. B **71**, 014514 (2005), URL `http://link.aps.org/doi/10.1103/PhysRevB.71.014514`.

[40] N. Mott, Philosophical Magazine **6**, 287 (1961).

[41] N. Mott, Philosophical Magazine **19**, 835 (1969).

[42] C.-T. Liang, J. Frost, M. Simmons, D. Ritchie, and M. Pepper, Solid state communications **102**, 327 (1997).

[43] A. Efros and B. Shklovskii, Journal of Physics C: Solid State Physics **8**, L49 (1975).

[44] M. Paalanen, T. Rosenbaum, G. Thomas, and R. Bhatt, Phys. Rev. Lett. **48**, 1284 (1982).

[45] C. Sürgers, M. Wenderoth, K. Löser, J. Garleff, R. G. Ulbrich, M. Lukas, and H. v Löhneysen, New Journal of Physics **15**, 055009 (2013).

[46] Y. Zhou and S. Ramanathan, Critical Reviews in Solid State and Materials Sciences **38**, 286 (2013).

[47] E. Abrahams, P. W. Anderson, D. C. Licciardello, and T. V. Ramakrishnan, Phys. Rev. Lett. **42**, 673 (1979).

[48] H. Stupp, M. Hornung, M. Lakner, O. Madel, and H. v. Löhneysen, Physical review letters **71**, 2634 (1993).

[49] H. Von Loehneysen, Philosophical Transactions of the Royal Society of London A: Mathematical, Physical and Engineering Sciences **356**, 139 (1998).

[50] S. V. Kravchenko, G. V. Kravchenko, J. E. Furneaux, V. M. Pudalov, and M. D'Iorio, Phys. Rev. B **50**, 8039 (1994).

[51] K. Kim, J. Lee, T. Noh, S. Lee, and K. Char, Phys. Rev. B **71**, 125104 (2005).

[52] R. K. Sahu, S. K. Pandey, and L. Pathak, Journal of Solid State Chemistry **184**, 523 (2011).

[53] A. S. Sefat, J. E. Greedan, G. M. Luke, M. Niéwczas, J. D. Garrett, H. Dabkowska, and A. Dabkowski, Phys. Rev. B **74**, 104419 (2006).

[54] N. Mott, Advances in Physics **16**, 49 (1967).

[55] N.F.Mott, in *Metal-Insulator Transitions* (2nd ed. (Taylor and Francis, London, 1990), 1990).

[56] S. V. Kravchenko and M. P. Sarachik, Reports on Progress in Physics **67**, 1 (2004).

[57] M. Paalanen and R. Bhatt, Physica B: Condensed Matter **169**, 223 (1991).

[58] Z. Qu, J. Peng, T. Liu, D. Fobes, V. Dobrosavljević, L. Spinu, and Z. Mao, Phys. Rev. B **86**, 014434 (2012).

[59] E. Miranda, V. Dobrosavljevič, and G. Kotliar, Journal of Physics: Condensed Matter **8**, 9871 (1996).

[60] K. Byczuk, W. Hofstetter, U. Yu, and D. Vollhardt, The European Physical Journal Special Topics **180**, 135 (2009), ISSN 1951-6355.

[61] E. Miranda and V. Dobrosavljević, Reports on Progress in Physics **68**, 2337 (1997).

[62] K. Byczuk, W. Hofstetter, and D. Vollhardt, Phys. Rev. Lett. **94**, 056404 (2005).

[63] M. C. O. Aguiar, V. Dobrosavljević, E. Abrahams, and G. Kotliar, Phys. Rev. Lett. **102**, 156402 (2009).

[64] C. E. Ekuma, S.-X. Yang, H. Terletska, K.-M. Tam, N. S. Vidhyadhiraja, J. Moreno, and M. Jarrell, Phys. Rev. B **92**, 201114 (2015).

[65] M. C. O. Aguiar and V. Dobrosavljević, Phys. Rev. Lett. **110**, 066401 (2013).

[66] E. C. Andrade, E. Miranda, and V. Dobrosavljević, Phys. Rev. Lett. **102**, 206403 (2009).

[67] V. Dobrosavljević and G. Kotliar, Philosophical Transactions of the Royal Society of London A: Mathematical, Physical and Engineering Sciences **356**, 57 (1998).

[68] P. Coleman, Phys. Rev. B **29**, 3035 (1984).

[69] S. E. Barnes, Journal of Physics F: Metal Physics **6**, 1375 (1976), URL `http://stacks.iop.org/0305-4608/6/i=7/a=018`.

[70] J. Kroha, P. Hirschfeld, K. Muttalib, and P. Wlfle, Solid State Communications **83**, 1003 (1992).

[71] H. Lee, Y.-Z. Zhang, H. O. Jeschke, R. Valentí, and H. Monien, Physical review letters **104**, 026402 (2010).

[72] M. Potthoff and W. Nolting, Phys. Rev. B **59**, 2549 (1999).

[73] J. K. Freericks, Phys. Rev. B **70**, 195342 (2004).

[74] R. Elliott, J. Krumhansl, and P. Leath, Reviews of Modern Physics **46**, 465 (1974).

[75] C. E. Ekuma, H. Terletska, Z. Y. Meng, J. Moreno, M. Jarrell, S. Mahmoudian, and V. Dobrosavljeviȁ, Journal of Physics: Condensed Matter **26**, 274209 (2014).

[76] C. E. Ekuma, H. Terletska, K.-M. Tam, Z.-Y. Meng, J. Moreno, and M. Jarrell, Phys. Rev. B **89**, 081107 (2014).

[77] V. Dobrosavljeviȁ, A. A. Pastor, and B. K. Nikoliȁ, Europhys. Lett. **62**, 76 (2003).

[78] M. R. Galpin and D. E. Logan, Journal of Physics: Condensed Matter **17**, 6959 (2005).

[79] N. S. Vidhyadhiraja, V. E. Smith, D. E. Logan, and H. R. Krishnamurthy, Journal of Physics: Condensed Matter **15**, 4045 (2003).

Chapter 2

Theoretical Frameworks

Contents

Chapter 1 provided us with a brief overview of the kind of systems that we aim to look at in this thesis. It also described some of the strongly correlated lattice models that we use to describe the relevant physics of our systems. We realized that for looking into strongly correlated systems, we need approximate frameworks. In this chapter, we shall discuss some of these frameworks, like the dynamical mean field theory, the dynamical cluster approximation. We shall also look at a particular impurity solver called the local moment approach and subsequently also describe how these basic frameworks may be adapted to investigate inhomogeneous strongly correlated models, that serves to be the prime purpose of this thesis.

2.1 The Dynamical Mean Field Theory: Local Approximation

The dynamical mean field theory (DMFT) [1] that has been developed over last decade has significantly contributed to our understanding of strongly correlated systems [2]. In this section we review some of the basic concepts of DMFT and for a more detailed explanation the reader is referred to the available review articles [1]. Theoretical investigations of correlated lattice systems are faced with severe difficulties due to the complicated quantum dynamics present in these systems. Since, the number of possible energy states increases exponentially with the number of lattice sites, numerical solutions of the Hubbard and related models are limited to relatively small systems. Hence, insights into the thermodynamic and spectral properties of such systems through finite sized methods is nearly impossible. Hence, one needs *non-perturbative*, tractable approximation schemes that can handle strongly correlated systems providing insights into the thermodynamic properties. The DMFT is one such theory.

2.1.1 The 'classic' concept of mean-field on a classical lattice model: Ising model

Let us very briefly go through an example of "classical" mean field theory; this will help us build an analogy to the quantum case. We refer to the Ising model with ferromagnetic couplings, represented by the Hamiltonian,

$$\mathcal{H} = -\sum_{\langle i,j\rangle} J_{ij} S_i S_j - h \sum_i S_i; \quad J_{ij} > 0, \tag{2.1}$$

where, S_i's are classical.

The main idea of a mean field theory is to neglect the spatial (and temporal) fluctuations such that a *static effective single particle* problem is created. In order to build a consistent mean field theory, we focus on a specific site, say site o, and replace the effect of the rest of the lattice on this site, by an effective field, thus reducing the many site problem to a single site in an effective field. For, the Ising model, described in Eq. (2.1), the effective Hamiltonian would be,

$$\mathcal{H}_{eff} = -h_{eff} S_o, \tag{2.2}$$

where, h_{eff} is the effective field at site o, and S_o represents the spin at the respective site. This effective field, h_{eff} is what is known as the Weiss field and can be approximated by the thermal average of the field imposed by the neighbouring spins, j, such that,

$$h_{eff} \approx h + \sum_j J_{\langle o,j\rangle} m_j = h + zJm, \tag{2.3}$$

where, z is the number of nearest neighbours, m is the average magnetization, $m_i = \langle S_i \rangle = m$. So we see that, h_{eff} is a functional of m, $h_{eff} = h_{eff}[m]$ and should be chosen such that, the value of m is accurately reproduced. This requires,

$$\beta h_{eff} = \tanh^{-1} m, \tag{2.4}$$

where, β is the inverse temperature. So, m should be determined self-consistently from the following (transcendental) equation:

$$m = \tanh(\beta h + z\beta J m), \tag{2.5}$$

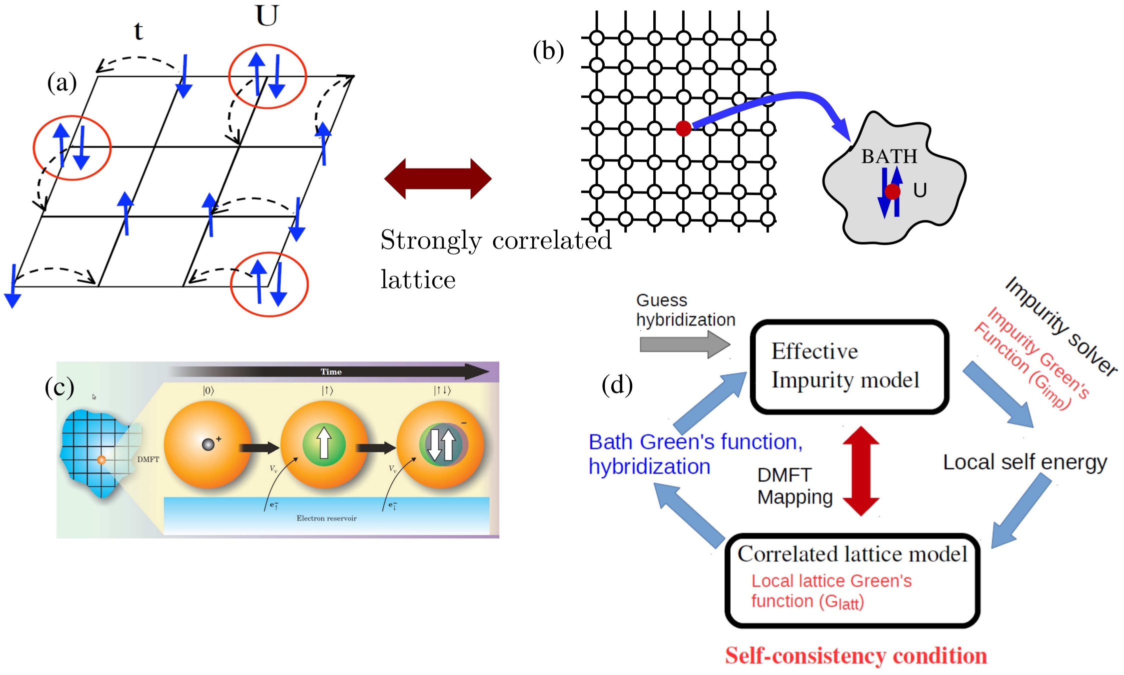

Figure 2.1: **DMFT:** (a) Schematic illustration of the Hubbard model as has also been shown and described in Eq. (1.3), representing an example of a correlated lattice model. (b) Illustration of the cavity construction, where we focus only on one correlated site and integrate out all the other lattice degrees of freedom, as described in the text. This amounts to an effective mapping of the many body lattice model to a single correlated impurity embedded in a self-consistently determined bath that mimics the original many body lattice system in an optimal fashion. (c) The DMFT mapping loses all non-local fluctuations due to this effective single impurity mapping but retains all temporal fluctuiations among the different atomic configurations of the central atom (in orange), shown here as snapshots in time. In this figure, one such possible sequence is illustrated. The hybridization V_ν represents the quantum mechanical amplitude with which an electron hops to and from the reservoir. This schematic is taken from Ref. [2] with permission. (d) The DMFT self-consistency loop.

2.1.2 Generalisation to quantum systems: DMFT

The classical mean field idea can now be extended to a quantum many body system with itinerant degrees of freedom, for example, the Hubbard model (Eq. (1.3)), shown as a schematic in Fig. 2.1(a). However, we need to keep in mind that in the quantum version, the mean field cannot freeze out the temporal degrees of freedom, since quantum fluctuations are a vital ingredient for describing the correct physics. Again, the overall idea is to map the multi-site many body problem on to an effectively single site many body problem. As a demonstration of the prescription, we follow main ideas behind the 'cavity construction' of the Hubbard model (Eq. (1.3)) as outlined below.

2.1.3 Cavity construction

We focus on one site of the many body lattice model described in Eq. (1.3) and shown in Fig. 2.1(b), say, site o and break the total action of the full lattice into three terms, namely,

$$S = S^{(o)} + S_o + \Delta S, \tag{2.6}$$

where, $S^{(o)}$ is the action of the full lattice in absence of site o; this is also referred to as the cavity lattice, or cavity action, and hence the name 'cavity construction'. S_o is the action of site o, and ΔS is the interaction of site o with the cavity lattice. We can now build an effective action for this site or an effective field acting on this site, by integrating out all degrees of freedom, except those pertaining to site o. This effective action, S_{eff} would be given by,

$$S_{eff} = -\int_0^\beta d\tau \int_0^\beta d\tau' \sum_\sigma c^*_{o\sigma}(\tau)\mathcal{G}_0^{-1}(\tau-\tau')c_{o\sigma}(\tau) + U\int_0^\beta d\tau n_{o\uparrow}(\tau)n_{o\downarrow}(\tau) \tag{2.7}$$

The Green's function, $\mathcal{G}_0(\tau-\tau')$ represents the effective field experienced by the single site o and it contains all the effects of the rest of the lattice, namely, the interactions present on these sites, the hopping between the site o and the rest of the lattice. In this regard, S_{eff} would have interactions which are much higher than the quartic Hubbard interaction. The simplification comes in the infinite dimensional limit, $D \to \infty$.

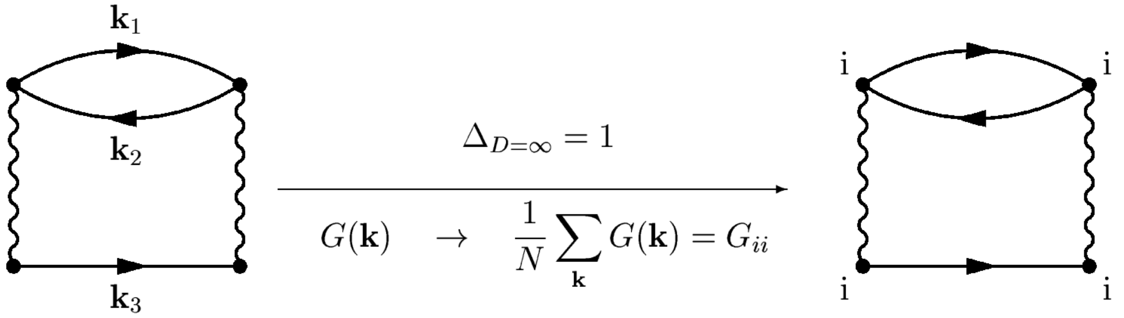

Figure 2.2: **Local self energy in infinite dimensions:** The Laue function defined as, $\Delta(\mathbf{k}_1, \mathbf{k}_2, \mathbf{k}_3, \mathbf{k}_4) = \sum_r \mathbf{e}^{i(\mathbf{k}_1-\mathbf{k}_2+\mathbf{k}_3-\mathbf{k}_4).\mathbf{r}}$. However, as $d \rightarrow \infty$, $\Delta \approx 1$ and therefore the momentum dependence of the self-energy collapses as illustrated in this figure, for a second order diagram. Only local contributions are retained in DMFT.

2.1.4 Limit of infinite dimensions

For models like the Hubbard model, the single particle self-energy, $\Sigma_{ij}(\omega)$ in real space is defined by the single particle Green's function, $G_{ij}(\omega) = \langle\langle c_{i\sigma}; c^\dagger_{j\sigma}\rangle\rangle_\omega$ ($\leftrightarrow G(t) = -i\langle\hat{T}(c_{i\sigma}(t)c^\dagger_{j\sigma}(0))\rangle$)[1] by the Dyson equation,

$$G_{ij}(\omega) = G^0_{ij}(\omega) + \sum_{kl} G^0_{ik}(\omega)\Sigma_{kl}(\omega)G_{lj}(\omega), \tag{2.8}$$

where, G^0 is the non-interacting Green's function.

By inspecting the lattice self-energy, $\Sigma_{ij}[G_{ij}]$, Metzner and Vollhardt [3] demonstrated that in the limit, $d \rightarrow \infty$, the skeleton expansion for Σ collapses onto local diagrams only; therefore the single particle self-energy will be purely local in real space,

$$\Sigma_{ij} = \Sigma_{ij}\delta_{ij}. \tag{2.9}$$

Müller-Hartmann derived the same result in momentum space thus giving an interpretation in terms of the Laue function [4]. The Green's functions can now be

---

[1] t representing the time index

replaced by its local counterparts, such that,

$$\Sigma[G(\mathbf{k})] = \Sigma[G_{ii}] \equiv \Sigma. \tag{2.10}$$

This is also illustrated in Fig. 6.5 for a second order in U diagram. Thus, the mean field idea, which is exact in $d \to \infty$ corresponds to interpreting the single particle lattice self-energy, $\Sigma_{ij}(\omega)$ by a local $\Sigma(\omega)$. The dynamical mean field theory approximation amounts to retaining the same idea even in finite dimensions. Analogously, this whole interpretation leads to the mapping of the lattice model onto an effective local problem.

2.1.5 Mapping to the single impurity Anderson model

The single impurity Anderson model (SIAM) is represented by the Hamiltonian,

$$\mathcal{H} = \sum_{k,\sigma} \epsilon_k c^\dagger_{k\sigma} c_{k\sigma} + \sum_{\sigma} \epsilon_i c^\dagger_{i\sigma} c_{i\sigma} + \sum_{k\sigma} V_k \left(c^\dagger_{i\sigma} c_{k\sigma} + h.c. \right) + U n_{i\uparrow} n_{i\downarrow}. \tag{2.11}$$

This model represents a single correlated site, i, with onsite energy, ϵ_i, coupled to a non-interacting bath with dispersion, ϵ_k. that has effectively the same action representation as Eq. (2.7).

$$S_{eff} = -\int_0^\beta d\tau \int_0^\beta d\tau' \sum_\sigma d^*_\sigma(\tau) \mathcal{G}^{-1}_{SIAM,0}(\tau - \tau') d_\sigma(\tau) + U \int_0^\beta d\tau n_{i\uparrow}(\tau) n_{i\downarrow}(\tau), \tag{2.12}$$

where,

$$\mathcal{G}^{-1}_{SIAM,0}(\omega) = \omega^+ - \epsilon_i - \Delta(\omega), \tag{2.13}$$

with $\Delta(\omega) = \sum_k \frac{|V_k|^2}{\omega + i\eta - \epsilon_k}$. It is this hybridization that has to be chosen or derived self-consistently such that it mimics the original lattice model optimally. In other words, it has to be chosen such that the SIAM Green's function, G_{SIAM} coincides with the lattice Green's function, G_{latt}, where,

$$G_{latt}(\omega) = \sum_k \frac{1}{\omega^+ - \epsilon_k - \Sigma(\omega)}. \tag{2.14}$$

In other words, within DMFT, $\Sigma_{latt}(\omega) = \Sigma_{SIAM}(\omega)$. This self-consistent scheme is depicted in Fig 2.1(d). As illustrated in Fig 2.1(c), the DMFT retains all temporal fluctuations but neglects all spatial correlations. We will briefly look at the local moment approach [5] that serves to be the impurity solver for all the problems looked at in this thesis. Subsequently, we will now briefly review the dynamical cluster approximation [6, 7] which represents on of the non-local extensions of DMFT.

2.2 The Local Moment Approach

The most difficult step in the above is the solution of the effective impurity problem. While there exists several such impurity solvers, analytical, semi-analytical or numerically exact solver, each has their their advantages and drawbacks. In Table. 2.1 we list some of these solvers and highlight some of their characteristics, like the interaction and temperature regime in which it works well, the level of computational complexity involved etc.. There exists only a handful of impurity solvers that can describe the SIAM spectrum in strong coupling, with the ability of recovering both the exponential narrowing of the Kondo resonance and the concomitant many-body broadening of the Hubbard bands. This necessarily requires the use of a non-perturbative framework. The numerically exact numerical renormalization group (NRG) and the continuous time Quantum Monte Carlo (CTQMC) are two such solvers. However, CTQMC yield imaginary frequency quantities and hence requires analytic continuation to real frequency, which is again a complicated procedure. Moreover, it cannot be employed at zero temperature. Other methods like the NRG, exact diagonalization (ED) are computationally expensive and produce discrete features that need broadening, the procedure for which is not systematic.

In this thesis we have employed the local moment approach (LMA) as the impurity solver. A brief discussion of the formalism and the pros and cons of LMA are discussed below. In the following we will discuss some of the basic concepts of the

Table 2.1: **Some commonly impurity solvers within DMFT:** QMC: Quantum Monte-Carlo, IPT: Iterated perturbation theory, NCA: Non-crossing approximation, ED: Exact diagonalization, NRG: Numerical renormalization group, LMA: Local moment approach, DMRG: Density matrix renormalization group. The level of approximation are mentioned under the column 'Category'; the applicability of the solver for large U and low T are mentioned under the columns 'large U' and 'low T' respectively. Additionally, the computational cost involved is mentioned under the column 'Cost' and finally, some of the limitations are mentioned under the column 'Issues'.

Impurity Solvers	Category	large U	low T	Cost	Issues
QMC	exact	good	hard	expensive	need Wick's rotation for real frequency data
IPT	approximate	good	very good	cheap	cannot capture Kondo scales correctly
NCA	approximate	good	very good	cheap	fails to capture Fermi liquid
ED	exact	very good	very good	expensive	discrete single particle spectrum
NRG	exact	very good	very good	expensive	low frequency problems
LMA	approximate	very good	very good	cheap	difficult to extend to cluster theories
DMRG	exact	very good	very good	very expensive	stability issues and numerical artifacts

zero temperature formalism of the LMA. A key physical aspect of this method is the inclusion of the low energy spin-flip excitations in the single-particle dynamics. This is facilitated at the inception by starting from from the unrestricted Hartree Fock (UHF) state: local moments are introduced from the outset, to get a direct handle on the low energy spin-flip processes like the ones illustrated in Fig. 2.3.

(a) Elastic scattering

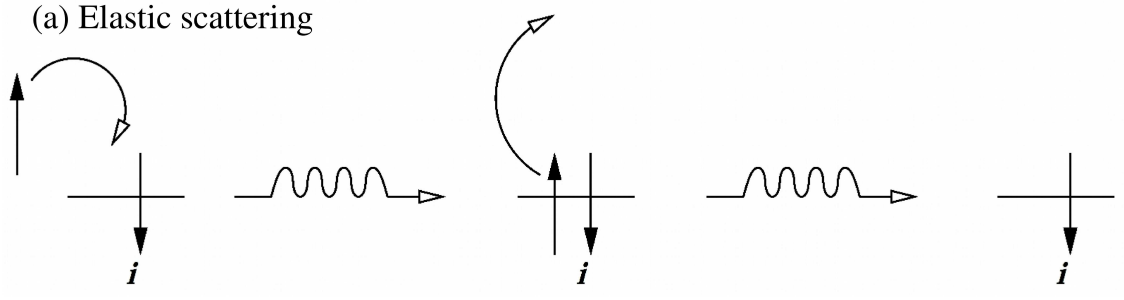

(b) Inelastic scattering

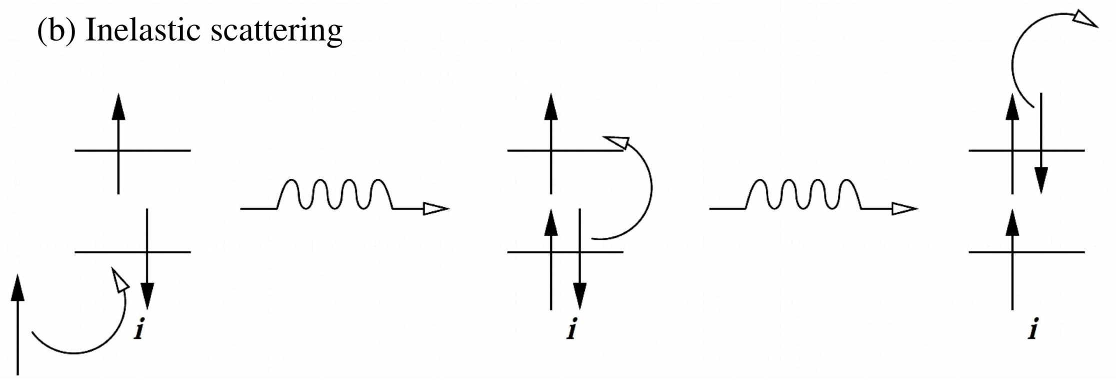

Figure 2.3: **Examples of scattering processes:** (a) Elastic scattering process where only the added spin is allowed to hop off the site. This is a static process as the original spin remains on the site. Such *static* processes are well described by the UHF approximation as they are devoid of any essential dynamics. (b) Inelastic spin flip scattering introducing a local singlet-triplet excitation at the impurity site leaving behind a spin-flip at the impurity site.

2.2.1 Starting point: UHF

Local moments, μ are introduced explicitly and self-consistently at the outset. The solutions are built around simple symmetry broken static mean-field, UHF, states, containing two degenerate states $\mu = \pm|\mu|$, where, $|\mu| = |\langle \hat{n}_{i\uparrow} - \hat{n}_{i\downarrow} \rangle|$, the average being over the UHF ground state. We label A and B for solutions $\mu = +|\mu|$ or $-|\mu|$ respectively. [8]. For an understanding of the formal details the reader is referred to [5, 8]. Here, we briefly recap the main equations. The single particle

UHF Green's functions for the paramagnetic case, are given by,

$$\mathcal{G}_{A\sigma}(\omega) = \frac{1}{\omega + i\eta - \Sigma^0_{A\sigma} - \Delta(\omega)} = \frac{1}{\omega^+ - \epsilon_i - \frac{U}{2}n + \frac{U}{2}\sigma|\mu| - \Delta(\omega)} \tag{2.15}$$

$$\mathcal{G}_{B\sigma}(\omega) = \frac{1}{\omega^+ - \Sigma^0_{B\sigma} - \Delta(\omega)} = \frac{1}{\omega^+ - \epsilon_i - \frac{U}{2}n - \frac{U}{2}\sigma|\mu| - \Delta(\omega)} \tag{2.16}$$

$\Delta(\omega)$ is the hybridization function for the impurity-host coupling. For the paramagnetic case, the hybridizing medium is spin independent. In this case, the A and B solutions are related by symmetry and we can drop the respective labels. We rewrite the above as the following:

$$\mathcal{G}_{\uparrow}(\omega) == \frac{1}{\omega^+ - e_i + x - \Delta(\omega)}, \tag{2.17}$$

$$\mathcal{G}_{\downarrow}(\omega) == \frac{1}{\omega^+ - e_i - x - \Delta(\omega)}, \tag{2.18}$$

where, $x = \frac{1}{2}|\mu|U$ and $e_i = \epsilon_i + \frac{1}{2}Un$. The density of the single-particle excitations is given by,

$$\mathcal{D}_\sigma = -\frac{1}{\pi}\text{Im}\mathcal{G}_\sigma(\omega), \tag{2.19}$$

where, $\sigma = \uparrow / \downarrow$. The local moment, in general, would be given by,

$$|\tilde{\mu}| = \int_{-\infty}^{0} d\omega \left(\mathcal{D}_{\uparrow}(\omega) - \mathcal{D}_{\downarrow}(\omega)\right), \tag{2.20}$$

and has to be obtained *self-consistently* generically. When we are away from particle-hole symmetry (p-h) then we also need the impurity occupancy to be given by,

$$\tilde{n} = \int_{-\infty}^{0} d\omega \left(\mathcal{D}_{\uparrow}(\omega) + \mathcal{D}_{\downarrow}(\omega)\right). \tag{2.21}$$

For the pure mean-field UHF solution, we have,

$$\tilde{\mu} = \mu \tag{2.22}$$

$$\tilde{n} = n, \tag{2.23}$$

to be solved self-consistently through Eqs. (2.22) and (2.23). So, if we now fix x and ${e_i}^2$, then Eqs. (2.22) and (2.23) would provide the solution at one shot and accordingly, the bare parameters may be inferred as $U = 2x/|\mu|$ and $\epsilon_i = e_i - Un/2$. However, if U and ϵ_i are fixed then this has to be obtained by iterative cycling. The UHF solution is however severely deficient (see [5, 8–10]), as most important, is the violation of the Fermi liquid picture. In any case, being a static approximation, one has to go beyond it to incorporate dynamics.

2.2.2 Inclusion of spin-flip scattering dynamics

In this part we will look at the transverse-spin polarization propagators, defined as,

$$\Pi^{+-}_{\alpha\alpha}(t) = i\langle 0|T\left\{\hat{S}^{+}_{\alpha}(t)\hat{S}^{-}_{\alpha}(0)\right\}|0\rangle, \tag{2.24}$$

$$\Pi^{-+}_{\alpha\alpha}(t) = i\langle 0|T\left\{\hat{S}^{-}_{\alpha}(t)\hat{S}^{+}_{\alpha}(0)\right\}|0\rangle, \tag{2.25}$$

where, $\alpha = A, B$ labels the type of site, $\hat{S}^{\pm}_{\alpha}$ are the spin-raising/lowering operators at an α-type site. Within the LMA, one includes spin-flip diagrams as shown in Fig. 2.4, where the bare propagators are that of UHF and therefore the inclusion of all these diagrams constitute the UHF+RPA scheme. The RPA may be cast in the form,

$$\Pi^{+-}(\omega) = \frac{{}^{0}\Pi^{+-}}{1 - U\,{}^{0}\Pi^{+-}}, \tag{2.26}$$

where, ${}^{0}\Pi^{+-}(\omega)$ is the pure UHF transverse spin polarization bubble, whose elements are given as convolutions of the UHF Greens functions, as given in the following,

$${}^{0}\Pi^{+-}(\omega) = \frac{i}{2\pi}\int_{-\infty}^{\infty} d\omega' \mathcal{G}_{\downarrow}(\omega')\mathcal{G}_{\uparrow}(\omega' - \omega) \tag{2.27}$$

At pure UHF level, $|\mu| = |\tilde{\mu}|$ would result in a zero frequency pole in the RPA $\Pi^{+-}(\omega)$. While such behaviour would be correct for the symmetric SIAM with a gapped host, it violates Fermi liquid properties of the gapless SIAM. In the latter

---

[2] Note that they are not the bare parameters of the Hamiltonian.

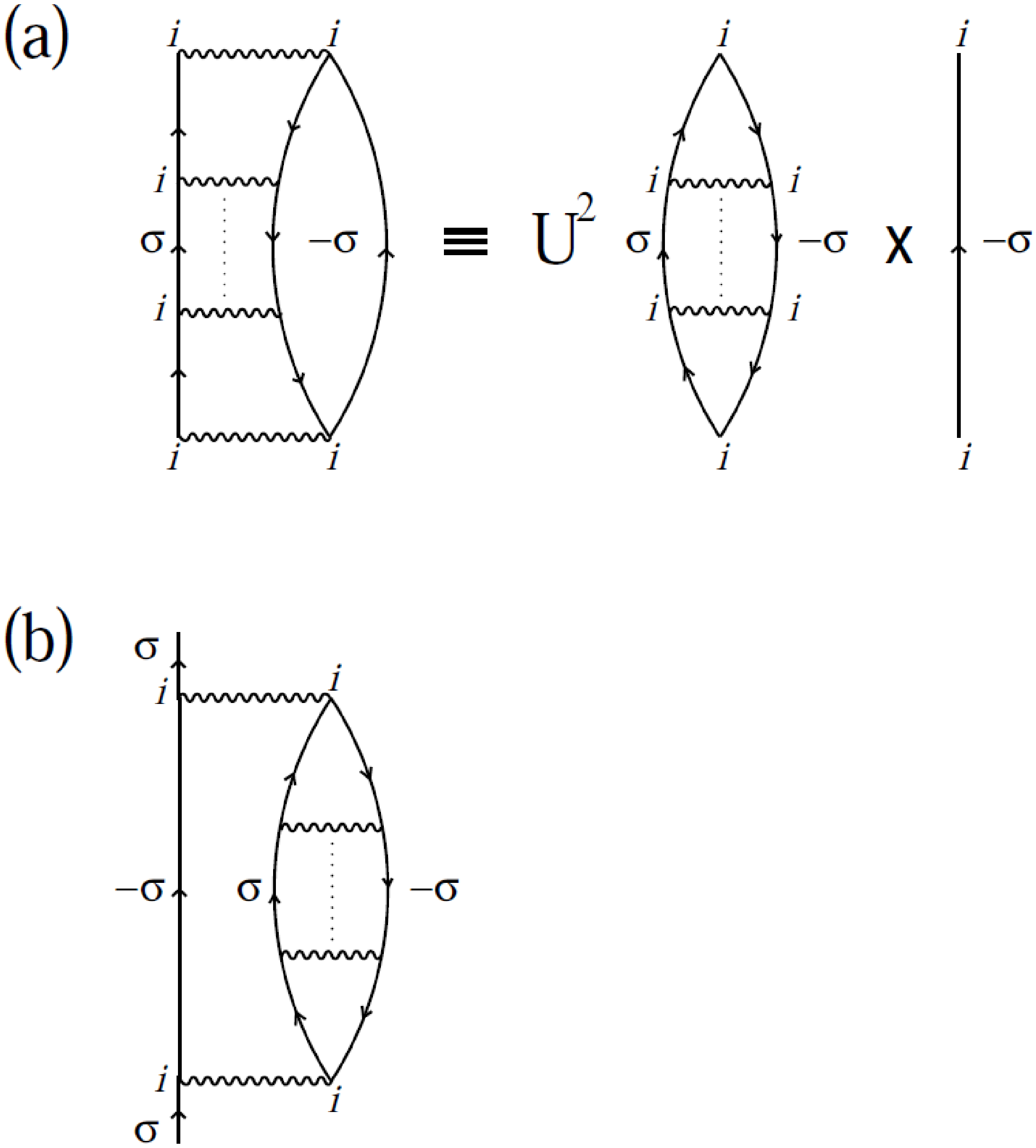

Figure 2.4: **Self-energy within the LMA for the SIAM:** (a) Diagrammatic representation of the dynamic self-energy, $\Sigma(\omega)$ in terms of the polarization bubble, Π^{+-}_{ii}; (b) equivalent recasting of (a) with the in- and out-going propagators included illustrating the physical processes embodied within the approximation, where the added particle/hole is scattered off/coupled to the transverse spin fluctuations. This schematic is taken from Ref. [5]

situation, the characteristic energy for the spin-flip scale is finite and on the order of the Kondo screening scale. However, it can be shown that $|\tilde{\mu}| > |\mu(U)|$, in which case, the zero-frequency pole in $\Pi^{+-}(\omega)$ disappears and the spectral weight shift to finite frequencies, appearing as a resonance at an energy scale, ω_m signifying the spin-flip scale, proportional to the Kondo scale. Hence, beyond UHF we have to determine the *exact* local moment self-consistently from a different equation such that the diktats of Fermi liquid theory are respected. For this let us now construct the self-energy.

We build a two self-energy description, as represented in Fig. 2.4, expressed as a convolution of the UHF-Green's functions and the polarisation propagator:

$$\Sigma_\sigma(\omega) = U^2 \int_{\infty}^{\infty} \frac{d\omega'}{2\pi i} \mathcal{G}_{\bar{\sigma}}(\omega - \omega') \Pi^{\bar{\sigma}\sigma}(\omega') \tag{2.28}$$

The UHF propagators should result in a self-energy that satisfy the basic criteria for a Fermi liquid. After some detailed algebra [5], we can then arrive at self-consistency equation for determining the exact local moment.

$$\sum_\sigma \sigma \Sigma_\sigma(0; e_i, x) = |\tilde{\mu}(e_i, x)| U \tag{2.29}$$

Finally, the single self-energy may be obtained as,

$$\Sigma(\omega) = \frac{1}{2}\left[\tilde{\Sigma}_\uparrow(\omega) + \tilde{\Sigma}_\downarrow(\omega)\right] + \frac{\frac{1}{2}\left(\tilde{\Sigma}_\uparrow(\omega) - \tilde{\Sigma}_\downarrow(\omega)\right)^2}{\mathcal{G}^{-1}(\omega) - \frac{1}{2}\left[\tilde{\Sigma}_\uparrow(\omega) + \tilde{\Sigma}_\downarrow(\omega)\right]}, \tag{2.30}$$

where,

$$\tilde{\Sigma}_\sigma(\omega) = \frac{U}{2}(\tilde{n} - \sigma|\tilde{\mu}|) + \Sigma_\sigma(\omega), \tag{2.31}$$

with $\sigma = \uparrow / \downarrow$ and the impurity Green's function,

$$G = \frac{1}{2}\sum_\sigma G_\sigma, \tag{2.32}$$

with

$$G_\sigma(\omega) = \left[\mathcal{G}^{-1}(\omega) - \tilde{\Sigma}_\sigma(\omega)\right]^{-1} \tag{2.33}$$

and

$$\mathcal{G}(\omega) = \frac{1}{\omega^+ - \epsilon_i - \Delta(\omega)} \tag{2.34}$$

Additionally, for p-h asymmetric situations [11] one also needs to satisfy the Luttinger's theorem given by,

$$I_L = \mathrm{Im} \int_{-\infty}^{0} \frac{d\omega}{\pi} \frac{\partial \Sigma(\omega)}{\partial \omega} G(\omega) = 0 \tag{2.35}$$

Eq. (2.29) constitutes the *symmetry restoration* (SR) condition that is central to the LMA and which, if satisfied, guarantees Fermi liquid behaviour. The self-consistent imposition of Eq. (2.29) amounts to a self-consistency condition for the local moment $|\mu|$ that enters Eqs. (2.17), (2.18). A low energy spin-flip scale, ω_K is generated; this scale that manifests as a strong resonance in the transverse spin polarization propagator, $\mathrm{Im}\Pi^{+-}(\omega)$ is proportional to the Kondo scale [5, 11]. If the SR condition equation 2.29 is not satisfied then a spin-flip scale occurs at $\omega_m = 0$ signalling the breakdown of a Fermi liquid.

It can be seen that in Eqs. (2.17), (2.18) for the UHF Green's functions, the mean-field self-energy enters as $x = \frac{1}{2}U|\mu|$ and neither U nor $|\mu|$ enter separately. So, the UHF Green's functions and hence ${}^0\Pi^{+-}_{\alpha\alpha}$ are purely functions of x and the explicit U-dependence of $\Sigma_{\uparrow/\downarrow}(\omega = 0; e_i, x)$ stems from the dependence of Π^{+-} on U itself and the U^2 prefactor in Eq. (2.28). A numerically efficient and cheap solution may be thus obtained by fixing x and e_i and fine tuning U so that Eq. (2.29) may be solved without requiring the UHF Greens functions and ${}^0\Pi^{+-}_{\alpha\alpha}$ to be calculated several times. Then with the converged $\Sigma(\omega)$ and the respective U we can solve for Eq. (2.35) by tuning ϵ_i. It typically requires 5-6 steps of iterations for solving Eq. (2.35). Conventionally, the LMA had been implemented following this fixed x algorithm.

Contribution of this thesis:

We would like to highlight the contribution of this thesis towards the numerical implementation of the LMA. The specific problems looked at in this thesis, especially, in Chapters 5 and 6, require us to fix the bare parameters of the SIAM, namely, U and ϵ_i. However, we should also note that if ϵ_i is fixed instead of e_i then, Eq. (2.29) and Eq. (2.35) would have to be solved self-consistently requiring several $\sim 20-30$ SR steps increasing the computation time enormously. Instead, if we fix U and e_i and tune μ we can drastically reduce this requirement again ending up in solving 5-6 SR iterations, as in the fixed x, fixed e_i algorithm. However, note that the computation time would be about 2 times higher than the latter. This is because, now we would need to recalculate Eqs. (2.17), (2.18) and (2.27) (that involves a convolution) for each SR step as described in Fig. 2.5.

In this thesis, we have therefore modified the fixed x algorithm, such that the fine tuning of U is avoided. The code is now provided with a fixed U as conventionally used in other solvers. The detailed outline of the current algorithm is provided in Fig. 2.5.

1. We start with an initial guess local moment, μ with which we calculate $\mathcal{G}_{\uparrow/\downarrow}$ and subsequently, $\tilde{\mu}$ from UHF spectral functions.
2. The calculation of ${}^0\Pi^{+-}_{\alpha\alpha}$ and Π^{+-}, and, $\Sigma_{\uparrow/\downarrow}$ follows.
3. Eq. (2.29) is checked and steps (1), (2), (3) are repeated until convergence 10^{-6} is achieved. With this step it can be realized that the entire process involves calculations of coupled equations for finding the root of Eq. (2.29), for which one therefore has to provide a judicious guess to reach the solution correctly and efficiently.
4. The algorithm for solving the highly non-linear SR and Luttinger's integral Eqs. (2.29), (2.35), has been modified substantially to make them robust.
5. Finally, with proper guesses for the underlying self-consistency equations a converged $\Sigma(\omega)$ is obtained. With this self-energy, we can now satisfy Eq. (2.35)

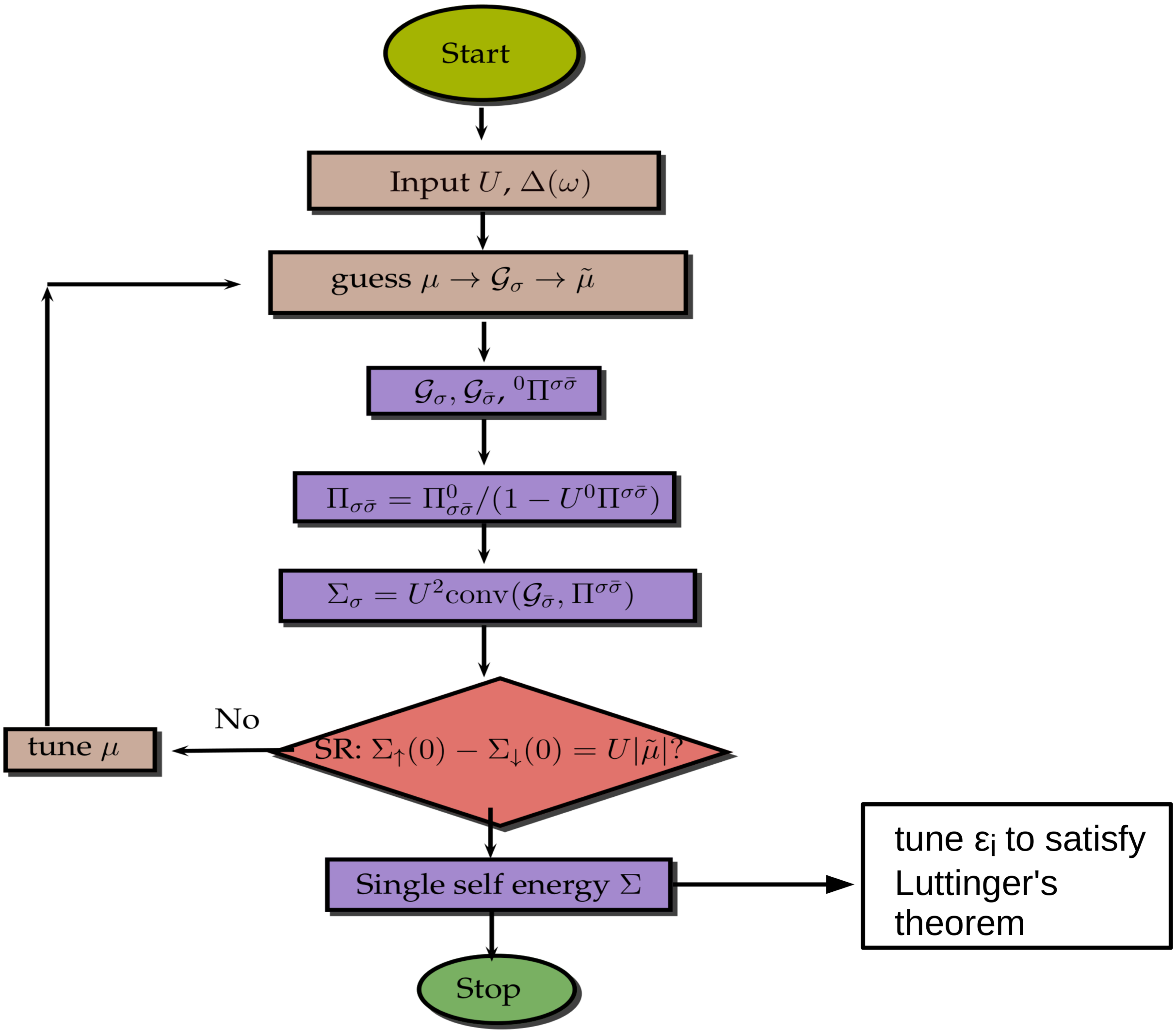

Figure 2.5: **Numerical implementation of the LMA:** In this schematic, we illustrate the fixed U algorithm that have been used in this thesis. Δ represents the SIAM host in which the correlated impurity is embedded in, 'conv' is an abbreviation used for 'convolution' and 'SR' is an abbrevation for the *symmetry restoration* that lies in the heart of LMA.

by tuning ϵ_i.

The above fixed U implementation has advantages, particularly, for the problems in Chapters 5 and 6, pertaining to the disordered Hubbard model, where the effective SIAMs are supplied with a random hybridization. Since the disorder problems necessitate the use of the LMA as a black box (where no manual tuning is possible), the modifications in the algorithm have focused on creating a standalone impurity solver that requires no intervention, either for the initial guesses or for the root finding. In particular to the problems treated in Chapters 5 and 6, we also had to take care of the computation time required to be able to sample sufficient number of disorder realizations. We achieved this by bringing in some additional *schemes* which would be discussed in detail in the respective chapters.

2.3 Dynamical Cluster Approximation: Inclusion of short range correlations

As described in Section 2.1.2, DMFT approximates the Σ by a constant in real or momentum space although it retains all the temporal (quantum) fluctuations. Over the years several theoretical frameworks have been developed to handle the effects due to non-local fluctuations in the effective hybridizing medium [7] and the interaction self-energy; these frameworks include cluster extensions of DMFT, namely, cluster DMFT, dynamical cluster approximation (DCA), variational cluster approximation etc.. In this thesis we use the DCA, and hence in the following, we briefly review the main concepts of the same.

In the previous section we realized that the formulation of DMFT was based on mapping the many body lattice on to a self-consistently determined single site problem. This involved the calculation of a local Green's function and local self-energy. We also saw that DMFT is exact in infinite dimensions and in finite dimensions it is an approximate theory. There also exist finite size methods, like the determinantal quantum Monte Carlo (QMC) [12] or Lanczos diagonalization [13] that attempt to make the many body lattice problem tractable by considering finite size lattices, small enough to be able to calculate the Green's function of the finite sized lattice. However, one could now imagine the computational effort required to describe thermodynamic physics, when the lattice size should tend to ∞. The DCA [6] however takes a different approach: it *maps* the many body lattice on to a finite cluster, self-consistently embedding it into an effective medium; this effective medium mimics the rest of the correlated lattice in the same spirit as the cavity construction of

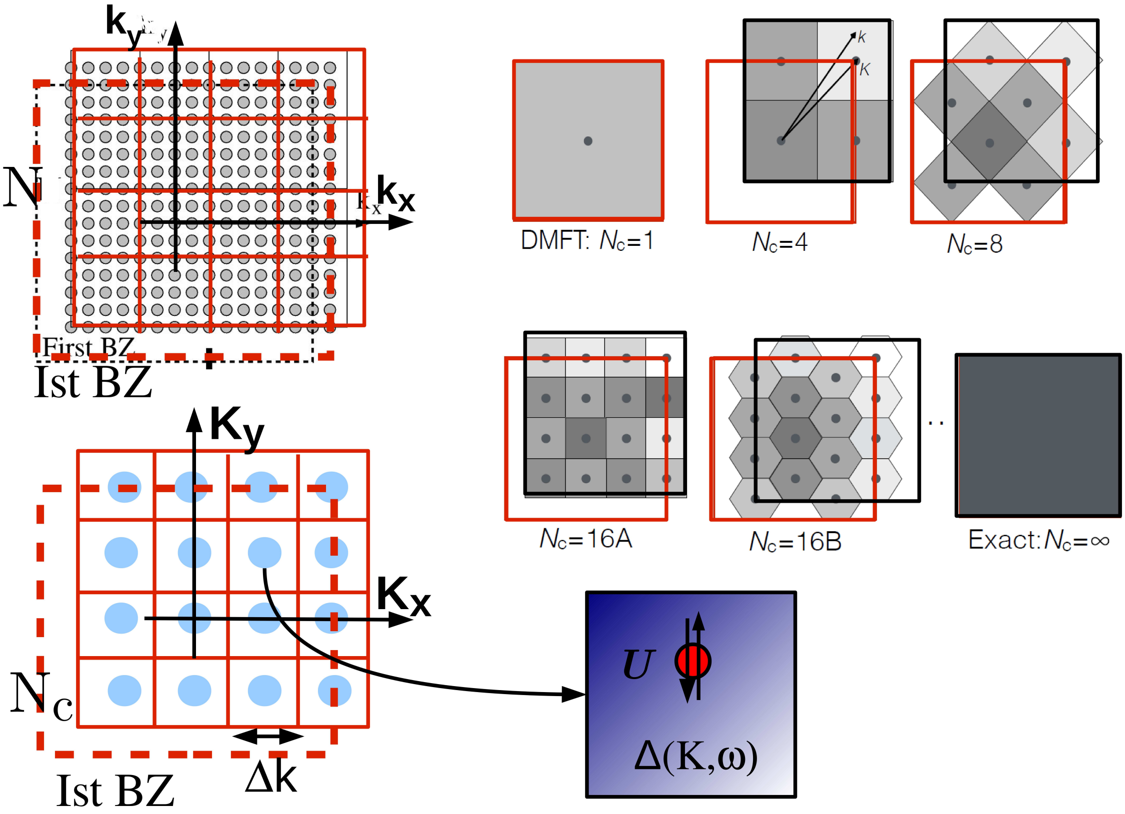

Figure 2.6: **Dynamical cluster approximation:** This figure illustrates the basic idea of DCA, where, we divide the first Brillouin zone into a finite number of N_c patches or cells, such that each cell is represented by a momentum $\mathbf{K}$. The green's function is coarse-grained to represent the system by a reduced number of N_c "cluster" degrees of freedom. In other words, the original lattice problem is represented as a cluster embedded in a self-consistently determined host. The right hand side demonstrates that for $N_c = 1$, the DMFT is recovered, while for $N_c \to \infty$, the scheme becomes exact. For a given cluster size N_c one can have different shapes of coarse-graining patches.

DMFT.

2.3.1 Basic Formulation

The DCA is formulated in the reciprocal space of the lattice model under consideration. A simple diagrammatic interpretation of DCA was provided by Hettler *et al.* in Ref. [6]. In the DCA, the Brillouin zone of the respective lattice is split into

N_c cells of equal size as shown in Fig. 2.6, where N_c is a finite number. As illustrated in Fig 2.6, each cell would be represented by a cluster momentum, $\mathbf{K}$ located at the center of the cell; each cell would also be represented by a patch function,

$$\phi_{\mathbf{K}}(k) = \begin{cases} 1, & \text{if } k \text{ in patch } \mathbf{K}. \\ 0, & \text{otherwise} \end{cases} \tag{2.36}$$

that would be used to restrict the momentum sums over k inside the $\mathbf{K}$th patch. With this function, the general momentum dependent Green's functions, $G(k)$ are replaced everywhere by their *coarse grained averages* over the cell to which k belongs, *i,e.*,

$$G_k \to \bar{G}_{\mathbf{K}} = \sum_{\tilde{k}} G_{\mathbf{K}+\tilde{k}}, \tag{2.37}$$

where, $\tilde{k} = k - \mathbf{K}$ belongs to the cell represented by $\mathbf{K}$. Given this coarse-graining, the Luttinger Ward functional now becomes a functional only of $\bar{G}_{\mathbf{K}}$ defined on the cluster momenta, $\mathbf{K}$ permitted for a periodic cluster of size N_c. In the process, therefore, the Σ and the vertex functions of the original lattice Hamiltonian, for a general momentum k gets mapped onto a cluster of momentum $\mathbf{K}$. In other words, the original lattice problem is mapped on to an effective problem of a cluster of size N_c embedded in a self-consistently determined host. The host propagator is computed using the Dyson equation,

$$\mathcal{G}_0^{-1}(\mathbf{K},\omega) = (G^c)^{-1}(\mathbf{K},\omega) + \Sigma(\mathbf{K},\omega). \tag{2.38}$$

This propagator will also be called the cluster excluded Green's function as it mimics the rest of the lattice that couples to the cluster. G^c represents the cluster green's function and $\Sigma(\mathbf{K},\omega)$ the cluster self-energy that approximates the original lattice self-energy. The lattice Green's function is approximated as the coarse-grained Green's function,

$$\bar{G}(\mathbf{K},\omega) = \frac{N_c}{N}\sum_{\tilde{k}} \left[\omega - \epsilon_{\mathbf{K}+\tilde{k}} + \mu - \Sigma(\mathbf{K},\omega)\right]^{-1}, \tag{2.39}$$

where, N is the total number of lattice sites and μ is the chemical potential. The self-energy has to obtained self-consistently. At convergence, $\bar{G} = G^c$ within some tolerance. The DCA is a causal, systematic, Φ-derivable theory that becomes conserving as the cluster size increases [6]. While the DMFT is recovered by taking the cluster to be a single site, the theory converges towards the exact thermodynamic limit as the cluster size is increased.

2.4 DMFT and DCA for inhomogeneous scenarios

The successes of DMFT for strongly correlated systems are numerous [2]. Strongly correlated models like the Hubbard model and the periodic Anderson model solved within the framework of DMFT have successfully described various experimental observations. Applications of DMFT have thus led to a lot of advancements in solving many of the problems that are particularly inherent to strongly correlated electron systems, such as the Mott metal-insulator transition, and the competition of spin, charge, and orbital order. The DMFT framework is not just restricted to model strongly correlated systems but has also recently being applied to real materials scenarios in combination with first-principles based methods like the density functional theory and GW approaches [14–16]. Cluster extensions of DMFT [7] like the DCA [17] and CDMFT [18] have further enriched our understanding of such strongly correlated phenomena. Although there exist several physical scenarios where DMFT or DCA has been extended to, below we discuss the ones particularly relevant to this thesis, namely their generalization to spatially and energetically inhomogeneous systems.

2.4.1 Inhomogeneous DMFT for heterostructures

The local approach of DMFT can be extended to spatially inhomogeneous systems with slab geometries composed of different materials and hence serves to be non-uniform in one direction, as illustrated in Fig 2.7. The DMFT formalism works when the lattice is a translationally invariant system; the heterostructure geome-

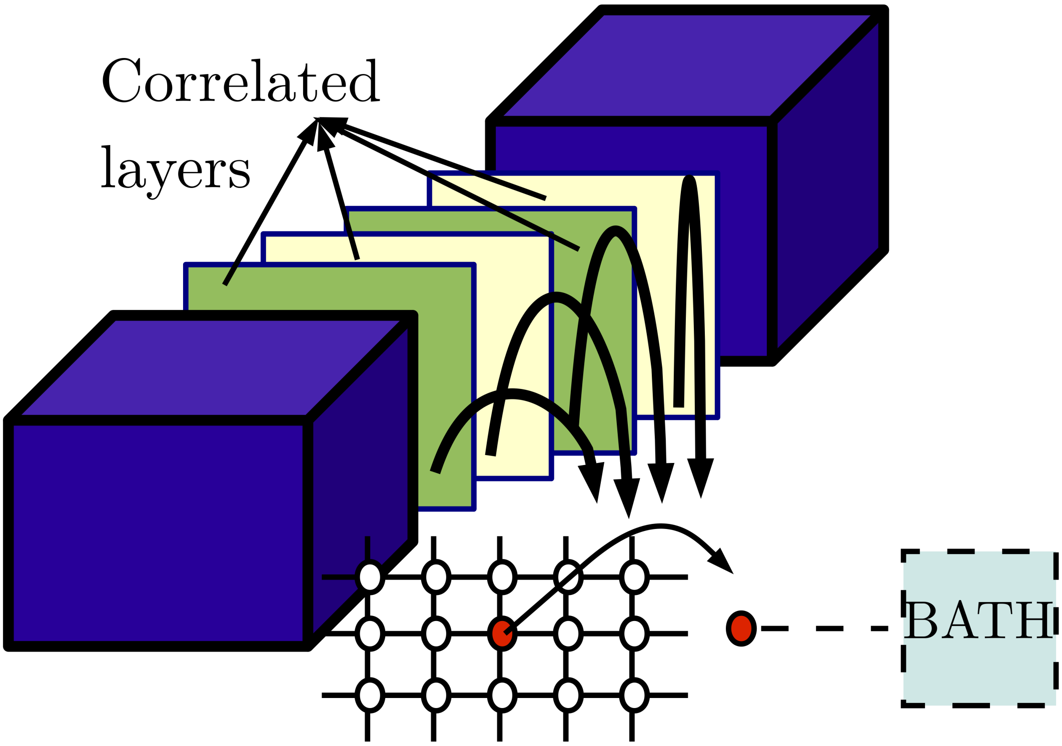

Figure 2.7: **Inhomogeneous DMFT for layers:** This figure illustrates the basic idea of inhomogeneous DMFT, that constitutes an approximate framework for heterostructures. Here, we map each layer on to an effective SIAM, and the heterostructure information enters through a matrix structure of the lattice Green's function.

try described in Fig. 2.7 has broken translational invariance in one direction; the in-plane direction is periodic. Potthoff and Nolting [19] and subsequently Freericks [20] introduced/utilized the idea of using a mixed basis in such geometries, the basis being a layer index, α for the z direction and the Bloch momentum $\mathbf{k}_{||}$ for the in-plane direction.

With this idea, we can now write down a layer resolved Green's function in this basis and map each layer on to an effective single impurity model, the self-energy of which would approximate the self-energy of each layer. The details of this formalism shall be explained in Chapter 3, where we apply this framework for looking into Kondo hole substituted layers of a model heavy fermion heterostructure.

In the subsequent parts of this chapter we discuss some of the numerical approaches for looking into systems with quenched disorder.

2.4.2 Numerical and effective medium approaches for energetically disordered systems

Owing to its importance in real life systems, disordered electron models have received numerous experimental, theoretical and numerical attention. However simple the Anderson model may look, this problem poses severe theoretical challenges, even at the level of non-interacting electrons, owing to the random nature of quenched energetic disorder. Initial valuable progress was achieved by the single parameter scaling theory [21, 22] that showed the dimension (d) two is *lower critical* and Anderson transition can take place only for $d > 2$ [23]. Such analytical investigations were phenomenological or adhered to certain limits, such as describing only weak disorder. The various computational techniques adopted are numerically exact methods ranging from the method of exact diagonalization (ED), transfer matrix method, kernel polynomial method to renormalization group technique [24–30]. These numerically exact methods have been successfully used to study Anderson localization effects in non-interacting systems; but they generally require very large clusters and hence are limited to two dimensional systems or/and non-interacting systems. Extending these methods to strongly correlated electron systems or chemically specific models is extremely difficult (almost impossible). The investigation of strongly correlated disordered systems using non-perturbative techniques still remains a challenging task. Alternative approximate approaches like the mean-field coherent potential approximation (CPA) [31–33] and its extensions [34–36], or the typical medium theory (TMT) [37] offer tractable solutions, that can be easily extended to interacting systems in combination with DMFT [1] or its cluster extensions [36, 38, 39]. Unfortunately, these methods being single site are unable to treat the localization physics properly. Cluster extensions of CPA like the cluster typical medium theory (CTMT) [36] and the typical medium dynamical cluster approximation (TMDCA) [39] offer promising solutions in this direction. We shall now briefly discuss some of these effective medium approaches.

2.4.3 Coherent potential approximation

The coherent potential approximation [31–33] is the most commonly used self-consistent mean field theory in the study of disordered electron systems. In the CPA, the original disordered lattice is self-consistently replaced by an averaged local (momentum independent), static (energy independent), effective medium. The CPA successfully describes some one-particle properties such as the density of states (DoS) in substitutionally disordered alloys. However, it **fails** to describe the Anderson localization transition.

This stems from the fact the single site nature of the CPA prevents it from capturing the multiple backscattering effects that is supposed to lead to localization. Jarrell and Krishnamurthy [34] modified the dynamical cluster approximation to include disorder by incorporating non-local corrections to local CPA. The disordered lattice problem was mapped onto a self-consistently embedded finite sized cluster problem. This systematic modification over the CPA did capture the precusor effects of the localization transition but failed to capture the localization transition itself. The molecular CPA also serves to be an extension of the CPA.

2.4.4 Typical medium theory and its cluster extensions

It is now well realized that the failure of CPA lies in the latter not being able to incorporate disorder induced spatial fluctuations that are key to the physics of Anderson localization transition (ALT). However, even the cluster extensions like the DCA [34] or the molecular CPA [35] failed to capture the ALT. The reason being the averaging procedure involved in the stochastic phenomenon arising due to the presence of random disorder configurations. These methods, namely, the CPA, DCA and molecular CPA involve arithmetic averages of the random one-particle DoS.

In a disordered system, during the time evolution, a particle cannot explore the full phase space, or in other words, the particle cannot probe all the possible random realizations with equal probability owing to the presence of backscattering effects. Any property of such a physical system is thus ‘non self-averaging’. A property

X of a system is self-averaging if ‘most’ realizations of the randomness have the same value of ‘X’, in the thermodynamic limit. Doing an arithmetic averaging of the DoS, to restore, translational invariance, would imply that all the lattice sites effectively behave in the same way. However, such a self-averaging quantity would be inadequate to describe the non-self-averaging nature of Anderson localization physics [40–42]. Especially, close to the critical point the probability distribution functions (PDFs) of the physical observables are not Gaussian and generally have log-normal behaviour. The PDFs could be extremely asymmetric marked by the presence of long tails. These long tails demand the consideration of infinitely many moments of the PDF in order to come up with a correct description of the system. In some cases, the moments might not even exist. This happens especially close to the critical point. The arithmetic mean of such a PDF would be strongly biased by the rare fluctuations and thus would be unable to determine the physics due to the ‘typical’ nature of the system [40–42].

In most such systems, the nature of the PDF is an emergent quantity and is not known *a priori*; thus we have limited information via the moments and cumulants of the PDFs. Under such circumstances, the ’typical’ or the most probable value of the PDF contains important information. In contrast to the arithmetic average, the geometrical average [43] gives a better approximation of the typical value of the local DoS. Dobrosavljević *et al.* [37] proposed the replacement of the arithmetically averaged local DoS with the typical DoS (TDoS) as a modification of the single-site CPA. This is called the typical medium theory (TMT). They showed that the TDOS vanishes continuously as the disorder strength increases and thus can behave as an effective mean field order parameter for the Anderson localization. The local TMT being a single site theory, fails to provide a correct description of the Anderson localization in three dimensions (3D). It underestimates the critical disorder strength and the critical exponent on a disordered cubic lattice. In Ref. [36], Ekuma *et al.* extended the local TMT to a cluster version utilizing the ideas from the DCA [6]. It is known that the DCA systematically incorporates spatial inter-site correlations, crucial, to describe the physics leading to ALT. This cluster extension of the local TMT [37] is called the cluster TMT (CTMT) [36]. However, the CTMT method could capture the weak localization effects in 1-dimensional and 2-dimensional. It failed to capture the evolution of the localization edge in 3-dimensional lattices. This was overcome in the typical medium dynamical cluster extension (TMDCA) framework with a proper mixing of the local and non-local density of states [39]. This method will be discussed in more detail later in this chapter. Before we move on to the TMDCA framework, let us first see how the concepts of TMT may be utilized for disordered interacting systems.

2.4.5 TMT-DMFT for energetically disordered interacting systems

Within DMFT each correlated lattice site is mapped onto a single impurity, which is coupled to a self-consistently determined dynamical mean-field bath representing the influence of all remaining lattice sites. This coupling is represented by the hybridization function $\Gamma(\omega)$ and within DMFT, the self-consistent solution of a *single* single impurity problem describes the physics of the entire lattice. However, in presence of quenched disorder, as represented by the AHM represented by Eq. (1.7), the translational invariance is broken. So, for a particular realization of onsite energies $\epsilon_1, \ \epsilon_2, \ \epsilon_3, \ \ldots, \ \epsilon_{N_L}$, where, N_L is the total number of lattice sites, we would need to map each of these sites to a self-consistently determined bath, $\Gamma_i(\omega)$ that is now site dependent. This site dependent *dynamical* bath would formally represent all the other scattering potential due to all the other sites. So, now, we would have to solve N_L DMFT equations self-consistently. We, obtain the local Dyson equations of the form,

$$\Sigma_i(\omega) = \omega + i\eta + \mu - \epsilon_i - \Gamma_i(\omega) - \frac{1}{G_{ii}(\omega)}, \tag{2.40}$$

for each of the N_L sites. One would need to compute such local self-energies for several disorder realizations in order to get the correct stochastic physics.

However, it is only when $N_L \to \infty$ that the correct physics due to Anderson localization may be obtained reliably. Thus one faces a difficult situation in terms of computational physics. A solution to this problem may be obtained by a *statistical* approach in combination with DMFT [44, 45]. The main idea relies on mapping the disordered lattice on to $N_{disorder}$ number of independent impurity models embedded

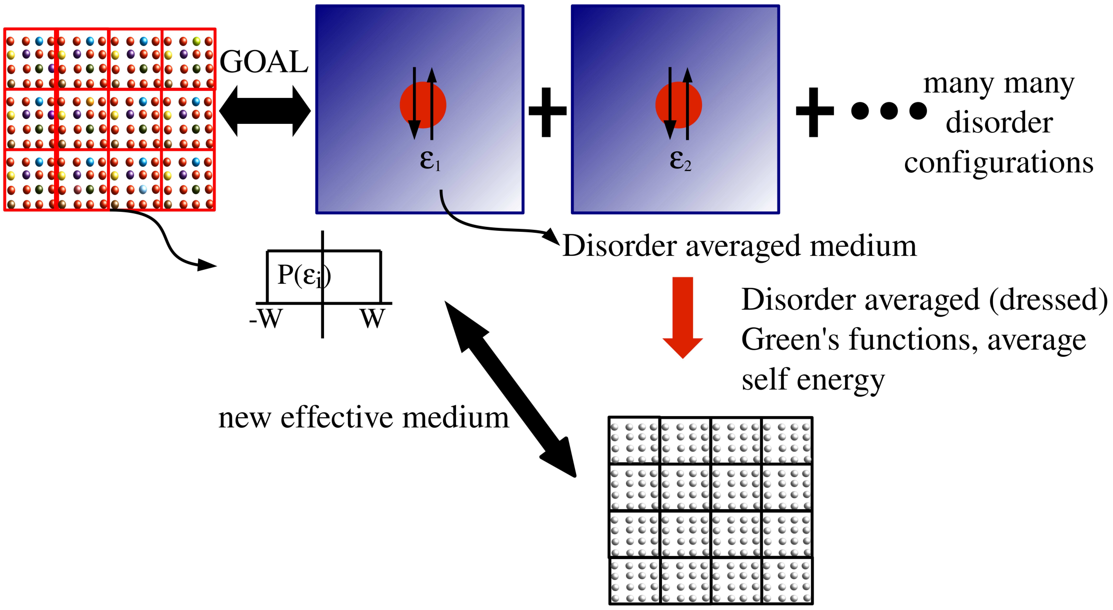

Figure 2.8: **Typical medium theory-DMFT:** This figure illustrates the basic idea of TMT-DMFT, where, the original disordered lattice model maps the system on to an ensemble of SIAMs, each with a certain potential energy, depending on the random disorder configuration. This constitutes the basic essence of an *effective medium theory* or the DMFT mapping of the correlated electrons. However, as had been highlighted in Chapter 1, the disordered medium should not suffer from any self-averaging issues and the geometric average of the LDoS serves to be an ideal candidate to be utilized to obtain the effective *typical* medium.

in an *appropriately* disorder averaged hybridizing medium, $\Gamma(\omega)$, where $N_{disorder}$ is a sufficiently large number of realizations for performing the disorder averaging. In other words, this boils down to the following statistical interpretation of Eq. (2.40),

$$\Sigma(\omega) = \omega + i\eta + \mu - \langle \epsilon_i \rangle - \Gamma(\omega) - \frac{1}{\langle G(\omega) \rangle}, \tag{2.41}$$

where, $\langle \epsilon_i \rangle$ represents an average onsite energy and $\langle G(\omega) \rangle$ represents a average Green's function obtained from the disorder averaged local density of states. In TMT, the *typical* density of states, ρ_{typ} and thereby the G_{typ} is used to construct the effective medium. The ρ_{typ} is obtained by a geometric averaging over the disorder configurations and is given by,

$$\rho_{typ}(\omega) = \exp \int d\epsilon_i P(\epsilon_i) \ln \rho_i(\omega) \tag{2.42}$$

Such an effective medium theory greatly reduces the numerical complexity while describing the physical effects due to interactions and disorder on an equal footing. However, it pays the price of losing all non-local effects due to disorder and/or interactions. Below, we discuss one formalism based on the DCA that incorporates non-local effects of disorder and/or interactions and hence can describe Anderson localization effects accurately while simultaneously reducing the computational effort substantially [39]. This development, for interacting disordered systems, in fact, embodies the main work of Chapter 6, in this thesis. In order to maintain a continuity, the detailed numerical implementation will discussed in Chapter 6.

2.4.6 Typical medium Dynamical Cluster approximation for energetically disordered systems

The DCA for disordered systems utilizes the same self-consistent framework of the standard DCA with the important usage of an environment defined by a non-local hybridization function $\Delta(K, \omega)$, where K represents the cluster momentum of the effectively disorder averaged lattice that represents the same underlying lattice structure of the original disordered model. In the same spirit as in the TMT-DMFT approach [37], the embedding medium needs to be appropriately disorder averaged. The simple DCA embeds the respective cluster into a medium obtained from the ADoS [34], while the CTMT [36] embeds the cluster into a medium obtained from the TDoS. Although, these methods systematically incorporate short range correlation effects of disorder, they fail to capture the localization transition in 3D. The reason for the failure of CTMT to describe the ALT in 3D, lies in the fact, that in 3D, in the limit of large clusters and disorder, $W \to W_c$, the geometric averaging suffers from a 'self-averaging' issue. For details see reference [36, 39].

This failure is overcome by using the following ansatz for the disordered averaged

DoS.

$$\rho^c_{typ}(K,\omega) = \exp\overbrace{\left(\frac{1}{N_c}\sum_{i=1}^{N_c}\langle \ln \rho^c_i(\omega,V)\rangle\right)}^{\text{local TDoS}}\underbrace{\left\langle\frac{\rho^c(K,\omega,V)}{\frac{1}{N_c}\sum_i \rho^c_i(\omega,V)}\right\rangle}_{\text{non}-\text{local}} \tag{2.43}$$

Here, the cluster momentum (K) resolved TDOS for each K is split into local and nonlocal parts. The local part is treated either with geometrical averaging over the disorder configurations, while the nonlocal part is treated with either algebraic or geometric averaging over the disorder configurations. This explicit separate treatment of the local and non-local parts with equal importance improves upon the CTMT drastically, such that the TMDCA successfully captures the ALT in 3D and also the re-entrant behaviour of the mobility edges [39]. The method has been extended to non-interacting systems with off-diagonal disorder [46] and more than one orbital [47] relevant for more realistic scenarios. Very recently, it has also been employed for looking into the effects of weak interactions on the mobility edge in a disordered interacting system [48].

Bibliography

[1] A. Georges, G. Kotliar, W. Krauth, and M. J. Rozenberg, Rev. Mod. Phys. **68**, 13 (1996).

[2] G. Kotliar and D. Vollhardt, Physics Today **57**, 53 (2004).

[3] W. Metzner and D. Vollhardt, Phys. Rev. Lett. **62**, 324 (1989).

[4] E. Müller-Hartmann, Zeitschrift für Physik B Condensed Matter **74**, 507 (1989).

[5] D. E. Logan, M. P. Eastwood, and M. A. Tusch, Journal of Physics: Condensed Matter **10**, 2673 (1998).

[6] M. Hettler, M. Mukherjee, M. Jarrell, and H. Krishnamurthy, Phys. Rev. B **61**, 12739 (2000).

[7] T. Maier, M. Jarrell, T. Pruschke, and M. H. Hettler, Reviews of Modern Physics **77**, 1027 (2005).

[8] V. E. Smith, D. E. Logan, and H. R. Krishnamurthy, The European Physical Journal B **32**, 49 (2003).

[9] M. T. Glossop and D. E. Logan, Journal of Physics: Condensed Matter **14**, 6737 (2002).

[10] D. E. Logan and M. T. Glossop, Journal of Physics: Condensed Matter **12**, 985 (2000).

[11] M. T. Glossop and D. E. Logan, Journal of Physics: Condensed Matter **14**, 6737 (2002).

[12] C.-C. Chang, S. Gogolenko, J. Perez, Z. Bai, and R. T. Scalettar, Philosophical Magazine **95**, 1260 (2015).

[13] P. W. Leung and P. E. Oppenheimer, Computers in Physics **6**, 603 (1992).

[14] C. Taranto, M. Kaltak, N. Parragh, G. Sangiovanni, G. Kresse, A. Toschi, and K. Held, Phys. Rev. B **88**, 165119 (2013).

[15] X. Ren, I. Leonov, G. Keller, M. Kollar, I. Nekrasov, and D. Vollhardt, Phys. Rev. B **74**, 195114 (2006).

[16] G. Kotliar, S. Y. Savrasov, K. Haule, V. S. Oudovenko, O. Parcollet, and C. Marianetti, Reviews of Modern Physics **78**, 865 (2006).

[17] M. Hettler, A. Tahvildar-Zadeh, M. Jarrell, T. Pruschke, and H. Krishnamurthy, Phys. Rev. B **58**, R7475 (1998).

[18] O. Parcollet, G. Biroli, and G. Kotliar, Phys. Rev. Lett. **92**, 226402 (2004).

[19] M. Potthoff and W. Nolting, Phys. Rev. B **60**, 7834 (1999).

[20] J. K. Freericks, Phys. Rev. B **70**, 195342 (2004).

[21] P. A. Lee and T. V. Ramakrishnan, Rev. Mod. Phys. **57**, 287 (1985).

[22] B. Kramer and A. MacKinnon, Rev. Prog. Phys. **56**, 1469 (1993).

[23] V. Dobrosavljević, N. Trivedi, and J. M. Valles Jr, *Conductor insulator quantum phase transitions*, vol. 16 (Oxford University Press, 2012).

[24] B. Kramer, A. MacKinnon, T. Ohtsuki, and K. Slevin, International Journal of Modern Physics B **24**, 1841 (2010).

[25] A. MacKinnon and B. Kramer, Zeitschrift für Physik B Condensed Matter **53**, 1 (1983).

[26] P. Markoš, arXiv preprint cond-mat/0609580 (2006).

[27] R. Silver and H. Röder, International Journal of Modern Physics C **5**, 735 (1994).

[28] R. Silver and H. Röder, Phys. Rev. E **56**, 4822 (1997).

[29] A. Weiße, G. Wellein, A. Alvermann, and H. Fehske, Reviews of modern physics **78**, 275 (2006).

[30] G. Schubert, J. Schleede, K. Byczuk, H. Fehske, and D. Vollhardt, Phys. Rev. B **81**, 155106 (2010).

[31] P. Soven, Phys. Rev. **156**, 809 (1967).

[32] R. Elliott, J. Krumhansl, and P. Leath, Reviews of Modern Physics **46**, 465 (1974).

[33] B. Velickỳ, S. Kirkpatrick, and H. Ehrenreich, Phys. Rev. **175**, 747 (1968).

[34] M. Jarrell and H. Krishnamurthy, Phys. Rev. B **63**, 125102 (2001).

[35] T. A. Maier and M. Jarrell, Phys. Rev. B **65**, 041104 (2002).

[36] C. E. Ekuma, H. Terletska, Z. Y. Meng, J. Moreno, M. Jarrell, S. Mahmoudian, and V. Dobrosavljevìc, Journal of Physics: Condensed Matter **26**, 274209 (2014).

[37] V. Dobrosavljević, A. A. Pastor, and B. K. Nikolić, EPL (Europhysics Letters) **62**, 76 (2003).

[38] E. Miranda and V. Dobrosavljevic, ArXiv e-prints (2011), `1112.6184`.

[39] C. E. Ekuma, H. Terletska, K.-M. Tam, Z.-Y. Meng, J. Moreno, and M. Jarrell, Phys. Rev. B **89**, 081107 (2014).

[40] A. Aharony and A. B. Harris, Phys. Rev. Lett. **77**, 3700 (1996).

[41] S. Wiseman and E. Domany, Phys. Rev. E **52**, 3469 (1995).

[42] E. Orlandini, M. Tesi, and S. Whittington, Journal of Physics A: Mathematical and General **35**, 4219 (2002).

[43] A. Gonis (1992).

[44] K. Byczuk, W. Hofstetter, U. Yu, and D. Vollhardt, The European Physical Journal Special Topics **180**, 135 (2009), ISSN 1951-6355.

[45] R. Abou-Chacra, D. J. Thouless, and P. W. Anderson, Journal of Physics C: Solid State Physics **6**, 1734 (1973).

[46] H. Terletska, C. Ekuma, C. Moore, K.-M. Tam, J. Moreno, and M. Jarrell, Phys. Rev. B **90**, 094208 (2014).

[47] Y. Zhang, H. Terletska, C. Moore, C. Ekuma, K.-M. Tam, T. Berlijn, W. Ku, J. Moreno, and M. Jarrell, Phys. Rev. B **92**, 205111 (2015).

[48] C. Ekuma, S.-X. Yang, H. Terletska, K.-M. Tam, N. S. Vidhyadhiraja, J. Moreno, and M. Jarrell, Phys. Rev. B **92**, 201114 (2015).

Chapter 3

Proximity effects of substitutional disorder in heavy fermion multilayers[§]

Contents

[§] Work reported in this chapter is published in: **Sudeshna Sen**, Juana Moreno, Mark Jarrell, N. S. Vidhyadhiraja, “Spectral changes in layered f-electron systems induced by Kondo hole substitution in the boundary layer”, Physical Review B, **91**, 155146 (2015)

3.1 Introduction

Several surprises have emerged through extensive experimental and theoretical investigations of layered correlated systems over the last decade. The pioneering study of Ohtomo *et al.* led to the discovery of a two-dimensional electron gas at the interface of Mott insulating $LaTiO_3$ and band insulating $SrTiO_3$ in atomically resolved heterostructures [1]. A dimensional driven crossover from metal to insulator transition [2] and an anomalous effective mass enhancement [3] was observed by Yoshimatsu *et al.* in digitally controlled $SrVO_3$ thin films. Theoretical predictions in this regard had been reported and semiquantitatively explained by Okamoto *et al.* in Ref. [4]. An early work in this regard may also be found in Ref. [5]. In general, strongly correlated interfaces exhibit several other unexpected properties such as superconductivity [6], coexistence of ferromagnetism and superconductivity [7], and electronic phase separation [8]. Such investigations have led to a renewed focus on a number of intriguing aspects of layered systems. Some of these issues are due to atomic reconstruction, enhanced correlation effects due to reduced coordination number and emergent energy scales owing to the presence of disparate orbital, charge, and spin degrees of freedom [9].

A significant number of theoretical studies on the proximity effects of electron-electron interaction in layered systems have been carried out. Such studies include proximity effects in Hubbard layers [10–25], Falicov-Kimball layers [26] or f-electron superlattices [27, 28]. Zenia *et al.* [18] demonstrated that a Mott insulator transforms to a “fragile” Fermi liquid if sandwiched between metallic leads. Helmes *et al.* [23] studied interfaces of strongly correlated metals with Mott insulators. The rate of decay of the quasiparticle weight into the Mott insulator was quantified and further corroborated in the spirit of a Ginzburg-Landau mean field treatment. Ishida and Liebsch [21] investigated the effect of an interplanar Coulomb interaction using the cellular Dynamical Mean Field Theory (DMFT) and observed a non-local correlation induced reduction of the proximity effect. Cluster extensions of DMFT was employed by Okamoto *et al.* in Ref. [29] to examine the proximity effect in superlattices involvng cuprates, predicting a novel enhancement in the superconducting transition temperature.

Recent experimental investigations of heavy fermion (f-electron) superlattices indicate a fascinating interplay of heavy fermion physics, low dimensionality and interface effects [30]. In the heavy fermion superlattices mCeIn$_3$-nLaIn$_3$, by reducing the thickness of the CeIn$_3$ layers grown on metallic LaIn$_3$, it was demonstrated that the dimensionality of the f-electrons and the magnetic order could be controlled. These dimensionally confined heavy fermion systems then displayed non-Fermi liquid properties that manifested as a linear temperature dependence in resistivity, $\rho_{xx} \sim T$, with a T^2 behavior recovered on increasing the number of CeIn$_3$ layers. This has been followed up with very recent theoretical investigations of the Kondo effect and dimensional crossover in f-electron superlattices [27, 28, 31]. Tada *et al.* [28] analyzed the formation of heavy electrons in f-electron multilayers. They demonstrated the existence of two (in-plane and out of plane) coherence temperatures in such systems. This implies a crossover in dimensionality of the heavy fermions from two to three dimensions as the temperature and the geometry of the system change. In a study of interfaces of Kondo lattice layers and normal metals, Peters *et al.* [27] showed that such a coupling transformed the full gap of the Kondo lattice layers into a vanishing soft gap. They also demonstrated the strong influence of the Kondo effect on the density of states of the metallic layer. This proximity effect was further shown to be strongly dependent on the number of non-interacting metallic layers.

Although the proximity effects of strong interactions have been addressed quite rigorously, the effects of disorder have not been considered. Incoherent scattering due to impurities is inevitable in heterogeneous interfaces and therefore the physical effects stemming from disorder could be significant. In fact, in heavy fermion compounds, when magnetic sites are substituted by non-magnetic impurities a substantial reduction of the coherence temperature T_{coh} occurs [32]. Shimozawa *et al.* studied the effects of Kondo hole disorder on epitaxial thin films of divalent-Yb substituted CeCoIn$_5$ [33]. It has been shown in Ref. [34] that dynamical scattering from Kondo holes can even yield a non-Fermi liquid behavior for bulk systems. Hence, a theoretical study of Kondo hole substituted f-electron interfaces is highly relevant.

In this chapter, we shall explore the spectral dynamics of a single substitutionally disordered Kondo-insulator layer at the boundary of several clean layers of which three types have been considered: (i) non-interacting metals or (ii) band-insulators and (iii) strongly interacting Kondo insulators. We have investigated the penetration of disorder induced impurity scattering into the proximal layers. An interplay of interactions and Kondo hole disorder lead to significant differences in the spectral weight transfer at low frequencies versus the overall spectrum.

3.2 Model and method

The Hamiltonian of a heavy fermion layered system may be constructed through a slight generalization of the standard Periodic Anderson model (PAM) as:

$$\begin{aligned}\mathcal{H} = &-\sum_{ij\alpha\sigma} t^{||}_{i\alpha j\alpha}\left(c^{\dagger}_{i\alpha\sigma}c_{j\alpha\sigma} + h.c.\right) + \sum_{i\alpha\sigma} V_{\alpha}\left(f^{\dagger}_{i\alpha\sigma}c_{i\alpha\sigma} + h.c.\right)\\ &+ \sum_{i\alpha\sigma}\left(\epsilon_{c\alpha}c^{\dagger}_{i\alpha\sigma}c_{i\alpha\sigma} + \epsilon_{f\alpha}f^{\dagger}_{i\alpha\sigma}f_{i\alpha\sigma}\right) + \\ &+ \sum_{\alpha} U_{\alpha}n_{fi\alpha\uparrow}n_{fi\alpha\downarrow} - \sum_{i\alpha\sigma} t^{\perp}_{\alpha\alpha+1}\left(c^{\dagger}_{i\alpha\sigma}c_{i\alpha+1\sigma} + h.c.\right),\end{aligned} \tag{3.1}$$

where, $t^{||}_{i\alpha j\alpha}$ represents the in-plane hopping between the conduction band (c-electron) orbitals at sites i and j, in the plane α; $\epsilon_{c\alpha}$ and $\epsilon_{f\alpha}$ are the onsite energies of the c- and f-electrons, respectively; V_{α} is the hybridization between the heavy f-electrons and the c-electrons in the plane α; U_{α} is the onsite Coulomb repulsion between two electrons occupying an f orbital in the plane α; and $t^{\perp}_{\alpha\alpha+1}$ represents the inter-plane hopping between the delocalized c-orbitals. We explicitly assume here that the f-orbitals being local have negligible overlap between the layers.

For an isolated Kondo insulator, the c and f-electron Greens functions are given by:

$$G^{c}(\omega) = \left[\omega^{+} - \frac{V^{2}}{\omega^{+} - \Sigma_{f}(\omega)} - \Delta(\omega)\right]^{-1} \tag{3.2}$$

$$G^{f}(\omega) = \left[\omega^{+} - \Sigma_{f}(\omega) - \frac{V^{2}}{\omega^{+} - \Delta(\omega)}\right]^{-1} \tag{3.3}$$

In Equation (3.2) we define a purely local conduction electron self-energy related to the f-electron self-energy by, $\Sigma_c(\omega) = \frac{V^2}{\omega^+ - \Sigma_f(\omega)}$. $\Sigma_f(\omega)$ is the conventional self-energy of the f-electrons in a PAM. The c-electrons thus incur a self-energy due to the correlated f-orbitals through the c-f hybridization, V. A Kondo insulator has a vanishing $\Sigma_f(\omega)$ in the Kondo insulator gap, leading to a divergence in $\Sigma_c(\omega)$ at $\omega = 0$, thereby acquiring a gap in the corresponding spectra. Equation(3.3) connects to an effective impurity model inherent to the DMFT single impurity form given by, $G^f(\omega) = [\omega^+ - \Sigma_f(\omega) - \Delta_{eff}]^{-1}$, with, $\Delta_{eff}(\omega) = \frac{V^2}{\omega^+ - \Delta(\omega)}$, being the effective hybridization seen by the f-electrons and needs to be determined self-consistently. This self-consistent hybridization thus depends on the $\Delta(\omega)$, which is thus determined self-consistently within DMFT. This is therefore termed as the self-consistently determined hybridization function for the c-electrons.

For, a system of coupled heavy fermion layers, the layer resolved Green's functions, $G^{cc}_{\alpha\alpha}$ for the c-orbitals, may be obtained through an equation of motion method, applied in real space [26]. For an N-layered system, the entire matrix of the c-Green's functions is given by the following expression:

$$\hat{G}^{cc}(\omega, \mathbf{k}^{||}) \tag{3.4}$$
$$= \begin{pmatrix} \lambda_1 - \epsilon(\mathbf{k}^{||}) & -t_\perp & 0 & \dots & \\ -t_\perp & \lambda_2 - \epsilon(\mathbf{k}^{||}) & -t_\perp & \dots & \\ 0 & -t_\perp & \lambda_3 - \epsilon(\mathbf{k}^{||}) & \dots & \\ \vdots & \vdots & \vdots & \vdots & \vdots \\ 0 & 0 & 0 & \lambda_N - \epsilon(\mathbf{k}^{||}) & \end{pmatrix}^{-1},$$

with $\lambda_\alpha = \omega^+ - \epsilon_{c\alpha} - \Sigma_{c\alpha}$, $\omega^+ = \omega + i\delta$, and $\mathbf{k}^{||}$ denotes the Bloch vector along the planar direction. Equation (3.4) assumes the existence of translational invariance along the in-plane direction. The term $\Sigma_{c\alpha}$ is the c-selfenergy arising due to the hybridization with the correlated f-orbitals, related to the $\Sigma_{f\alpha}$ as described before. It is to be noted that the term $\Sigma_{c\alpha}$ for each layer shall be related to $\Sigma_{f\alpha}$ in the same manner as for an isolated heavy fermion layer, because we have neglected the interlayer f-orbital hopping. However, now one needs to self-consistently derive an effective Anderson impurity model and hence $\Sigma_{f\alpha}$ for each layer utilizing the full matrix structure of the local c-Green's functions (Eq (3.4)). The above expression is not restricted to the PAM, and can be used in more general situations, e.g. if the c-orbitals were correlated and thus had an intrinsic selfenergy. Thus the λ_α are determined by the Hamiltonian of the α^{th} layer. Note that the band insulator is constructed using a fictitious non-interacting localized orbital that plays no role except to hybridize with the conduction orbital and create a band gap. Thus in our calculations, the band insulators have a $\Sigma_{c\alpha}(\omega) = \frac{V_\alpha^2}{\omega^+}$. For, the non-interacting metallic system, there exists no f-orbitals and hence $V = 0$ thus giving $\Sigma_{c\alpha}(\omega) = 0$. And for the Kondo insulators, $\Sigma_c(\omega) = \frac{V^2}{\omega^+ - \Sigma_f(\omega)}$. Therefore, λ_α in Eq. (3.4) is given by $\omega^+ - \frac{V_\alpha^2}{\omega^+}$, ω^+ and $\omega^+ - V_\alpha^2/(\omega^+ - \epsilon_f - \Sigma_{f\alpha})$ for band-insulators, metals and Kondo insulators respectively, with $\Sigma_{f\alpha}$ being the local f-selfenergy in the α^{th} layer. Within dynamical mean field theory, where the local approximation is valid, an impurity solver is needed to obtain the f-selfenergy. We have employed the local moment approach to solve the effective self consistent impurity problem.

The local c-Green's functions are given by a $\mathbf{k}^{||}$ summation of the $\hat{G}^{cc}(\omega, \mathbf{k}^{||})$ matrix. In order to avoid the numerically expensive step of summation over k_x, k_y for each frequency ω, we employ the method used in Ref. [23]. If the inverse c-Green's function matrix, $(\hat{G}^{cc})^{-1}(\omega, \mathbf{k}^{||})$ (in Eq. (3.4)) is denoted as $\hat{M}'$, such that $\hat{M}' = \hat{M} - \epsilon(\mathbf{k}^{||})\mathbb{I}$, $\mathbb{I}$ being a unit matrix; a similarity transformation may be then used to transform the $\hat{M}$ matrix into diagonal form, such that, $\hat{M} = \hat{S}\,\text{Diag}[\Gamma_1, \Gamma_2, \ldots]\,\hat{S}^{-1}$, $\hat{S}$ being the unitary matrix that diagonalizes $\hat{M}$.

$$\hat{G}^{cc}(\omega) = \hat{\mathcal{S}} \begin{pmatrix} H[\Gamma_1] & 0 & 0 & \ldots \\ 0 & H[\Gamma_2] & 0 & \ldots \\ 0 & 0 & H[\Gamma_3] & \ldots \\ \vdots & \ldots & \vdots & \ldots \end{pmatrix} \hat{\mathcal{S}}^{-1}, \tag{3.5}$$

where the Hilbert transform, $H[z] = \int_{-\infty}^{\infty} d\epsilon\rho_0(\epsilon)(z-\epsilon)^{-1}$ over $\rho_0(\epsilon)$, the non-interacting planar density of states, represents the result of the $\mathbf{k}^{||}$ summation and $\hat{S}$ is the similarity transformation matrix diagonalizing M. The N eigenvalues of M are denoted by Γ_r with $r = 1 \cdots N$. The above procedure is valid as long as the band-dispersion is the same for every layer. Within layer-DMFT, each layer is treated as a single-impurity embedded within a non-interacting host. Thus the c-Green's function for the $\alpha^{\rm th}$ layer may be written as

$$G^{cc}_{\alpha\alpha}(\omega) = \sum_{r=1}^{N} S_{\alpha r}\, H[\Gamma_r]\, (S^{-1})_{r\alpha} \tag{3.6}$$

$$= \frac{1}{\lambda_\alpha(\omega) - \Delta_\alpha(\omega)}, \tag{3.7}$$

where $\lambda_\alpha(\omega) = \omega^+ - \epsilon_{c\alpha} - \Sigma_{c\alpha}$ and $\Delta_\alpha(\omega)$ is the host hybridization for the $\alpha^{\rm th}$ PAM layer and N is the total number of layers. Note that Eq. (3.6) and (3.7) become the definition of $\Delta_\alpha(\omega)$. In all the calculations represented we set the f-orbital site energy, in the α-th layer, $\epsilon_{f\alpha} = -U_\alpha/2$, where U_α is the interaction strength present only on the localized f-orbitals of the α-th layer and the c-orbital site energy, $\epsilon_{c\alpha} = 0$, such that the chemical potential, $e_\mu = 0$, on all the layers. Thus the Luttinger sum rule implemented on the local quantities given by, $I_L = \mathrm{Im}\int_{-\infty}^{0} \frac{d\omega}{\pi} \frac{\partial \Sigma_{f\alpha}(\omega)}{\partial\omega} G^f_\alpha(\omega) = 0$, is always satisfied locally on each layer. The temperature, T, is set to zero.

An alternative way to approach this problem is through a Feenberg selfenergy approach [35, 36]. Consider any site on the $\alpha^{\rm th}$ layer. The $\Delta_\alpha(\omega)$ for this site may be written as a sum of self avoiding walks on the entire lattice with the lines representing hopping (intralayer given by $-t^{||}$ and interlayer by $t_\perp$), and the vertices being the site-excluded Green's functions [35, 36]. The definition of the hybridization through equations (3.6) and (3.7) is a practical route to summing all these diagrams. The local approximation of DMFT implies that the full selfenergy is momentum independent, hence the λ_r will get modified if interactions are included on the $r^{\rm th}$ layer. However, since that is a local change, the diagrams for the $\Delta_\alpha(\omega)$ do not change.This implies that the definition of the host hybridization in the presence of interactions remains the same as that for the non-interacting case within DMFT, albeit computed with a new set of λ_r. Including Kondo-hole disorder on the r^{th} layer within the Coherent Potential Approximation (CPA) does not change this definition and is hence tantamount to redefining λ_r in the following way [34]:

$$\frac{1}{\lambda_r(\omega) - \Delta_r(\omega)} = \frac{1-p}{\gamma_r(\omega) - \Delta_r(\omega)} + \frac{p}{\gamma_{0r}(\omega) - \Delta_r(\omega)}, \tag{3.8}$$

where $\gamma_r(\omega) = \omega^+ - \epsilon_{cr} - \Sigma_{cr}$ represents the sites with f-electrons and $\gamma_{0r}(\omega) = \omega^+ - \epsilon_{cr}$ represents the Kondo hole sites. Thus, for a given set of $\Sigma_{cr}(\omega)$, the $\lambda_r(\omega)$ and $\Delta_r(\omega)$ need to be determined self consistently by combining equations (3.6) and (3.7) with equation (3.8). A practical computational procedure is the following. Step-1: Guess a set of $\Delta_r(\omega)$ and use them to find λ_r from equation (3.8). Step-2: Use these λ_r in equations (3.6) and (3.7) to find a new set of $\Delta_r(\omega)$. Go back to Step-1 until convergence is achieved. The obtained $\lambda_r(\omega)$ may be used to define a disorder-averaged selfenergy for the r^{th} layer as

$$\Sigma_{cr}^{CPA}(\omega) = \omega^+ - \epsilon_{cr} - \lambda_r. \tag{3.9}$$

A schematic of the above framework is depicted in Fig. 3.1.

The self consistent interacting impurity problem is solved here using the local moment approach (LMA). The LMA is a diagrammatic perturbation based approach, built around the two broken-symmetry, local moment solutions ($\mu = \pm|\mu_0|$) of an unrestricted Hartree-Fock mean field approximation. Spin-flip dynamics are subsequently built in through an infinite-order resummation of a specific class of diagrams that embody transverse spin-flip processes. A key ingredient of LMA is the symmetry restoration condition which is equivalent to imposing adiabatic continuity to the non-interacting limit, and is hence crucial to recovery of Fermi liquid behaviour and the emergence of a low energy scale. Any violation of this condition signals a quantum phase transition to another phase such as a local moment phase. By construction, the scope of LMA is limited to investigations of Kondo physics, and a generalization of the method to ordered phases or cluster problems is not straightforward. Moreover, the practical implementation of the resummation is through a random phase approximation, which introduces certain undesirable features in

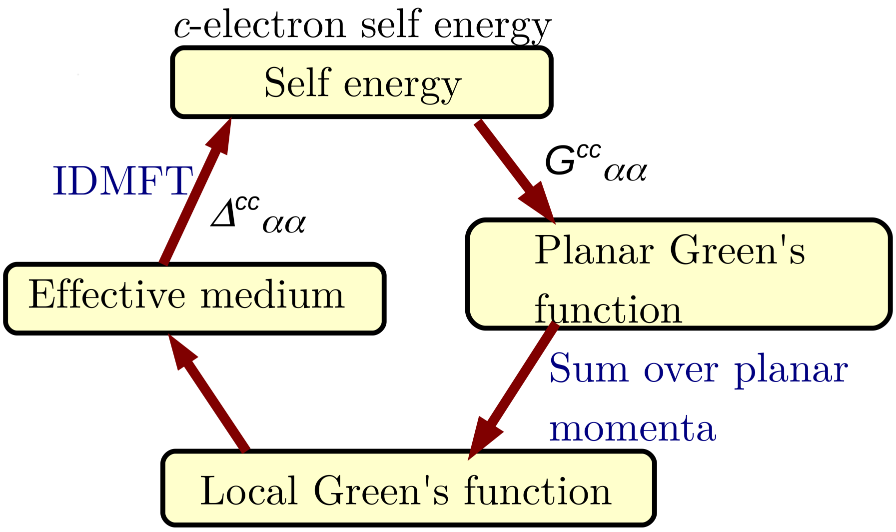

Figure 3.1: **Self-consistent scheme for IDMFT+CPA:** The self-consistent computational scheme proposed to embed a CPA kind of averaging procedure within the framework of IDMFT is represented as a flowchart. The framework is essentially the same as for IDMFT, the difference lies in the crucial step of obtaining a disorder averaged effective medium for which we propose combining equations (3.6) and (3.7) with equation (3.8).

the transverse spin polarization propagator (see Ref. [37]). Nevertheless, the LMA has been found to benchmark excellently against numerical renormalization group (NRG) [38], and Bethe Ansatz for the SIAM and the Kondo problem respectively [37]. It has henceforth been employed in studies on Kondo insulators and heavy fermion systems [39–42]. It has also been used in studying specific cases of impurity systems with many orbitals, the pseudogap Anderson model and the gapped Anderson impurity model [43–46]. The study on the soft gap Anderson model has also been compared to NRG in Ref. [47]. The extension to finite disorder may be found in Ref. [34]. We combine LMA, CPA and the inhomogeneous DMFT [26] to explore the effect of disorder and interactions in layered-PAM systems.

At this point it is worth mentioning that although the DMFT systematically incorporates the dynamical effects of strong correlation by its construction, it ignores the feedback of the spatially non-local intersite interactions into single particle quantities in either the charge channel (nearest neighbour) or the spin channel (exchange).

Particularly, here, in the context of heavy fermion systems the investigation of the competition between the Kondo effect and the Rudderman-Kittel-Kasuya-Yosida (RKKY) interaction is therefore beyond the scope of DMFT. The Coherent Potential Approximation (CPA) is also a single site approximation. In the present context, the CPA equations lead to a self-consistently obtained disorder averaged f-electron self energy, $\Sigma_f^{CPA}(\omega)$ that is equal for all sites. Hence the CPA too cannot describe physical scenarios stemming from beyond mean field disorder effects. For example, effects like Anderson localization or non-Fermi liquid physics that occur due to a distribution of Kondo scales cannot be explored within this approach. Our investigation is therefore a minimal model that may look at the some effects of disorder in layered systems.

3.3 Results

We have explored the proximity effects of a Kondo hole-disordered heavy fermion layer in thin films, by studying geometries where the substitutionally disordered Kondo insulator is in proximity to several clean interacting or non-interacting layers. Before we delve into results obtained using the numerical implementation of the local moment approach within inhomogeneous DMFT, we present a few general results that are exact within this framework of layered systems.

3.3.1 Analytical results for a few special cases

Using the equations detailed in Section 3.2, it is easy to obtain closed-form expressions for the Green's functions in certain simple cases. We present and discuss a few results for a non-interacting layered system, a bilayer and a trilayer system.

Non-interacting case

For N-identical layers the matrix on the right hand side of Eq. (3.4) has the structure of a symmetric tridiagonal Toeplitz matrix [48]. The complete eigenspectrum and corresponding eigenvectors for such a matrix are known in closed form

[48], and hence may be used in combination with Eq. (3.4) to find the exact Green's functions for the n^{th} layer of a system of N identical non-interacting metallic layers (see also Ref. [49]). The density of states at a fixed ω as a function of layer-index becomes:

$$A_n(\omega) = \frac{2}{N+1} \sum_{m=1}^{N} \sin^2\left(\frac{mn\pi}{N+1}\right) \rho_0\left(\omega + 2t_\perp \cos\frac{m\pi}{N+1}\right) . \tag{3.10}$$

With the replacement of ω by $\omega - V^2/\omega$ in the above equation, the result describes N identical non-interacting band-insulators also. $A_n(\omega)$, shown in Figure 3.2, exhibits

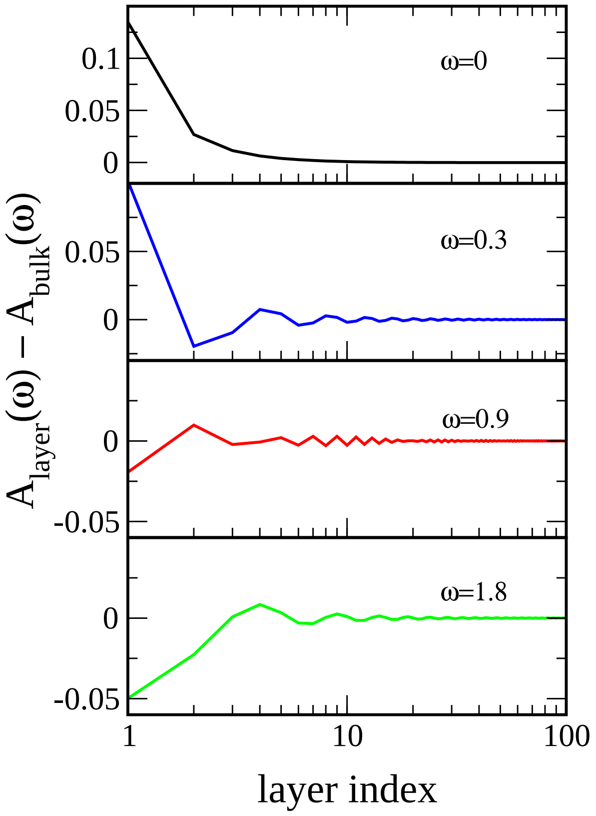

Figure 3.2: **Change in layer resolved density of states (compared to bulk) for a non-interacting system** The change in layer density of states (compared to the bulk) as a function of layer index, for various frequencies. The result was obtained using Equation (3.10) for a system of 500 layers. The bare density of states for each layer ($\rho_0(\epsilon)$) is chosen to be of semi-elliptic form, $\rho_0(\epsilon) = \sqrt{1 - \epsilon^2/t_{||}^2}/(2\pi t_{||})$.

oscillatory behavior for all ω values except $\omega = 0$ where a monotonic decay is observed. These well-known surface Friedel oscillations arise because the Fermi surface of the infinite metallic system has been perturbed by the presence of terminal surfaces [11, 26].

Bilayer systems: General considerations

For a bilayer system, the Green's functions are given by

$$G_{11}(\omega) = a\, H[\Gamma_+] + b\, H[\Gamma_-], \tag{3.11}$$

$$G_{22}(\omega) = a'\, H[\Gamma_+] + b'\, H[\Gamma_-], \tag{3.12}$$

where

$$\begin{aligned} \Gamma_\pm &= \frac{1}{2}\left(\lambda_1 + \lambda_2 \pm \sqrt{(\lambda_1 - \lambda_2)^2 + 4t_\perp^2}\right), \qquad (3.13)\\ \lambda_r &= \omega^+ - \epsilon_c - \Sigma_{cr}(\omega), \quad r = 1, 2, \end{aligned}$$

$$\begin{aligned} a &= \frac{\Gamma_+ - \lambda_2}{\Gamma_+ - \Gamma_-} \ \text{ and } \ b = \frac{\lambda_2 - \Gamma_-}{\Gamma_+ - \Gamma_-}, \qquad (3.14)\\ a' &= -\frac{\lambda_1 - \Gamma_+}{\Gamma_+ - \Gamma_-} \ \text{ and } \ b' = \frac{\lambda_1 - \Gamma_-}{\Gamma_+ - \Gamma_-}, \qquad (3.15) \end{aligned}$$

and $H[z]$ represents the Hilbert transform with respect to the non-interacting layer density of states. These equations may now be analyzed for a few specific cases.

A clean Kondo insulator-metal bilayer system

As a first application of Equations (3.11) and (3.12), we consider a Kondo-insulator-metal interface. The paramagnetic Kondo insulator is just a renormalized band-insulator, hence in the particle-hole symmetric limit, $\epsilon_c = 0$ and $\Sigma_c(\omega) = V^2/(\omega^+ - \epsilon_f - \Sigma_f)$. In the low frequency limit, the Fermi-liquid form of the f-selfenergy may be used to get $\Sigma_c \overset{\omega\to 0}{\sim} ZV^2/\omega^+$, where $Z = (1 - \partial\Sigma_f/\partial\omega)^{-1}$ is the

f-electron quasiparticle weight. Thus, $\lambda_1 = \omega^+ - ZV^2/\omega^+$ for the Kondo insulator and $\lambda_2 = \omega^+$ for the non-interacting metal. Given these, the c-spectral functions $A_l(\omega) = -\text{Im}G^c_{ii}(\omega)/\pi$ for the Kondo insulator ($i = 1$, $l = KI$) and metal ($i = 2$, $l = M$) layers in the low frequency limit are given by,

$$\begin{aligned} A_{KI}(\omega) \overset{\omega \to 0}{\sim} & \left(\frac{\omega t_\perp}{ZV^2}\right)^2 \rho_0\left(\omega\left[1+\frac{t_\perp^2}{ZV^2}\right]\right) \\ & + \left(1-\left(\frac{\omega t_\perp}{ZV^2}\right)^2\right)\rho_0\left(\omega\left[1-\frac{t_\perp^2}{ZV^2}\right]-\frac{ZV^2}{\omega}\right), \end{aligned} \tag{3.16}$$

$$\begin{aligned} A_M(\omega) \overset{\omega \to 0}{\sim} & \left(1-\left(\frac{\omega t_\perp}{ZV^2}\right)^2\right)\rho_0\left(\omega\left[1+\frac{t_\perp^2}{ZV^2}\right]\right) \\ & + \left(\frac{\omega t_\perp}{ZV^2}\right)^2 \rho_0\left(\omega\left[1-\frac{t_\perp^2}{ZV^2}\right]-\frac{ZV^2}{\omega}\right). \end{aligned} \tag{3.17}$$

From the above expressions, we see that the presence of interlayer coupling ($t_\perp > 0$) leads to a linear mixing of the Kondo-insulator and metallic layer spectra in all layers. In $A_{KI}(\omega)$, the first term contributes a quadratically vanishing spectral weight into the hybridization gap, while the second-term leads to the usual gapped spectrum of the Kondo insulator. In $A_M(\omega)$, the first term implies that the spectrum of the non-interacting metal is strongly renormalized by the proximity to the Kondo insulator, and a Kondo resonance like feature must emerge in the vicinity of the Fermi level. The second term is gapped at the Fermi level, but should lead to a step like feature at $\omega \sim ZV^2$. Thus, the metallic states tunnel into the gap of the Kondo insulator giving rise to a quadratically vanishing gap, while the strongly correlated Kondo insulator tunnel into the non-interacting metal leading to strong renormalization of the non-interacting spectrum. In the Kondo insulator, the f-electron spectrum is related to the c-electron spectrum through $A^f_{KI}(\omega) = (Z^2V^2/\omega^2)A_{KI}(\omega)$ in the limit $\omega \to 0$. Due to the tunneling of the metallic states into the Kondo insulator, the f-spectrum thus becomes gapless. These proximity effects are quite general and only assume a linear expansion in frequency of the real part of the f-selfenergy. Similar results have been observed numerically in a recent study on a single Kondo insulator embedded in a three-dimensional non-interacting metallic host [27] and in a theoretical analysis of the surface density of states of heavy fermion materials [31]. This concept of “Kondo Proximity Effect” was used to qualitatively explain the experimental surface spectra of CeCoIn_5 reported by Aynajian *et al.* [50].

A clean Kondo insulator-band insulator bilayer system

Next, we consider a Kondo-insulator-band-insulator interface. For the band insulator, $\lambda_2 = \omega^+ - V^2/\omega^+$. Thus, the spectral functions are again given by a linear mixing of the Kondo and the band insulator spectra. A low frequency analysis similar to the one carried out above for the Kondo insulator-metal system leads to the following. The gap in the Kondo insulator is well known to be substantially reduced compared to the band insulator due to the exponentially small quasiparticle weight factor Z arising in the strong coupling limit. Thus, from our analysis, we see that the Kondo insulator spectrum close to the Fermi level remains almost unchanged. However, in the frequency region where the band insulator had a gap, but the Kondo insulator had states, a quadratically vanishing spectral weight tunnels in from the Kondo insulator layer into the band insulator.

A dirty Kondo insulator-metal bilayer system

In this sub-section, we consider, in detail, a substitutionally disordered-Kondo-insulator interfaced with a non-interacting metal. The random substitution of f-sites in the Kondo insulator-layer leads to Kondo hole disorder, which is known to lead to an impurity band at the Fermi level [51–54]. Specifically, λ_1 becomes complex because of the static contribution to the selfenergy from scattering by impurities [34]. Thus $\lambda_1 = \omega^+/Z + i\Gamma_0$, where Z is the local f-electron quasiparticle weight and $\Gamma_0 = -\mathrm{Im}\Sigma_c^{CPA}(0)$ is the scattering rate at the Fermi level. In a previous paper [34], we showed that Σ_c^{CPA} may be related to Σ_c through a cubic equation if $\rho_0(\epsilon)$ has a semi-elliptic form that corresponds to an infinite-dimensional Bethe lattice. This equation, if used for a single isolated Kondo insulator, yields that

$$\Sigma_c^{CPA}(0) = -it_{\|}\frac{1-p}{2\sqrt{p}}\,, \tag{3.18}$$

Thus, at the Fermi level, the conduction electrons acquire a selfenergy that is non-analytic in the concentration of Kondo holes, p. It was also shown in Ref. [54] that the f electron selfenergy acquires a $1/\sqrt{p}$ dependence when $p \to 0$. However, in the presence of interlayer coupling, Γ_0 becomes a complicated function of $t_\perp$ and $t_{||}$ and we have not been able to find a simple closed form expression like Equation (3.18) for the bilayer case. Nevertheless, numerical calculations lead us to the conclusion that Γ_0 does retain the same form as the isolated layer case.

Our natural focus is on the strong coupling regime of the Kondo insulator, where the quasiparticle weight becomes exponentially small, i.e $Z \to 0$. In such a situation, and with $\lambda_1 = \omega^+/Z + i\Gamma_0$ and $\lambda_2 = \omega^+$, the values of $\Gamma_\pm$ in Equation (4.9) may be simplified to

$$\Gamma_\pm \xrightarrow{Z\to 0} \frac{1}{2}\left(\lambda_1 \pm \sqrt{\lambda_1^2 + 4t_\perp^2}\right) . \tag{3.19}$$

The coefficients of the Hilbert transforms in equation (3.11) and (3.12) are given by

$$\begin{aligned} & a \to \frac{\Gamma_+}{\sqrt{\lambda_1^2 + 4t_\perp^2}} \quad b \to \frac{-\Gamma_-}{\sqrt{\lambda_1^2 + 4t_\perp^2}} \\ & a' = b \ \text{ and } \ b' = a \, . \end{aligned} \tag{3.20}$$

These equations are quite easy to analyze at the Fermi level ($\omega = 0$). In fact, the results from this analysis do not assume strong coupling, because if we substitute $\omega = 0$ in the above expressions, the quasiparticle weight does not appear in them. Hence the following results are valid for any coupling strength. At the Fermi level, the eigenvalues are given by

$$\Gamma_\pm = \frac{i}{2}\left(\Gamma_0 \pm \sqrt{\Gamma_0^2 - 4t_\perp^2}\right) . \tag{3.21}$$

Γ_0 is a monotonically decreasing function of the Kondo hole concentration (see equation (3.18)) and hence in the dilute limit ($p \to 0$), the eigenvalues will be purely imaginary; with increasing p, $\Gamma_\pm$ become degenerate at $\Gamma_0 = 2t_\perp$, which translates to a specific concentration, p_d. In general, p_d is a complicated function of Γ_0. However, we have numerically verified that when the ratio $t_\perp/t_{||} \ll 1$, Eq. (3.18) can be used as an estimate of p_d for multi-layer systems. For such a regime $p_d = (\sqrt{1+(2t_\perp/t_{||})^2} - 2t_\perp/t_{||})^2$. For $p > p_d$, the two eigenvalues have the same imaginary part but differ in the real part. It turns out that the density of states at the Fermi level can be easily obtained in two limits: the dilute limit ($p \to 0$) and the degenerate limit ($\Gamma_0 = 2t_\perp$ or $p = p_d$). We proceed to obtain these.

In the dilute limit, $\Gamma_0 \gg t_{||}, t_\perp$, so $\Gamma_+ \to i(\Gamma_0 - t_\perp^2/\Gamma_0)$ and $\Gamma_- \to it_\perp^2/\Gamma_0$. For purely imaginary arguments ($z = i\eta$), the Hilbert transform with respect to a semi-elliptic density of states may be written in closed form as

$$\mathcal{H}(i\eta) = \int \frac{\rho_0(\epsilon)}{i\eta - \epsilon} = -\frac{2\,i}{t_{||}}\left[\sqrt{1+\bar{\eta}^2} - \bar{\eta}\right], \tag{3.22}$$

where $\bar{\eta} = \eta/t_{||}$. So the Hilbert transform is also purely imaginary, which can be expected in the particle-hole symmetric limit. Using the above Hilbert transform result and the simplification of the eigenvalues in the dilute limit, the density of states of the Kondo insulating layer and the non-interacting metallic layer are given by (to $\mathcal{O}(1/\Gamma_0^2)$)

$$A_{KI}(\omega = 0) \xrightarrow{p\to 0} \frac{1}{\pi\Gamma_0}\left[1 - \frac{2t_\perp^2}{\Gamma_0 t_{||}}\right] \tag{3.23}$$

$$A_M(\omega = 0) \xrightarrow{p\to 0} \frac{2}{\pi t_{||}}\left[1 - \frac{t_\perp^2}{\Gamma_0 t_{||}} + \frac{t_\perp^2}{\Gamma_0^2}\right]. \tag{3.24}$$

Note that in all the equations above and below, $A_{KI}(\omega)$ denotes the c-electron spectral function of the Kondo insulator. The above equations reveal the proximity effect of disorder on the two layers. In the absence of inter-layer tunneling, the impurity band in the Kondo insulator grows as $\sqrt{p}$ with increasing Kondo hole substitution (since $\Gamma_0 \sim 1/\sqrt{p}$ in the dilute limit); and the metallic layer has a fixed density of states ($= 2/(\pi t_{||})$) at $\omega = 0$. When $t_\perp$ is turned on, the impurities introduced in the Kondo insulating layer affect the density of states of the non-interacting clean metallic layer, and the relative change in the density of states with respect to the isolated layers ($t_\perp = 0$) case is $\sim \sqrt{p}$ for both layers.

In the degenerate limit, $\Gamma_0 = 2t_\perp$, the eigenvalues are degenerate, and Eq. (3.11) and (3.12) cannot be used. We revert back to the basic equation (3.5) and after a bit of algebra, obtain the density of states of the two layers as

$$A_{KI}(\omega=0) \xrightarrow{p=p_d} \frac{2}{\pi t_{||}} \frac{\left(t_r - \sqrt{1+t_r^2}\right)^2}{\sqrt{1+t_r^2}}, \tag{3.25}$$

$$A_M(\omega=0) \xrightarrow{p=p_d} \frac{2}{\pi t_{||}} \frac{1}{\sqrt{1+t_r^2}}, \tag{3.26}$$

where $t_r = t_\perp/t_{||}$ is the ratio of the inter-layer to intra-layer hopping. We have seen that the metallic layer acquires a Kondo resonance at the Fermi level due to the proximity to the Kondo insulator. Since in the concentrated limit ($p \to 1$), the entire system simply becomes a non-interacting metallic bilayer, the density of states must approach the value of $\rho_0(t_\perp)$. It can also be shown that, the $A_M(\omega=0) > \rho_0(t_\perp)$. This implies that both the metallic layer and the Kondo insulating layer experience a monotonic change in the density of states with increasing Kondo hole concentration; the Kondo insulating layer steadily transforming into a single-impurity system.

Symmetric tri-layer systems

Another class of systems, for which closed form expressions may be readily obtained is a set of three layers in which the outer two layers are identical in all respects while the middle layer is different. The c-Green's function for such a system (denoted by $1-2-3$) is given by

$$G_{11}(\omega) = G_{33}(\omega) = \frac{1}{2}H[\lambda_1] - t_\perp^2\left(a\,H[\Gamma_+] + b\,H[\Gamma_-]\right), \tag{3.27}$$

$$G_{22}(\omega) = a'\,H[\Gamma_+] + b'\,H[\Gamma_-], \tag{3.28}$$

where,

$$\begin{aligned}
\Gamma_{\pm} &= \frac{1}{2}\left(\lambda_1 + \lambda_2 \pm \sqrt{(\lambda_1-\lambda_2)^2 + 8t_{\perp}^2}\right), \\
\lambda_r &= \omega^{+} - \epsilon_c - \Sigma_{cr}(\omega), \\
a &= \frac{1}{(\lambda_1-\Gamma_+)(\Gamma_+-\Gamma_-)} \text{ and} \\
b &= \frac{-1}{(\lambda_1-\Gamma_-)(\Gamma_+-\Gamma_-)}, \\
a' &= -\frac{\lambda_1-\Gamma_+}{\Gamma_+-\Gamma_-} \text{ and } b' = \frac{\lambda_1-\Gamma_-}{\Gamma_+-\Gamma_-}.
\end{aligned} \tag{3.29}$$

For the trilayer system, if the layers are uncoupled ($t_{\perp} = 0$) then the Green's functions should be simply given by $G_{ii}(\omega) = H[\lambda_i]$. In order to approach the uncoupled layers limit, in the equations above, the limit of $t_{\perp} \to 0$ must be taken with care. We have investigated the symmetric tri-layer system in several situations, that are similar to the ones discussed for the bilayer system. One of these is a Kondo insulator, which could be clean or substitutionally Kondo hole disordered, sandwiched between two metallic or band-insulating layers. The conclusions reached in such cases were found to be qualitatively very similar to those in the bilayer systems, hence we now proceed to larger systems and investigate the penetration of disorder into several clean, non-interacting or interacting layers.

In the next sub-section, we discuss full numerical solutions using the formalism described in Section 3.2.

3.3.2 Numerical results

It is evident that the spectral changes in the c- and f-electron Green's functions are a combined effect of the three physical parameters in the problem, namely: (i) interlayer-hopping, $t_{\perp}$, (ii) interaction, U, and (iii) Kondo hole concentration (p). In order to disentangle the sole effect of disorder from the results, we first discuss briefly the non-interacting and clean layered systems. Then, we add interactions and note the combined effect of inter layer coupling and interactions. Finally, we add disorder and by comparing the obtained spectra to those of the non-disordered case,

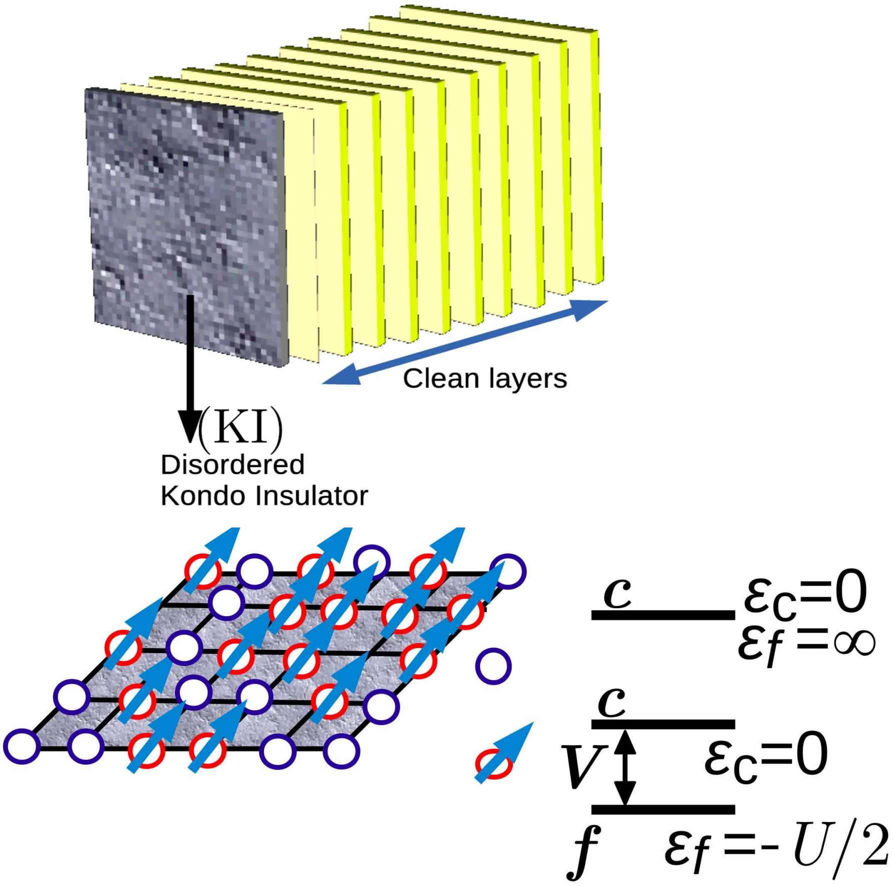

Figure 3.3: **Schematic of the geometry considered in this work.** While the boundary layer is chosen to be a dirty Kondo insulator (shown as the gray shaded layer), the proximal layers are clean. Three distinct possibilities for these clean layers have been investigated, namely band-insulators, metals or Kondo insulators.

we isolate the proximity effects of disorder, which represents the main objective of this work. We study three different cases, with a single substitutionally disordered Kondo insulator layer next to (a) several band-insulator, (b) several uncorrelated metal and (c) several clean Kondo insulator layers. These three cases will be referred to as disordered Kondo insulator-band insulator, disordered Kondo insulator-metal and disordered Kondo insulator-Kondo insulator, respectively. A schematic of the geometries is shown in Fig. 3.3. The number of clean layers has been varied from 1 to 11.

The clean metals are just $U = 0$ layers with a simple tight-binding Hamiltonian. In the disordered Kondo insulator-Kondo insulator case, all the Kondo-insulating layers including the disordered layer have the same U and V. All of the numerical results have been obtained by using a semi-elliptic bare density of states for each layer, namely, $\rho_0(\epsilon) = \sqrt{1 - \epsilon^2/t_{||}^2}/(2\pi t_{||})$, with $t_{||} = 1$ as the unit of energy. We begin this section by considering the effects of $t_\perp$ only, in a clean, non-interacting, f-conduction-electron system, interfaced with several non-interacting metals or several other non-interacting f- conduction-electron systems.

Effects of inter-layer hopping: $t_\perp \neq 0$, $U = 0$, $p = 0$

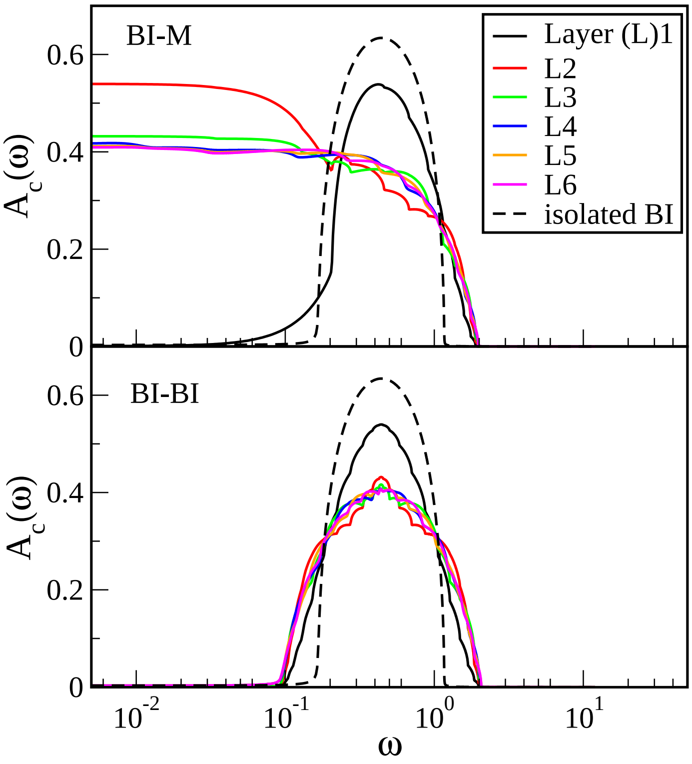

Figure 3.4: **Spectral density of the c electrons** in the presence of non-zero interlayer coupling for a single band insulator layer (L1) at one end of a 11-layer (L2-L12) metallic system (top panel) and a single band insulator at one end of a 11-layer band insulating system (bottom panel) plotted on a logarithmic energy scale. The model parameters are $t_\perp = 0.5$, $U = 0$, $V = 0.44$. Note that only $\omega > 0$ is displayed due to particle hole symmetry. For comparison, the spectrum of an isolated band insulator layer is shown as a dashed line.

In Fig. 3.4, the layer-resolved c-spectra for a single band insulator coupled to 11 metallic layers is shown. Since the entire system is particle-hole symmetric, we choose to display only the $\omega > 0$ spectrum on a logarithmic energy scale. The spectrum for an isolated band insulator layer is shown as a dashed line in both panels. From the top panel of figure 3.4, we observe that the presence of $t_\perp$ between a metallic layer next to a band insulator leads to the tunneling of metallic states into the otherwise large hybridization gap of the band insulator. We had predicted earlier, in Section 3.1.4, that the presence of $t_\perp$ leads to a quadratic rounding off of the band insulator band edge, which is evident when compared with the hard band edge of the isolated layer's hybridization gap (dashed line). The multiple Friedel oscillations due to a non-zero $t_\perp$ are also visible in Fig. 3.4. Although the predictions were exact for a bilayer system, the layer resolved spectra follow the same qualitative changes in this multi-layered system. These oscillations naturally attenuate sharply in the layers that lie far from the boundaries. However, for all the finite-layer systems that we have studied, these oscillations are present. Nevertheless, as Freericks *et al.* discussed in Ref. [26], and also found by us, the amplitude of these oscillations in the surface layers become frozen-in once the system becomes large ($\gtrsim$ 10 layers in practice).

Next, we explore the combined effect of inter-layer coupling and interactions.

Combined effect of inter-layer hopping and interactions: $t_\perp \neq 0$, $U \neq 0$, $p = 0$

In Fig. 3.5 we show the layer-resolved c-spectra for a single Kondo insulator and 11 metallic layer system (top panel) and a single Kondo insulator and 11 band insulator layer system (bottom panel). In this bottom panel, due to the presence of finite density of states in the proximal Kondo insulator, we see that the c-spectra of the second neighboring band insulator layer acquires a quadratic rounding off around the band edge. The farther band insulator layers are however inert to these effects.

The top panel of Fig. 3.5 shows that, for a metallic layer adjacent to a Kondo

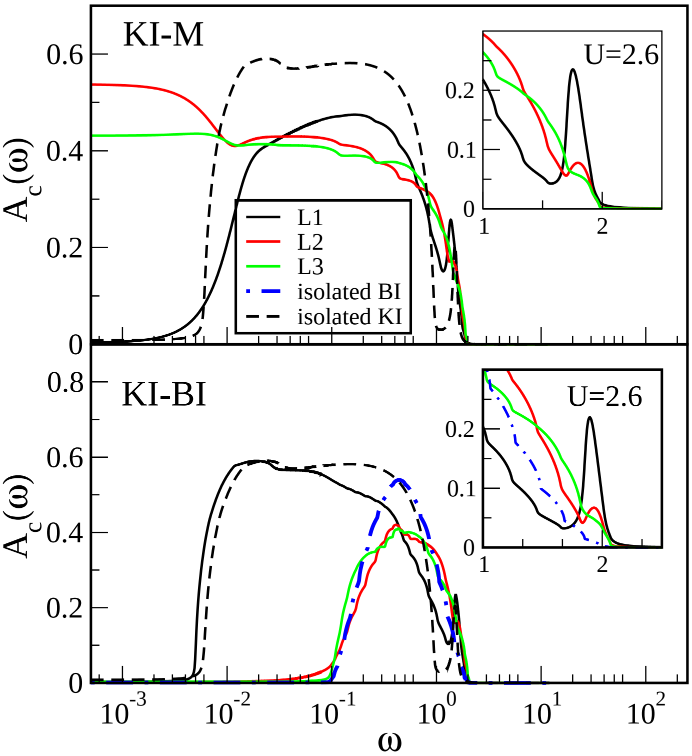

Figure 3.5: **Layer resolved spectral function for the c-electrons due to non-zero interlayer hopping and interactions.** A single Kondo insulator layer (L1) is coupled to a 11 layer metallic system (top panel) and a 11 layer band insulating system (bottom panel). The spectra for the nearest (L2) and second nearest (L3) metallic (top panel) and the band insulator (bottom panel) is shown. For both panels inter-layer hopping $t_\perp = 0.5$, and $c-f$ hybridization is set to $V = 0.44$ for both the Kondo insulators and the band insulators, Coulomb repulsion in the Kondo insulating layer $U = 1.7$ in the main panels and $U = 2.6$ in both insets. For comparison, the c-DOS of an isolated Kondo insulator and an isolated band insulator is also shown as (black) dashed (top and bottom panel) and (blue) dashed-dotted lines (bottom panel), respectively. The insets show the Hubbard bands that emerge as a result of their proximity to the coupled Kondo insulator. This effect is visibly detectable only until the second nearest neighbor layer.

insulator, the proximity effect results in a Kondo-like resonance at the Fermi level of the otherwise non-interacting metal. This is consistent with the the numerical renormalization group results of Peters *et al.* on Kondo superlattices and the emergent Kondo proximity effect as discussed in Ref. [27]. An insight into this can already be realized by looking at the analytical predictions of Section 3.3.1. Thus the low energy analysis of Section 3.3.1 although derived for bilayer (Kondo insulator-band insulator and Kondo insulator-metal) systems, remain robust even when the number of band insulator or metal layers is increased. Proximity to a strongly interacting Kondo insulator induces changes not only at low energies such as the Kondo scale, but also at high energies such as Hubbard bands. The adjacent non-interacting band-insulating or metallic layers also acquire minute Hubbard bands indicating the tunneling of electron correlations into the non-interacting layers. Similar effects occur even in bulk heavy fermions, modeled by the periodic Anderson model, where although the U is present only for f-electrons, the mixing between c- and f-electrons through the hybridization produces Hubbard bands in the spectrum of the conduction band electrons. Whether the single Kondo insulator is coupled to band-insulating or metallic layers, these high energy proximity effects are the same, which is evident from the insets of Fig. 3.5. Now we proceed to explore the spectral modifications induced in the layer resolved spectra when we introduce Kondo holes in the boundary Kondo insulator layer.

Effects of Kondo hole disorder in the boundary layer

The effects of Kondo-hole disorder in the bulk PAM have been extensively investigated [32, 34, 51–54]. It is well known that there is a crossover from coherent lattice behavior to incoherent single-impurity behavior as the disorder p changes from zero to one [32, 34]. Such a crossover is reflected in all physical quantities, including resistivity, thermopower and density of states. For layered systems, the range and extent of disorder effects may be quantified through a measurement of integrated spectral weight difference in a given frequency interval $|\omega| \leq \lambda$. We define $\chi_\nu(p, p_0; \alpha; \lambda)$, as the spectral weight difference of the α^{th} layer, computed through

$$\begin{aligned} &\chi_\nu(p; p_0; \alpha; \lambda) \\ &= \int_{-\lambda}^{\lambda} d\omega \ |A\left(p; \{U_\beta\}; \alpha; \omega\right) - A(p_0; \{U_\beta\}; \alpha; \omega)| \end{aligned} \tag{3.30}$$

for a set of fixed interaction strengths $\{U_\alpha\}$. Here $\nu = c/f$ and $A(p; \{U_\beta\}; \alpha; \omega) = -\text{Im}G_\alpha(p; \{U_\beta\}; \omega)/\pi$ is the spectral function of the α^{th} layer's when the Kondo hole concentration is p. Physically, this quantity represents the extent to which the layer density of states changes when disorder goes from p_0 to p or vice-versa when all other parameters are fixed. We have employed $n_c = 1$ and $n_f = 1$ for an isolated Kondo insulator layer. We have observed that for an isolated layer, the spectral weight difference between the disordered and the clean case integrated over all frequencies (with the cutoff $\lambda \to \infty$ in Equation (3.30)) rises rapidly as a function of increasing p and roughly saturates at the "maximally random" concentration of $p \sim 0.5$ The spectral weight difference at $p \sim 0.5$ is large when compared with either clean case ($p = 0$) or the $p \to 1^-$ single-impurity case. Hence we choose a fixed disorder $p = 0.5$ on the boundary layer in all of our subsequent discussion, unless otherwise mentioned. The rest of the layers are chosen to be clean.

With the experimental realizations of CeIn$_3$/LaIn$_3$ superlattices [30] and thin films of non-magnetic Yb substituted into CeCoIn$_5$ [33], the possibility of having an interface between a Kondo hole disordered layer and a clean layer cannot be ignored. We focus on the following questions: How does the random dilution of f-electrons in a single Kondo insulator boundary layer (see schematic Fig. 3.3) affect the dynamics of the electrons in the adjoining clean layers? How far do the disorder effects penetrate? And does this range get enhanced or suppressed by the presence of interactions?

In order to answer these questions, we therefore investigate the interface of a single disordered Kondo insulator and several clean layers that could be non-interacting metals or band-insulators or strongly interacting Kondo insulators. We start our discussion with a system of 12 layers where the boundary layer is a disordered Kondo insulator and the rest of the layers are non-interacting metals. We refer to this as a disordered Kondo insulator-metal system. The proximity of a clean Kondo insulator to a metal leads to (i) a quadratic band bending at the Kondo hybridization band edge of the Kondo insulator layer and (ii) appearance of a Kondo resonance and a strongly renormalized low energy spectra induced by the "Kondo proximity effect". This has already been discussed earlier for a bilayer Kondo insulator-metal interface. In the presence of disorder, it is well known that Kondo holes introduce an impurity band in the center of the Kondo hybridization gap [51–53]. This impurity band then fills up the gap with increasing disorder concentration, leading to a continuum

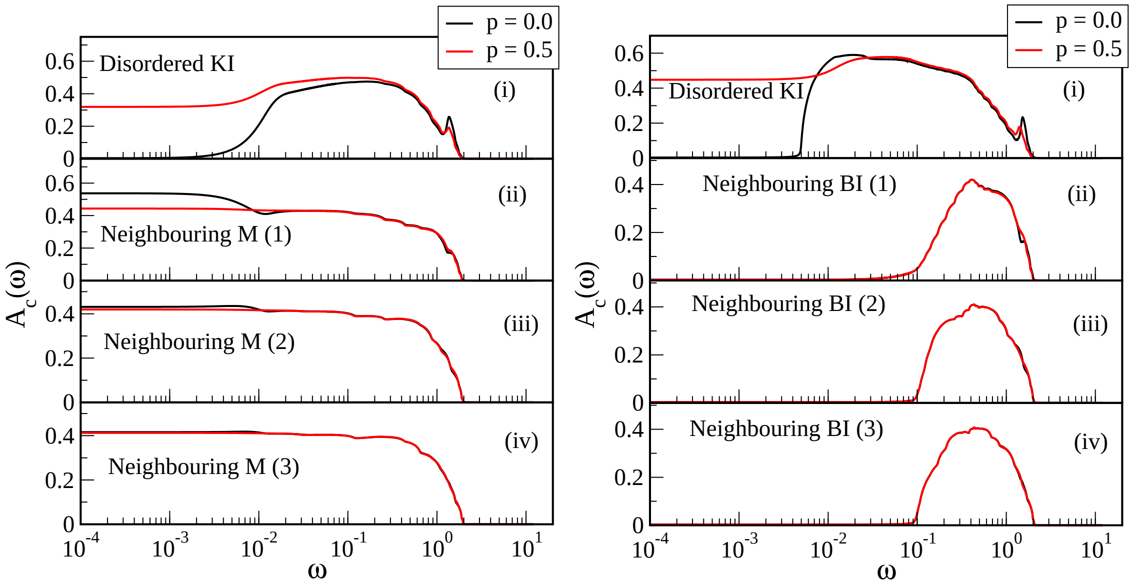

Figure 3.6: **The c-electron spectra** of the respective layers as denoted in the panels for a single disordered Kondo insulator interfaced with a 11-layer metallic (M) (left panel) or band insulating (BI) (right panel) system for a clean ($p = 0$) (solid black) and a disordered ($p = 0.5$) Kondo insulating (KI) layer (solid red). For the disordered Kondo insulator this represents the CPA average of $-\Im G_{\mathrm{CPA}}/\pi$. The model parameters are $t_\perp = 0.5$, $V = 0.44$, $U = 1.7$.

of metallic states spanning the entire gap. This observation holds here too as seen in the panel (i) of Fig. 3.6. This phenomenon due to Kondo holes manifests itself in both the CPA averaged c-electron spectra and the local (impurity) f-electron spectra of the disordered Kondo insulator (not shown here). Additionally, the Hubbard bands get depleted due to the presence of Kondo holes. The important aspect however, is that these disorder effects do not just remain confined to the disordered layer but also penetrate into the neighboring clean layers depicted in the lower panels of figure 3.6. Disorder in fact destroys the proximity effects of interactions. The Kondo resonance in the adjoining metallic layer at zero disorder appreciably reduces in intensity when the Kondo hole concentration, p is 0.5 and tends to disappear as p increases. This is more clearly visible from figure 3.7. The low energy spectra of the farther neighbors also acquire visible low energy spectral changes that evolve with change in disorder concentration, tending to crossover to the noninteracting limit of a clean metal/metal interface, as seen from figure 3.7. The tiny Hubbard bands in the non-interacting layers also disappear with increasing disorder. This can be

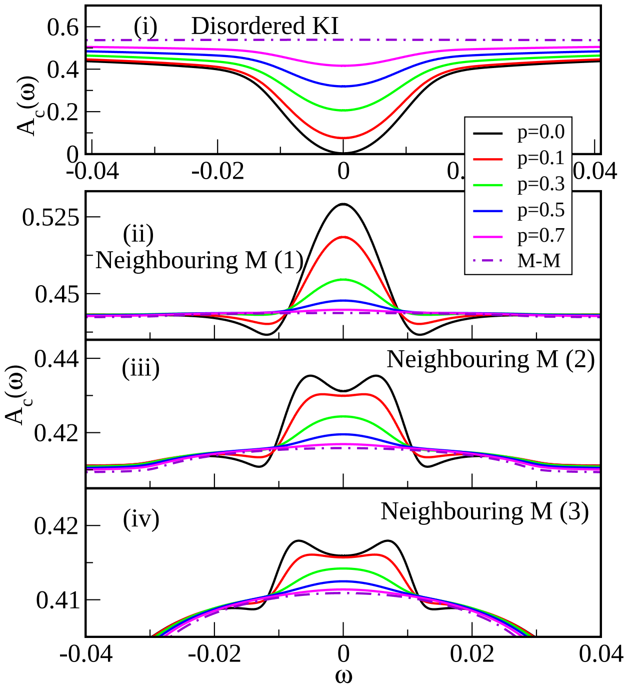

Figure 3.7: **Spectral evolution at low energies** for the disordered Kondo insulator (panel(i)) and the proximal clean metals (panel((ii)-(iv))). A system of a single disordered Kondo insulator and 11 clean metallic layers is used.The respective layer-resolved metallic spectra corresponding to a 12 layer metal-metal (M-M) system is also shown for comparison. The model parameters are the same as used in Fig. 3.6

.

expected qualitatively because introducing Kondo holes implies that sites with f-orbitals in the boundary layer are randomly being replaced by non-interacting sites, hence the effects of interactions should get mitigated not only in the layer but also in the adjoining layers.

The penetration of Kondo holes into proximal band insulating layers is however different (than the proximity to metals discussed above). The exponentially larger non-interacting hybridization gap of the proximal band insulators prohibit electrons from tunneling into the insulating gap. Thus, disorder induced spectral changes in proximal band insulators remain confined to the band edges and the high energy Hubbard bands. To this end, we refer back to our discussion on the Kondo insulator/band insulator bilayer interface in section 3.3.1. There we realized that, around the band edges of the proximal band insulator, where the Kondo insulator has available states, a quadratic band bending would occur owing to the interlayer coupling. If the clean layers are also interacting Kondo-insulators, the proximity effects of disorder span over all frequency scales, from the universal, hybridization gap scale to the non-universal, Hubbard bands. This shall be discussed now.

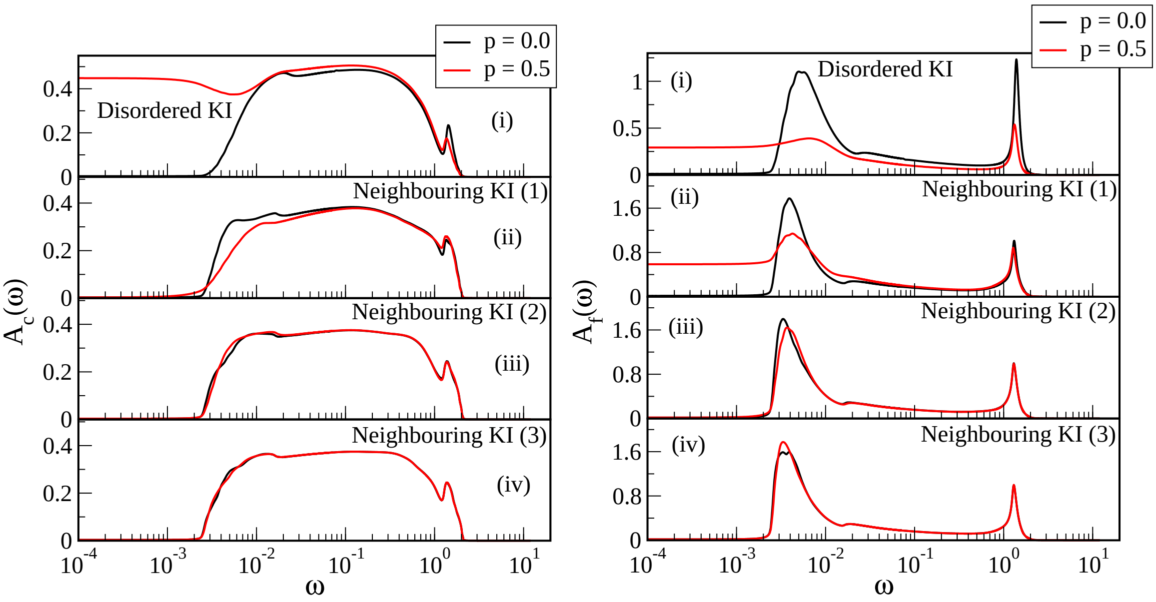

Figure 3.8: (Left panel): The layer resolved c-electron spectra of a single disordered Kondo insulator coupled to 11 clean Kondo insulating (KI) layers. The respective layers are denoted in the panels;(right panel): The same for the CPA averaged f-electrons of the disordered Kondo insulator and the interacting f-electrons of the clean Kondo insulators. The parameters used are $t_\perp = 0.5$, $V = 0.44$, $U = 1.7$

The boundary layer metallic states introduced by Kondo hole disorder now tunnel into the adjoining Kondo insulator, causing the quadratic bending of the gap in the adjacent layer (see figure 3.8). This tunneling effect does propagate into the further layers, but is attenuated by the ω^2 factor and is hence too small to be observed. The mechanism of penetration of the Kondo hole disorder induced metallic states from the disordered Kondo insulator to the coupled clean Kondo insulator is thus physically very similar to that of a clean metal interfaced with a clean Kondo insulator (Eqs (3.16), (3.17)).

In the disordered Kondo insulator layer, spectral weight transfer occurs across all scales. It is well known that Kondo hole substitution results in a coherent lattice to an incoherent single-impurity crossover. This manifests in the transfer of weight from high energy Hubbard bands to the Kondo resonance. Concomitantly, the hybridization experienced by the interacting sites in the boundary layer crosses over to a featureless non-interacting lineshape. The adjacent layers get strongly affected by these changes and the spectral weight transfer occurs across all energy scales in the nearest neighbor Kondo insulator as well. The Hubbard bands in the second layer too acquire an explicit Kondo hole induced depletion. Although there exists no explicit interlayer f-c hybridization the f-electrons in the clean layers get strongly influenced by the presence of Kondo holes in its adjacent layer. This is because the f-e$^-$s of the proximal clean layers see a self consistently determined layer dependent host hybridization function, $\Delta_\alpha(\omega)$, as can be seen from Eq(3.7). We now quantify the spectral weight transfers focusing on the role of interactions in the proximity effects of disorder.

As explained earlier, the spectral weight difference between the spectra, with and without disorder, integrated in a given frequency interval, represents one measure of the proximity effect of disorder. We have chosen two frequency intervals: (i) a 'low' frequency interval defined by $|\omega| \leq \Omega_{BI}$, where $\Omega_{\rm BI} = \frac{1}{2}\left(-t_{||} + \sqrt{t_{||}^2 + 4V^2}\right)$, represents the hybridization gap edge of an isolated band insulator and (ii) the entire frequency range. This classification into low frequencies and all frequencies is done to emphasize that the low frequency spectral changes could be tiny ($\sim \omega_L \rho_0(0)$, which is exponentially small in strong coupling) but affect low temperature properties, especially transport, in a major way. The spectral changes over *all* frequencies will show up in photoemission and optical properties measurements, and hence are important from a different perspective. Since the Kondo holes are introduced only in the boundary layer, the spectral weight transfers would be maximal there. Moving away from the disordered Kondo insulator layer, the changes in the spectra due to the boundary layer disorder must decrease. Indeed, this expectation is borne out, as seen in figure 3.9. The spectral weight difference defined in equation (3.30) decreases sharply with distance from the disordered Kondo insulator layer for all the three cases considered (interfacing the disordered Kondo insulator with either 11 metals, or 11 band/Kondo insulators) thus far. These spectral weight changes

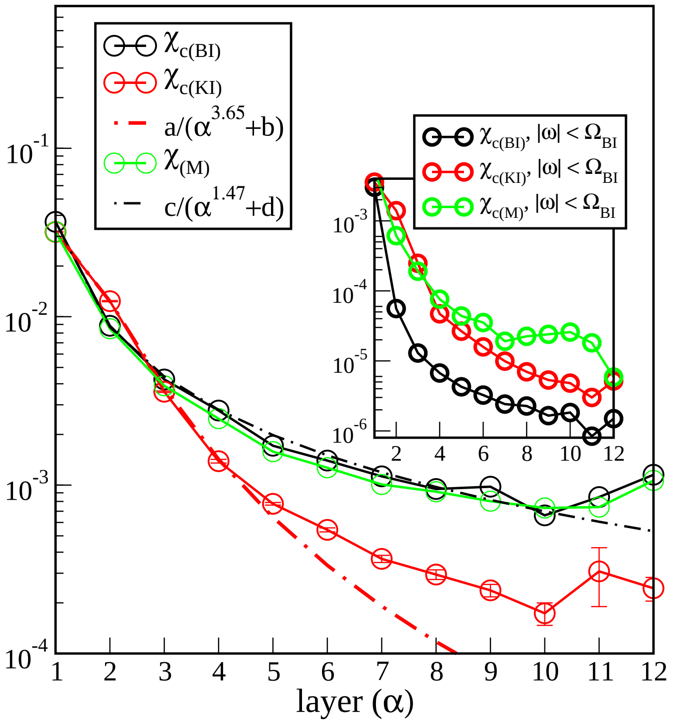

Figure 3.9: **Proximity effect of disorder:** The integrated spectral weight difference (between the disordered and the clean systems, see equation (3.30)) as a function of the layer index for a system of a single doped Kondo insulator interfaced with (a) 11 clean band-insulators (black); (b) 11 clean Kondo insulators (red) and (c) 11 metallic layers (green). The main panel is the spectral weight difference with a cutoff, $\lambda \to \infty$. In the inset, $\Omega_{\rm BI} = \frac{1}{2}\left(-t_{||} + \sqrt{t_{||}^2 + 4V^2}\right)$, representing the hybridization gap edge of an isolated band insulator, has been used as the cutoff (λ) in energy space to get the spectral weight difference at 'low' energies ($|\omega| < \Omega_{\rm BI}$). The dot-dashed lines are algebraic decay fits, with black for (a) and (c), and red for (b). $U = 1.7$ in the Kondo insulating layers, $V = 0.44$ in both the band insulating and Kondo insulating layers, the inter-layer hopping is set to $t_\perp = 0.5$.

quantify the proximity effects of disorder, in the absence or presence of interactions. The fits of the spectral weight difference (dot-dashed lines in figure. 3.9) show that the proximity effects decay algebraically with increasing distance from the boundary layer. Such a decay profile indicates that changes made in the boundary layer can penetrate quite deep into the system.

Apart from the overall decay profile, there are subtle aspects of the spectral weight difference that we highlight now. The main panel in figure 3.9 shows the spectral weight difference computed over all frequency scales ($\lambda \to \infty$). The spectral changes in the non-interacting as well as interacting layers are see to be similar up to the third layer, beyond which the Kondo insulating layers are far less affected than the non-interacting metallic or band-insulating layers. However, the low frequency spectral weight difference ($\lambda = \Omega_{BI}$), shown in the inset, presents an entirely different picture. The band-insulators are seen to be least affected, since the spectral weight difference drops rapidly by over a decade even for the layer adjacent to the disordered Kondo insulator boundary layer. In contrast, the metallic and Kondo-insulating layers experience similar levels of spectral changes due to the disorder in the boundary layer. Thus, when viewed over all scales, interactions indeed screen the proximity effects of disorder. However, in the neighborhood of the Fermi level, the presence of a spectral gap makes the band-insulator immune to the changes in the boundary layer, and the presence or absence of interactions is irrelevant.

3.4 Discussion

For the results in the previous section, it is clear that Kondo hole substitution in a single boundary layer does indeed affect neighboring layers to varying degrees on different energy scales. Although we have considered finite systems, a few general remarks may be made for infinite, periodic structures.

3.4.1 f-electron Superlattices:

A superlattice structure comprises a periodic array of unit cells, each of which consist of a finite number of $(m)f$-e^- and $(n)c$-e^- layers. For example, in Ref. [30], $(m,4)$CeIn$_3$/LaIn$_3$ superlattices were grown and m was tuned. The authors surmised that Kondo hole disorder at the Ce/La interface is inevitable. As shown in figure 3.9, the extent of proximity induced disorder effects is appreciable in the neighboring layers. Owing to the periodic nature of a superlattice, it is thus expected that this proximity effect would be even more pronounced stemming from penetration of disorder effects from the adjacent unit cells of the superlattice.

3.4.2 A scenario for disorder induced non-Fermi liquid:

Thus far, we have considered the particle-hole symmetric limit. However, an interesting situation might emerge by varying the chemical potential such that the system does not have particle-hole symmetry. Dynamical effects of impurity scattering even at the single-site mean field level have been shown (in Ref. [34]) to lead to a non-Fermi liquid form of the average selfenergy. Thus the Kondo hole disordered layers in such an array of f electron layers would show non-Fermi liquid behavior. The non-Fermi liquid nature of the Kondo hole disordered layers would thus introduce a further anisotropy in the system that would possibly manifest itself in the transport properties of these systems. Moreover, if the Ce/La interfaces in the superlattice unit cell are separated by a larger number of clean layers, the non-Fermi liquid effects would be expected to attenuate. Hence a non-Fermi liquid to Fermi liquid crossover can be expected simply by increasing the ratio of the number of layers to the number of Ce/La interfaces.

3.4.3 Anderson Localization:

One of the important consequences of disorder, ignored in this work, is that of Anderson localization (AL). The CPA employed here to treat disorder effects is incapable of incorporating AL. The addition of coherent back-scattering and deep trap physics beyond CPA should lead to profound consequences for the adjacent layers. A first step in this direction could be the incorporation of the (single site) Typical Medium Theory (TMT) [55] in the context of such layered systems. A subsequent advancement would then be an systematic inclusion of non-local dynamical corrections to the TMT. The typical medium -dynamical cluster approximation (TMDCA) developed recently [56] has been found to be an excellent approach for obtaining the correct phase diagram of the non-interacting Anderson model. It would be interesting to extend the TMDCA for interacting models and explore the interplay of Anderson localization physics and strong interactions in layered systems.

3.5 Summary and Conclusions

In this work, we have employed the inhomogeneous dynamical mean field theory [26] framework to obtain self consistent many body solutions for layered Kondo hole substituted f-electron systems. The substitutional disorder, treated within the coherent potential approximation, was introduced in a single boundary layer, and the consequent spectral changes in the neighboring layers were explored. Three distinct types of clean adjacent layers were considered: (a) non-interacting metals (disordered Kondo insulator/metals), (b) non-interacting band insulators (disordered Kondo insulator/band insulator), and, (c) several clean Kondo insulators.

Combining simple analytical expressions for bilayer and trilayer systems with full numerical calculations using the local moment approach, we have (a) explained the strong renormalization of the low energy spectra of the proximal layers, (b) spectral interference among the layers in presence of an inter-layer coupling ($t_\perp$), and (c) a mechanism for penetration of Kondo hole disorder induced incoherence into clean layers. We highlight the differences between three distinct types of interfaces with a disordered Kondo insulator layer. We also demonstrate that, in addition to a robust low energy quasiparticle peak [27], proximity effects of interactions also manifest through the appearance of minute Hubbard bands in the neighboring non-interacting layers.

A finite concentration of Kondo holes leads to the formation of an impurity band at the Fermi level in a Kondo insulator [51–53], thus creating metallic states in the otherwise gapped insulator. In the layered geometry, these disorder induced metallic states can further tunnel into the immediately neighboring clean Kondo insulator, rendering a quadratic bending in its Kondo hybridization gap edge. This further induces metallic states in the f-e$^-$ spectra of the the nearest neighbor layer. These disorder induced states do propagate into the further layers but the tunneling is attenuated by the ω^2 factor for each layer and hence is too small to be observed beyond the nearest neighbor layer. Introduction of disorder further destroys the proximity effect of interactions. We showed that a manifestation of proximity induced interaction effect, on the adjacent non-interacting layers, is the appearance of tiny Hubbard bands and a proximal Kondo effect induced low frequency spectral renormalization. This proximity effect of interactions, on the non-interacting layers, is mitigated when they are coupled to a disordered Kondo insulator layer.

The presence of disorder induces spectral weight transfer from the high energy Hubbard bands to the low energy Kondo scaling regime not only in the disordered Kondo insulator but in the adjacent clean layers as well. We have quantified the penetration of disorder effects in these interfaces through the spectral weight difference function (equation (3.30). The spectral weight difference is maximum in the disordered Kondo insulator and decays algebraically with distance from the disordered Kondo insulator layer.

Our analysis implies that, while for thin films, the spectral weight difference of the clean layers is appreciable only until the third neighboring layer; for superlattice geometries, this effect of penetration of disorder would be quite pronounced due to the occurrence of multiple disordered interfaces.

We foresee a Fermi liquid to non-Fermi liquid crossover in the transport properties across disordered interfaces by tuning the number of disordered layers. The full study of such a crossover and inclusion of localization effects beyond the coherent potential approximation will be the subjects of future projects.

Bibliography

[1] A. Ohtomo, D. Muller, J. Grazul, and H. Hwang, Nature **419**, 378 (2002).

[2] K. Yoshimatsu, T. Okabe, H. Kumigashira, S. Okamoto, S. Aizaki, A. Fujimori, and M. Oshima, Phys. Rev. Lett. **104**, 147601 (2010).

[3] K. Yoshimatsu, K. Horiba, H. Kumigashira, T. Yoshida, A. Fujimori, and M. Oshima, Science **333**, 319 (2011).

[4] S. Okamoto, Phys. Rev. B **84**, 201305 (2011).

[5] M. Potthoff and W. Nolting, Physica B **259**, 760 (1999).

[6] N. Reyren, S. Thiel, A. D. Caviglia, L. F. Kourkoutis, G. Hammerl, C. Richter, C. W. Schneider, T. Kopp, A.-S. Retschi, D. Jaccard, et al., Science **317**, 1196 (2007).

[7] J. A. Bert, B. Kalisky, C. Bell, M. Kim, Y. Hikita, H. Y. Hwang, and K. A. Moler, Nature Physics **7**, 767 (2011).

[8] X. W. Ariando, G. Baskaran, Z. Q. Liu, J. Huijben, J. B. Yi, A. Annadi, A. R. Barman, A. Rusydi, S. Dhar, Y. P. Feng, et al., Nature Communications **2** (2011).

[9] P. Zubko, S. Gariglio, M. Gabay, P. Ghosez, and J.-M. Triscone, Ann. Rev. Condens. Matter Phys. **2**, 141 (2011).

[10] M. Potthoff and W. Nolting, Phys. Rev. B **60**, 7834 (1999).

[11] S. Schwieger, M. Potthoff, and W. Nolting, Phys. Rev. B **67**, 165408 (2003).

[12] M. Potthoff and W. Nolting, The European Physical Journal B **8**, 555 (1999).

[13] M. Potthoff and W. Nolting, Phys. Rev. B **59**, 2549 (1999).

[14] M. Potthoff and W. Nolting, Journal of Physics: Condensed Matter **8**, 4937 (1996).

[15] S. Okamoto and A. J. Millis, Phys. Rev. B **70**, 241104 (2004).

[16] S. Okamoto and A. J. Millis, Physica B: Condensed Matter **359-361**, 1378 (2005), ISSN 0921-4526.

[17] S. Okamoto and A. J. Millis, Phys. Rev. B **72**, 235108 (2005).

[18] H. Zenia, J. K. Freericks, H. R. Krishnamurthy, and T. Pruschke, Phys. Rev. Lett. **103**, 116402 (2009).

[19] A. Euverte, F. Hébert, S. Chiesa, R. T. Scalettar, and G. G. Batrouni, Phys. Rev. Lett. **108**, 246401 (2012).

[20] H. Ishida and A. Liebsch, Phys. Rev. B **79**, 045130 (2009).

[21] H. Ishida and A. Liebsch, Phys. Rev. B **82**, 045107 (2010).

[22] H. Ishida and A. Liebsch, Phys. Rev. B **85**, 045112 (2012).

[23] R. W. Helmes, T. A. Costi, and A. Rosch, Phys. Rev. Lett. **101**, 066802 (2008).

[24] A. Rüegg, S. Pilgram, and M. Sigrist, Phys. Rev. B **75**, 195117 (2007).

[25] A. Rüegg, S. Pilgram, and M. Sigrist, Phys. Rev. B **77**, 245118 (2008).

[26] J. K. Freericks, Phys. Rev. B **70**, 195342 (2004).

[27] R. Peters, Y. Tada, and N. Kawakami, Phys. Rev. B **88**, 155134 (2013).

[28] Y. Tada, R. Peters, and M. Oshikawa, Phys. Rev. B **88**, 235121 (2013).

[29] S. Okamoto and T. A. Maier, Phys. Rev. Lett. **101**, 156401 (2008).

[30] H. Shishido, T. Shibauchi, K. Yasu, T. Kato, H. Kontani, T. Terashima, and Y. Matsuda, Science **327**, 980 (2010).

[31] R. Peters and N. Kawakami, Phys. Rev. B **89**, 041106 (2014).

[32] C. Grenzebach, F. B. Anders, G. Czycholl, and T. Pruschke, Phys. Rev. B **77**, 115125 (2008).

[33] M. Shimozawa, T. Watashige, S. Yasumoto, Y. Mizukami, M. Nakamura, H. Shishido, S. K. Goh, T. Terashima, T. Shibauchi, and Y. Matsuda, Phys. Rev. B **86**, 144526 (2012).

[34] N. S. Vidhyadhiraja and P. Kumar, Phys. Rev. B **88**, 195120 (2013).

[35] E. Feenberg, Phys. Rev. **74**, 206 (1948).

[36] E. N. Economou, *Green's Functions in Quantum Physics* (Springer; 3rd edition, 2006).

[37] D. E. Logan, M. P. Eastwood, and M. A. Tusch, Journal of Physics: Condensed Matter **10**, 2673 (1998).

[38] M. R. Galpin and D. E. Logan, Journal of Physics: Condensed Matter **17**, 6959 (2005).

[39] N. S. Vidhyadhiraja, V. E. Smith, D. E. Logan, and H. R. Krishnamurthy, Journal of Physics: Condensed Matter **15**, 4045 (2003).

[40] N. S. Vidhyadhiraja and D. E. Logan, European Physical Journal B **39**, 313 (2004), ISSN 1434-6028.

[41] D. E. Logan and N. S. Vidhyadhiraja, Journal of Physics: Condensed Matter **17**, 2935 (2005).

[42] N. S. Vidhyadhiraja and D. E. Logan, Journal of Physics: Condensed Matter **17**, 2959 (2005).

[43] M. T. Glossop and D. E. Logan, Journal of Physics: Condensed Matter **15**, 7519 (2003).

[44] M. T. Glossop and D. E. Logan, EPL (Europhysics Letters) **61**, 810 (2003).

[45] D. E. Logan and M. T. Glossop, Journal of Physics: Condensed Matter **12**, 985 (2000).

[46] M. R. Galpin and D. E. Logan, The European Physical Journal B **62**, 129 (2008), ISSN 1434-6028.

[47] R. Bulla, M. T. Glossop, D. E. Logan, and T. Pruschke, Journal of Physics: Condensed Matter **12**, 4899 (2000).

[48] W.-C. Yueh, Applied Mathematics E-Notes **5**, 66 (2005).

[49] M. Potthoff, Habilitation Thesis, Humboldt-Universitt zu Berlin, Berlin (1999).

[50] P. Aynajian, E. H. da Silva Neto, A. Gyenis, R. E. Baumbach, J. D. Thompson, Z. Fisk, E. D. Bauer, and A. Yazdani, Nature **486**, 201 (2012).

[51] P. Schlottmann, Phys. Rev. B **54**, 12324 (1996).

[52] P. S. Riseborough, Phys. Rev. B **68**, 235213 (2003).

[53] T. Mutou, Phys. Rev. B **64**, 165103 (2001).

[54] P. Schlottmann, Phys. Rev. B **46**, 998 (1992).

[55] V. Dobrosavljevi, A. A. Pastor, and B. K. Nikoli, EPL (Europhysics Letters) **62**, 76 (2003).

[56] C. E. Ekuma, H. Terletska, K.-M. Tam, Z.-Y. Meng, J. Moreno, and M. Jarrell, Phys. Rev. B **89**, 081107 (2014).

Chapter 4

Quantum critical Mott transitions in a Kondo insulator-metal heterojunction[§]

Contents

[§] Work reported in this chapter is available as:
Sudeshna Sen, N. S. Vidhyadhiraja, “Quantum critical Mott transitions in a bilayer Kondo insulator-metal model system”, (Submitted) preprint: arxiv:1511.06712v1

4.1 Introduction

Recent experiments [1, 2] and theoretical calculations [3–7] on finite layered systems provide promising directions for studying emergent phases in strongly correlated systems [1, 2, 8]. A typical example is that of ^{3}He that represents a unique realization of a Fermi liquid and also features a relevant quantum critical point (QCP) at a critical filling of the layers [1]. The experimental observations on ^{3}He bilayers reveal a unique artificial realization of heavy fermion physics and has guided several theoretical calculations. Experiments on such finite layered systems provide ideal scenarios to engineer and test unique realizations of phases in strongly correlated electron systems. In this work, we look into a model that comprises of a heterojunction half filled heavy fermion system, namely, a Kondo-insulator coupled to a non-interacting metal.

The periodic Anderson model (PAM) is a basic microscopic model for a theoretical understanding of heavy fermion materials. The key physics governing this model involves spin flip scattering of the itinerant conduction electrons by the localized f-electrons leading to large effective masses and low energy scales symptomatic of the Kondo effect [9, 10]. The Mott transition [9] generally observed in the Hubbard model (HM) is another intriguing phenomenon driven by strong electronic correlations. The generic scenario for Mott MITs is that they are first order in nature, with a finite temperature critical end point [9, 11–13], and are usually accompanied by large hysteresis curves, as seen for example in experiments on the vanadium oxides, V_2O_3 and VO_2 [14, 15]. The two possible exceptions are (a) a bilayer ^{3}He system [16], that can be pushed to a layer selective quantum critical Mott transition by tuning the filling of the layers [1, 4, 5, 17–19]; and (b) two-dimensional organic insulators, where a pressure driven Mott quantum critical point (QCP) has been found very recently [20].

The idea of a QCP in a Mott transition has thus far appeared as an exception rather than the rule, unlike in the case of heavy fermions that offer numerous examples of quantum criticality, which are driven either by spin or valence fluctuations [21, 22]. A recent work by Senthil [23] proposed the possibility of observing a second order Mott transition from a Fermi liquid metal to a Mott insulator with a spinon Fermi surface in two dimensions. The role of critical fermionic quasiparticles has been proposed in the context of continuous Mott transitions and orbital selective Mott transitions at zero temperature [21, 23, 24]. Recent study of quantum critical transport near the Mott transition in half-filled Hubbard model [25] has been interpreted as evidence of a hidden Mott quantum criticality. Further study on doped Hubbard models reveal a clear connection between bad metal phenomenology and signatures of Mott quantum criticality. [26]. Studies of holographic duality propose the existence of yet-unspecified quantum critical regimes for strange metals in cuprates [27, 28]. In order to obtain a better understanding of the continuous Mott MIT, it would be desirable to identify new systems where Mott quantum criticality may be observed.

In this work, we consider a bilayer heavy fermion system comprising a Kondo insulator (KI), represented by a symmetric periodic Anderson model (PAM) [9, 10], coupled to a non-interacting metal (M). Previous theoretical studies on coupling a KI layer to metallic layers have shown[29, 30] that the normally gapped f and c-bands of the KI acquire a finite density of states and a quadratically vanishing gap respectively due to the coupling. This emergent metallic phase of the f-electrons leads us to anticipate an interaction driven Mott transition. To our surprise, we find a plethora of interaction driven Mott QCPs in the KI-M system. The quantum critical nature of the Mott transitions is established by the vanishing of the coherence scale from the Fermi liquid side, and of the Mott gap from the insulating side at the same point in the parameter space. The competition between itinerancy and localization might lead to as yet unknown universality classes for the Mott transition [27, 28], and indeed, the system under consideration, might serve as an ideal model to investigate the universality and scaling associated with Mott quantum criticality.

4.2 Model, Theoretical Framework and Analytical results

The Hamiltonian of the bilayer KI-M model system is given by,

$$\mathcal{H} = \begin{pmatrix} f_\sigma^\dagger & c_{k\sigma}^\dagger & c_{M,k\sigma}^\dagger \end{pmatrix} \begin{pmatrix} \epsilon_f & V & 0 \\ V & \epsilon_c + \epsilon_k & t_\perp \\ 0 & t_\perp & \epsilon_{cM} + \epsilon_k \end{pmatrix} \begin{pmatrix} f_\sigma \\ c_{k\sigma} \\ c_{M,k\sigma} \end{pmatrix} + U \sum_i n_{fi\uparrow} n_{fi\downarrow} \tag{4.1}$$

where ϵ_f is the orbital energy of the non-dispersive f-band, which is coupled to a conduction band with dispersion ϵ_k and orbital energy ϵ_c through a hybridization V. These f-and c-orbitals belong to the KI layer, which is coupled to the metallic layer, characterised by a conduction band, ϵ_k, and a orbital energy, ϵ_{cM}, through an inter-layer hopping, $t_\perp$. The second term represents the cost of double occupancy, U, of the f-orbitals of the KI layer.

In this work, we consider the particle-hole limit of this model where $\epsilon_c = \epsilon_{cM} = \epsilon_f + U/2 = 0$, and each of the three bands are half-filled. The KI-M model may be solved exactly in the non-interacting limit ($U = 0$), and the atomic limit ($V = 0$) [29]. In order to investigate the system beyond these simple limits, we employ the DMFT framework [9], within which the self-energy becomes local or momentum-independent. A cavity construction [9] for the bilayer model considered in Eq. (4.1) yields the following effective action for the f electrons:

$$S_{eff} = -\int_0^\beta d\tau \int_0^\beta d\tau' \sum_\sigma f_\sigma^*(\tau) \mathcal{G}_{0f}^{-1}(\tau - \tau') f_\sigma(\tau) + U \int_0^\beta d\tau n_{f\uparrow}(\tau) n_{f\downarrow}(\tau), \tag{4.2}$$

with,

$$\mathcal{G}_{0f}(\omega) = \int \frac{\rho_0(\epsilon)}{\omega^+ - \frac{V^2}{\omega^+ - \epsilon - t_\perp^2/(\omega^+ - \epsilon)}} d\epsilon \tag{4.3}$$

The f-Green's function may be written as

$$G^f(\omega) = \sum_k G^f(\omega, \epsilon_k) = \int_{-\infty}^{\infty} d\epsilon \, \rho_0(\epsilon) G^f(\omega, \epsilon), \tag{4.4}$$

where, the $\rho_0(\epsilon) = 2\sqrt{1 - \epsilon^2/D^2}/(\pi D)$ is a semi-elliptic non-interacting conduction band density of states (DoS) of width $2D$, appropriate for a system with long-range hoppings, chosen to suppress magnetic ordering [9];

$$G^f(\omega, \epsilon) = \frac{\rho_0(\epsilon)}{\omega^+ - \frac{V^2}{\omega^+ - \epsilon - t_\perp^2/(\omega^+ - \epsilon)} - \Sigma_f(\omega)} \tag{4.5}$$

with $\Sigma_f(\omega)$ being the momentum-independent f-self-energy. Several results may be derived from these expressions, that are outlined below. For $U = V = 0$, the bilayer system undergoes a metal to band-insulator transition when the interlayer hopping exceeds the conduction band width. However, with $V \neq 0$, the non-interacting f-density of states, given by $D^f(\omega; U = 0) = -\text{Im}G^f(\omega; U = 0)/\pi$ does not vanish for any $t_\perp \neq 0$, although the $\omega = 0$ peak in the density of states gets progressively narrower with increasing $t_\perp$: $D^f(\omega; U = 0) \overset{t_\perp \gg 1}{\longrightarrow} \frac{t_\perp^2}{V^2} \rho_0\left(\frac{\omega t_\perp^2}{V^2}\right)$. From the above expression, it is easy to see that, when $t_\perp \gg 1$, the effective bandwidth, D_{eff} of the f-DoS is greatly reduced as $\sim V^2/t_\perp^2$, hence the interaction strength needed for the Mott metal to insulator transition may be estimated as

$$U_c \sim D_{eff} \overset{t_\perp \gg 1}{\longrightarrow} D \, V^2/t_\perp^2, \tag{4.6}$$

implying that the interaction strength required to drive the Mott transition should decrease rapidly with increasing inter-layer hopping.

The c-electrons in the heavy fermion layer acquire a self-energy, $\Sigma_{c1}(\omega)$ that can be related to $\Sigma_f(\omega)$ as, $\Sigma_{c1}(\omega) = \frac{V^2}{\omega^+ - \Sigma_f(\omega)}$. For, the non-interacting metallic layer, $V = 0$ and hence, $\Sigma_{c2}(\omega) = 0$. In our previous work [29] we had shown that for a bilayer system, the c-electron Greens functions are given by,

$$G_{11}(\omega) = a \, H[\Gamma_+] + b \, H[\Gamma_-], \tag{4.7}$$

$$G_{22}(\omega) = a' \, H[\Gamma_+] + b' \, H[\Gamma_-], \tag{4.8}$$

where

$$\Gamma_\pm = \frac{1}{2}\left(\lambda_1 + \lambda_2 \pm \sqrt{(\lambda_1 - \lambda_2)^2 + 4t_\perp^2}\right), \tag{4.9}$$
$$\lambda_r = \omega^+ - \epsilon_c - \Sigma_{cr}(\omega), \quad r = 1, 2$$

$$a = \frac{\Gamma_+ - \lambda_2}{\Gamma_+ - \Gamma_-} \text{ and } b = \frac{\lambda_2 - \Gamma_-}{\Gamma_+ - \Gamma_-}, \tag{4.10}$$
$$a' = -\frac{\lambda_1 - \Gamma_+}{\Gamma_+ - \Gamma_-} \text{ and } b' = \frac{\lambda_1 - \Gamma_-}{\Gamma_+ - \Gamma_-}, \tag{4.11}$$

and $H[z]$ represents the Hilbert transform with respect to the bare DoS of the conduction electrons. Using these expressions one may then derive a low energy form of the respective spectral function. In the low frequency regime of a Fermi liquid (FL) phase, where the f self-energy may be expanded in a Taylor series as: $\Sigma_f(\omega) = \Sigma_f(0) + \omega(1 - 1/Z) + \mathcal{O}(\omega^2)$ (where Z is the quasiparticle weight), the DoS of the c-e$^-$s of the heavy fermion layer has the following form:

$$\begin{aligned} D_1^c(\omega) \overset{\omega\to 0}{\sim} & \left(\frac{\omega t_\perp}{ZV^2}\right)^2 \rho_0\left(\omega\left[1 + \frac{t_\perp^2}{ZV^2}\right]\right) \\ & + \left(1 - \left(\frac{\omega t_\perp}{ZV^2}\right)^2\right)\rho_0\left(\omega\left[1 - \frac{t_\perp^2}{ZV^2}\right] - \frac{ZV^2}{\omega}\right). \end{aligned} \tag{4.12}$$

Further, since $D^f(\omega) = (Z^2V^2/\omega^2)D_c(\omega)$, the f-e$^-$ DoS at $\omega = 0$ is pinned to the non-interacting limit namely, $V^2D^f(0)/t_\perp^2 = \rho_0(0)$, thus exhibiting adiabatic continuity to the non-interacting limit and hence satisfying a necessary condition for a Fermi liquid (FL). In a Mott insulating phase, on the other hand, the self-energy must have a pole at $\omega = 0$ with the form $\Sigma_f(\omega) \xrightarrow{\omega\to 0} \alpha/\omega^+$, where the residue of the pole is $\alpha \sim \mathcal{O}(U^2)$ [9, 31]. So, if the bilayer system should have a Mott insulating phase, the denominator of $G^f(\omega;\epsilon)$ should not have zeroes for any $|\epsilon| < D$ as $\omega \to 0$, since that would imply a non-zero density of states in the single-particle spectrum at the chemical potential. It may be shown easily that such a condition is satisfied only for $t_\perp > D$. This condition can also be derived by substituting, $\Sigma_f(\omega) \xrightarrow{\omega\to 0} \alpha/\omega^+$, in Equation (4.8). Thus, a Mott insulating phase can be sustained only if $t_\perp > D$.

From the above analysis, we can anticipate a line of Mott transitions in the $t_\perp - U$ plane, where the critical U should decrease at least as rapidly as $1/t_\perp^2$ for $t_\perp \gg 1$ and for $U \to \infty$, the critical $t_\perp$ should asymptotically approach the bandwidth D. In order to determine the phase diagram quantitatively, we must obtain the self-energy $\Sigma_f(\omega)$ and examine the quasiparticle weight as well as the Mott gaps. In this work, we choose the local moment approach (LMA) as the solver for the $T = 0$ quantum impurity problem. It is a diagrammatic perturbation theory based approach, which is built around the two broken-symmetry, local moment solutions ($\mu = \pm|\mu_0|$) of an unrestricted Hartree-Fock mean field approximation. The spin-flip dynamics are subsequently incorporated through an infinite order resummation of a specific class of diagrams that represent the spin flip process necessary to capture the Kondo effect. Finally, a key ingredient of LMA is to impose adiabatic continuity to the noninteracting limit, that is crucial for the recovery of Fermi liquid behaviour and the emergence of a low energy scale. This is known as the symmetry restoration condition and any violation of this condition is a signal of a quantum phase transition to another phase such as a local moment phase. More details of the LMA may be found in previous work[10, 32, 33]. The LMA has been shown to benchmark excellently against numerical renormalization group (NRG) [34], and Bethe Ansatz for the single impurity Anderson model and the Kondo problem respectively [32]. Subsequently, it has been employed in studies on Kondo insulators and heavy fermion systems, where the dynamics and transport properties of several heavy fermions systems were quantitatively explained[10, 33, 35]. The LMA has also been used in studying specific cases of impurity systems with many orbitals [36], the pseudogap Anderson model, the gapped Anderson impurity model and the soft-gap Anderson model [37–40]. The study on the soft gap Anderson model has also been benchmarked with NRG [41]. The resultant LMA phase boundary was in good quantitative agreement with NRG results [40]. However, generalizing LMA for employing it as a cluster solver to incorporate non-local dynamical correlations has not been attempted yet.

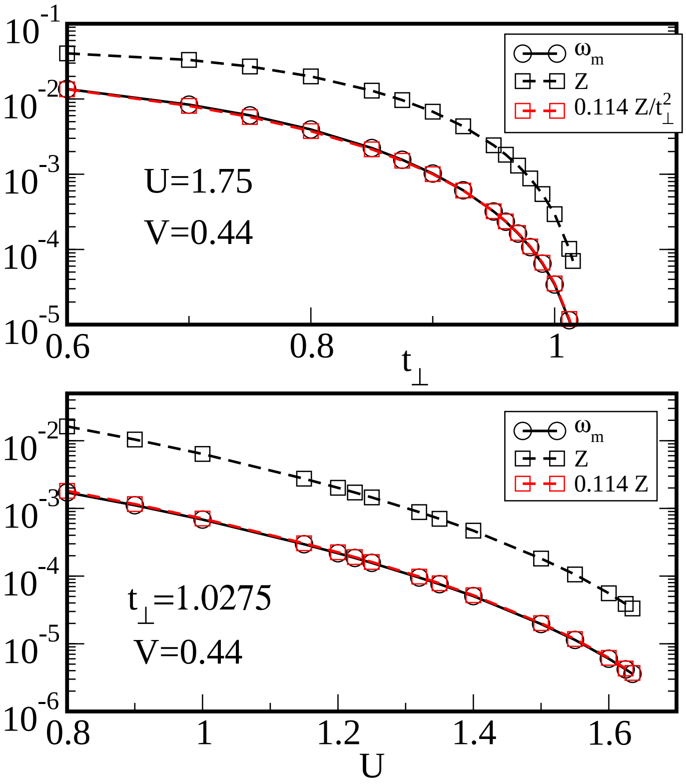

Figure 4.1: **Comparison of the low energy spin flip scale, ω_m and the quasiparticle weight, Z:** ω_m (black circles) and the corresponding quasiparticle weight, Z (black squares), shown on the same scale. A simple multiplicative rescaling of the Z makes it identical to the ω_m data as shown by the red squares.

4.3 Numerical Results

4.3.1 Phase diagram

As discussed earlier, the LMA captures the Kondo effect through the calculation of the transverse spin-flip processes embodied in the infinite-order resummation of a specific class of diagrams [32]. The low energy spin flip scale, 'ω_m', thereby generated and identified through the position of the peak of the imaginary part of the transverse spin polarization propagator within LMA, is known to be proportional to the Kondo scale in the single impurity Anderson model [32]. The 'ω_m' scale is proportional to

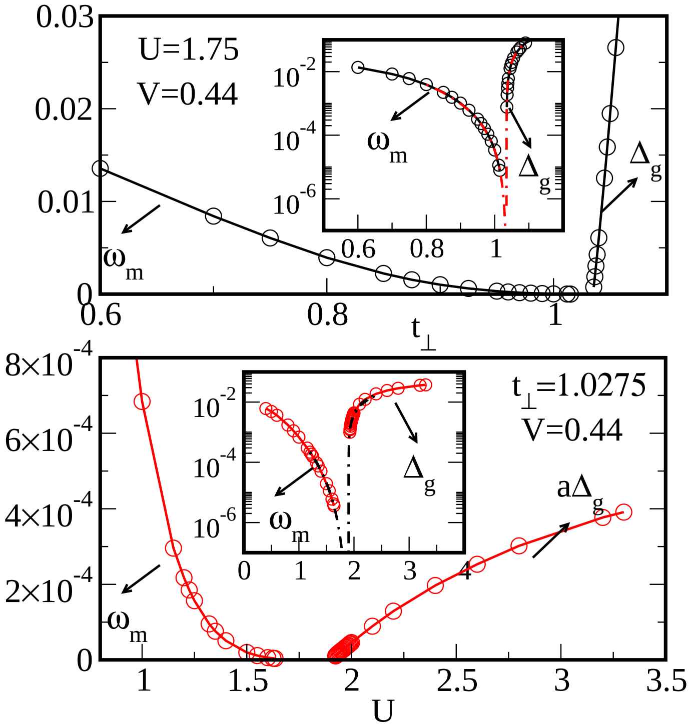

Figure 4.2: **The low energy spin flip scale, ω_m and the Mott gap, Δ_g for $V = 0.44$ as a function of $t_\perp$ (top panel, $U = 1.75$, $t_{\perp c} \approx 1.03$) and U (bottom panel, $t_\perp = 1.0275$, $U_c \approx 1.9$).** Note that in the main part of the bottom panel, the Mott gap values have been scaled by a multiplicative factor ($a = 1/95$) to show the ω_m and Δ_g on the same scale. In the insets, the same is plotted on a linear-log scale but the Mott gap is not rescaled. The extrapolation (dot-dashed line) to the critical value is shown to highlight that the Kondo scale and the Mott gap approach zero at the same critical point.

the quasiparticle weight ($Z = \left[1 - \frac{\partial \mathrm{Re}\Sigma(\omega)}{\partial \omega}\right]^{-1}$) also, as shown in Fig. 4.1, where both Z and the ω_m are plotted and rescaled with simple multiplicative factors to highlight their equivalence.

Thus, we choose ω_m to be the coherence scale in the Fermi liquid phase. The vanishing of the ω_m scale then signifies the divergence of the effective mass at the Mott transition. In the Mott insulating phase, this low energy scale vanishes, i.e. $\omega_m = 0$ indicating a zero energy cost to flip an unscreened local moment and a Mott gap develops. The Mott gap then serves as the relevant energy scale in the Mott insulating phase. Conventionally, one then probes the behaviour of these two relevant energy scales as a function of U to determine if there exists any regime of U where the metallic and the Mott insulating states may coexist, which would imply a first order Mott transition [9, 15, 42–44].

In Fig. 4.2 we therefore show the behavior of the FL scale ω_m, in the Kondo screened phase and the Mott gap, Δ_g in the Mott insulating state as a function of $t_\perp$ (top panel) and as a function of U (bottom panel). Indeed, we find that the two scales vanish as power laws given by $\omega_m \sim (g_c - g)^{\alpha_{FL}}$ and $\Delta_g \sim (g - g_c)^{\alpha_{MI}}$, where the athermal parameter, g, represents $t_\perp$ or U. It is seen from the top and bottom panels that either of the scales vanish at precisely the same (extrapolated) $t_{\perp c}$ (top) or U_c (bottom), thus indicating a quantum critical point in the $t_\perp - U$ plane.

A similar analysis for a wide range of values of U, V and $t_\perp$ yields a family of lines of QCPs in the $t_\perp - U$ plane for various V values, as shown in Fig. 4.3(a). In Fig. 4.3(a) we show the line separating a Kondo screened phase from the Mott insulating phase, for different V's, namely, $V = 0.44$ in the main panel and $V = 0.35,\ 0.5$ in the inset. These lines of QCPs represent a $t_\perp$ driven Mott transition and the procedure adopted to obtain the $t_{\perp c}$ at a fixed U is demonstrated in Fig. 4.3(b, c). Additionally, we also demonstrate the line of QCPs corresponding to a U driven transition for $V = 0.5$ as represented as red squares in the inset of Fig. 4.3(a), found to be identical with the critical points obtained for a $t_\perp$ driven transition. This confirms that U and $t_\perp$ would drive the respective Mott MITs at the same critical point, irrespective of the direction of approach. In Fig. 4.3(a) (main panel), we find that the curve *qualitatively* represent the analytical insight due to Eq. (4.6); however, the high $t_\perp$ and low U asymptote appears to fit well with a form, $t_{\perp c} \sim f(V)/U_c^{0.2}$. While this quantitative discrepancy could stem from the approximate analytical argument, it could also be possible that we need to go to even lower U's and even higher $t_\perp$'s to extract the form of the asymptote obtained from the numerical data.

We now mention the procedure adopted to extract the critical points in detail. For demonstration, we use the same data as shown in the top panel of Fig. 4.2. In the Fermi liquid phase (Fig. 4.3(b)), the calculations were performed until a Kondo scale of $\sim 5 \times 10^{-5}$ was reached. Starting from an initial guess value, $t_{\perp c}^{guess}$ of

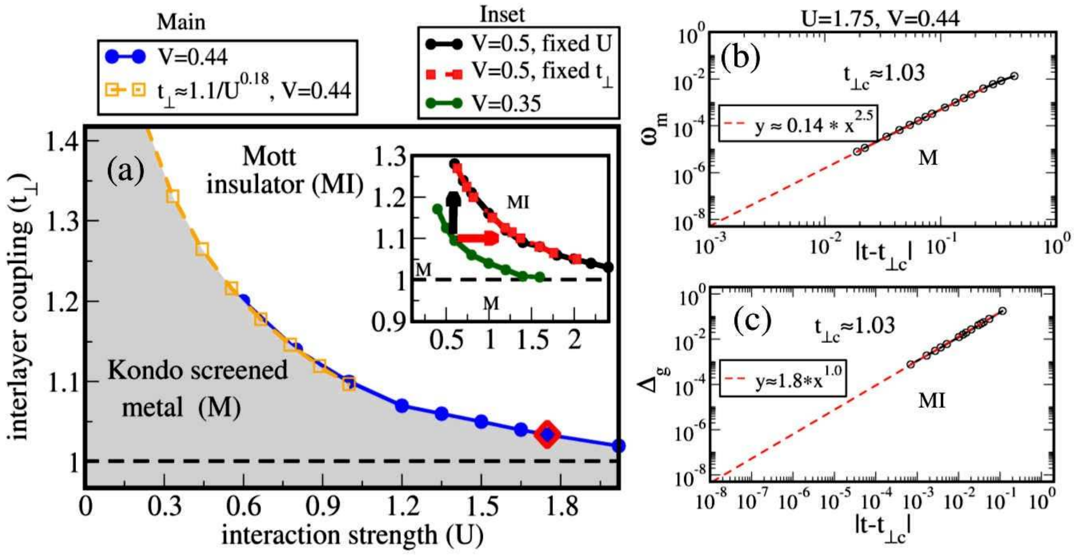

Figure 4.3: **The phase diagram in the $t_\perp - U$ plane for the transition from a Kondo screened Fermi liquid to a Mott insulating phase**: (a) The main panel shows the line of QCPs obtained, for $V = 0.44$ (blue circles), and, the inset shows the same for $V = 0.5$ (black circles, red squares) and $V = 0.35$ (green circles). While for $t_\perp \gg 1$ it was estimated that $t_{\perp c} \sim \sqrt{DV^2/U_c}$, the numerical data, corresponding to low U asymptote, fits well to a form $t_{\perp c} \sim f(V)/U_c^{0.2}$ as represented by the orange dashed line with squares for $V = 0.44$ (also see main text). The black dashed line represents the $t_\perp = D$ boundary for the existence of the Mott transition. Additionally, in the inset, we also show, (for $V = 0.5$) that the line of quantum critical Mott transitions is the same irrespective of the direction of approach, namely, $t_\perp$ driven (black circles, black arrow) or U driven (red squares, red arrow). (b, c) In order to identify the $t_\perp c$ or the U_c, we plot the ω_m (shown in (b) for $t_\perp c$) or the Δ_g (shown in (c) for $t_{\perp c}$) on a log-log scale. Starting from an initial guess value, $t_{\perp c}^{guess}$, we then add/subtract a small number ~ 0.001 from the simulated data points, plotted on a log-log scale. This subtraction/addition is continued until a visually inspected straight line was obtained that was fitted to the form $y = a|x - x_c|^\alpha$. The same procedure is repeated for U driven transitions. The representative plot corresponds to $U = 1.75,\ V = 0.44$ that also represents the top panel of Fig. 4.2. The corresponding extrapolated point is also highlighted as a red diamond in (a). The same is repeated for several other parameters and the phase diagram (a) in the $t_\perp$-U plane is generated.

the respective athermal variable, we then added/subtracted a small number ~ 0.001 from the simulated data points, plotted on a log-log scale. This subtraction/addition was then continued until a visually inspected straight line was obtained on the log-log scale and a fitting of the form $\omega_m = a|g - g_c|^{\alpha_{FL}}$ was done. The same was repeated for extrapolating the $t_{\perp c}$ while approaching the MIT from the Mott insulating side. This is shown in Fig. 4.3(c). As, shown in Fig. 4.3(b) and Fig. 4.3(c), ω_m and Δ_g vanish at the same critical point unlike a conventional Hubbard model at $T = 0$, indicating that the Mott MIT obtained in this model is a second order first transition. It is straightforward to see that each of these lines of QCPs is just a cut in the surface of QCPs in the $t_\perp - U - V$ space. This finding of an entire surface of Mott transitions, in a 'new' model, namely a bilayer KI-M model, that has not been explored before, represents the main result of this work. Moreover, our $T = 0$ calculations show that the Mott transitions are quantum critical in nature. The quantum critical surface separates two distinct phases, namely, a Kondo screened phase and a Mott insulating phase.

Our calculations show that the Mott quantum criticality that we discuss here involves a complete destruction of the Fermi surface (FS) in the f as well as c-spectrum (discussed in detail below) and is thus not a 'large to small FS' transition, in contrast to the generic QCPs observed in most heavy fermion systems[22]. Within DMFT, the electronic self energy is independent of momentum, and, hence the Mott critical points found here are local in nature. The possibility of a quantum critical Mott transition has been proposed earlier [23, 45]. Recent experiments [20] on quasi-two dimensional organic systems suggest the existence of a $T = 0$ continuous Mott transition. Recent analyses of scaling behaviour of finite temperature resistivity curves in the half-filled [25] and doped Hubbard model, computed through a continuous time quantum Monte Carlo solver within DMFT, [26] have been interpreted as evidence of hidden Mott quantum criticality. The current model of coupled symmetric PAM and noninteracting metal represents a new avenue where Mott quantum criticality can be studied in great detail within a microscopic Hamiltonian framework. Ideally one should analyse properties such as the specific heat and susceptibility in the proximity of a QCP and determine the critical exponents associated with them. Further the fixed points of the model should be found through renormalization group analysis in order to identify the universality class. We plan to carry out such analyses in future work.

4.3.2 Single-particle dynamics

A standard paradigm for investigating the Mott transition is the single band Hubbard model, where the first-order MIT (at $T = 0$) occurs by a continuous vanishing of Z at a critical interaction strength with the resonance pinned at $\omega = 0$ in the middle of a preformed gap [9, 42–44, 46]. However, the Mott transition is not confined to just the Hubbard model but has also been observed in the symmetric PAM [47–49] or other heavy fermion models, albeit with a dispersing f band [50]. The Mott transition in the symmetric PAM with nearest neighbour hybridization was justified [49] through the equivalence of the model to a single-band Hubbard model close to the Mott transition and at low frequencies ($\omega \sim ZD$). The bilayer KI-M model under consideration also has a similar equivalence, albeit with a difference. In a tiny neighbourhood of $\omega = 0$, the f-density of states has the form, $D^f(\omega) = (Z^2V^2/\omega^2)D_1^c(\omega)$. Thus, from (Equation (4.12)), it may be inferred that the current model is equivalent to a Hubbard model with a bare bandwidth of $V^2/t_\perp^2$ (from the first term) at the lowest frequencies ($|\omega| \ll ZD$); while for all other frequencies, the second term (gapped at the Fermi level) has a finite contribution. Moreover, it is clear that the first term is a function only of $\tilde{\omega} = \omega t_\perp^2/ZV^2$ while in the second term, a single scaling variable cannot be defined.

In Fig. 4.4 we plot the representative f-spectrum over all energy scales for different U's and $t_\perp$'s in the FL phase (top panel) and the Mott insulating phase (bottom panel) at a fixed $V = 0.44$. In the Fermi liquid the structure on all scales is similar to that of the single band HM, namely that there are two Hubbard bands that move away from (towards) the Fermi level with increasing U (increasing $t_\perp$). In the Mott insulating phase at a fixed $t_\perp$ (Fig. 4.4, left bottom panel), in accordance with the conventional single band Hubbard model, Δ_g decreases with increasing U, simultaneously pushing the Hubbard bands out. However, with increasing $t_\perp$ and a fixed U, the high energy Hubbard bands seem unaffected to a large extent (Fig. 4.4, right bottom panel).

We now look into the low energy sector of the correlated (f) and the conduction (c) electron spectrum of the heavy-fermion layer and the non-interacting metallic

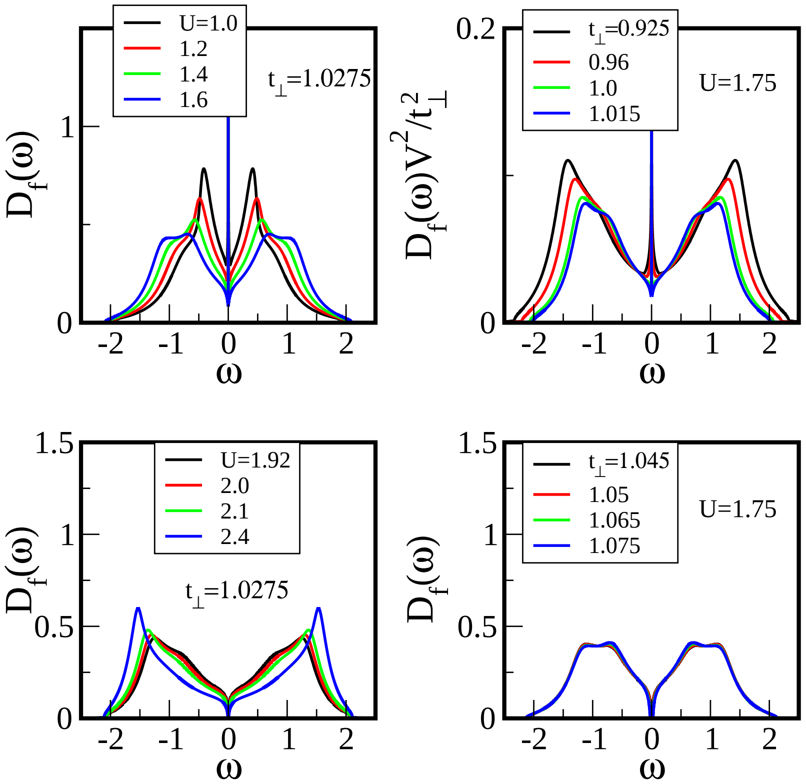

Figure 4.4: The f electron spectrum across a U driven (left panels) and a $t_\perp$ driven(right panels) QCP shown over all energy scales.

layer. Figure 4.5 shows the representative f-spectrum for the metallic case (top panels) and the insulating case (bottom panels) for a given QCP, reached either by increasing U (left panels) at a fixed $t_\perp = 1.0275$ or by increasing $t_\perp$ at a fixed $U = 1.75$ for $V = 0.44$. The critical interaction strength for the left panels is $U_c \approx 1.9$ while the critical interlayer coupling for the right panels is $t_{\perp c} \approx 1.03$. The FL spectra, when scaled by $V^2/t_\perp^2$, are seen to be universal functions of $\tilde{\omega} = \omega t_\perp^2/ZV^2$ in the scaling regime ($Z \to 0$ and finite $\tilde{\omega}$) as seen by the collapse of the spectra for a range of U or $t_\perp$ values (left and right panels respectively). The insets in the two top panels show the same spectrum as the main panels, but on a 'bare' frequency scale that show the rapid narrowing of the central resonance peak upon approaching the QCP. The bottom panels show the Mott insulating spectra that show the single-particle gap to increase when the U or $t_\perp$ is increased beyond the critical value. The insets in the bottom panel show that the Fermi surface is completely destroyed since the Mott gap in the f-DoS is identical to that in either of the conduction bands.

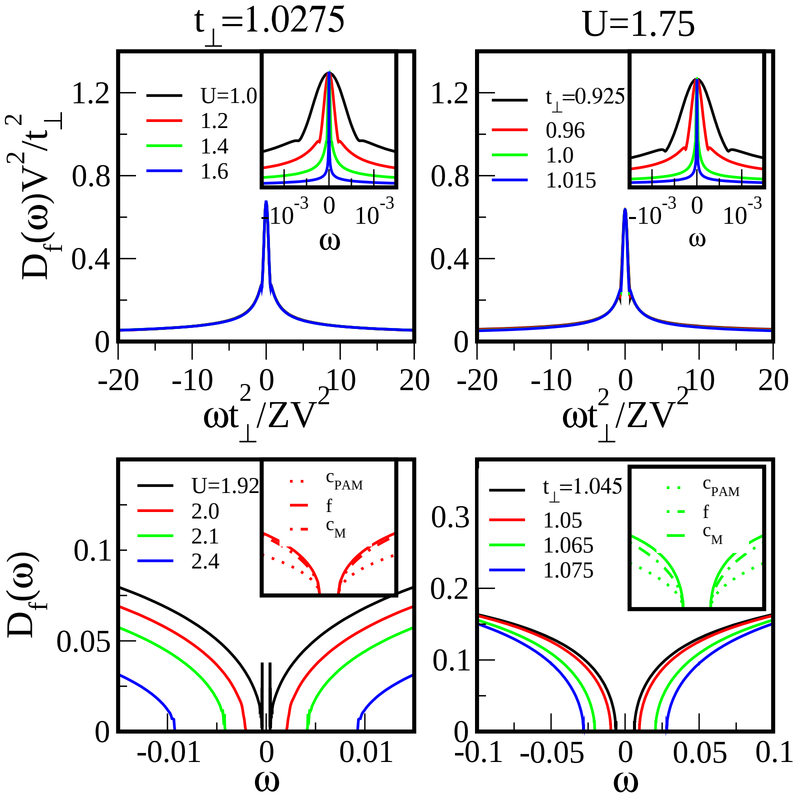

Figure 4.5: **f-spectrum across a U-driven (left panels) and a $t_\perp$ driven (right panels) QCP.** The top panels show the collapse of the Fermi liquid metallic spectra when plotted as a function of $\tilde{\omega} = \omega t_\perp^2/ZV^2$, while the insets show the same spectra on a bare frequency scale. The bottom panels show the increase in the gap in the Mott insulating spectra with increasing U (left bottom) or increasing $t_\perp$ (bottom right). The insets in the bottom panel show the c-spectrum of the heavy fermion layer (c_{PAM}) and the non-interacting metallic layer (c_M) on the same scale as the f-spectrum.

Thus it is not orbital selective unlike the MIT observed in other related models [49, 50].

We now show in Fig. 4.6 that, although the overall spectrum of the f electrons looks same as that of a single band HM, there lies a crucial difference: there is an absence of a preformed gap. It is now well known [44] that in the single band Hubbard model, the Kondo resonance in the metallic phase, resides inside a preformed insulating gap, such that at U_{c2} the resonance vanishes leaving behind a fully formed insulating Mott gap [42, 43]. In fact, this serves to be a spectral fingerprint of the

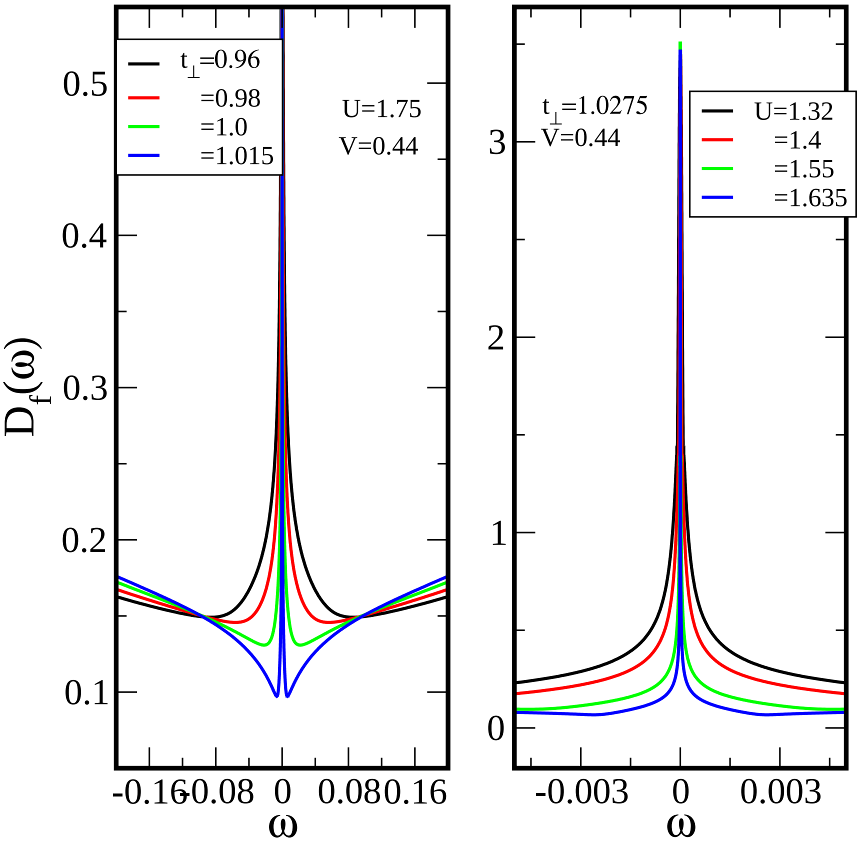

Figure 4.6: **Absence of a preformed gap:** The f electron spectrum across a U driven (left panels) and a $t_\perp$ driven (right panels) QCP (close to the transition) shown over the low energy scales to highlight the absence of the formation of any preformed gap. The critical values are: $t_{\perp c} \approx 1.03$ in the left panel and $U_c \approx 1.9$ in the right panel.

first-order Mott transition observed in such systems [9, 15, 42, 43]. The absence of such a preformed gap in the metallic spectra of the f-electrons, as shown in Fig. 4.6 is crucially in agreement with the quantum critical nature of the Mott transition observed in the model. Here, the Hubbard band edges and the central Kondo resonance tails are connected by a finite density of states at all $t_\perp$'s (Fig. 4.6)(left panel) and at all U's (Fig. (4.6))(right panel) sufficiently close to the transition, indicating that at the Mott transition, when the resonance vanishes, an insulating gap between the Hubbard bands just opens.

4.4 Summary and Conclusions

We find a surface of Mott QCPs in a bilayer KI-M model, which may be accessed through three athermal parameters, namely the on-site Coulomb repulsion U, the interlayer-hopping $t_\perp$ and the hybridization between f and c electrons, V. Experimental fabrication of precisely layered heavy fermion systems is indeed possible currently, and hence leads us to hope that the model proposed may be realized experimentally. In fact, we find that an M-KI-M system with the KI layer sandwiched between two non-interacting layers with interlayer hopping of $\sqrt{2}t_\perp$ is exactly equivalent to the bilayer KI-M model (equation 4.1), thus offering some more freedom in experimental fabrication. Additionally, we have checked that the use of a different c-electron DoS, such as a flat band or a two-dimensional tight-binding DoS with a van-Hove singularity at $\omega = 0$ does not change the scenario of a surface of QCPs qualitatively. Particularly, in the context of the current perspective, although a tuning of U and V is not straightforward, the $t_\perp$ can be increased through uniaxial pressure, and hence the latter should be used as the experimental athermal parameter. Uniaxial pressure perpendicular to the planes could correspond to varying $t_\perp$, D and V simultaneously in a material-specific way. Theoretically, the equation of state, derived e.g. from a first-principles approach, might be able to yield the possible directions of approach that correspond to a single experimental variable. The structure of the model is not limited to a Kondo-insulator-metal system but similar observations are expected to occur in any three orbital model that can be parametrized accordingly. However, the model Hamiltonian (equation 4.1) might not be a true representation of the real system, since many aspects of the latter such as f-orbital degeneracy, crystal field splitting, multiple conduction bands, and Hund's exchange, have been neglected. Moreover, for solving the model, we have neglected two-dimensional dynamical correlations (due to the use of the DMFT framework) and any symmetry breaking.

Nevertheless, the KI-M system could serve as a paradigmatic theoretical model, that brings together the phenomena of Mott transition, quantum criticality, and heavy fermions. Our work opens up a number of theoretical directions for exploration, such as the universality class and the relation of the QCPs found here to those found in impurity models [51] such as the pseudogap Anderson model [37, 38] or the gapped Anderson model [40] as well as lattice models incorporating competition between Kondo screening and Ruderman-Kittel-Kasuya-Yosida interactions [52]. Further investigations such as finite temperature critical scaling of transport and thermodynamic properties of the model are in progress.

Bibliography

[1] M. Neumann, J. Nyéki, B. Cowan, and J. Saunders, Science **317**, 1356 (2007).

[2] H. Shishido, T. Shibauchi, K. Yasu, T. Kato, H. Kontani, T. Terashima, and Y. Matsuda, Science **327**, 980 (2010).

[3] H.-S. Tao, Y.-H. Chen, H.-F. Lin, H.-D. Liu, and W.-M. Liu, Scientific reports **4** (2014).

[4] A. Benlagra and C. Pépin, Phys. Rev. Lett. **100**, 176401 (2008).

[5] A. Benlagra and C. Pépin, Phys. Rev. B **79**, 045112 (2009).

[6] K. S. D. Beach and F. F. Assaad, Phys. Rev. B **83**, 045103 (2011).

[7] J. Werner and F. F. Assaad, Phys. Rev. B **90**, 205122 (2014).

[8] J. Custers, K. Lorenzer, M. Müller, A. Prokofiev, A. Sidorenko, H. Winkler, A. Strydom, Y. Shimura, T. Sakakibara, R. Yu, et al., Nature materials **11**, 189 (2012).

[9] A. Georges, G. Kotliar, W. Krauth, and M. J. Rozenberg, Rev. Mod. Phys. **68**, 13 (1996).

[10] N. S. Vidhyadhiraja and D. E. Logan, European Physical Journal B **39**, 313 (2004).

[11] G. Kotliar, E. Lange, and M. J. Rozenberg, Phys. Rev. Lett. **84**, 5180 (2000), URL `http://link.aps.org/doi/10.1103/PhysRevLett.84.5180`.

[12] H. Park, K. Haule, and G. Kotliar, Phys. Rev. Lett. **101**, 186403 (2008), URL `http://link.aps.org/doi/10.1103/PhysRevLett.101.186403`.

[13] E. Gull, P. Werner, X. Wang, M. Troyer, and A. J. Millis, EPL (Europhysics Letters) **84**, 37009 (2008), URL `http://stacks.iop.org/0295-5075/84/i=3/a=37009`.

[14] Z. Yang, C. Ko, and S. Ramanathan, Ann. Rev. Mater. Res. **41**, 337 (2011).

[15] P. Limelette, P. Wzietek, S. Florens, A. Georges, T. A. Costi, C. Pasquier, D. Jérome, C. Mézière, and P. Batail, Phys. Rev. Lett. **91**, 016401 (2003).

[16] D. Vollhardt, Rev. Mod. Phys. **56**, 99 (1984).

[17] K. S. D. Beach and F. F. Assaad, Phys. Rev. B **83**, 045103 (2011).

[18] J. Werner and F. F. Assaad, Phys. Rev. B **90**, 205122 (2014).

[19] A. Ran çon Schweiger, A. Benlagra, and C. Pépin, Phys. Rev. B **83**, 073102 (2011).

[20] T. Furukawa, K. Miyagawa, H. Taniguchi, R. Kato, and K. Kanoda, Nature Physics **11**, 221 (2015).

[21] M. Vojta, Journal of Low Temperature Physics **161**, 203 (2010), ISSN 0022-2291.

[22] Q. Si and F. Steglich, Science **329**, 1161 (2010).

[23] T. Senthil, Phys. Rev. B **78**, 045109 (2008).

[24] T. Senthil, M. Vojta, and S. Sachdev, Phys. Rev. B **69**, 035111 (2004).

[25] H. Terletska, J. Vučičević, D. Tanaskovi, and V. Dobrosavljević, Phys. Rev. Lett. **107**, 026401 (2011).

[26] J. Vučičević, D. Tanaskovi, M. J. Rozenberg, and V. Dobrosavljević, Phys. Rev. Lett. **114**, 246402 (2015).

[27] S. Sachdev, Phys. Rev. Lett. **105**, 151602 (2010), URL `http://link.aps.org/doi/10.1103/PhysRevLett.105.151602`.

[28] R. A. Davison, K. Schalm, and J. Zaanen, Phys. Rev. B **89**, 245116 (2014), URL `http://link.aps.org/doi/10.1103/PhysRevB.89.245116`.

[29] S. Sen, J. Moreno, M. Jarrell, and N. S. Vidhyadhiraja, Phys. Rev. B **91**, 155146 (2015).

[30] R. Peters, Y. Tada, and N. Kawakami, Phys. Rev. B **88**, 155134 (2013).

[31] H. Barman and N. S. Vidhyadhiraja, International Journal of Modern Physics B **25**, 2461 (2011).

[32] D. E. Logan, M. P. Eastwood, and M. A. Tusch, Journal of Physics: Condensed Matter **10**, 2673 (1998).

[33] V. Smith, D. Logan, and H. Krishnamurthy, The European Physical Journal B **32**, 49 (2003).

[34] M. R. Galpin and D. E. Logan, Journal of Physics: Condensed Matter **17**, 6959 (2005).

[35] N. S. Vidhyadhiraja and D. E. Logan, Journal of Physics: Condensed Matter **17**, 2959 (2005).

[36] M. R. Galpin, A. B. Gilbert, and D. E. Logan, Journal of Physics: Condensed Matter **21**, 375602 (2009).

[37] M. T. Glossop and D. E. Logan, Journal of Physics: Condensed Matter **15**, 7519 (2003).

[38] M. T. Glossop and D. E. Logan, EPL (Europhysics Letters) **61**, 810 (2003).

[39] D. E. Logan and M. T. Glossop, Journal of Physics: Condensed Matter **12**, 985 (2000).

[40] M. R. Galpin and D. E. Logan, The European Physical Journal B **62**, 129 (2008), ISSN 1434-6028.

[41] R. Bulla, M. T. Glossop, D. E. Logan, and T. Pruschke, Journal of Physics: Condensed Matter **12**, 4899 (2000).

[42] M. J. Rozenberg, G. Kotliar, and X. Y. Zhang, Phys. Rev. B **49**, 10181 (1994), URL `http://link.aps.org/doi/10.1103/PhysRevB.49.10181`.

[43] X. Y. Zhang, M. J. Rozenberg, and G. Kotliar, Phys. Rev. Lett. **70**, 1666 (1993), URL `http://link.aps.org/doi/10.1103/PhysRevLett.70.1666`.

[44] D. E. Logan and M. R. Galpin, Journal of Physics: Condensed Matter **28**, 025601 (2016).

[45] T. Misawa and M. Imada, Phys. Rev. B **75**, 115121 (2007).

[46] P. Nozières, Journal of the Physical Society of Japan **74**, 4 (2005).

[47] C. Huscroft, A. K. McMahan, and R. T. Scalettar, Phys. Rev. Lett. **82**, 2342 (1999).

[48] K. Held, C. Huscroft, R. T. Scalettar, and A. K. McMahan, Phys. Rev. Lett. **85**, 373 (2000).

[49] K. Held and R. Bulla, The European Physical Journal B **17**, 7 (2000), ISSN 1434-6028.

[50] C. Pépin, Phys. Rev. B **77**, 245129 (2008).

[51] D. E. Logan, A. P. Tucker, and M. R. Galpin, Phys. Rev. B **90**, 075150 (2014), URL `http://link.aps.org/doi/10.1103/PhysRevB.90.075150`.

[52] Q. Si, S. Rabello, K. Ingersent, and J. L. Smith, Nature **413**, 804 (2001).

Chapter 5

A Local theory for the Anderson-Mott localization [§]

Contents

[§] Work reported in this chapter is to be submitted as: **Sudeshna Sen**, Hanna Terletska, Juana Moreno, N. S. Vidhyadhiraja, Mark Jarrell, "A local theory for the Anderson Mott localization"

5.1 Introduction

It is, by now, well evident from the previous Chapters of this thesis, that the investigation of strong electron correlations in condensed matter systems has always proven to be an intriguing subject of research [1, 2]. In fact, the same holds true for disordered systems since the pioneering work by Anderson [3]. When combined together, disorder and interactions are known to influence material properties in non-trivial ways, a scenario already introduced in the introductory chapter (Chapter 1) of this thesis. Over the last few decades, several experimental works on a range of systems [4–12], have highlighted the importance of the interplay of disorder and interactions. The disorder driven metal insulator transition for non-interacting systems is by now well understood [4, 13, 14]; but a precise understanding of the combined effects due to disorder (W) and interactions (U) under a unified framework still remains elusive owing to the complexities involved. Several early theories focused on the weak disorder limit, perturbing around Fermi liquid theory [15]; further studies included the famous *scaling theories of disordered Fermi liquids* [15, 16]. These concepts were subsequently extended to interacting disordered systems [17–20] which were later given a simple physical interpretation in terms of Fermi liquid ideas [21, 22]. The experiments of Paalanen *et al.* [23] were described successfully within a phenomenological two fluid model of itinerant carriers and local moments. The first attempt to test this theory within a well defined microscopic model is due to Milovanović *et al.* [24]. The authors looked into the Anderson-Hubbard model with both diagonal and site energy disorder and off-diagonal hopping disorder. The interactions were treated at the mean field Hartree-Fock level and the disorder was treated exactly by numerical calculations. A complete phase diagram was then later given by Tusch and Logan [25] with an unrestricted Hartree-Fock mean field treatment of the interacting electrons. Several other early studies in interacting disordered systems relied on exact numerical methods like quantum Monte Carlo [26] or exact diagonalization [27], which were nevertheless severely limited in temperature range and system sizes.

A particularly flexible approach for treating disorder in correlated electron systems is provided by the frameworks based on the DMFT [6, 28, 29]. The DMFT in its simplest form [2] is unable to capture the disorder induced localization effects in interacting systems and it needs to be refined [28–30]; a resolution is provided by the introduction of the statistical DMFT (statDMFT) [28, 31, 32] also mentioned earlier in Chapter 2. For non-interacting systems this framework reduces to the very early framework proposed by Abou-Chacra *et al.* [33]. However, being numerically expensive, this method has been limited to a handful of calculations revolving around the infinite-dimensional Bethe lattice [31, 32, 34] or the two-dimensional square lattice [35–37]. Instead, a much simpler approach is based on the combination of a *typical* medium for the DMFT mapping. This framework, called the typical medium theory (TMT) [35, 38–41] captures several qualitative aspects of Anderson localization in non-interacting disordered systems. It is this framework within DMFT that we employ in this Chapter.

Based on our introduction to the TMT in Chapter 2, it is clear that this method relies on the use of a real frequency solver. Earlier studies of this model were based on the use of the numerical renormalization group (NRG) [39] or slave-boson based (SB) mean-field approaches [35, 40]. Particularly, in Ref. [39], Byczuk *et al.* explored the W-U paramagnetic phase diagram of the AHM. Although, NRG is highly efficient in capturing the Kondo effect, the distribution of Kondo scales, a natural occurrence in interacting disordered systems (also see Chapter 1), was not explored in Ref. [39]. Such a direction was however explored using SB mean-field theory based calculations [35], highlighting that the *typical* quasi-particle weight may also serve as an order parameter for the Anderson-Mott localization physics. However, it is also well known, that, the SB based solvers fail to account for the inelastic scattering thus failing to predict the correct lineshape of the spectral functions and the scattering rates. Moreover, the physics at low energies, may be highly affected by the physics at higher energy scales. Thus, in order to have a precise understanding of the transport properties in a correlated system, we require all energy scales and interaction strengths, from weak to strong coupling, to be handled within a unified theoretical framework. In this work, we revisit the problem using the local moment approach (LMA) [42] already described in Chapter 2. While it has been extensively benchmarked [43, 44] earlier and has proved to be highly efficient on several occasions for clean systems [45–48], this Chapter serves as a comparison for the LMA with the earlier studies [35, 39, 40] on disordered interacting systems within the TMT-DMFT framework. This should help us set up the platform for a broader goal, namely, utilizing this method to look into short-range correlation effects of disorder in Chapter 6. In addition to the distribution of Kondo scales, we also explore the scattering dynamics, within the current non-perturbative local framework and identify universal dynamics and scaling similar to the clean interacting scenario.

5.2 Model

One of the minimal models that may be used to describe the interplay of strong correlations and disorder is the Anderson-Hubbard model given by,

$$\mathcal{H} = \sum_{ij,\sigma} t_{ij} c^{\dagger}_{i\sigma} c_{j\sigma} + \sum_{i,\sigma} (V_i - \mu) \hat{n}_{i\sigma} + U \sum_{i} \hat{n}_{i\uparrow} \hat{n}_{i\downarrow}, \tag{5.1}$$

where t_{ij} is the hopping matrix element from site i to site j, U represents the onsite Coulomb interaction energy, V_i denotes the onsite potential energy of an electron occupying site i, $c^{\dagger}_{i\sigma}$ ($c_{i\sigma}$) is the fermionic creation (annihilation) operator for an electron with spin σ at site i and $\hat{n}_{i\sigma}$ is the particle number operator for site i and spin σ. The random onsite energy, V_i represents the disordered lattice background in which the electron dynamics would occur. We consider the disorder to follow a box distribution $P(V_i)$ of width W and centred at $V_i = 0$, given by, $P(V_i) = \frac{1}{2W}\Theta(W - |V_i|)$, where $\Theta(x)$ is a step function. The disorder averaging is represented using the shorthand notation, $\langle \ldots \rangle = \int dV_i P(V_i)(\ldots)$. We also focus on the half-filled or particle-hole (p-h) symmetric case by setting $\mu = U/2$. For all our notations further, we will denote the onsite energy as, $\epsilon_i = -U/2 + V_i$.

In order to solve the Hamiltonian given by Equation (5.1) we adopt the TMT-DMFT formalism in this chapter. Within TMT-DMFT, we map the disordered lattice model on to an ensemble of single impurity Anderson models. Each of these single impurity problems correspond to lattice sites with different onsite energies, each being embedded in a self-consistently determined averaged effective medium, obtained from a *geometrical* average of the local density of states (LDOS), so that the medium represents the *typical* nature of the disordered problem [49]. In order to solve the single impurity Anderson models we use the local moment approach (LMA) [50] as the impurity solver. As has been highlighted in Chapter 2, the LMA is a non-perturbative semi-analytical real frequency impurity solver. Already introduced in Chapter 2, we realize that the TMT framework requires the local density of states (LDoS) for calculating the *typical* medium. Hence, for investigating interacting disordered systems within frameworks based on the TMT, we require a real-frequency impurity solver. The LMA suits very well for this purpose because it provides us with real-frequency Green's functions and is non-perturbative by construction. In the following section we describe the TMT-DMFT framework and also provide some details of our implementation of the LMA within this framework.

5.3 TMT-DMFT: A local effective medium approach

5.3.1 Formalism

The TMT-DMFT framework was introduced in Chapter 2. For the sake of completeness, in this section we shall briefly outline the main steps involved in the implementation of this framework. It is exactly similar as the DMFT self-consistency for a clean system, except for the fact that we need to embed an ensemble of effective impurity problems in a single self-consistently obtained disorder averaged medium.

Step 1:

One starts with an initial guess hybridization, $\Gamma(\omega)$ and solves N single impurity problems, (with different on-site energies, ϵ_i's), where N represents the number of disorder realizations that should be large enough. These impurities hybridize with the embedding medium via $\Gamma(\omega)$. For, completeness and for future reference, let us write down the impurity Anderson model:

$$\mathcal{H} = \sum_{k,\sigma} \epsilon_k c^\dagger_{k\sigma} c_{k\sigma} + \sum_{\sigma} \epsilon_i c^\dagger_{i\sigma} c_{i\sigma} + \sum_{k\sigma} V_k \left(c^\dagger_{i\sigma} c_{k\sigma} + h.c. \right) + U n_{i\uparrow} n_{i\downarrow}. \tag{5.2}$$

The first term represents the non-interacting host with dispersion ϵ_k; the third denotes the coupling of the impurity (site i) with the host. The second term refers to the correlated (single-)impurity with an onsite energy ϵ_i with onsite electron-electron interaction U represented by the fourth term. Note that each random disorder configuration would be characterised by a random ϵ_i but the same $\Gamma(\omega)$ since we have restricted ourselves to a local framework. $\Gamma(\omega)$ would represent a disorder averaged medium as described later.

As outlined in Chapter 2 (Section 2.2) employing the LMA with the bare parameters U and ϵ_i, would require a lot of computational time. This results from the fact that, away from 1/2-filling the impurity parameter e_i that acts like a *pseudo chemical potential* and explicitly enters the unrestricted Hartree Fock Green's functions via Eqs. (2.17), (2.18), would have to be tuned so that the SR (Eq. (2.29)) and the Luttinger's theorem (Eq. (2.35)) are self-consistently satisfied. Recall that this would result in repeating the symmetry restoration (SR) (Eq. (2.29)) step described in Chapter 2 (Section 2.2) several times. Instead, the impurity self-energy may be obtained at a much cheaper effort if the bare parameters U and the impurity parameter e_i is fixed. In that case, once the symmetry restored impurity self-energy and Green's functions are obtained, one can tune the ϵ_i such that the the Luttinger's theorem (Eq. (2.35)) is satisfied. This can be done without having to repeat the impurity self-energy calculation. This issue is discussed in detail in Chapter 2 (Section 2.2).

However, in the current problem, the ϵ_i is a random quantity following a particular distribution. So, in order to resort to the fixed U, fixed e_i scheme discussed in Chapter 2 and above, we have to first build a database for the respective (e_i, ϵ_i) pair with the given hybridization. In other words, before going to the actual calculation we do the following:

1. Given a $\Gamma(\omega)$ we start from the particle-hole symmetric limit with $e_i = 0$ and $\epsilon_i = -U/2$, for which the Luttinger's theorem (Eq. (2.35)) is naturally satisfied. So, in this step the LMA solver is provided with (a) $\Gamma(\omega)$, (b) U, (c) $e_i = 0$.

2. We now increment the e_i by a small step, say 0.02[1]. So, in this step the LMA solver is provided with (a) $\Gamma(\omega)$, (b) U, (c) $e_i = 0.02$. Accordingly, the ϵ_i is derived by satisfying the Luttinger's theorem (Eq. (2.35)) and an (e_i, ϵ_i) pair for the given $\Gamma(\omega)$ is generated.

3. The above step (2) is continued until the ϵ_i obtained overshoots the limit set by the disorder strength, W. Note that, $\epsilon_i = -U/2 + V_i$, where V_i is a random number between $-W \leq V_i \leq W$.

4. For the actual random configuration, V_i, and therefore, the ϵ_i, we now interpolate the corresponding e_i from the database and compute the local self-energy, Σ_i using the equations outlined in Chapter 2. Finally, we construct the local Green's function, $G_i(\omega)$ which would be used to construct the $\rho_{typ}(\omega)$.

Step 2:

The output of the **Step 1** comprises N local impurity self-energies, $\Sigma_i(\omega)$ that gives us N local impurity Green's function, $G_i(\omega)$. With the local spectral functions, $\rho_i(\omega) = -\frac{1}{\pi}\mathrm{Im}G_i(\omega)$, we construct the disorder averaged DoS, using geometric averaging:

$$\rho_{typ}(\omega) = \exp \int d\epsilon_i P(\epsilon_i) \ln \rho_i(\omega) \tag{5.3}$$

Using Eq. (5.3) we can now construct the *typical* Green's function, $G_{typ}(\omega)$, from the Hilbert transform of ρ_{typ}:

$$G_{typ}(\omega) = \int \frac{\rho_{typ}(\omega')d\omega'}{\omega - \omega'}. \tag{5.4}$$

Step 3: The disorder averaged lattice Green's function, $\bar{G}(\omega)$, is given by,

$$\bar{G}(\omega) = \int \frac{\rho_0(\epsilon)\, d\epsilon}{[G_{typ}(\omega)]^{-1} + \Gamma(\omega) - \epsilon}, \tag{5.5}$$

---

[1] This is optimized by experience to get an idea of the minimum number of steps or (e_i, ϵ_i) pairs required to obtain a *good* database.

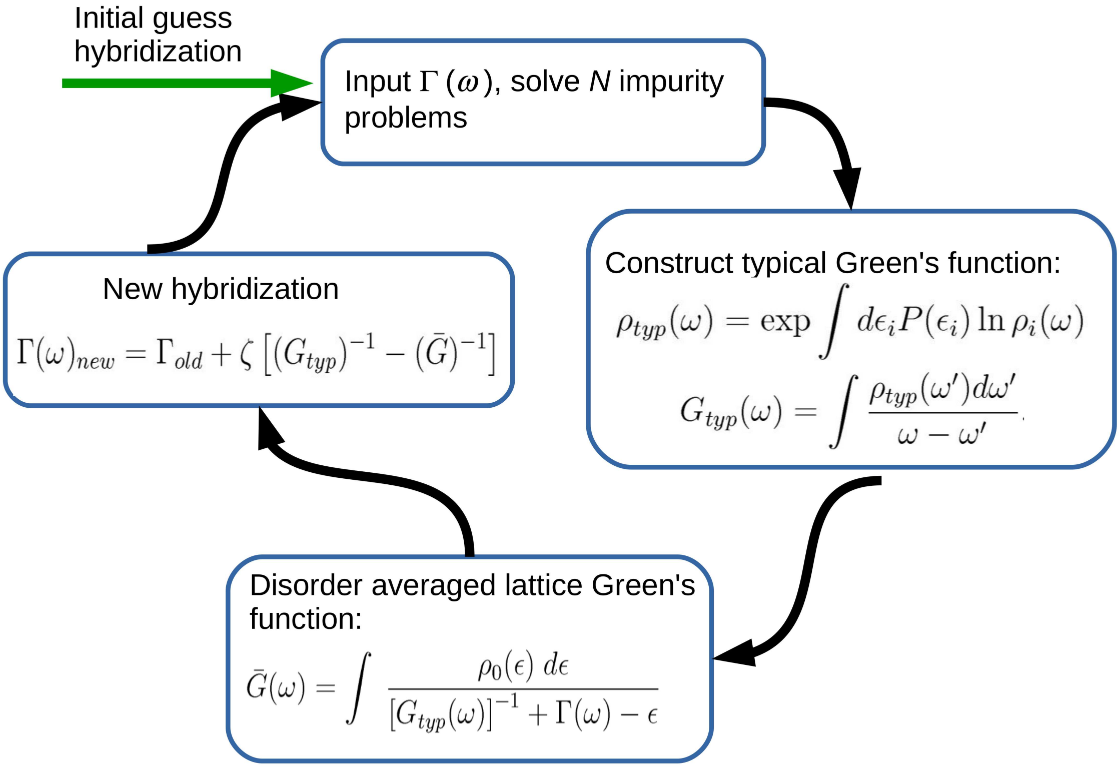

Figure 5.1: **The TMT-DMFT self-consistent framework shown as a flowchart** illustrating Steps (1-4) shown above.

where $\rho_0(\epsilon)$ refers to the bare density of states, that in the current problem is that of the 3-dimensional cubic lattice.

Step 4: The new hybridization may be obtained as,

$$\Gamma(\omega)_{new} = \Gamma_{old} + \zeta\left[(G_{typ})^{-1} - (\bar{G})^{-1}\right], \tag{5.6}$$

where, ζ is a mixing parameter typically set to a value of 0.5. With $\Gamma(\omega)_{new}$ we can go back to **Step 1** and continue until -Im$\int |\,(\Gamma(\omega)_{new} - \Gamma(\omega)_{old})\,| d\omega$ converges within some tolerance.

The above algorithm is also illustrated in Fig. 5.1. In order to obtain a correct physical description of the system, one also needs to sample a sufficiently large number, N, of disorder realizations. For the results presented in the subsequent sections,

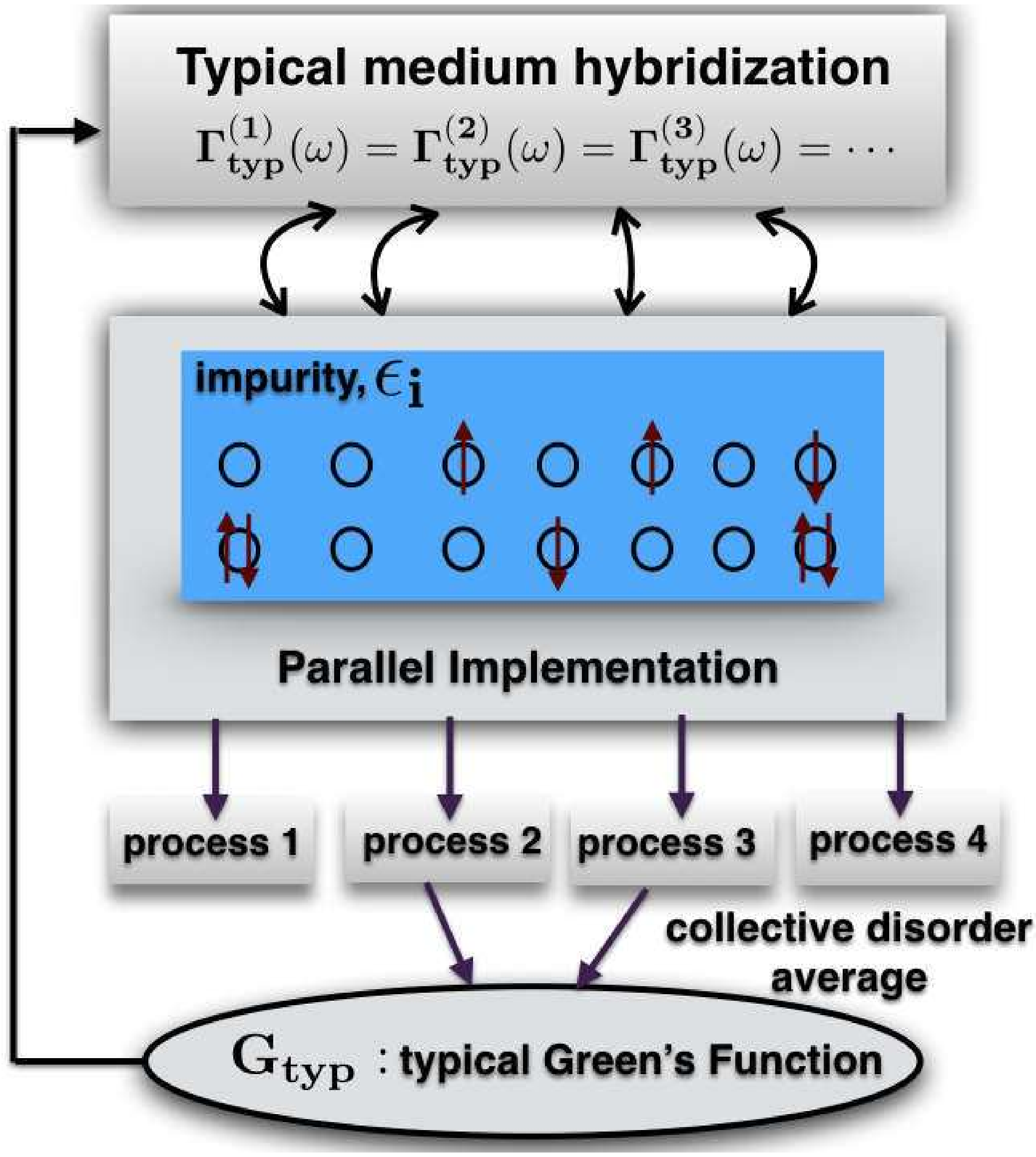

Figure 5.2: **The parallel implementation of Fig. 5.1.** In all our calculations we typically used $N \sim 10^5$ for getting relatively smooth distribution functions shown in the following sections. A typical runtime for such a calculation is about 40 hours for $N \sim 10^5$ distributed over 60 processors.

$N \approx 10^4$ for moderate disorder strengths (compared to U) and $N \approx 10^5$ close to the metal-insulator (high) disorder driven transitions. Considering the large value of N we relied on a parallel algorithm, parallelized over the disorder realizations, that solves several such effective impurity problems in parallel. A typical runtime for such a calculation is about 40 hours for $N \sim 10^5$ distributed over 60 processors. The parallel implementation is described in Fig. 5.2.

With this framework we would now describe the results obtained in this chapter. However, before we embark upon the results, let us understand some basic aspects of this model described by Eq. (5.1). The very nature of the problem results in the emergence of a distribution of Kondo scales due to the presence strong electron-electron interactions in a disordered medium. Each member of the ensemble of impurity problems has an associated Kondo temperature, resulting in a distribution of Kondo scales. The behaviour of this distribution is thus expected to be strongly dependent on the effective medium that the impurities are embedded in. One of the prime aims of this thesis is to systematically investigate the evolution of this distribution as a function of interaction, U in presence of *quenched* disorder or as a function of the disorder strength, W, at a fixed interaction U. However, this also requires an efficient impurity solver that is capable of capturing Kondo scales ranging from $\sim 10^{-1}$ to $\sim 10^{-6}$. The LMA has been successfully applied in this regard capturing the strong coupling physics of the single impurity Anderson model or the Kondo model [42, 50–53], correctly. It has also been applied successfully within the DMFT for clean lattice models like the Hubbard model [45] or the periodic Anderson model [46–48, 54]. In Chapter 3 we employed the LMA for disordered layered system within the framework of inhomogeneous-DMFT and coherent potential approximation (CPA). However, its application to disordered models beyond the level of CPA [55–57] has not been explored before. Thus one of the purposes of this chapter is to systematically (and qualitatively) analyse the use of LMA within a TMT+DMFT framework and also compare with earlier results wherever applicable. Let us now briefly recall some of the known results of the AHM.

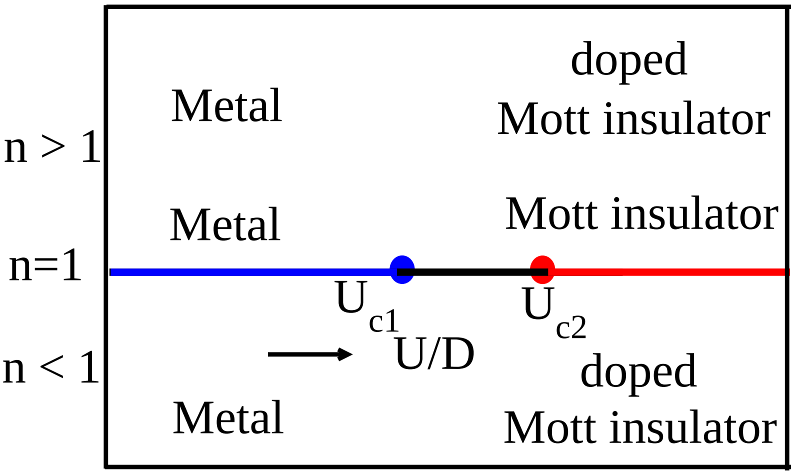

Figure 5.3: **Phase diagram of the single band Hubbard model on the filling-interaction (n-U) plane.** At 1/2 -filling ($n = 1$) a metal insulator transition from a strongly correlated metal (blue solid line) to a Mott insulator (red solid line) can be driven by U, marked by a coexistence regime (black solid line).

5.4 Known results of the AHM

$W = 0$, $U \neq 0$:

In this limit Eq. 5.1 reduces to the conventional single-band Hubbard model (SBHM) (Eq. 1.3) [58]. Figure 5.3 shows a schematic phase diagram of the zero temperature ($T = 0$) single band Hubbard model (SBHM) in the filling (n) and the interaction (scaled by the bandwidth, D) U/D plane. At 1/2 filling in the SBHM one can drive a strongly correlated metal through a U driven metal insulator transition (MIT) into a Mott insulating phase [2, 59]. In this local moment phase each site would be occupied by a single electron. Away from half filling there are always empty sites available for the added electrons to hop onto and therefore the Mott insulator gets destroyed. This is termed as the doped Mott insulator phase in Fig. 5.3. Within DMFT [2], the Fermi liquid to Mott insulator transition may be characterised by a single energy scale, represented by the Kondo energy scale, T_K^0, that vanishes at the transition. Similarly, the Mott-insulator to Fermi liquid transition is characterized by a vanishing Mott gap, Δ_g. Moreover, at half-filling the U driven Mott transition is first order and is associated with a coexistence regime shown as the black solid line on the U/D axis, marked by two transition points, U_{c1} and U_{c2}, where U_{c1} is the critical U where Δ_g vanishes and U_{c2} represents the the critical U where T_K^0 vanishes. This scenario in the $W = 0$ case motivates us to look at the regimes, $U < U_{c2}$ and $U > U_{c2}$ distinctly. In Fig. A.1 of Appendix A we have demonstrated the behaviour of T_K^0 as a function of U, for the p-h symmetric SBHM, on a 3-dimensional cubic lattice, as obtained within the LMA. The Mott MIT occurs is estimated to occur at $U_{c2}/D \sim 0.8$ (see Appendix A for details), the bandwidth (D) being equal to 3. This result compares well with the value predicted by NRG calculations ($\sim 1.1D$) [60].

<u>$U = 0$, $W \neq 0$:</u>

In this limit Eq. 5.1 reduces to the (quenched disorder) Anderson model of non-interacting electrons [3]. This system undergoes a metal-insulator transition as a function of W [3]. In 3-dimensions, the numerical value of the critical disorder strength (W_c) for the transition is found to be, $W_c \approx 2.1$ [4, 61–65]. The local TMT framework reproduces some of the expected features of the Anderson localization transition, but underestimates the critical disorder strength with $W_c \approx 1.65$. However, by construction the local TMT framework is able to describe, qualitatively the effects of strong localization due to disorder.

<u>$U \neq 0$, $W \neq 0$:</u>

As already mentioned in the introduction to this Chapter, the TMT-DMFT method was first applied to the AHM by Byczuk *et al.* [39], who derived the paramagnetic W-U phase diagram with a Bethe lattice density of states (DoS) using the NRG as the impurity solver. Three distinct phases were identified namely, a correlated metallic phase, a Mott insulating phase and an Anderson insulating phase. Additionally, a coexistent regime of the metal-MI phase was reported. The Mott and Anderson insulator phases were found to be continuously connected. The characterization of these phases were based on the behaviour of the band center of the TDoS, $\rho_{typ}(0)$ and the arithmetically averaged DoS (ADoS), $\rho_{arith}(0)$. The metallic phase featured a non-zero $\rho_{typ}(0)$ and $\rho_{arith}(0)$. For weak to moderate W, a sharp transition from the metallic to a gapped insulating phase was observed where both the $\rho_{typ}(0) = 0$ and $\rho_{arith}(0) = 0$. This MIT was similar in characteristics with the conventional SBHM and hence this insulating phase was termed as the Mott insulator. Moreover, the DoS in this phase featured prominent Hubbard subbands. Additionally a metal-MI coexistence regime similar to the SBHM was identified in the W-U plane that terminated at a single W. The Anderson insulator phase featured $\rho_{typ}(0) = 0$ and $\rho_{arith}(0) \neq 0$. Additionally, the Hubbard bands were broad and diffused.

The above work was subsequently followed by that of Aguiar *et al.* [35] where SB mean-field method was employed to derive the phase diagram. An overall similar phase diagram was derived but with subtle differences. The coexistence regime was absent, although that should be attributed to the fact that SB based methods provide a Brinkman-Rice [66] scenario for the Mott MIT. A second order parameter was identified in terms of the local quasi-particle weight, Z_i, where i represents the site i. According to their results the Mott insulator was characterized by $\rho_{typ} = 0$ and $Z_i \to 0$ on all the sites representing Mott localization of all the electrons. In the Anderson insulator phase $Z_i \to 0$ only on a fraction of sites and a *two fluid* picture was proposed, where Mott fluid droplets were interlaced with regions containing Anderson localized particles. So, in this picture, the transition from an interacting metal to an Anderson insulator phase was characterised by some sites with $Z_i \neq 0$, some sites $Z_i \to 0$, $\rho_{arith}(0) \neq 0$ and $\rho_{typ} = 0$. With these pictures in mind let us now discuss the results obtained within our implementation.

It is also worth mentioning that several studies have investigated the AHM within the framework of stat-DMFT. However, as mentioned earlier, the numerical demands of the latter has restricted these studies to solvers like the modified perturbation theory [34], SB mean-field [35], or Hubbard-I approximation [37].

5.5 Results and Discussion

5.5.1 Single particle dynamics

In any effective medium theory, the hybridization function is an important quantity representing the nature of the effective medium in which the single impurity in the context of DMFT is embedded in. It is in fact a measure of the rate of diffusion of the electrons between the impurity and the bath (which is disordered in this case). We therefore begin this discussion with a description of the self-consistently obtained effective medium pertaining to our model.

An obvious phenomenon associated with a metal insulator transition is the depletion of density of states (DoS) at the Fermi level with respect to a change in the transition inducing parameter. In the current system being considered such tuning parameters are represented by the W and U. This change in the DoS ($\rho(\omega)$) may be gradual and the $\rho(0)$ may reach a zero value monotonically as in the case of Anderson transition in the Anderson model [67, 68] or may be sudden as in the case of Mott transition in the particle hole symmetric SBHM [2]. We will therefore proceed in this section with a subsequent discussion of the behaviour of the disorder averaged DoS.

Hybridization function: $U < U_{c2}$, $W \neq 0$

In Fig. 5.4 we plot the hybridization function ($\Gamma(\omega)$) for $U = 1.2$ that serves to be a representative parameter for this regime. The main panel demonstrates $\Gamma(\omega)$ on a low energy scale highlighting the fact that as we increase disorder, the effective medium loses spectral weight at the Fermi energy thus moving towards a disorder induced metal insulator transition. The $W = 0$ Kondo resonance is no more pronounced due to the presence of disorder. As W is increased this remnant of a Kondo resonance first broadens but then progressively reduces in intensity and subsequently in its width. The high energy Hubbard bands shown in the right inset of Fig. 5.4, broaden due to the presence of disorder indicating a higher rate of

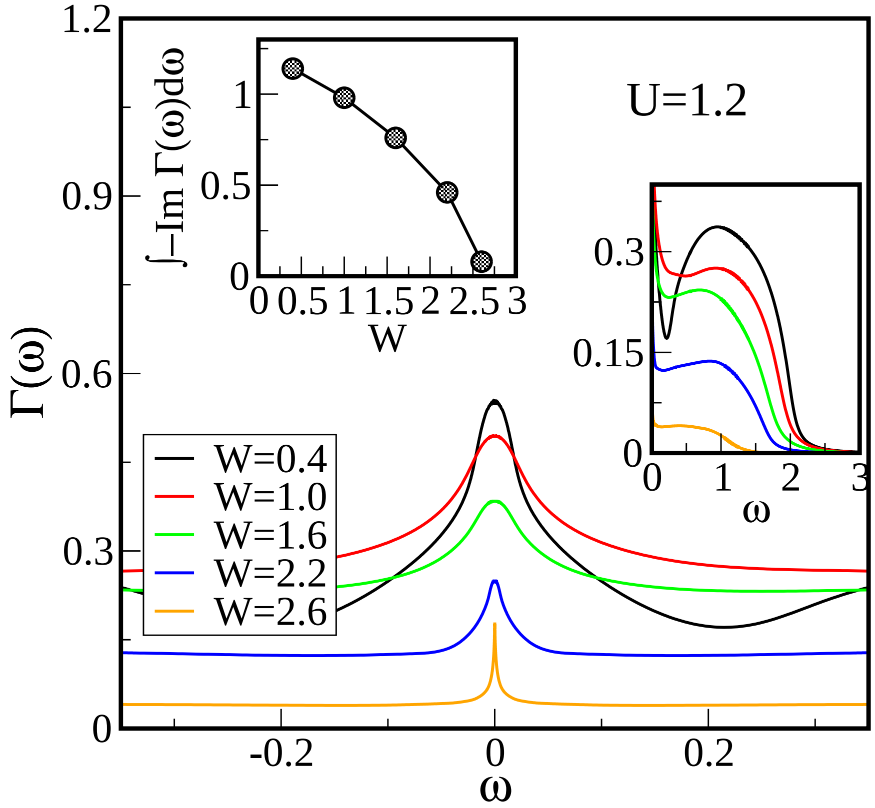

Figure 5.4: **Hybridization function ($\Gamma(\omega)$) for $U = 1.2$:** The evolution of the hybridization function, Γ for different disorder strengths, W, shown over a low energy scale (main panel). The **left** inset represents the integrated Γ that decreases monotonically as the transition is approached. The **right** inset illustrates the reduction of the intensity of the Hubbard bands and an associated broadening as W is increased indicating a disorder induced screening of interactions on these high energy scales.

loss of electrons from the impurity site to the disorder averaged host medium. In the left inset of Fig. 5.4 we plot the integrated escape rate (-$\int$ Im $\Gamma(\omega)d\omega$) that monotonically vanishes as the disorder is increased. This decay consistently brings out the physical picture that a vanishing escape rate over all energy scales including $\omega = 0$, essentially means the absence of hybridization paths leading towards a disorder induced localization transition.

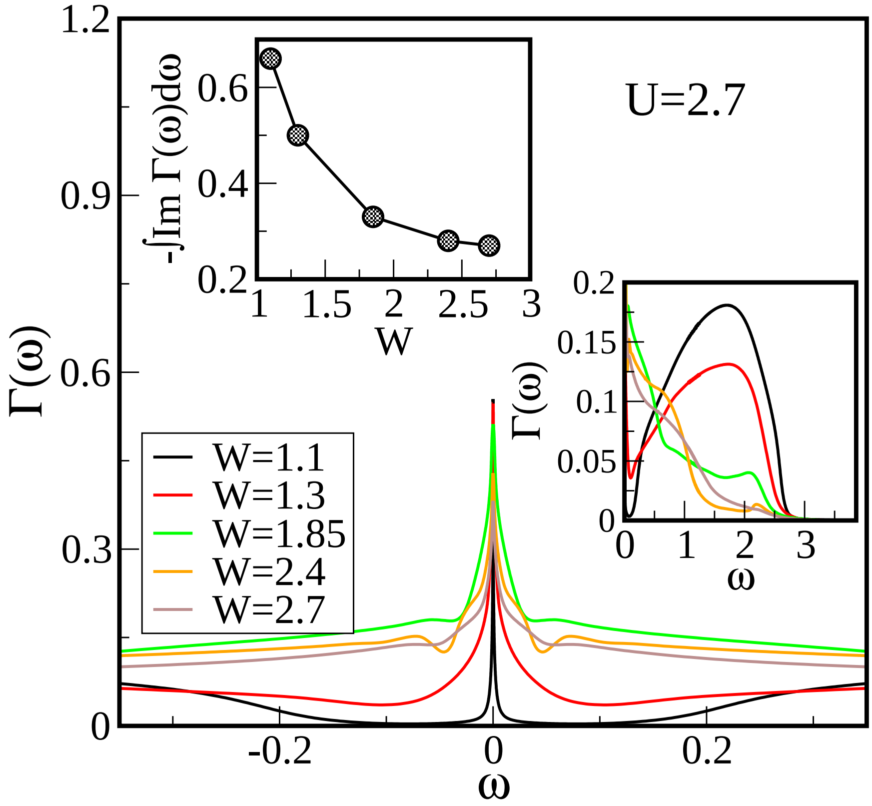

Figure 5.5: **Hybridization function ($\Gamma(\omega)$) for $U = 2.7$:** (Main panel) The low energy evolution of Γ as a function of increasing W. The formation of a preformed gap can be seen at $W = 1.1$ reminiscent of Mott gap in the clean limit at $U = 2.7$. (Right inset) The reduction of the intensity of the Hubbard bands and the associated broadening as W is increased. (Left inset) represents the integrated Γ. The rate of this decrease is much slower compared to $U = 1.2$ and an evident change in the slope. This has serious implications in the determination of the critical disorder strength for the Anderson MIT corresponding to this interaction strength.

Hybridization function: $U < U_{c2}$, $W \neq 0$

In Fig. 5.5 we plot the hybridization function ($\Gamma(\omega)$) for $U = 2.7$. This regime in the $W = 0$ limit represents a Mott insulating state for a cubic lattice, with $D = 3$ considered in this work. When we put in a sufficient amount of disorder concentration within this system, we drive some of the sites away from half-filling. However, due to the global particle-hole symmetry present in the current problem, a symmetric Kondo resonance appears in the middle of an insulating gap (shown as the solid black line in the main panel of Fig. 5.5, for $W = 1.1$). But then as the disorder strength increases this gap gets diffused and vanishes. The otherwise sharp Kondo resonance in the low disorder limit broadens and also loses intensity. However, the progress towards an MIT is very gradual unlike the $U = 1.2$ case, suggesting the dominance of strong interactions over disorder. This is particularly evident from the left inset where we show the integrated hybridization function as a function of increasing W. A notably distinct difference from the $U = 1.2$ is the functional dependence of this decay on W. The decay is extremely gradual and with a negative slope. In fact it is this dependence that makes it extremely diificult to determine the critical disorder strength, W_c for the metal-insulator transition from a disordered metallic phase with $U = 2.7$ as the disorder is increased. This phase boundary will be discussed again, later, in this chapter. The high energy bands, shown in the right inset behave in a conventional fashion as the $U = 1.2$ case and hence we will not repeat it.

It has already been discussed earlier that the Anderson localization in non-interacting systems is a non self-averaging phenomenon, with long and broad tails in the distribution of the LDoS. In such a scenario, the geometric mean of the LDoS serves to be the best approximation to the typical value. The use of the geometric mean of DoS for determining the embedding hybridization serves to be the key for obtaining a self-consistent description of the metal insulator transition associated with disorder. In the subsequent discussions in this section we shall corroborate this fact with our calculations of the density of states and also compare with earlier predictions with other methods wherever applicable.

Density of states: $U < U_{c2}$, $W \neq 0$

In Fig. 5.6, we compare the TDoS and the ADoS for various disorder strengths ($W = 0.4,\ 1.2,\ 2.0,\ 2.6$ (bottom to top panel)). Clearly when the disorder, W, is small, both the ADoS and the TDoS produce almost the same density of states. With increasing disorder, the TDoS gets suppressed over all energy scales (note that this is not spectral weight transfer, because the TDoS is not normalized;) Moreover, the monotonic decrease of the $\rho_{typ}(0)$ as a function of increasing W suggests that,

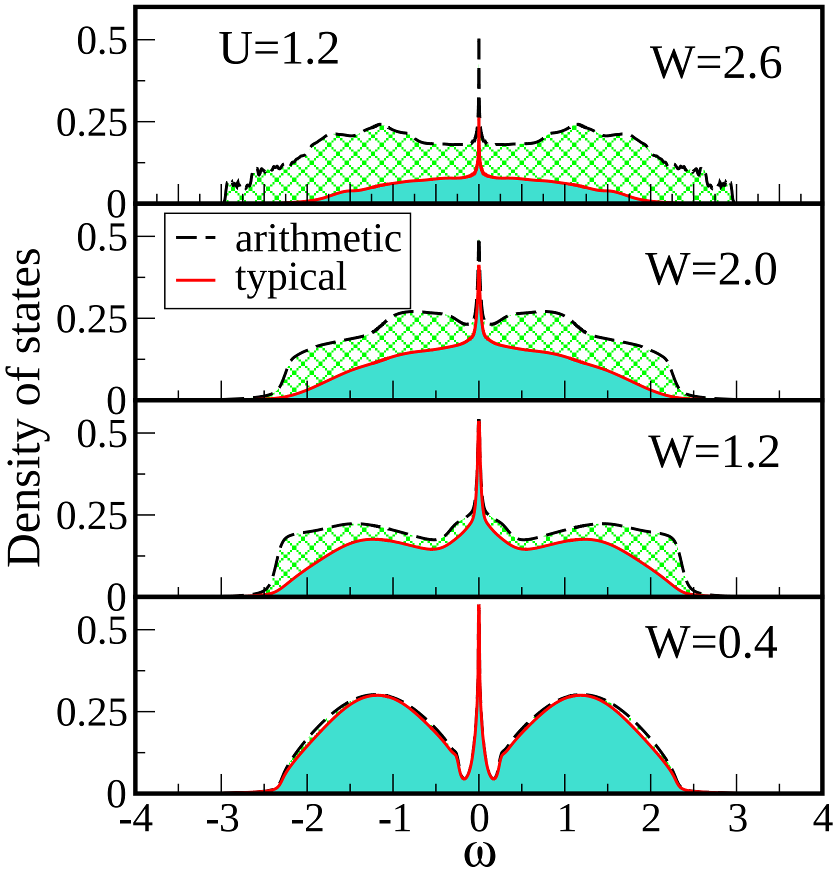

Figure 5.6: Comparison of the typical density of states (TDoS) and the arithmetically averaged DoS (ADoS) as a function of increasing (bottom to top panel) disorder strength, W for $U = 1.2$.

$\rho_{typ}(0)$ would serve to be a correct descriptor of the respective MIT (instead of the $\rho_{arith}(0)$. This behaviour of the TDoS is also consistent with the behaviour of the effective hybridization function as shown in Fig. 5.4).

We shall now discuss the spectral features in a little more detail. As seen in Fig. 5.6, there exists remnants of the $W = 0$ limit Kondo resonance centered around $\omega = 0$. With increasing disorder, this resonance initially broadens but then progressively narrows down. The high energy Hubbard bands in Fig. 5.6 demonstrate that with inclusion of disorder, they broaden and acquire reduced spectral intensities. This broadening that is also manifested in the self consistently determined hybridization function, shown in Fig. 5.4 (right inset), highlight the fact that pres-

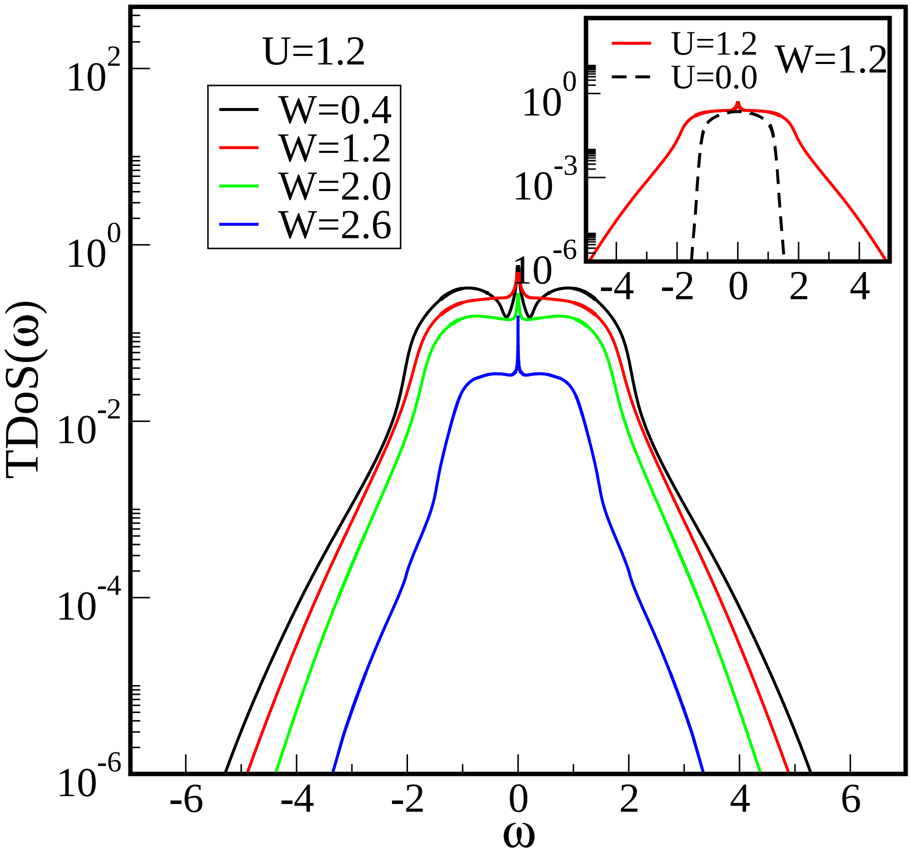

Figure 5.7: **Localization edge:** (Main panel) Behaviour of the localization edge of the single-particle DoS as a function of increasing disorder with the spectra plotted on a log-linear scale at $U = 1.2$. As W is increased, the edge moves inside, but as shown in the inset, the tails are extremely slowly decaying as compared to the $U = 0$ scenario.

ence of disorder introduces additional scattering pathways. In the context of DMFT, this increases the rate at which these high energy electrons hop off from the impurity site into the embedding host, thus reducing its lifetime and hence broadening the spectra.

We shall now discuss the behaviour of the localization edge of the spectrum as a function of increasing disorder. Figure 5.7 (inset) shows that interaction masks the localization edge, an observation consistent with a recent report [69], looking at a weakly interacting disordered system within a cluster theory. However, with the increase of disorder the respective tails move in towards the Fermi energy, although they never become as sharp as the $U = 0$ case.

Density of states: $U > U_{c2}$, $W \neq 0$

In Fig. 5.8 we again compare the ADoS and the TDoS for various disorder strengths, W, similar to the earlier case, but for $U = 2.7$ which is a Mott insulator in the $W = 0$ limit.

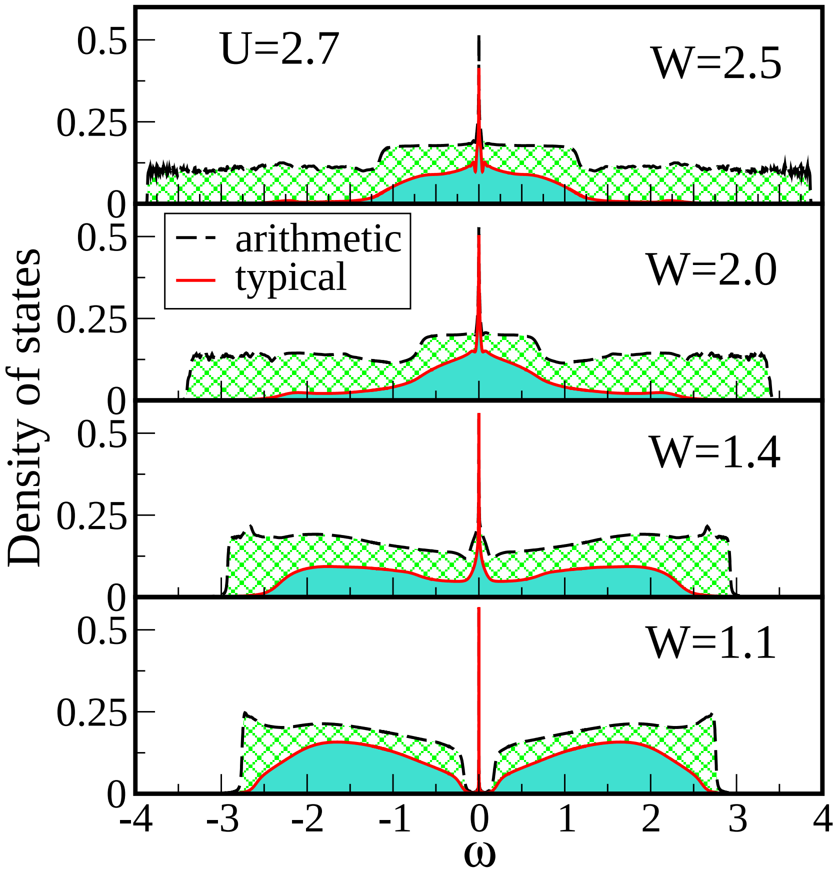

Figure 5.8: Comparison of the typical density of states (TDoS) and the arithmetically averaged DoS (ADoS) as a function of increasing (bottom to top panel) disorder strength, W, for $U = 2.7$. At $W = 0$ this system represents a Mott insulator.

Similar to the weakly interacting limit of the system, the comparison between the TDoS and the ADoS, as shown in Fig. 5.8 shows that with increasing disorder while the TDoS consistently shows a reduced spectral weight over all energy scales, the ADoS on the other hand undergoes spectral broadening, an observation that was also relevant for $U = 1.2$ illustrated in Fig. 5.6

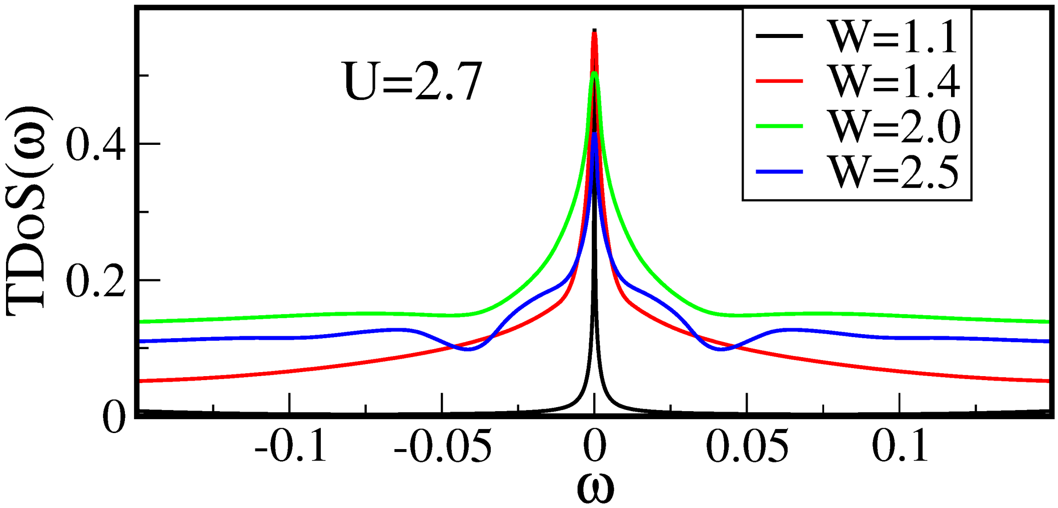

Figure 5.9: **Low energy sector of the TDoS:** At low disorder, $W = 1.1$, the spectra at low energy demonstrates the preformed Mott-Hubbard gap that would form at $W = 0$. With subsequent increase to $W = 1.4$ this gap gets filled up and completely vanishes at $W = 2.0$. Notice that the Kondo resonance also initially broadens until $W = 2.0$ in the figure, indicating disorder screening of U at low energies and at $W = 2.5$ it again shrinks indicating the onset of the strong coupling limit where both W and U tend to localize the system. This re-entrant behaviour has also been observed for $U = 1.2$, as seen in Fig. 5.6.

In the same spirit as the $U = 1.2$ case, we will now discuss the spectral features in more detail, in particular the low energy sector that is further shown Fig. 5.9. At, $W = 0$, the system is a Mott insulator. The introduction of randomness allows for new pathways for the localized moments to delocalize by allowing diffusion. This naturally manifests as the emergence of a finite density of states at the Fermi level. More interestingly, the sharp Kondo resonance reappears in the middle of a prominent gap, with the inclusion of a small amount of disorder; this gap is nothing but the remnant of the Mott insulating gap. In other words, the disorder being small, still renders a well formed Kondo resonance sitting in the middle of a sufficiently large preformed gap indicating the existence of a coexistence regime of a Mott type insulator and correlated metallic phase in the W-U plane. Note that such a coexistence regime was also observed by Byczuk *et al.* in Ref. [39], where the authors explored the AHM on a Bethe lattice using the TMT-DMFT framework. With further increase of disorder this gap vanishes, and the Kondo resonance also broadens further bringing out the disorder induced reduction in the effects of interactions. It is worth mentioning here that earlier NRG studies have shown that an increase in W, in this regime, initially increases the $\rho_{typ}(0)$ from zero to $\rho_{typ}(0) \sim \rho_0(0)$, (where $\rho_0(0)$ is the Fermi energy value of the bare DoS ($U = 0,\ W = 0$)) and further to some higher value at a sufficient enough impurity concentration. However, our current implementation limits us from exploring this intermediate disorder regime, between which, in the strong coupling limit, the crossover from $\rho_{typ}(0) = 0$ to $\rho_{typ}(0) = \rho_0(0)$ takes place.

We shall now look into the localization edge that is presented in Fig. 5.10. The same observation as in the $U = 1.2$ case holds for $U = 2.7$; the localization edge, although significantly masked due to interactions consistently move in towards the Fermi energy.

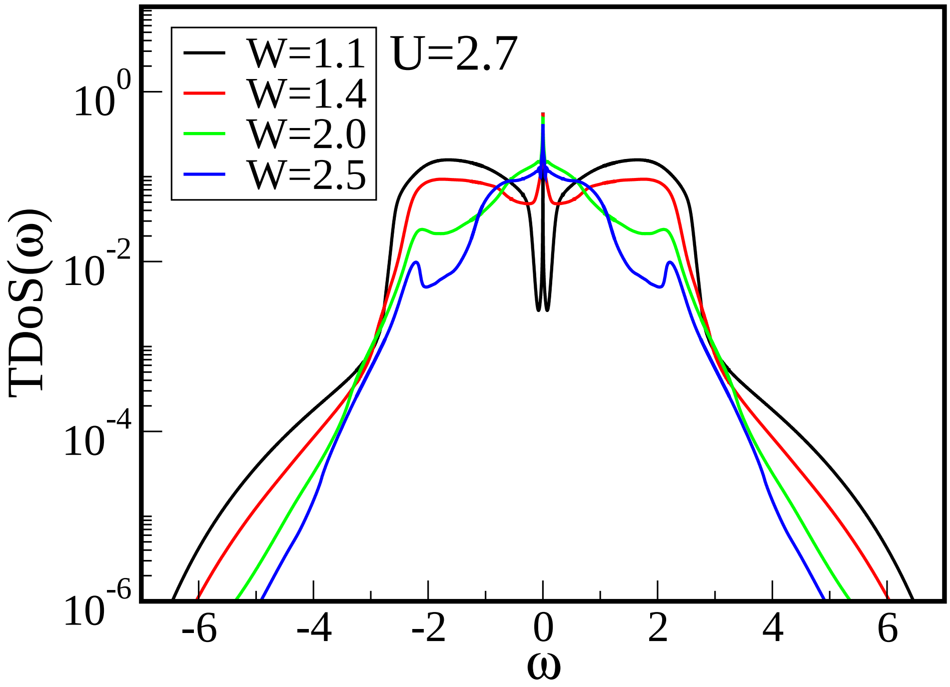

Figure 5.10: **Localization edge for $U = 2.7$:** (Main panel) Behaviour of the localization edge of the single-particle DoS as a function of increasing disorder with the spectra plotted on a log-linear scale.

We summarize this section by Fig. 5.11 where we compare the decay of the $\rho_{typ}(0)$ and the $\rho_{arith}(0)$ for the two regimes of interaction discussed above. Clearly,

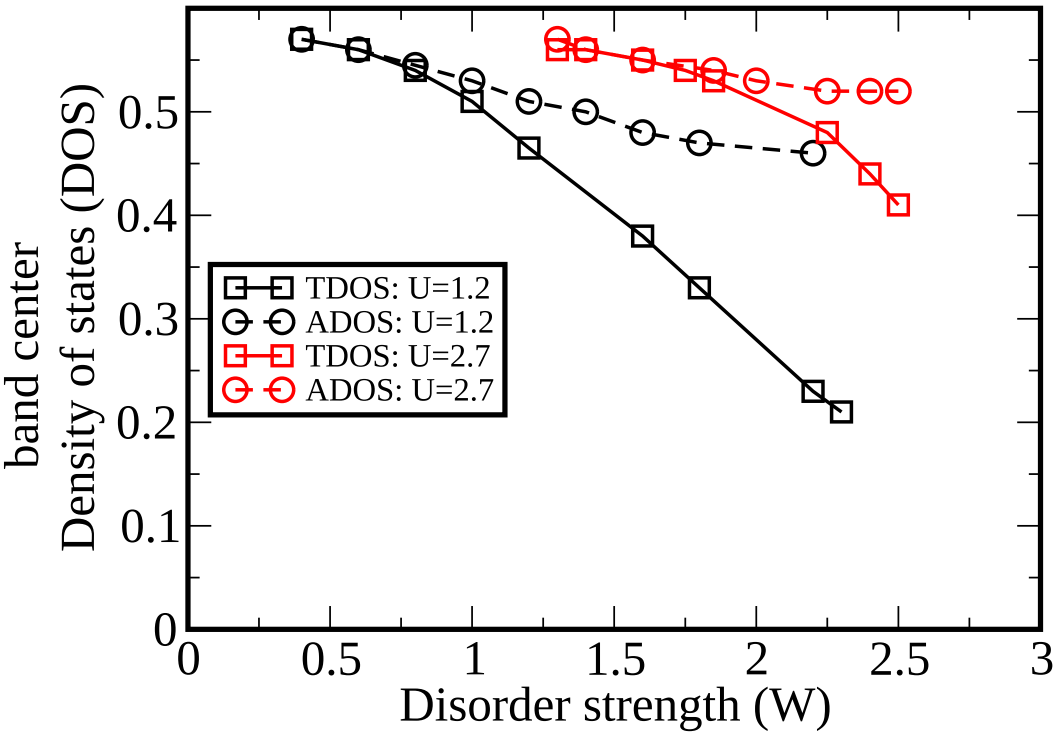

Figure 5.11: Comparison of the band center value of the TDoS and the ADoS

the $\rho_{typ}(0)$ behaves like an order parameter for the disorder induced metal insulator transition signifying the non-selfaveraging nature of the physics due to Anderson localization. In the weak disorder, strong interaction limit, a well pronounced Kondo resonance was formed signifying that interactions prevent the coherence of the quasiparticles and protect them from undergoing disorder induced impurity scattering. Moreover, the rate of decay of the $\rho_{typ}(0)$ for the strongly correlated regime is much slower compared to the weakly correlated regime, again suggesting that the cooperativity of disorder and interactions is reduced in case of stronger interactions. This slow decay rate of the $\rho_{typ}(0)$ in fact prohibits us from determining the metal to Anderson insulator phase boundary (as derived by NRG based calculations [39]) for these regimes of U. This will also be discussed later when the phase diagram will be demonstrated.

5.5.2 Distribution of Kondo scales

It is well known that the metallic DoS of the p-h symmetric SBHM, exhibits a three peak structure, with a well defined Kondo resonance centred around the Fermi energy, that signifies the low energy quasiparticle coherence present in the system [1]. The full width at half maximum (FWHM) of this resonance is one measure of the low energy Kondo coherence scale, T_K^0, present in the Fermi liquid. Above this coherence scale all physical properties are dominated by large incoherent electron-electron scattering and Fermi liquid theory loses its validity. Although, recent state-of-art DMFT calculations indicate a *resilient quasi-particle* regime before the system crosses over to a bad metal regime [70].

In presence of disorder, when the translational invariance is broken, this screening of the local moments by the mobile electrons, would represent a non-uniform behaviour resulting from the fluctuating environment around each lattice site. Therefore, in a strongly interacting disordered system, the Kondo coherence scale should in principle be viewed as a random position dependent quantity with an associated distribution. The LMA used in this work is designed to be able to capture the dynamical spin flip scattering processes encountered by an ↑ / ↓ spin occupied impurity. The energy scale associated with these spin flip scattering processes is on the order of the Kondo scale. Thereby, within LMA, a measure of the Kondo scale is provided by the position of the resonance in the transverse spin polarization propagator (as described in the Chapter 2). Within the TMT-DMFT implementation we solve an ensemble of such impurity problems embedded in an effectively disorder averaged medium, which in the current work are solved using the LMA. We therefore end up with a self-consistently determined distribution of such spin flip scattering energy scales that represent the energy scales associated with the Kondo screening of the impurities by the disorder averaged effective non-interacting host. In Fig. 5.12 and Fig. 5.13 we show such distributions of Kondo scales, T_K, for different disorder strengths, W, and for two representative interaction strengths, $U = 1.2$ and $U = 2.7$, respectively .

As evident from Fig. 5.12 and Fig. 5.13, the distributions are peaked and

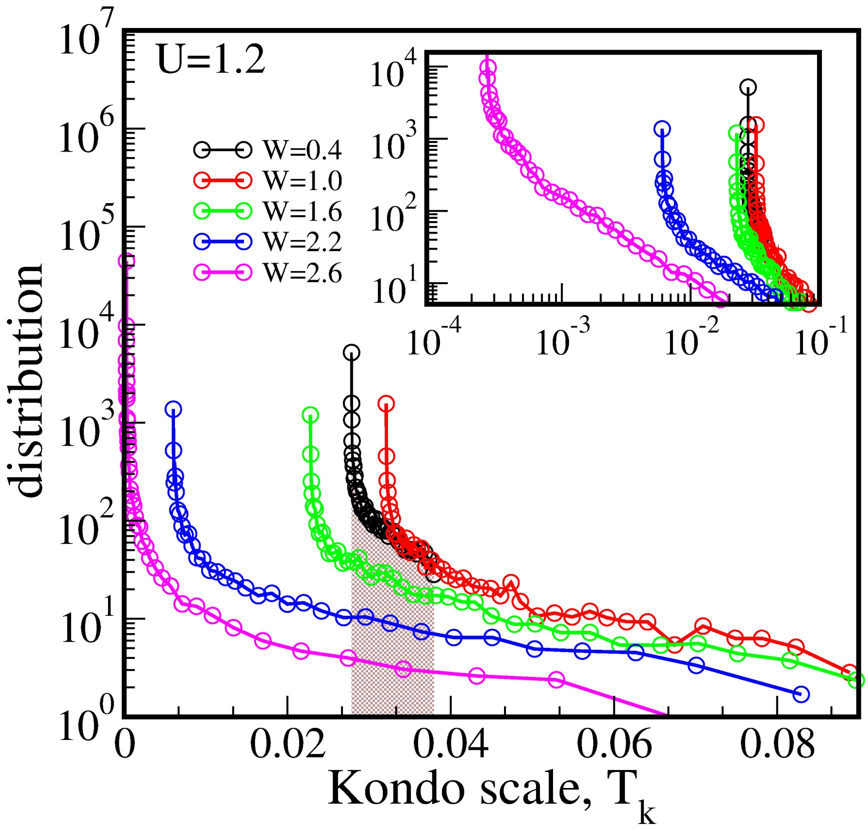

Figure 5.12: **Distribution of Kondo scales for $U = 1.2$:** In the main panel, the evolution of the T_K distribution for various W's is presented on a log-linear scale. The distributions are peaked at a characteristic energy, T_K^{peak} and (sharply) bounded from below by the scale associated with the respective particle-hole symmetric limit of the effective impurity problem embedded in the typical medium. The brown shaded region highlights the narrow range of T_K's spanned by small W in contrast to the higher T_K long tails spanned by larger W's. The same is plotted on a log-log scale in the inset.

bounded from below, by the Kondo scale, T_K^{peak}; this peak value of the Kondo scale, namely, T_K^{peak} is associated with the p-h symmetric limit of the effective impurity problem embedded in the disorder averaged medium. For the lowest disorder, namely $W = 0.4$ for $U = 1.2$ in Fig. 5.12 and $W = 1.3$ for $U = 2.7$ in Fig. 5.13, the distribution is not broad. The brown shaded region in Fig. 5.12 and Fig. 5.13 demonstrates the narrow area under this curve in contrast to the long tails in the distributions corresponding to the higher values of W. The sharp boundary owes its origin to the mean field nature of the disorder averaged hybridizing medium. It is

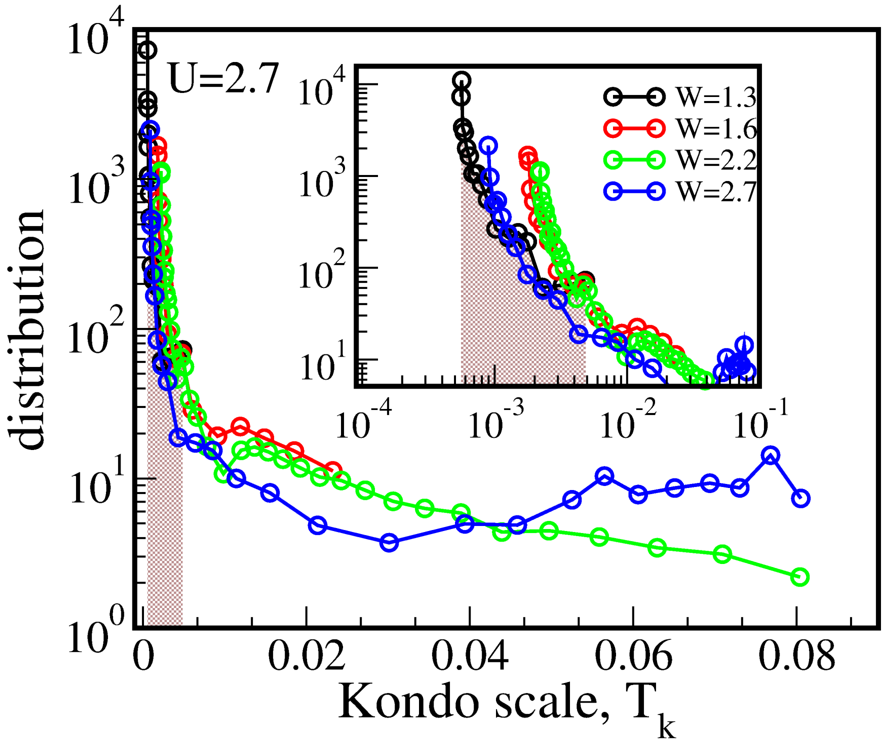

Figure 5.13: **Distribution of Kondo scales for $U = 2.7$:** The same observation as in the $U = 1.2$ case holds except that the T_K^{peak} is minimum for the lowest disorder ($W = 1.3$), this being close to the Mott insulating solution.

because of this mean field, that all short (and long) range correlation effects of disorder are neglected and each site therefore sees the same environment. The effective Kondo screening experienced by this impurity could thus be only dependent on the ϵ_i of the respective impurity. And since the $\Gamma_{typ}(\omega)$ is p-h symmetric the smallest Kondo scales will be possesed by those sites which are close to half filling.

Increasing W by a small amount results in pushing some sites away from half-filling, resulting in the development of a higher T_K tail in the distribution as shown in Fig. 5.12 and Fig. 5.13. It should be now noted that the initial effect of increasing W is to screen the effects of U even at the lowest energy scales, such that the T_K^{peak} is pushed to a higher value. This is represented by the distribution for $W = 1.0$ in Fig. 5.12 and $W = 1.6$ or $W = 2.2$ in Fig. 5.13. It is only after a certain crossover disorder strength that the T_K^{peak} consistently decreases towards lower and lower Kondo scales, signifying the onset of disorder induced incoherence cooperating with U driven incoherent scattering. This re-entrant behaviour of the interplay of U and W can also be inferred from the low energy spectral features of the effective hybridization $\Gamma_{typ}(\omega)$ shown in Fig. 5.4 for $U = 1.2$. The low energy resonance first broadens with an increase in disorder and then beyond a certain W starts losing spectral weight over all energy scales. This initial broadening is in sync with the enhanced effective screening observed in the distributions of the Kondo scales with an initial increase of disorder. However, for strong disorder potential, the effective hybridization between the impurities and the host starts decreasing for all energies. This has important consequences as this reduction of the integrated spectral weight of $\int -\text{Im}\Gamma(\omega)$, as shown in the left inset of Fig. 5.4 and Fig. 5.5 is the reason why the distribution of Kondo scales become more and more skewed as W increases. Due to an overall reduction in the hopping rate of the impurity moments from the impurity site to the disordered medium, most sites now experience a reduced screening. Hence, even sites that are not very close to half-filling may experience a reduced Kondo screening or a Kondo scale close to that corresponding to the p-h symmetric limit. Moreover, for strong disorder potential, the $\Gamma_{typ}(0)$ between any site and its host becomes sufficiently small such that the ratio, $U/\pi\text{Im}(\Gamma_{typ}(0))$ becomes comparable to the bare bandwidth and the sites close to half filling experience stronger correlation effects, pushing, T_K^{peak} towards zero.

In Fig.5.14 we plot the T_K^{peak} as a function of W for different interaction strengths, U. In the clean limit, the system with $U = 1.2,\ 1.8$ is a Fermi liquid with a certain coherence/Kondo scale $T_K^0 = T_K^{peak} \approx 0.025,\ 0.007$ respectively. With increasing W the Kondo scale develops a distribution as described earlier in this section, and correspondingly, the T_K^{peak} of the distribution initially increases and then decreases with increasing W. For $U = 2.7$, the clean limit is Mott insulating with $T_K^{peak} = 0$; it then increases consistently signifying the competitive nature of the interplay of W and U on this low energy scale. This competition continues until a crossover W, beyond which W and U cooperate and both try to localize the electrons. We note that this non-monotonic (reentrant) behaviour of the T_K^{peak} for $U = 2.7$, i.e. $U > U_{c2}$ is same as that observed for the lower U's, i.e. $U < U_{c2}$, the only difference being the value of T_K^{peak} in the clean limit. This also brings out the fact that the system with $U = 2.7$ tends to undergo two metal-insulator phase transitions, (Mott) insulator-

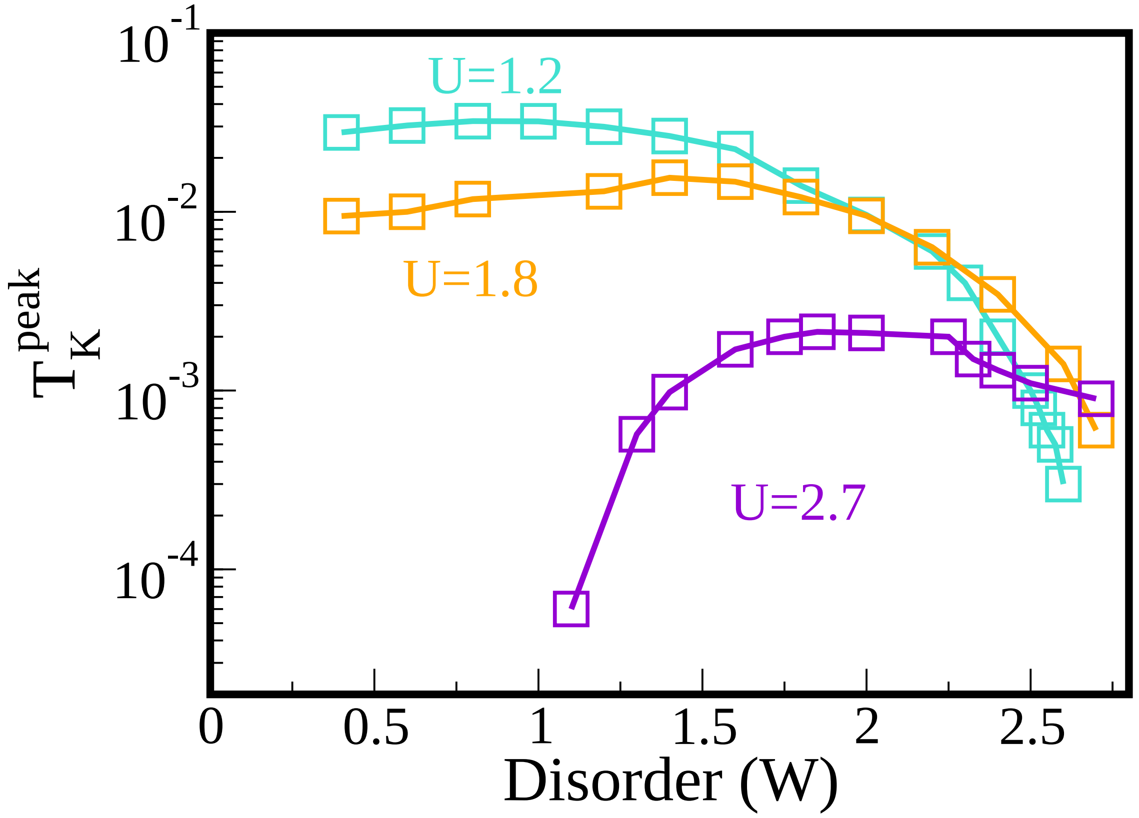

Figure 5.14: **Evolution of T_K^{peak}:** The T_K^{peak} extracted from the respective distribution of T_K's is plotted as a function of W for $U = 1.2$, 1.8, 2.7. While $U = 1.2$, 1.8 correspond to $U < U_{c2}$, $U = 2.7 > U_{c2}$. Hence the $W = 0$ limit corresponds to $T_K^{peak} = 0$ for $U = 2.7$ and $T_K^{peak} \neq 0$ for $U = 1.2$, 1.8.

metal-(Anderson-Mott) insulator. The transition from a metal to (Mott) insulator with a reduction of W should be accompanied by a sudden drop of the $\rho_{typ/arith}(0)$ at $W = 0$, but a continuous power law decay of T_K^{peak} (as seen in a conventional Mott transition assuming the same picture to hold since the $W/U < 1$). With this picture in hand we would derive the phase diagram in the U, W plane and also compare it with earlier predictions [35, 39]. Before delving into the phase diagram we would present a discussion on the self energy and try to identify characteristic energy scales, if present in the disordered scenario, or, whether any disorder induced non-Fermi liquid scattering emerges or not.

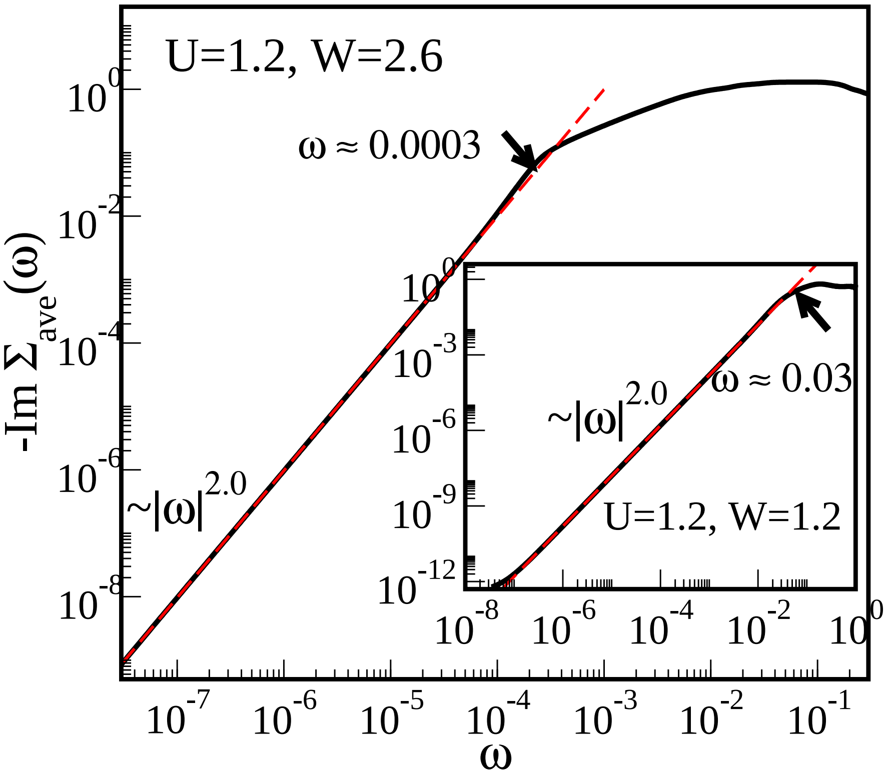

Figure 5.15: **Fermi liquid regime of** $\text{Im}\Sigma_{ave}(\omega)$**:** The $\text{Im}\Sigma_{ave}(\omega)$ is plotted on a log-log scale and the low energy Fermi liquid dynamics is illustrated for $U = 1.2$ with $W = 2.6$ in the main panel and $W = 1.2$ in the inset. The deviation from the ω^2 sets in at a scale, $\omega^* = T_K^{peak}$.

5.5.3 Self energy

In this section we shall now look at the scattering dynamics of the particles by exploring the imaginary part of the disorder averaged single-particle self-energy, $\Sigma_{ave}(\omega)$. We note that the physical selfenergy is the average-selfenergy $\Sigma_{ave}(\omega)$ obtained from the Dyson's equation corresponding to the arithmetically averaged Green's function, given by the equation, $\Sigma_{ave}(\omega) = \mathcal{G}(\omega)^{-1} - \langle G^c(\omega)\rangle^{-1}_{arith}$.

In a clean Fermi liquid, the $-\text{Im}\Sigma_{ave}(\omega) \sim |\omega|^2$ for $\omega < T_K^0$ (where T_K^0 is the lattice-coherence scale or the Kondo scale in a clean lattice). With a similar background we look at the low ω form of $-\text{Im}\Sigma_{ave}(\omega)$ in Fig. 5.15. Indeed we find that $-\text{Im}\Sigma_{ave}(\omega) \sim |\omega|^2$ for $\omega < \omega^*$, where ω^* represents the scale where the system crosses over to an incoherent regime. We illustrate this in Fig.5.15 where we plot the $-\text{Im}\Sigma_{ave}(\omega)$ on a log-log scale for $W = 2.6$ with $U = 1.2$ (main panel) and $U = 1.2$, $W = 1.2$ (inset). If we now look closely at the the value of $\omega = \omega^*$, we realize that this is exactly equal to the value of T_K^{peak} obtained from the respective distribution of Kondo scales.

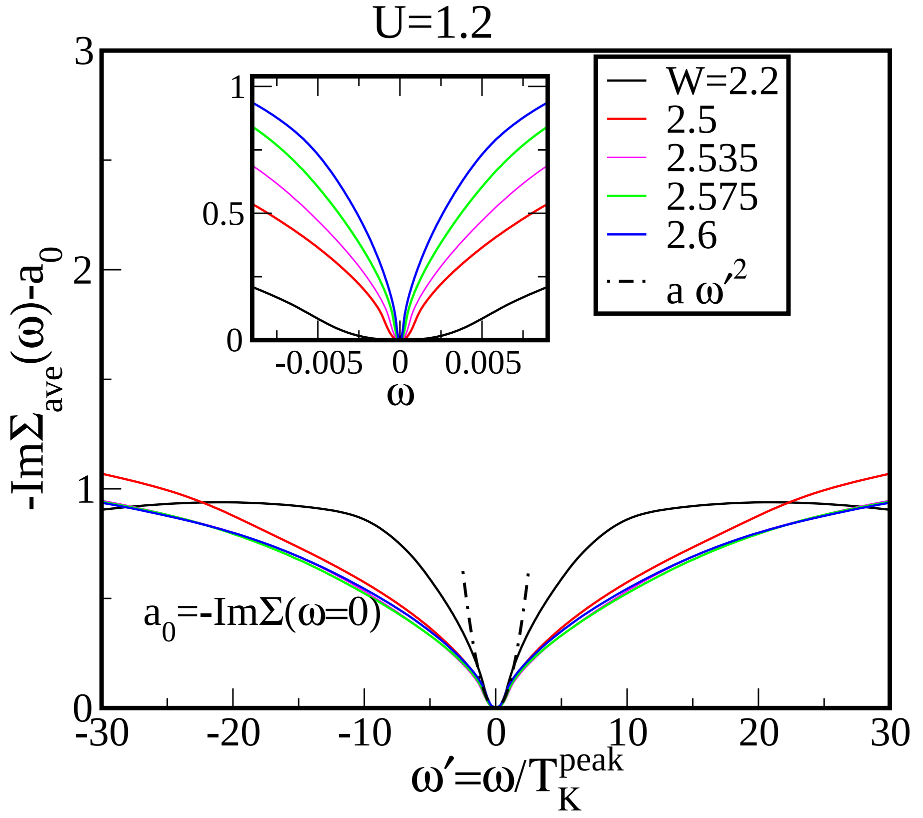

Figure 5.16: **Universal scaling of -Im$\Sigma_{ave}(\omega)$:** (Main panel) The Im$\Sigma_{ave}(\omega)$ with the static part ($a_0 = -\text{Im}\Sigma_{ave}(0)$) subtracted is plotted on an energy scale, ω', rescaled by T_K^{peak} obtained from the respective $P(T_K)$, for $U = 1.2$. (Inset) The same sets of data are plotted on a bare energy scale.

The significance of the above scale is further highlighted in Fig. 5.16 and Fig. 5.17, where we subtract the static contribution, $a_0 = -\text{Im}\Sigma_{ave}(0)$, and plot the low energy part of -Im$\Sigma_{ave}(\omega) - a_0$ for different disorder strengths and $U = 1.2$ and 2.7 in Fig. 5.16 and Fig. 5.17 respectively. In the main panels we plot the -Im$\Sigma_{ave}(\omega) - a_0$ on a frequency rescaled, $\omega' = \omega/T_K^{peak}$ axis, demonstrating a universal scaling collapse of the single-particle self-energy, with T_K^{peak} being the universal scale. In the

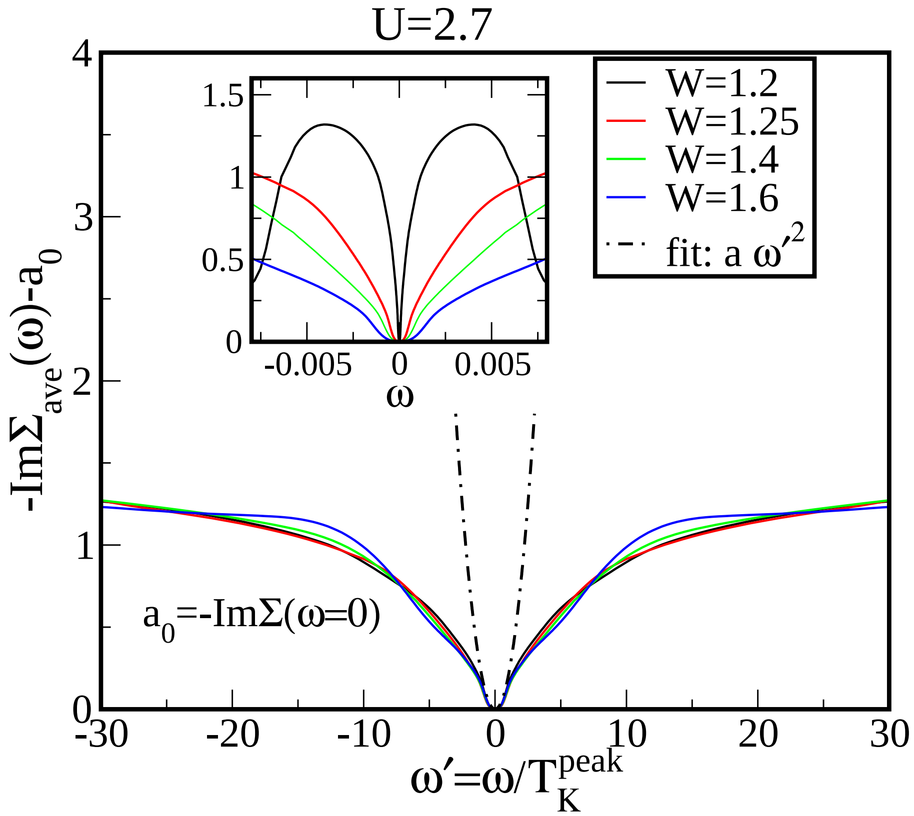

Figure 5.17: **Universal scaling of -Im$\Sigma_{ave}(\omega)$**: (Main panel) The Im$\Sigma_{ave}(\omega)$ with the static part ($a_0 = -\text{Im}\Sigma_{ave}(0)$) subtracted is plotted on an energy scale, ω', rescaled by T_K^{peak} obtained from the respective $P(T_K)$, for $U = 2.7$. (Inset) The same sets of data are plotted on a bare energy scale.

insets, the same data sets are plotted on an absolute scale. The clear collapse due to this rescaling suggests that indeed T_K^{peak} serves to be a (disordered-)Fermi liquid scale, in the same spirit as in the clean case. Moreover, as seen from Fig. 5.16 and Fig. 5.17, the universality is significantly observed until a much higher energy scale of $\omega \sim 10T_K^{peak}$, indicating the participation of such higher energy electrons in the screening of the local moments in the disordered background. In other words, this signifies that within a local theory for disordered systems, that is capable of capturing the physics due to deep trapped states, the quasi-particle excitations are in fact determined by a disorder renormalized single impurity Kondo scale, T_K^{peak}. Let us now comment on the parameter regime where this collapse is most significantly observed. The scaling collapse for $U = 1.2$ holds true for higher disorders and very close to the transition where the T_K^{peak} itself is exponentially small. Note that the values of $W = 2.575,\ 2.6$ in Fig. 5.16 corresponds to very small scales in Fig. 5.14, and, indeed these disorder strengths are very close to the disorder driven metal-insulator transition, where, $\rho_{typ}(0)$ also vanishes.

A similar scenario is observed for $U = 2.7$ where, $U = 2.7$ ($> U_{c2}$), U_{c2} being the critical U for Mott transition in a SBHM when approached from the FL side. (For a derivation of U_{c2} please see Appendix A). If we now locate $W = 1.2,\ 1.25,\ 1.4$ in Fig. 5.14 (violet curve), these values would approximately correspond to $T_K^{peak} \sim 0.00009,\ 0.0005,\ 0.001$ respectively, and would thus represent W's close to a metal-insulator translation resembling a clean Mott transition, where in, $\rho_{typ}(0)$, $\rho_{arith}(0)$ would vanish 'on the spot' and the T_K^{peak} would continuously vanish to zero at the critical W. So, as observed in Fig. 5.17, universal scaling, until $\omega' \approx 30$ is observed from $W = 1.2$ and $W = 1.25$, representing parameters very close to the *disordered Mott transition*.

In order to further confirm the robustness of our prediction about T_K^{peak} behaving like a universal scale, we also performed such an analysis as above for the *arithmetically* averaged DoS at a fixed $W = 0.2$ and various U's. This is illustrated in Fig. A.4 of Appendix A. Spectral scaling of the *arithmetically* averaged DoS at fixed $U = 1.2$ and $U = 2.7$ for different W's are illustrated in Fig. A.3(a,b) of Appendix A.

Several questions come up with this observation and we mention some of these here: (1) Does the intermediate universal regime bring out a *resilient quasi-particle* picture even in a disordered interacting system? (2) What is the non-interacting limit to which the disordered interacting scenario adiabatically connects to? (3) Does such a universal scale also exist when coherent back-scattering is included in the theory? Leaving such questions for future analysis, we now discuss the phase diagram in the following section.

5.5.4 Phase diagram

It is now intuitive to realize that the very nature of the model would give birth to phases with different characteristics. For example, if $U = 0$ then we obtain a transition from a disordered metal to an Anderson insulator phase [14]. On the other hand if $W = 0$ then it is known that a phase transition takes place between a strongly correlated metallic phase to a Mott insulating phase [2]. It would be thus interesting to see how the interplay of disorder and strong correlations interpolates between these two limits. This would also help us benchmark our LMA based calculations, against the earlier predictions based on NRG [39]. As can already be understood from the earlier discussions, there occur three distinct phases: (a) a disordered metallic phase, where $\rho_{typ}(0) \neq 0$, $T_K^{peak} \neq 0$, (b) an Anderson-Mott insulator phase where our calculations indicate that the approach to this phase to be accompanied by a linear decay of $\rho_{typ}(0)$, $\rho_{arith}(0) \neq 0$ and a corresponding power law decay of T_K^{peak}; (c) a disordered Mott insulator phase, where, our calculations indicate that the approach to this phase is associated with a sudden drop in the $\omega = 0$ DoS such that both $\rho_{typ}(0) = 0$ and $\rho_{arith}(0) = 0$ and a corresponding decay of T_K^{peak} as $T_K^{max} \sim |W - W_c|^{\alpha}$. In Fig.(5.18) we therefore plot the phase diagram of the paramagnetic Anderson-Hubbard model based on these characterisations. We shall now follow up with a discussion of the phase diagram in little more detail.

The disordered metallic phase is characterised by the presence of a finite $\rho_{typ}(0)$ and $\rho_{arith}(0)$ and a non-zero T_K^{peak}. This is essentially the regime where $U < U_{c2}$. In this weakly/moderately correlated regime, if we now increase W, we find that both $\rho_{typ}(0) \to 0$ and the $T_K^{peak} \to 0$ while $\rho_{arith}(0)$ is non-vanishing, suggesting that it is a disorder driven metal insulator transition. Hence, this transition is interpreted to be from a disordered metallic to an Anderson-Mott insulator phase. Our calculations suggest that in order to find out the critical value of disorder (W_c), for this phase transition, one could, in principle, use the power law decay of, T_K^{peak} as $T_K^{peak} \sim |W - W_c|^{\alpha}$. However, this extrapolation requires us to explore $T_K^{peak} \lesssim 10^{-4}$ at the least. The DMFT convergence becomes extremely oscillatory in such a regime and hence we avoid such regimes. Instead, we focus on the $\rho_{typ}(0)$, and stop our calculations when we reach a $\rho_{typ}(0) \leq 0.1$. The W_c is then found through

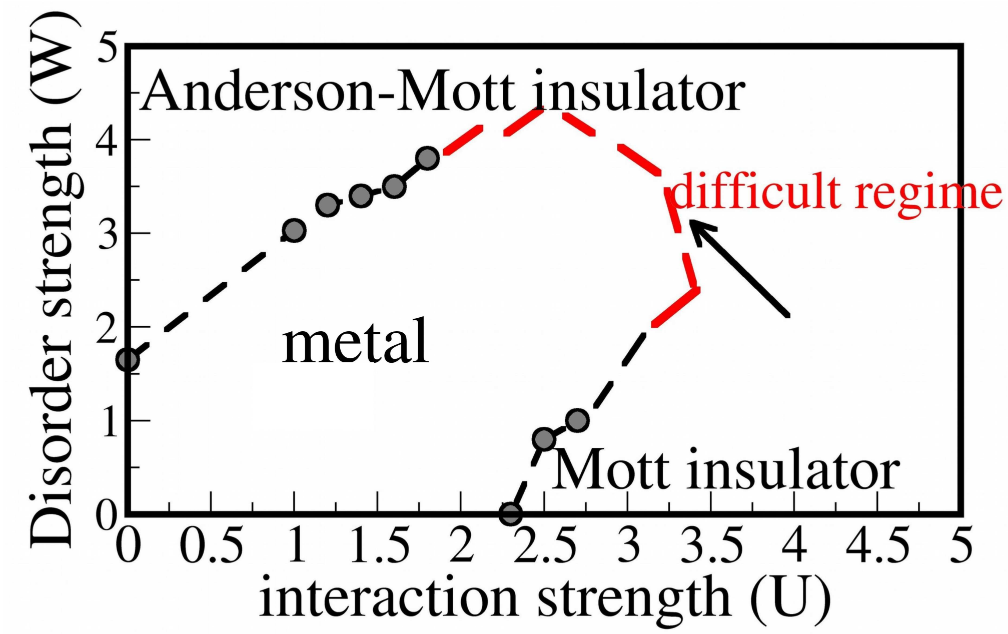

Figure 5.18: **Phase diagram in the $W - U$ plane (3D-cubic lattice):** Starting from a metallic phase, with $\rho_{typ}(0) \neq 0$ and $\rho_{arith} \neq 0$, by increasing W we have obtained an Anderson-Mott insulator phase where $\rho_{typ}(0) = 0$, $\rho_{arith} \neq 0$. The approach is also marked by $T_K^{peak} \to 0$. By decreasing W, for $U > U_{c2}$, we have obtained a Mott insulator phase, where, $\rho_{typ}(0) = 0$, $\rho_{arith} = 0$ and $T_K^{peak} = 0$. The DoS suddenly drops to zero as in a conventional Mott transition. The picture is consistent with that observed earlier in the literature [35, 39]. However, our calculations were very unstable for parameters in the vicinity of the red dashed curve and so our implementation could not explore this regime. Moreover, the formula for the TDoS only allows us to approach the metal-insulator transition from the metallic side. The results represented by the black dashed line with circles are in agreement with [39] that was performed on a Bethe lattice. The red dashed line is a schematic representation obtained in [39] for the Bethe lattice.

extrapolation as shown in Fig.5.19. This helps us determine the phase boundary separating metallic and the disorder driven Anderson-Mott insulator phase.

If we now look at a $U > U_{c2}$, we should, in principle, encounter two phase boundaries. Since our current numerical implementation limits us from starting from a Mott insulating phase, we choose to start from an intermediate W in the metallic phase and increase the disorder strength; then as shown in Fig. 5.11, we find that

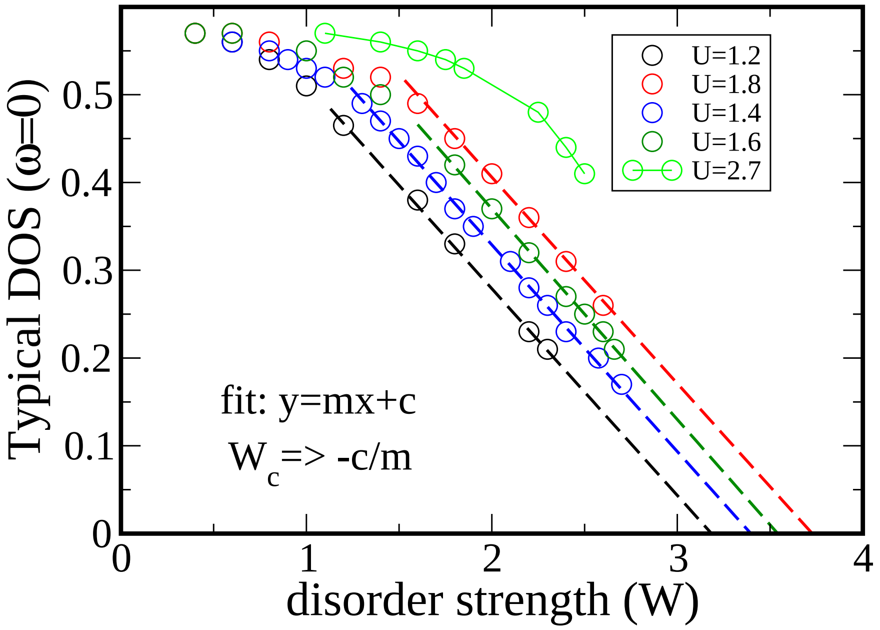

Figure 5.19: **Extrapolation procedure:** Illustration of the procedure used to obtain the phase boundary for disorder driven metal-insulator transition starting from the metallic phase at a $U < U_{c2}$. This transition is characterised by $\rho_{typ}(0) \rightarrow 0$, $T_K^{peak} \rightarrow 0$ and $\rho_{arith}(0) \neq 0$. The $\rho_{typ}(0)$ is linearly extrapolated to zero. Note that for $U > U_{c2}$, the $\rho_{typ}(0)$ vanishes extremely slowly and such a procedure could not be adopted.

both $\rho_{typ}(0) \rightarrow 0$ and $T_K^{peak} \rightarrow 0$, while $\rho_{arith}(0)$ is non-vanishing. This observation is same as the $U < U_{c2}$ scenario, however an important difference lies in the decay of the integrated hop rate given by -Im$\int \Gamma(\omega)d\omega$ as shown in the inset of Fig. 5.5. The corresponding slope is quite distinct from that corresponding to $U = 1.2$ (shown in Fig. 5.4) and the decay being much slower and tending to saturate. This difference has important consequence, namely, that the critical behaviour for the transition from a disordered metal to an Anderson-Mott insulator phase is different for these two regimes. This behaviour reflects as a slow convergence in the numerics thus making it difficult to identify the phase boundary for this metal-insulator transition. It also explains why the decay rate of $\rho_{typ}(0)$ or T_K^{peak} is much slower compared to $U = 1.2$. This is highlighted as a red dashed line in Fig. 5.18. It could be in fact possible that for $U > U_{c2}$ the $\rho_{typ}(0)$ would demonstrate a sudden drop when $W = W_c$. Also, what would be the behaviour of T_K^{peak}? As observed in Fig. 5.14, for $U = 2.7$, the T_K^{peak} tends to saturate as W is increased. The numerics in this

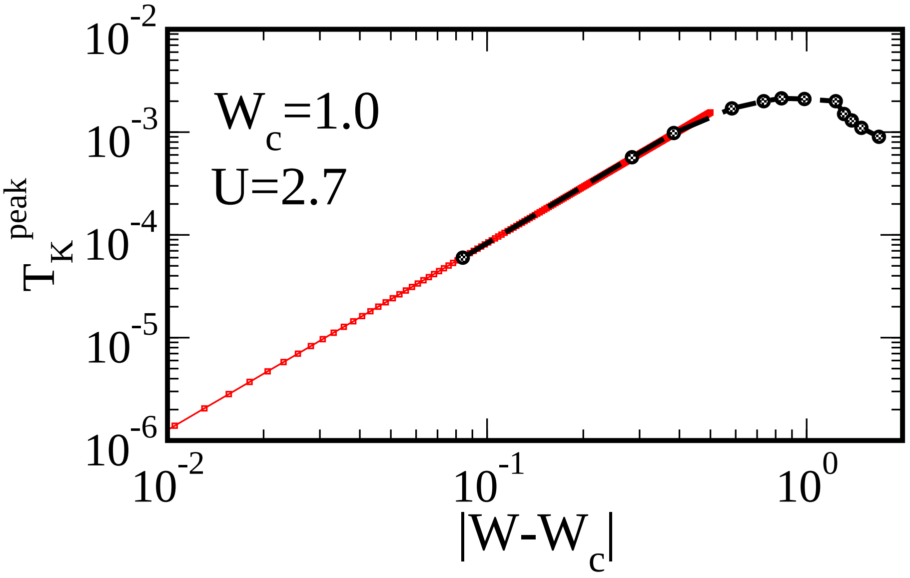

Figure 5.20: **Extrapolation of W_c for the metal to Mott insulating phase:** Illustration of the procedure used to obtain the phase boundary for the metal-Mott insulator transition. Again the starting point is the metallic phase. This transition is characterised by $\rho_{typ}(0)$, $\rho_{arith}(0)$ abruptly going to zero simultaneously, and $T_K^{peak} \to 0$. So, the boundary is obtained by extarpolating to the critical disorder, W_c where, $T_K^{peak} = 0$.

regime was found to be unreliable for realistic run times. It is possible that with a much increased run time or with a substantially higher processing power we could achieve reliability, however such resources are not available to us presently.

The transition from the metallic to disordered Mott insulating phase as a function of decreasing W is only possible for $U > U_{c2}$. We again start from an intermediate W that is well into the metallic phase and gradually decrease W until it reaches a $T_K^{peak} \sim 10^{-4}$. Note that the W being small, $\rho_{typ}(0) \sim \rho_{arith}(0) \neq 0$ while $T_K^{peak} \to 0$; moreover, the DoS shows pronounced Hubbard bands and prominent Kondo resonance indicating that the scenario is close to that of a clean Fermi liquid to Mott insulator transition. We therefore, derive this phase boundary by fitting $T_K^{peak} \sim |W - W_c|^{\alpha}$ as shown in Fig. (5.20). We note further, from Fig 5.9, that there exists a clear preformed gap the size of which decreases as W is increased. This gives a clear indication that there would exist a coexistent metallic and insulating phase in the phase diagram as had also been predicted by NRG calculations [39]. However, our current numerical implementation is incapable of capturing the transition from the Mott insulating side and is thus not able to probe this coexistent region. Moreover, the calculations in the regime of very high disorder and interaction becomes extremely difficult owing to the extremely low Kondo scales involved. Probing the re-entrant behaviour of the phase boundary as obtained through NRG [39] or slave-boson calculations [35] is also beyond the scope of the current analysis.

5.6 Summary and Conclusions

One of the main purposes of this chapter was to explore and validate the LMA implementation within the framework of a local theory, namely the TMT-DMFT framework for disordered interacting systems. In this regard, we revisited the AHM on a 3-dimensional cubic lattice. Indeed, our results are qualitatively well in agreement with the earlier calculations based on the NRG [39] or SB mean-field [35] approach. Of course, a quantitative benchmark was not possible owing to the fact that the former calculations were based on a Bethe lattice DoS.

In addition to an analysis from the perspective of the DoS we demonstrated the behaviour of the distribution of Kondo scale, $P(T_K)$. As emphasized earlier in Ref. [35], we showed how both $P(T_K)$ and the band center of the TDoS, $\rho_{typ}(0)$, would be useful to determine the different phases present. Additionally, we also predicted the existence of a single energy scale, T_K^{peak}, to be identified as the peak of $P(T_K)$. We illustrated *universal scaling* dynamics of the single-particle quantities like the disorder averaged DoS and inverse single-particle scattering rate (given by -Im$\Sigma_{ave}(\omega)$), when the frequency was rescaled by the respective T_K^{peak}. For, $\omega \leq T_K^{peak}$ coherent FL quasi-particles exist, beyond which the scattering dynamics crosses over to a *universal* regime wherein, T_K^{peak} continues to act like a single-universal scale until $\omega \sim 10T_K^{peak}$. This further establishes that the physics due to deep-trapped states results in an effective renormalised 'Kondo' screening such that the lattice *coherence* still persists in a disordered scenario. Thus, for systems where a mean-field theory should be adequate, one should expect such universal scaling in the thermodynamic and transport properties also.

Finally, we also characterised the different phases based on the behaviour of T_K^{peak} and $\rho_{typ}(0)$ which concur with the previously reported results [35, 39]. Our numerical analysis support the fact that, for weak disorder but strong interactions, namely, $W < W_{c0}$ (W_{c0} being the critical disorder strength for Anderson localization in the respective non-interacting case) and $U > U_{c2}$, both the $\rho_{typ}(0)$, $\rho_{arith}(0)$ vanish abruptly and simultaneously, while T_K^{peak} continuously vanishes to zero, thus resembling a clean scenario for the Mott transition. On the other hand, when $U < U_{c2}$, increasing W results in a metal-insulator transition characterised by a vanishing $\rho_{typ}(0)$ and T_K^{peak} but a non-critical $\rho_{arith}(0)$. Since both $\rho_{typ}(0)$, $T_K^{peak} \to 0$ this phase has been termed as an Anderson-Mott insulator. Although, our method cannot probe the transition from the insulating side the disorder averaged DoS do show clear indications of the presence of a coexistent metal/ Mott insulator regime in the (U, W) phase diagram, borne by the preformed gap in the spectra.

The LMA is an inherently non-perturbative impurity solver neither confined to low energies like the SB approach [71–73] nor to weak coupling like the second order perturbation theory [69] or the iterated perturbation theory [74]. While for non-disordered correlated systems this has clearly been demonstrated, our present calculations show that it does capture the strong correlation physics in qualitative agreement with the NRG calculations for the AHM (on the Bethe lattice) [39]. With this set up established, one then asks the question as to what happens if we include *non-local dynamical correlations* due to disorder. The TMT+DMFT approach considers physics due to impurity scattering from deep trapped states where spatial fluctuations of the disordered lattice is included in a mean-field level. Does the *universal* coherence scale established in this work still persist when short range correlation effects due to disorder are included? Several such questions come up, and in Chapter 6 we try to answer these.

Bibliography

[1] G. Kotliar and D. Vollhardt, Physics Today **57**, 53 (2004).

[2] A. Georges, G. Kotliar, W. Krauth, and M. J. Rozenberg, Rev. Mod. Phys. **68**,

13 (1996).

[3] P. W. Anderson, Phys. Rev. **109**, 1492 (1958).

[4] F. Evers and A. D. Mirlin, Rev. Mod. Phys. **80**, 1355 (2008).

[5] S. V. Kravchenko and M. P. Sarachik, Reports on Progress in Physics **67**, 1 (2004).

[6] E. Miranda and V. Dobrosavljević, Reports on Progress in Physics **68**, 2337 (2005).

[7] K. Maiti, R. S. Singh, and V. R. R. Medicherla, Phys. Rev. B **76**, 165128 (2007).

[8] K. W. Kim, J. S. Lee, T. W. Noh, S. R. Lee, and K. Char, Phys. Rev. B **71**, 125104 (2005).

[9] A. S. Sefat, J. E. Greedan, G. M. Luke, M. Niéwczas, J. D. Garrett, H. Dabkowska, and A. Dabkowski, Phys. Rev. B **74**, 104419 (2006).

[10] L. Sanchez-Palencia and M. Lewenstein, Nature Physics **6**, 87 (2010).

[11] M. White, M. Pasienski, D. McKay, S. Q. Zhou, D. Ceperley, and B. DeMarco, Phys. Rev. Lett. **102**, 055301 (2009).

[12] S. S. Kondov, W. R. McGehee, W. Xu, and B. DeMarco, Phys. Rev. Lett. **114**, 083002 (2015).

[13] B. Kramer and A. MacKinnon, Rev. Prog. Phys. **56**, 1469 (1993).

[14] E. Abrahams, *Fifty Years of Anderson Localization* (Singapore: World Scientific, 2010).

[15] P. A. Lee and T. V. Ramakrishnan, Rev. Mod. Phys. **57**, 287 (1985).

[16] E. Abrahams, P. W. Anderson, D. C. Licciardello, and T. V. Ramakrishnan, Phys. Rev. Lett. **42**, 673 (1979).

[17] A. Finkelstein, in *Soviet Science Reviews* (edited by I.M. Khalatnikov (Harwood Academic, London, 1990), 1990), vol. 9, p. 3.

[18] A. Finkelstein, Zh. Eksp. Teor. Fiz **86**, 367 (1984).

[19] A. Finkelshtein, Sov. Phys. JETP **57**, 97 (1983).

[20] D. Belitz and T. R. Kirkpatrick, Rev. Mod. Phys. **66**, 261 (1994).

[21] C. Castellani, G. Kotliar, and P. Lee, Phys.Rev.Lett **59**, 323 (1987).

[22] G. Kotliar, T. Ando, and H. Fukuyama, *Anderson Localization* (Berlin: Springer, 1987).

[23] M. A. Paalanen, J. E. Graebner, R. N. Bhatt, and S. Sachdev, Phys. Rev. Lett. **61**, 597 (1988).

[24] M. Milovanović, S. Sachdev, and R. N. Bhatt, Phys. Rev. Lett. **63**, 82 (1989).

[25] M. A. Tusch and D. E. Logan, Phys. Rev. B **48**, 14843 (1993).

[26] P. Denteneer, R. Scalettar, and N. Trivedi, Phys.Rev.Lett **83**, 4610 (1999).

[27] S. Chiesa, P. B. Chakraborty, W. E. Pickett, and R. T. Scalettar, Phys.Rev.Lett **101**, 086401 (2008).

[28] V. Dobrosavljević and G. Kotliar, Philosophical Transactions of the Royal Society of London A: Mathematical, Physical and Engineering Sciences **356**, 57 (1998).

[29] K. Byczuk, W. Hofstetter, U. Yu, and D. Vollhardt, The European Physical Journal Special Topics **180**, 135 (2009), ISSN 1951-6355.

[30] E. Miranda and V. Dobrosavljevic, ArXiv e-prints (2011), `1112.6184`.

[31] V. Dobrosavljević and G. Kotliar, Phys. Rev. Lett. **78**, 3943 (1997).

[32] V. Dobrosavljević, N. Trivedi, and J. M. Valles Jr, *Conductor insulator quantum phase transitions*, vol. 16 (Oxford University Press, 2012).

[33] R. Abou-Chacra, D. Thouless, and P. Anderson, Journal of Physics C: Solid State Physics **6**, 1734 (1973).

[34] D. Semmler, K. Byczuk, and W. Hofstetter, Phys. Rev. B **84**, 115113 (2011).

[35] M. C. O. Aguiar, V. Dobrosavljević, E. Abrahams, and G. Kotliar, Phys. Rev. Lett. **102**, 156402 (2009).

[36] Y. Song, S. Bulut, R. Wortis, and W. A. Atkinson, Journal of Physics: Condensed Matter **21**, 385601 (2009).

[37] Y. Song, R. Wortis, and W. A. Atkinson, Phys. Rev. B **77**, 054202 (2008).

[38] V. Dobrosavljević, A. A. Pastor, and B. K. Nikolić, Europhysics Letters **62**, 76 (2003).

[39] K. Byczuk, W. Hofstetter, and D. Vollhardt, Phys. Rev. Lett. **94**, 056404 (2005).

[40] M. C. O. Aguiar, V. Dobrosavljević, E. Abrahams, and G. Kotliar, Phys. Rev. B **73**, 115117 (2006).

[41] M. C. O. Aguiar and V. Dobrosavljević, Phys. Rev. Lett. **110**, 066401 (2013).

[42] D. E. Logan, M. P. Eastwood, and M. A. Tusch, Journal of Physics Condensed Matter **10**, 2673 (1998).

[43] M. R. Galpin and D. E. Logan, Journal of Physics: Condensed Matter **17**, 6959 (2005).

[44] R. Bulla, M. T. Glossop, D. E. Logan, and T. Pruschke, Journal of Physics: Condensed Matter **12**, 4899 (2000).

[45] D. E. Logan, M. P. Eastwood, and M. A. Tusch, Journal of Physics Condensed Matter **9**, 4211 (1997).

[46] V. Smith, D. Logan, and H. Krishnamurthy, The European Physical Journal B **32**, 49 (2003).

[47] N. S. Vidhyadhiraja and D. E. Logan, European Physical Journal B **39**, 313 (2004).

[48] D. E. Logan and N. S. Vidhyadhiraja, Journal of Physics: Condensed Matter **17**, 2935 (2005).

[49] V. Dobrosavljević, A. A. Pastor, and B. K. Nikolić, Europhysics Letters **62**, 76 (2003).

[50] D. E. Logan, M. P. Eastwood, and M. A. Tusch, Journal of Physics: Condensed Matter **10**, 2673 (1998).

[51] N. L. Dickens and D. E. Logan, Journal of Physics Condensed Matter **13**, 4505 (2001).

[52] M. T. Glossop and D. E. Logan, Journal of Physics Condensed Matter **14**, 6737 (2002).

[53] M. T. Glossop and D. E. Logan, Journal of Physics: Condensed Matter **14**, 6737 (2002).

[54] N. S. Vidhyadhiraja and D. E. Logan, Journal of Physics: Condensed Matter **17**, 2959 (2005).

[55] N. S. Vidhyadhiraja and P. Kumar, Phys. Rev. B **88**, 195120 (2013).

[56] P. Kumar and N. S. Vidhyadhiraja, Phys. Rev. B **90**, 235133 (2014).

[57] S. Sen, J. Moreno, M. Jarrell, and N. S. Vidhyadhiraja, Phys. Rev. B **91**, 155146 (2015).

[58] F. Gebhard, *The mott metal-insulator transition: models and methods*, vol. 137 (Springer, 2003).

[59] D. E. Logan and M. R. Galpin, Journal of Physics: Condensed Matter **28**, 025601 (2016).

[60] J. Bonča, T. Pruschke, et al., Phys. Rev. B **80**, 245112 (2009).

[61] K. Slevin and T. Ohtsuki, Phys.Rev.Lett **82**, 382 (1999).

[62] K. Slevin and T. Ohtsuki, Phys. Rev. B **63**, 045108 (2001).

[63] K. Slevin and T. Ohtsuki, New Journal of Physics **16**, 015012 (2014).

[64] K. Slevin and T. Ohtsuki, Phys.Rev.Lett **78**, 4083 (1997).

[65] A. Rodriguez, L. J. Vasquez, K. Slevin, and R. A. Römer, Phys. Rev. B **84**, 134209 (2011).

[66] W. F. Brinkman and T. M. Rice, Phys. Rev. B **2**, 4302 (1970).

[67] G. Schubert, J. Schleede, K. Byczuk, H. Fehske, and D. Vollhardt, Phys. Rev. B **81**, 155106 (2010).

[68] C. E. Ekuma, H. Terletska, K.-M. Tam, Z.-Y. Meng, J. Moreno, and M. Jarrell, Phys. Rev. B **89**, 081107 (2014).

[69] C. Ekuma, S.-X. Yang, H. Terletska, K.-M. Tam, N. S. Vidhyadhiraja, J. Moreno, and M. Jarrell, Phys. Rev. B **92**, 201114 (2015).

[70] X. Deng, J. Mravlje, M. Ferrero, G. Kotliar, A. Georges, et al., Phys.Rev.Lett **110**, 086401 (2013).

[71] P. Coleman, Phys. Rev. B **29**, 3035 (1984).

[72] J. Kroha, P. Hirschfeld, K. Muttalib, and P. Wölfle, Solid State Communications **83**, 1003 (1992).

[73] S. E. Barnes, Journal of Physics F: Metal Physics **6**, 1375 (1976), URL `http://stacks.iop.org/0305-4608/6/i=7/a=018`.

[74] H. Kajueter and G. Kotliar, Phys.Rev.Lett **77**, 131 (1996).

Chapter 6

Emergence of non-Fermi liquid dynamics through non-local correlations in an interacting disordered system[§]

Contents

[§] Work reported in this chapter is to be submitted as: **Sudeshna Sen**, Hanna Terletska, Juana Moreno, N. S. Vidhyadhiraja, Mark Jarrell, "Emergence of non-Fermi liquid dynamics due to non-local correlations in an interacting disordered electronic system"

6.1 Introduction

In the previous chapters we presented a brief overview of the existing methods and formalisms that are employed to look into disordered electronic systems. We realized that the numerical methods like the transfer matrix method (TMM) [1–3] or the exact diagonalization (ED) based methods like the kernel polynomial method (KPM) [4–8], are very accurate for looking at Anderson localization in non-interacting systems. Several important physical insights have been obtained using numerically exact renormalization group (RG) approaches [9, 10]. However, their application to interacting systems is nearly impossible owing to the high numerical cost involved. Moreover for looking into effects of disorder in chemically realistic systems or strongly correlated electron systems one has to resort to cheaper but effective methods. This need gave birth to the typical medium theory [11] which when combined with the usual DMFT [12–17] offered a self-consistent scheme for exploring the interplay of strong correlations and disorder in electronic systems with a significantly cheaper computational effort, at the price of being a mean-field theory. Efforts to include non-local effects were attempted using statistical-DMFT [18–21], but again, at a significantly higher level of numerical complexity. These effective medium theories relied on choosing the correct stochastic averaging procedure namely the use of the most probable value of the local density of states (DoS), best represented by the geometric average of the local DoS (LDoS) [22].Other efforts in this direction were based on exact-diagonalization or quantum Monte Carlo methods [23, 24], which are again limited in finite-sizes of the lattices and finite temperatures. On the other hand, a recent cluster framework proposed by Ekuma *et al.* , namely, the typical medium dynamical cluster approximation (TMDCA) [25] offer an attractive avenue for exploring the non-local effects of disorder with tremendous computational ease. For non-interacting systems, it has been shown to be computationally efficient, requiring only a small cluster (~ 64) to obtain data that is qualitatively and quantitatively in good agreement with other numerically exact results from ED and TMM, [1–8] at a fraction of the computational cost. The method has been extended to non-interacting systems with off-diagonal disorder [26] and more than one orbital [27] relevant for more realistic scenarios. In addition to correctly estimating the critical disorder strength it also captures the correct behaviour of the mobility edge. However, we note that in all such TMT-based effective medium theories the self-consistency equations and the disorder averaging procedure involves the local density of states. Therefore, when extended to interacting-disordered systems we require a real-frequency many-body impurity solver.

In the Chapter 5 we reported a study of the Anderson-Hubbard model (AHM) on a 3-dimensional cubic lattice using a non-perturbative real frequency solver namely the local moment approach (LMA). Our study produced results consistent with that of the previous numerical renormalization group (NRG) [13] and slave-boson (SB) mean-field based studies [15]. Moreover, our implementation could simultaneously probe the high and low energy features thus giving an efficient window to probe the distribution of Kondo scales while also simultaneously exploring the disorder averaged electronic self-energy. In the local theory, presented in Chapter 5, the single-particle quantities showed universal signatures well beyond the Fermi liquid (FL) regime, until energies, $\omega \gtrsim 10\omega^*$, where ω^* coincided with the peak in the respective distribution of Kondo scales. New questions opened up in this regard, for example: does a such a low energy scale like ω^* exist when non-local fluctuations due to disorder come into picture? If so, then does it still coincide with the peak of the distribution? In this chapter we intend to explore these aspects but in presence of short-range correlation effects due to disorder.

Previous theoretical works involving statistical-DMFT based approaches [20, 28, 29] on two-dimensional square lattices or the Bethe lattice, using slave-boson (SB) mean-field solver [30–32] have claimed that, in the strongly interacting regime, and at weak to moderate disorder strengths, the disordered interacting system may exhibit non-Fermi liquid (nFL) behaviour in the thermodynamic and transport properties. This is shown to manifest as a broad distribution of Kondo scales [33]. While we would like to validate this using the cluster theory developed in this chapter using state of art methods, we would also like to ask: how generic is this nFL scenario and is it possible to find its existence even at relatively weaker interactions but close to a disorder driven metal-insulator transition? Relatively recent RG calculations by Punnoose and Finkelstein revealed the existence of such a QCP, originating from the interplay of electron-electron interactions and disorder in two dimensions [34]. We ask the question: can we use the TMDCA to probe quantum criticality in 3-dimensions, if present, in the AHM due to the combined effect of interactions and disorder?

In order to answer the above questions, we employ the typical medium dynamical cluster approximation (TMDCA) [25] for interacting systems adapted for the use of LMA as the cluster solver. Before, we discuss our formulation and results, let us briefly review the known reports in the literature on strongly correlated models with *quenched* disorder. The discussion will particularly focus on disorder induced nFL dynamics that we also aim to look at within our framework.

6.1.1 Disorder induced non-Fermi liquid: A brief recapitulation

Several experiments on interacting disordered system, reported disorder-induced nFL behaviour [33], manifesting as power law anomalies and resulting in singular responses of the thermodynamic transport quantities like specific heat and magnetic susceptibility [33, 35, 36]. It was also speculated that inhomogeneities and glassy structure could be the possible origin of nFL behaviour in cuprates (for example see references in [33]). Such disorder induced anomalies are known to exist for a range of other systems like the correlated doped semi-conductors [33, 37] and in doped ruthenates [36]. In particular, while in the cleaner systems, the proximity to a quantum critical point dominated the observed properties [35, 38–43], for several other systems, disorder appears to play an essential role for understanding the nFL behaviour [36, 44–48]. Especially in experiments on heavy fermion alloys [35], this was attributed to the existence of broad distribution of Kondo temperatures, $P(T_K)$, such that it develops a lower T_K power law tail and beyond a certain disorder strength $P(T_K)$ develops a finite intercept ($P(T_K = 0)$) as $T_K \to 0$ [33, 44]. All the spins with $T_K < T$ will not be Kondo screened, (T being the temperature), thus providing a large contribution to thermodynamic response. Such nFL responses were often observed in heavy-fermion systems and were speculated to stem from the gradual unquenching of local moments as the temperature is raised [33, 49–52]. Several theoretical studies have followed in this connection [33]. Many experiments [see [33] for an overview] could be explained by a *phenomenological* "Kondo disorder model"[44, 53] with a broad distribution of Kondo temperatures [33]. In further investigations, this observation of a broad $P(T_K)$ was put on a stronger microscopical foundation using stat-DMFT approaches on the periodic Anderson model with infinite U constraint on the f orbitals, and with disorder present in either the c-f hybridization, or, the c electron energies or on the f electron energies [28, 54]. The calculations were performed using large-N [28], SB [54], static mean-field theory at $T = 0$. Similar analyses of $P(T_K)$ were also performed finite-sized square lattices [15] using the Anderson-Hubbard model (AHM), a particular model we would be looking at in this chapter.

Previous works involving statistical-DMFT and mean-field based solvers [20, 28, 29] have claimed that in the strongly interacting regime, weak to moderate disorder can introduce non-Fermi liquid behaviour through electronic Griffiths singularities [33, 55–57]. Griffiths singularities [55, 56] arise from rare, spatially localized regions that do not have large spatial correlations but result in strong disorder fluctuations in time [56]. Their contributions to thermodynamic quantities lead to non-analyticities, known as Griffiths singularities. In interacting disordered systems this is manifested as an 'infinitely broad' distribution of Kondo scales. This distribution has a low-T_K tail of the form $P(T_K) \sim T_K^{\alpha-1}$, independent of the microscopic details or the specific form of disorder [33]. The exponent, α is a smooth monotonically decreasing function of disorder, W and the nFL behaviour for a $W > W_{nFL}$, corresponds to $\alpha \leq 1$. Concomitantly, $P(T_K)$ becomes singular at the lowest T_K's. This behaviour has been dubbed as an electronic Griffiths phase scenario in the literature [20, 29, 53, 54]. In the particular context of the $U \to \infty$ PAM with random site energies, ϵ_i, in the conduction band (drawn from a uniform distribution, $P(\epsilon_i)$), it was shown that, such a $P(T_K)$ may also be obtained in a simpler, standard DMFT (instead of the numerically expensive stat-DMFT) picture, but with a judicious choice of (Gaussian)

$P(\epsilon_i) = (2\pi W^2)^{-1/2} \exp\left(-\frac{1}{2}\epsilon_i^2/W^2\right)$ [53], where, $P(\epsilon_i)$ represents the distribution for the random site energies, ϵ_i. The single-impurity interacting models within DMFT were solved using the SB mean field theory [58, 59]. A more recent investigation [20] of the half-filled PAM, with a Gaussian distribution for the random on-site energies of the conduction electrons, and solved within the stat-DMFT framework, again with the SB technique in the $U \to \infty$ limit, showed that the proposed nFL phase was *restricted* only close to interaction driven transitions and *not* close to disorder driven transitions concurring with the claim of Ref. [29] that investigated the AHM. A very early SB mean-field calculation of the AHM on the Bethe lattice using stat-DMFT had speculated such nFL physics in the large U limit of the model at a fixed electron density of $n = 0.3$ [60].

Based on the above reports, including the ones presented in Chapter 5, it is clear that a precise description of disorder driven nFL behaviour, requires the inclusion of *dynamical spatial* fluctuations due to disorder within the theoretical framework. Moreover, the current literature lacks a systematic cluster framework that can handle such physics. This chapter is thus aimed at proposing a non-local framework that can capture physics due to short range correlation effects of disorder.

6.1.2 Model Hamiltonian

With the above framework, we now investigate the AHM, known to represent a minimal model to describe the physics due to the interplay of disorder and electron-electron interactions. This model has also been looked at in Chapter 5 within the TMT-DMFT framework and for the sake of completeness, we describe it here again. The AHM is represented as,

$$\mathcal{H} = \sum_{ij,\sigma} t_{ij} c^{\dagger}_{i\sigma} c_{j\sigma} + \sum_{i,\sigma} (V_i - \mu)\hat{n}_{i\sigma} + U \sum_{i} \hat{n}_{i\uparrow}\hat{n}_{i\downarrow} \tag{6.1}$$

where, $c^{\dagger}_{i\sigma}$ ($c_{i\sigma}$) is the fermionic creation (annihilation) operator for an electron with spin σ at site i, and $\hat{n}_{i\sigma} = c^{\dagger}_{i\sigma} c_{i\sigma}$; t_{ij} is the site to site hopping amplitude, U is the onsite Coulomb interaction energy. The lattice is represented by a 3D cubic DoS with full bandwidth, $D = 3$ eV. The random disorder potential, V_i, is considered to follow a box distribution $P(V_i)$ of width W and represented as $P(V_i) = \frac{1}{2W}\Theta(W - |V_i|)$, where $\Theta(x)$ is a step function. The disorder averaging is represented using the shorthand notation, $\langle \ldots \rangle = \int dV_i P(V_i)(\ldots)$. The particle-hole (p-h) symmetry is imposed by setting $\mu = U/2$. Let us re-define the onsite energy as, $\epsilon_i = -U/2 + V_i$ for all our future references.

6.2 Method and Formalism

6.2.1 Formulation of the TMDCA

A successful (cluster) formalism for characterizing Anderson localization physics (1) should fulfill all the essential requirements expected of a cluster theory including causality and translational invariance, and (2) at the same time should be able to capture the non self-averaging nature of Anderson localization physics [17]. In presence of interactions the situation becomes substantially more intricate due to the emergence of low energy scales determined by Kondo physics. Therefore, one has to also focus on the use of an efficient real-frequency cluster solver for incorporating electron-electron interactions. In other words, in a site non-local effective medium framework, for interacting disordered systems, the electron many-body problem becomes even more complicated due to the spatially fluctuating random hybridization experienced by the lattice electrons. Moreover, in order to be able to look into disorder induced nFL dynamics or provide insights into the quantum critical nature of the Mott-Anderson physics, we should be able to use non-perturbative many-body impurity solvers that can capture the single particle spectrum over all energy scales efficiently; it should not be confined to low energies or to weak coupling and should be able to describe both low and high energy physics on an equal footing. The underlying (non-local) effective medium framework within which this would be utilized should therefore be computationally feasible and at the same time should be able to recover various thermodynamic limits (thus not suffering from the limitations of finite size methods). The TMDCA [25] has been proven to successfully take care of all these issues stated above and thus offers a suitable platform for looking into the interplay of strong electron interactions and disorder. Below we discuss its formulation for the current problem subsequently moving on to our Results.

The TMDCA [25] is based on the same self-consistent framework of the standard DCA [61, 62]. However, the crucial difference with the standard DCA lies in the utilization of an appropriately disorder averaged, (momentum) dependent hybridization, $\Gamma(\mathbf{K}, \omega)$, that takes care of all the essential requirements of a successful cluster theory, while also simultaneously taking care of the known limits of the disordered electronic lattice.

The TMDCA is a momentum space formalism based on the DCA cluster mapping to an effectively disorder averaged medium. In the following, we outline the main steps involved in the TMDCA implementation. We also discuss, in detail, the cluster solver implementation that incorporates the effects of interactions.

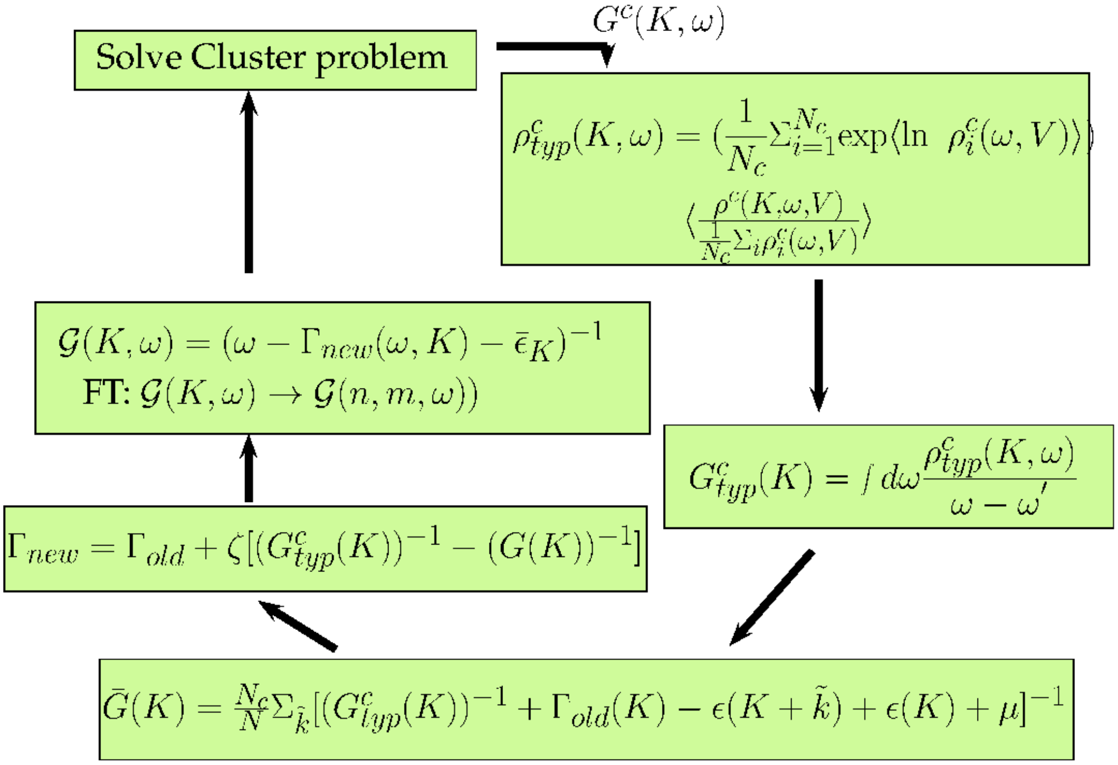

Figure 6.1: **The TMDCA self-consistent framework shown as a flowchart.**

Step 1:

One starts with the usual DCA cluster mapping of a translationally invariant (or disorder averaged to restore translational invariance) lattice as was shown in Fig. 2.6 of Chapter (2). The cluster consists of $N_c = L_c^d$ cells with $\mathbf{K}$ being the cell momentum.

Step 2:

This $\mathbf{K}$-space cluster is then embedded into a self consistently obtained effective medium, given by $\Gamma(\mathbf{K}, \omega)$. While initializing the problem, we shall consider it to be a uniform field, given by Γ_{init}. With this, one can obtain the cluster excluded Green's function, $\mathcal{G}(K, \omega)$, given by,

$$\mathcal{G}(\mathbf{K}, \omega) = \left[\omega^+ - \Gamma_{init} - \bar{\epsilon}_{\mathbf{K}}\right]^{-1}, \tag{6.2}$$

where $\bar{\epsilon}_{\mathbf{K}}$ is the coarse-grained bare dispersion. Hence, spatial correlations up to a range $\xi \lesssim L_c$ are explicitly retained, while the longer length scale physics are described at a mean-field level.

Step 3:

Since the onsite disorder has to be treated in real space, one now performs a Fourier transform of $\mathcal{G}(K, \omega)$ to get the real space cluster excluded Green's function, $\mathcal{G}_{i,j}(\omega) = \sum_{\mathbf{K}} \mathcal{G}(\mathbf{K}, \omega) \exp[iK.(r_i - r_j)]$

Step 4:

- **Incorporation of the effects of electron electron interactions: cluster solver implementation**
  1. The local part of $\mathcal{G}_{i,j}$, namely, $\mathcal{G}_{i,i}$ is considered and an initial guess for the local hybridization, $\Delta_i(\omega) = \omega^+ - 1/\mathcal{G}_{ii}(\omega)$ is constructed.
  2. The i-th lattice site locally driven away from half-filling in presence of quenched random disorder and is characterised with an energy, $\epsilon_i =$

$-U/2 + V_i$, where U is the Coulomb interaction energy at site i. The site local hybridization, $\Delta_i(\omega)$[1] and the local site energy, ϵ_i serves to be the input to the impurity solver. The choice of $-U/2$ is to maintain a global half-filling.

3. With these site local inputs the interacting self energy, $\Sigma_i(\omega)$ of site i is calculated using the local moment approach (LMA) solver.

4. The inverse cluster Green's function,

$$\left[\hat{G}^c(\hat{V}, \omega)\right]^{-1} = \hat{\mathcal{G}}^{-1}(\omega) - \hat{\Sigma}(\omega) - \hat{\epsilon} \tag{6.3}$$

is now calculated. Note that, $\hat{\Sigma}(\omega)$ and $\hat{\epsilon}$ are diagonal matrices and $\hat{\mathcal{G}}(\omega)$ has off-diagonal elements.

5. The new site local hybridization, $\Delta_i(\omega)$ is calculated,

$$\Delta_i(\omega) = \omega^+ - \Sigma_i(\omega) - \epsilon_i - [G^c_{ii}(\hat{V}, \omega)]^{-1} \tag{6.4}$$

6. The convergence is checked on the integrated $\Delta_i(\omega)$ given by $\int \Delta_i(\omega) d\omega$ and steps [2-5] (under Step 4) are repeated with the new $\Delta_i(\omega)$ until all the sites converge.

The above steps described under **Step 4** do resemble the stat-DMFT formulation in the sense that the diagonal Green's functions of a finite ($N_c \times N_c$) real-space cluster are being solved self-consistently within a DMFT like scheme.

Step 5:

The converged $\hat{G}^c(V, \omega)$, from the cluster solver in real space, is Fourier transformed to $\mathbf{K}$ space and the TDoS, $\rho^c_{typ}(\mathbf{K}, \omega)$ is constructed using the following

---

[1] Note that $\Delta_i(\omega)$ is a local hybridization in real space and is therefore different from $\Gamma(\mathbf{K}, \omega)$. In Chapter 5 there was no such distinction because we were working within a local framework.

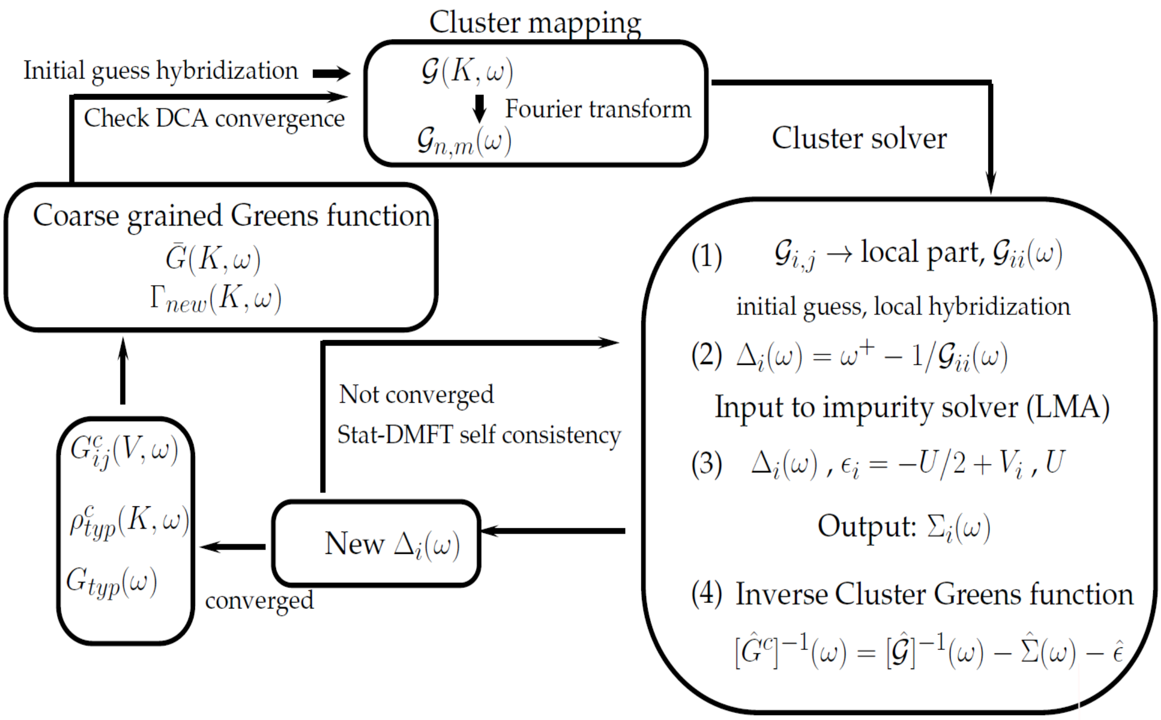

Figure 6.2: **The TMDCA scheme for the disordered interacting problem:** An additional self-consistency loop has to be implemented inside the cluster solver that in this work solves a local interacting problem in real space. This self-consistent scheme is similar to a stat-DMFT like scheme. The interacting site-dependent Green's functions are further embedded into the TMDCA self-consistency.

ansatz:

$$\rho^c_{typ}(\mathbf{K},\omega) = \exp\left(\overbrace{\frac{1}{N_c}\sum_{i=1}^{N_c}\left\langle \ln\ \rho^c_i(\omega,\hat{V})\right\rangle}^{\text{local TDoS}}\right)\underbrace{\left\langle \frac{\rho^c(\mathbf{K},\omega,\hat{V})}{\frac{1}{N_c}\sum_i \rho^c_i(\omega,\hat{V})}\right\rangle}_{\text{nonlocal}} \tag{6.5}$$

Here, the local DoS is given by, $\rho^c_i(\omega,\hat{V}) = -\frac{1}{\pi}\mathrm{Im}G^c_{ii}(\omega,\hat{V})$ and $\rho^c(K,\omega,\hat{V}) = -\frac{1}{\pi}\mathrm{Im}G^c(\mathbf{K},\omega,\hat{V})$. $\rho^c(K,\omega,\hat{V})$ is obtained from a diagonal Fourier transform of the cluster Green's function, $G^c_{ij}(\omega,\hat{V})$. As is evident from Eq.(6.5), the local TDoS is treated with geometrical averaging over disorder, while the non-local part is treated via algebraic averaging. The typical cluster Green's function, $G^c_{typ}(\omega)$ is then obtained via Hilbert transform of $\rho^c_{typ}(\mathbf{K},\omega)$.

$$G_{typ}(\omega) = \int \frac{\rho_{typ}(\omega')d\omega'}{\omega-\omega'}. \tag{6.6}$$

Step 6:

With the calculated $G^c_{typ}(\omega)$ one can now calculate the coarse-grained Green's function, $\bar{G}(K,\omega)$ as,

$$\bar{G}(\mathbf{K},\omega) = \int \frac{N^c_0(\mathbf{K},\epsilon)\ d\epsilon}{\left[G^c_{typ}(\mathbf{K},\omega)\right]^{-1} + \Gamma(\mathbf{K},\omega) - \epsilon + \bar{\epsilon}(\mathbf{K}) + \mu}, \tag{6.7}$$

where, $N^c_0(\mathbf{K},\epsilon)$ represents the bare partial DoS. The new momentum dependent hybridization, $\Gamma(\mathbf{K},\omega)$ can now be calculated as, $\Gamma(\mathbf{K},\omega)_{new} = \Gamma_{old} + \zeta\left[(G^c_{typ})^{-1} - (\bar{G})^{-1}\right]$, where ζ is a mixing factor used to get smooth convergence and is typically set to a value of 0.5. With $\Gamma(\mathbf{K},\omega)_{new}$ we can go back to Step 2. At convergence, $G^c_{typ}(\omega) = \bar{G}(\omega)$ within some tolerance.

6.2.2 Additional numerical details:

We note that the disordered problem being treated here requires one to sample several disorder realizations. Particularly, close to the localization transition we would see that the $P(T_K)$ would become extremely broad spanning several orders of T_K. In order to plot such distribution functions we typically require $N_{disorder} \sim 10^5$, where $N_{disorder}$ is the number of disorder realizations sampled; we also note that such a high $N_{disorder}$ is necessary to ensure that almost all the possible configurations are explored; additionally this ensures better numerical convergence. We therefore had to rely on a parallel implementation, where the parallelization was performed over the disorder realizations. Therefore Step 4 of the above algorithm is parallely solved over *nprocs* number of processors with each processor solving *nruns* number of disorder realizations. Typically, $N_{disorder} = N_c \times nruns \times nprocs$ with $nruns \sim 20$ and $nprocs \sim 200$ for $N_c = 38$, the highest cluster size that could be explored.

However, based on our discussion in Chapter 2 we realized that the symmetry restoration (SR) procedure (Eq. (2.29)), a key ingredient of LMA, could be solved within 5-6 iteration steps, provided one starts with good initial guesses for the local moment. Owing, to the extremely low energy scales involved we rely on an adaptive grid that is most dense in the vicinity of the respective T_K. Since, this is not known *apriori* one has to again rely on a guess for the Kondo scale that would determine the optimal grid. For an efficient numerical implementation we therefore need to make sure that optimal guesses for the local moment and the frequency grid parameters are provided.

Before we begin let us recall from Chapter 2 that the LMA is built around the two broken-symmetry, local moment solutions ($\mu = \pm|\mu_0|$) of an unrestricted Hartree-Fock (UHF) mean field approximation. Beyond mean-field, we include the transverse spin-flip processes through an infinite-order resummation of a specific class of diagrams. Finally, it also requires doing a symmetry-restoration (SR) (Eq. (2.29)) which is equivalent to imposing adiabatic continuity to the non-interacting limit, and is hence crucial for the recovery of Fermi-liquid behaviour and the emergence of a low energy scale. In Chapter 2 (Section 2.2) we discussed that away from particle-symmetry we would also have to satisfy the Luttinger's theorem (Eq. (2.35)) (for a Fermi-liquid) which requires us to find the impurity parameter, e_i; this parameter acts like a *pseudo chemical potential* and explicitly enters the unrestricted Hartree Fock Green's functions via Eqs. (2.17), (2.18). At 1/2-filling, $e_i = 0$ and away from 1/2-filling it to be tuned so that the SR (Eq. (2.29)) and the Luttinger's theorem (Eq. (2.35)) are self-consistently satisfied. As already discussed in Chapter 5 this increases the computation time enormously. For, the current problem where we require to solve an impurity cluster self-consistently, this becomes even more complicated. Hence, we need to come up with a way that may sufficiently reduce the computational effort. We discuss this in the following.

Ideally, U and ϵ_i should be fixed. However, in practice, for saving computation time we keep U and e_i fixed. For details we urge the reader to refer to Chapter 2 (Section 2.2) where, this has been discussed in greater detail. However, we also note that in the current problem, ϵ_i is a random parameter that follows a certain distribution $P(\epsilon_i)$. By necessity, then ϵ_i should be provided as an input but that as explained before enormously increases the computation time. Instead we resort to the following algorithm that helps us stick to the fixed-U, fixed e_i algorithm of the LMA. A part of the following has been discussed in Chapter 5[2].

1. Given an input hybridization, $\Delta_i(\omega)$, the e_i is incremented in certain optimal steps starting from $e_i = 0$ (locally p-h symmetric limit). Depending, on the disorder realization the increments are directed in the regime, towards $-\epsilon_i$ or towards ϵ_i. For each e_i therefore a corresponding LMA output is generated, namely, the LMA local moment, $\tilde{\mu}$, the respective symmetry restored Kondo scale, $w_K^{(i)}$ and the Luttinger's theorem (Eq. 2.35) satisfied ϵ_i's. Thus a database of such initial guess values are created for the input hybridization.
2. Each of the the above steps should continue until the respective ϵ_i's corresponding to the specific disorder realization has been reached. We therefore develop a database of such guesses to be provided to the LMA for the actual calculation.
3. Note that if the ϵ_i is close to 1/2-filling, one would require very less number of steps to achieve SR.
4. The time consumed by each such database calculation also depends on the nature of $\Delta_i(\omega)$. The frequency grid chosen was adaptive depending on the kind of scales generated by the random input hybridization. Typically, we require about 10 (out of N_c) such database calculations.
5. The above steps (1-4) constitutes the first cluster solver self-consistency loop. Now depending on the actual ϵ_i, the corresponding e_i (and other required guesses) would be interpolated from the database calculated, and provided as inputs to the LMA solver. With proper guesses the calculation with the actual parameters is highly efficient.
6. We require about 2-3 such database calculations depending on the disorder strength. The cluster solver convergence (set to 0.01) could be achieved within 5-6 steps.

---

[2] In the TMDCA some added numerical complexities arise due to the non-locality of the input hybridization seen by each impurity site in the cluster.

6.3 Results and Discussion

6.3.1 Distribution of Kondo scales

In strongly correlated electron systems, spin flip scattering of the essentially localized electrons by the itinerant electrons generically leads to large effective masses and low energy scale(s) symptomatic of what is known as the Kondo effect [63]. In correlated impurity models like the single impurity Anderson model [64] or lattice models like the Hubbard model or the periodic Anderson model [12], low energies and/or low temperatures (T's) coherent screening of the local moments is paramount, leading to a Fermi liquid (FL) phase and in presence of such screening, the system may be characterized by a single (Kondo) energy scale, T_K [63, 65, 66]. In the disordered context, an *a priori* intuition restricts the notion of a single energy scale. Here, the lattice translational symmetry is broken and the electrons move in an energetically fluctuating background. The disordered background renormalizes the interaction effects, such that, some sites are weakly hybridized with the rest of the system while some sites are strongly hybridized. Depending on this renormalized hybridization, sites that are weakly hybridized with the local environment tend to form local moments due to reduced charge fluctuations. One then naturally expects not a single screening energy scale but a distribution of Kondo scales, $P(T_K)$. Indeed, this is what has been observed universally in several calculations [20, 29] including ours presented in Chapter 5 (within a local approximation).

However, as been emphasized in Chapter 5 and earlier works [15], the nature of this distribution crucially depends on the level at which non-local fluctuations due to disorder is included in the theory. We first look into the evolution of $P(T_K)$ by gradually increasing the disorder strength, at a fixed $U = 1.6$ and cluster size, $N_c = 38$, sufficiently large enough to capture the essential non-local physics. In the clean limit of Equation (6.1), *i.e.*, in the single band Hubbard model, on a 3-dimensional cubic lattice with full bandwidth, $D = 3$, $U = 1.6$ corresponds to a moderately correlated regime with a bare Kondo scale, $T_K^0 \sim 10^{-2}$ (see Fig. A.1 of Appendix A as predicted by the LMA). As shown in Appendix A, the LMA predicts

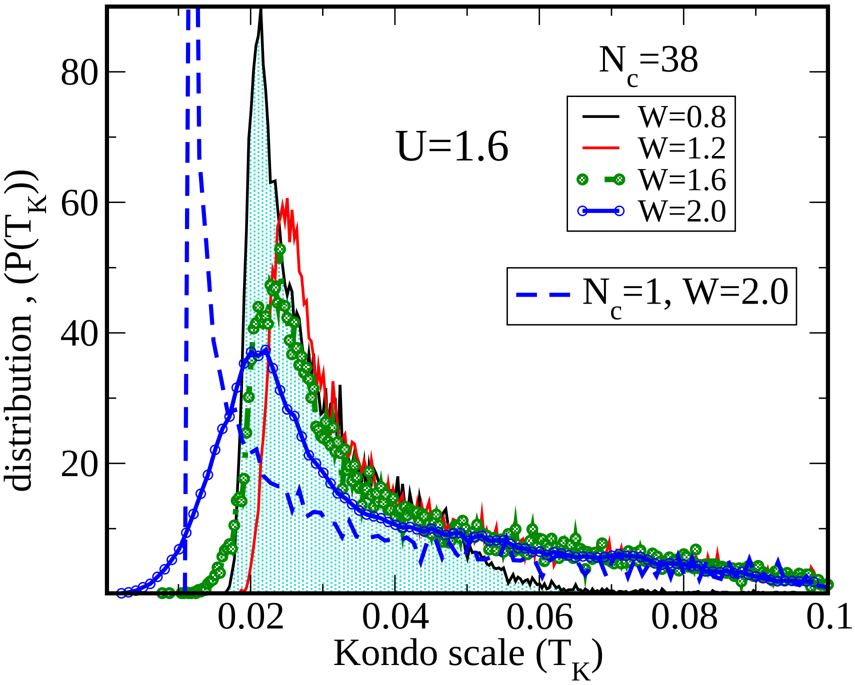

Figure 6.3: **Distribution of Kondo scales for lower disorder strengths:** The evolution of the distribution of Kondo scales, $P(T_K)$, is demonstrated as a function of increasing the disorder strength, shown for, $W = 0.8,\ 1.2,\ 1.6,\ 2.0$ at a fixed interaction strength, $U = 1.6$. A well formed peak at an energy, T_K^{peak} can be identified that initially shifts towards higher energy scales and only beyond a certain disorder strength shifts towards lower energy scales. At $W = 0.8$, a relatively narrow distribution is obtained in contrast to higher W's where $P(T_K)$ starts developing broad tails on the higher T_K side and also tails reaching lower and lower T_K's as W is increased. The TMT-DMFT ($N_c = 1$) limit is also shown as a blue dashed curve.

a Mott transition at a critical interaction strength of $U_c \approx 0.8D$. [3]

In Fig. 6.3, we plot $P(T_K)$ for several W's ranging from $W = 0.8$ to $W = 2.0$. A well defined peak at an energy scale, T_K^{peak} can be identified for these disorder strengths. Such T_K^{peak}'s were also identified within the TMT-DMFT calculations, and were identified as universal low energy scales, within a local theory (see Chapter 5 for details). In the next section we would see if such an inference may be drawn within a non-local theory. In concurrence with the local theory, T_K^{peak} initially increases and

---

[3] This is in good agreement with the numerical renormalization group calculation that predicts a $U_c \approx 1.1D$ [67].

only beyond a certain W does it start decreasing, reflecting upon an initial disorder-screening of U followed by a subsequent co-operative effect where both W and U tend to suppress the effective hybridization resulting in reduced charge fluctuations and thus manifesting as a reduced Kondo scale (see Chapter 5 for details). However, unlike a local theory, inclusion of short-range correlation effects of disorder, leads to the emergence of a low-T_K tail [29] that was completely absent in the TMT-DMFT calculations presented in Chapter 5. In Fig. 6.3 this fact is illustrated as blue-dashed line for $N_c = 1$ and as blue-solid line with open circles for $N_c = 38$ and for a particular disorder strength of $W = 2.0$. For a relatively low disorder, $W = 0.8$, the distribution is narrower, while long tails spanning higher T_K's develop as W is gradually increased. More importantly, systematic inclusion of short range correlation effects makes the system explore such low energy scales that were left untrod within a local theory.

In Fig. 6.4 we look at the effects of even higher disorder strengths [4] for, *e.g.*, $W = 2.5,\ 2.7,\ 2.9,\ 3.1$. In the main panel, $P(T_K)$ is illustrated on a linear scale. We observe that unlike low disorders, the distribution is much broader; the lower T_K tails grow further spanning even lower energies, such that at $W = 2.9$ it merges with the T_K^{peak} resulting in a broad distribution; on further increasing disorder to $W = 3.1$ $P(T_K)$ tends to acquire a finite weight as $T_K \to 0$. At such W's extremely low Kondo scales, $T_K \lesssim 10^{-5}$, emerge to be highly probable. [5]. This behaviour is even more evident in the inset of Fig. 6.4 where we show the same on a log-log scale. Fig. 6.4 is in fact reminiscent of the $P(T_K) \sim T_K^{\alpha-1}$ form obtained in earlier calculations ([29] (for the AHM) and [20] for the charge transfer model), that related the W's with $\alpha < 1$ to EGPs and an associated nFL behaviour of the response functions. In particular, in Ref. [29], where, SB based finite-sized lattice calculations of the AHM on a 2-dimensional square lattice with box disorder distribution were reported, such a behaviour of $P(T_K)$ was shown to occur only in the vicinity of a Mott-insulating

---

[4] in Chapter 5, for $U = 1.6$ the Anderson-Mott metal-insulator transition was found to occur at a critical disorder strength, $W_c = 3.5$ on a 3-dimensional cubic lattice.

[5] Note that we have used an adaptive binning procedure described in Appendix B. As seen in Fig. 6.4, for as W increased the $P(T_K)$ spans Kondo scales of 5-6 orders of magnitude. We have chosen an optimal bin resolution to represent the entire span of T_K's obtained. However in the process, some extremely low $T_K < 10^{-5}$ or the low T_K tails at such low values may not be properly captured in Fig. 6.4. See Fig. B.2 of Appendix B for details.

phase at a fixed $W \lesssim U$. SB calculations within the framework of stat-DMFT, but for the particle-hole asymmetric AHM on the Bethe lattice did provide similar insights in the vicinity of a disorder driven metal insulator transition at a fixed U [60]. Our results, on the particle-hole symmetric AHM on a 3-dimensional cubic lattice show that the observation of broad $P(T_K)$'s with finite weight as $T_K \to 0$, is not just confined to a narrow window close to U dominated Mott-like transitions but can also be realized as a consequence of W driven physics at a moderate U.

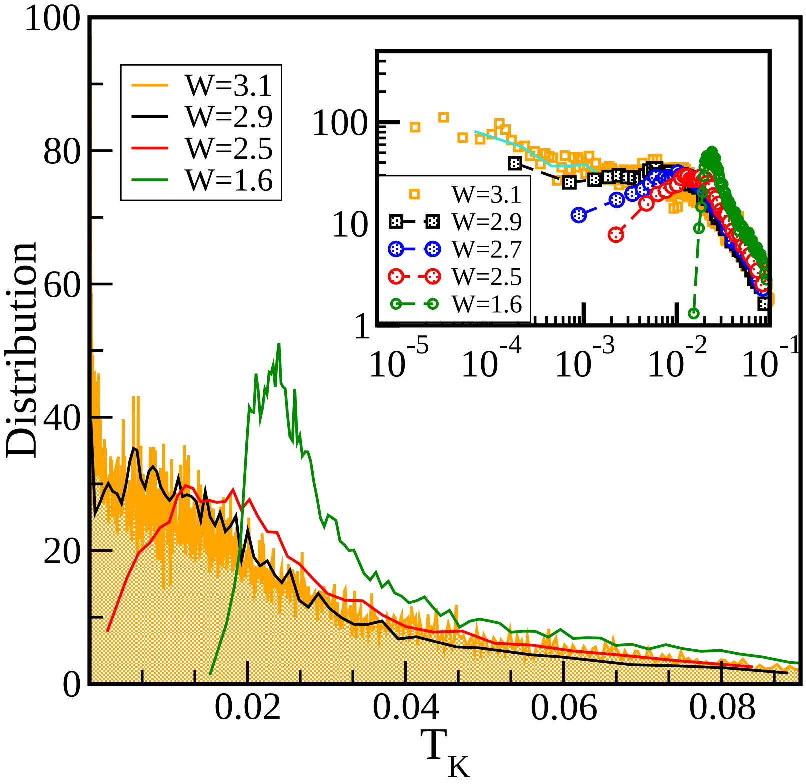

Figure 6.4: **Distribution of Kondo scales:** In presence of disorder, one obtains a distribution of Kondo scales as shown in the main panel on a linear scale for $U = 1.6$, $N_c = 38$ and increasing $W = 1.6,\ 2.5,\ 2.9,\ 3.1$. For low enough disorder, $W = 1.6$, the distribution is marked by the presence of a prominent maximum and a lower T_K tail bounded from below. At intermediate W, $(= 2.5)$, far lower scales emerge indicated by a broader lower T_K tail and a broader maximum of the distribution that gradually merges with the tail. At such high W's, $(= 2.9,\ 3.1)$, distribution tends to acquire a finite weight as $T_K \to 0$. This is depicted the inset where the T_K distribution is plotted on a log-log scale to highlight the evolution of the lower T_K tail. The turquoise line for $W = 3.1$ is a guide to the eye.

Our results on the cubic lattice thus hint at a much generic scenario of nFL physics to be observed unlike the square lattice [29]. In order to have further insights as to whether such a distribution of T_K's indeed correspond to an nFL behaviour, we choose to investigate the single particle scattering dynamics; it is this aspect that we take up in the following section.

6.3.2 Disorder averaged self-energy

In electronic systems, the inverse scattering rate is measured by the imaginary part of the self-energy, $\Sigma(\omega)$. In the current, disorder problem, we explore the disorder averaged self-energy, $\Sigma_{ave}(\omega)$, calculated from the Dyson's equation involving the *arithmetic* average of the cluster Green's function ($G^c(K,\omega)$), (the average being denoted as $\langle G^c(\mathbf{K},\omega)\rangle_{ave}$), that in turn is obtained from the Hilbert transform of $\langle \rho^c(\mathbf{K},\omega,V)\rangle$, where, $\rho^c(K,\omega,V) = -\frac{1}{\pi}\text{Im}G^c(K,\omega,V)$. The disorder averaged local self-energy is then obtained as following,

$$\Sigma_{ave}(K,\omega) = \mathcal{G}^{-1}(K,\omega) - \langle G^c(K,\omega)\rangle^{-1}_{ave} \tag{6.8}$$

$$\Sigma_{ave}(\omega, \mathbf{R}=0) = \sum_{\mathbf{K}} \Sigma_{ave}(\mathbf{K},\omega). \tag{6.9}$$

In Fig. 6.5 (left panel) we plot $\text{Im}\Sigma_{ave}(\mathbf{R}=\mathbf{0};\omega)$ as a function of increasing disorder strengths. The non-zero, $\omega = 0$, contribution (a_0) in the self-energy represents the static elastic impurity scattering, while the $|\omega| \to 0$ has both *inelastic* and elastic contributions due to the complex interplay of interactions and disorder in the system. Also, physically consistent is the observation that at sufficiently weak disorder, *e.g.* $W = 0.8$, a_0 is sufficiently small such that we can expect a Drude like expression and an arbitrarily large d.c. conductivity. This picture however breaks down as one increases W. Furthermore, beyond a certain disorder strength, $W = 2.25$, *even* on a linear scale, the lineshape develops a clear cusp in the immediate vicinity of the Fermi energy, showing clear indications of a deviation from the FL-ω^2 behaviour and acquiring a power law energy dependence, $-\text{Im}\Sigma_{ave}(\mathbf{R}=0;\omega) \sim a_0 + |\omega|^{\alpha(W)}$, where, the exponent, α, depends on the disorder strength.

In Fig. 6.5 (right panel) we therefore analyse the low energy functional depen-

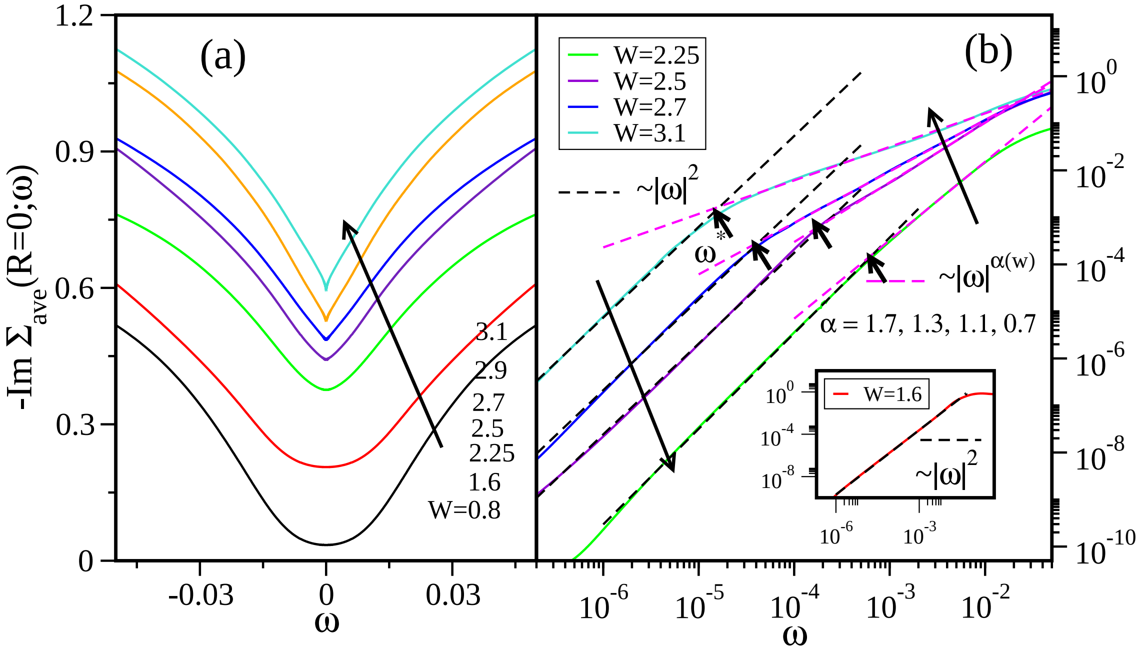

Figure 6.5: **Disorder averaged electronic self energy:** (a) The low energy part of the average self-energy, -Im$\Sigma_{ave}(\omega)$ is shown for $U = 1.6$, $N_c = 38$ and various W's as indicated. A clear crossover from a Fermi liquid, $\sim \omega^2$ to non-Fermi liquid $\sim |\omega|^\alpha$ is observed. On a linear scale this features as the formation of a cusp at low energies, indicative of a non-universal power law energy dependence. (b) (Main panel) Some representative data ($W = 2.25,\ 2.5,\ 2.7,\ 3.1$) of (a) are plotted on a log-log scale to deduce the power, α as a function of W and also deduce the crossover frequency, ω^* (marked by an arrow in the figure), beyond which -Im$\Sigma_{ave}(\omega)$ evolves from $\sim \omega^2$ to $|\omega|^{\alpha(W)}$, where $\alpha(W) = 1.7,\ 1.3,\ 1.1,\ 0.7$ for $W = 2.25,\ 2.5,\ 2.7,\ 3.1$ respectively, as shown in main panel. (Note that the data corresponding to $W = 2.25$ is offset by a factor of 5 on the $y-$axis for clarity.) (b) (Inset) A similar analysis as in (b) (main panel) is illustrated for a relatively lower W, namely, $W = 1.6$. Here, the crossover occurs at a sufficiently higher energy identified as the peak of the respective distribution presented in Fig. 6.3.

dence of the $-\mathrm{Im}\Sigma_{ave}(\omega)$; one can clearly identify, a crossover energy scale, ω^*, that marks the deviation from FL dynamics. As shown in Fig. 6.5 (right panel) the systems exhibit FL dynamics in the regime $|\omega| < \omega^*$ for any W; however, while for low disorder, $W \lesssim 2.2$ $(U = 1.6)$, $\omega^* \sim T_K^{peak}$, for higher disorder, as the cusp becomes more and more pronounced, and the associated $P(T_K)$ becomes broad, we observe that the ω^* is determined by extremely rare events. (In the current representation one may not be able to exactly identify it from the low-T_K tail of the associated

$P(T_K)$, owing to its finite resolution;) for example, for $W = 2.7$, ω^* obtained from the analysis of the ImΣ_{ave} as shown in Fig. 6.5 (right panel) is 3×10^{-5}; this is clearly not visible in the inset of Fig. 6.4 (inset, blue dashed-line with circles), but may be identified to be originating from very rare disorder configurations. This phenomenon is therefore reminiscent of the EGP scenario discussed earlier [29]. Note that for $W = 3.1$, for which, $\alpha \approx 0.8$, $\omega^* = 3 \times 10^{-6}$ and for such disorder strengths, the $P(T_K)$ tends to acquire a finite intercept ($P(T_K = 0)$ as $T_K \to 0$.

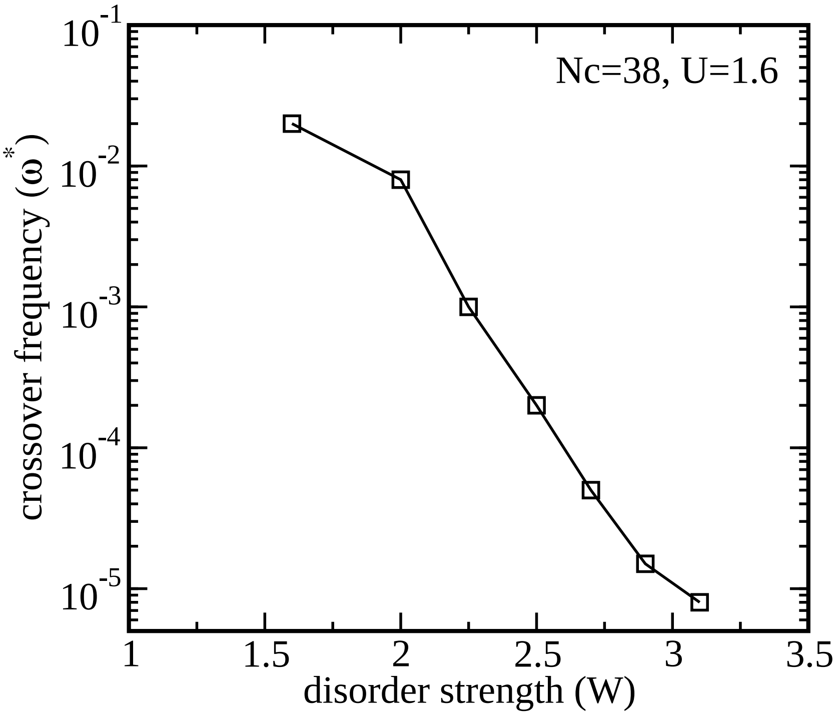

Figure 6.6: **Energy scale for disorder induced FL to nFL crossover:** The ω^* extracted from Fig. 6.5 (right panel) is plotted as a function of W establishing the same as a vanishing energy scale for a disorder induced FL to nFL crossover.

In order to highlight these aspects, we plot ω^* as a function of W in Fig. 6.6. In the local theory presented in Chapter 5, T_K^{peak} emerged as a characteristic energy scale indicating the crossover from a coherent universal Fermi liquid to an incoherent universal regime. While we did not perform similar scaling analyses of the single-particle quantities as in Chapter 5, in the current non-local theory, we do identify the role of ω^*. As shown in Fig. 6.6, ω^* emerges as a *unique* vanishing energy scale indicating the emergence of a disorder induced non-Fermi liquid at a critical $W = W_c$. Fig. 6.6 thus serves as a (low-) energy boundary that separates the physics of the Mott-Anderson quantum critical point from the conventional Fermi-liquid.

We now explore the manifestations of the above in the low energy form of the single particle density of states.

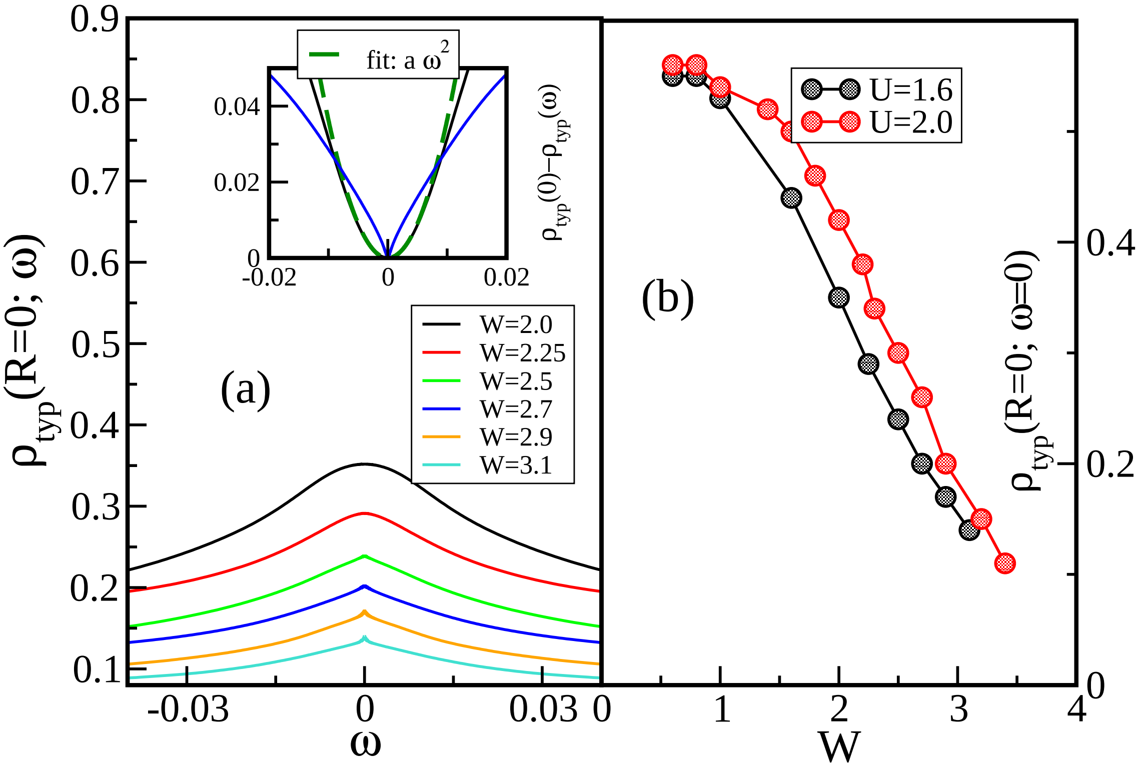

Figure 6.7: **Low energy features of the TDoS:** (a) (Main panel) Development of a cusp in the low energy spectral lineshape of the TDoS as W is increased, shown for $U = 1.6$. (Inset) Two representative data for $W = 2.0$ and $W = 2.7$ are plotted with the $\rho_{typ}(\mathbf{R};0)$ subtracted. The low energy form of $\rho_{typ}(\mathbf{R};0) - \rho_{typ}(\mathbf{R};\omega)$ for $W = 2.0$ fits well to a form $\sim \omega^2$ as dictated by the FL theory where as for $W = 2.7$ clear deviation from conventional lineshape is evident. However, note that at the lowest energy scales a FL form should still hold because the self-energy is still a FL at the lowest energy scales. (b) The decay of the TDoS(0) as a function of W shown for $U = 1.6$ and $U = 2.0$.

6.3.3 Density of states

As a manifestation of the nFL scattering dynamics, the spectral lineshape in the vicinity of the Fermi-energy develops a cusp that becomes more pronounced as $\omega^* \to 0$ and one approaches towards the Anderson-Mott metal-insulator transition. This evolution of the spectral lineshape is depicted in Fig. 6.7(a) where we present the $\rho_{typ}(\omega)$ for $U = 1.6$ and $N_c = 38$; it should be noted that although the $\rho_{arith}(\omega) = \rho_{DCA}$ is not an *order parameter* for the disorder driven metal-insulator transition, but behaves similarly in terms of spectral lineshape. In Fig. 6.7(b) we plot $\rho_{typ}(\omega = 0)$ and recover the conventional physics, namely, with increasing W, $\rho_{typ}(\omega = 0)$ tends to vanish at a critical, W_c. It would be now interesting to see if the W_c obtained from the vanishing $\rho_{typ}(\omega = 0)$ and the W_c obtained from Fig. 6.6 are equal (within some accuracy). However, this is beyond the scope of the current implementation because as the system nears such a transition, it explores configurations resulting in scales even lower than 10^{-6} thus rendering the numerics impossible within the available computational resources.

6.3.4 Importance of typical medium and non-local correlations

Finally, in this part we highlight the importance of considering both a correct *disorder averaging* procedure and inclusion of short range correlation effects of disorder. In Fig. 6.8(a) we compare the $P(T_K)$ obtained from the TMDCA and the DCA scheme, for the parameter sets $U = 1.6$, $W = 2.9$ (main panel) and $U = 1.6$, $W = 1.2$ (inset). Note that in the DCA scheme [68], the average DoS at each cluster momentum $\mathbf{K}$ is defined as, $\rho^c_{avg}(\mathbf{K}, \omega) = \langle \rho^c(\mathbf{K}, \omega) \rangle = -\frac{1}{\pi} \langle \mathrm{Im}\ G^c(\mathbf{K}, \omega) \rangle$. In the main panel, we notice that while the DCA scheme shown as red solid line with circles) do capture the low-T_K tails essential for observing the emergence of an FL to nFL crossover energy scale in the scattering dynamics, it underestimates the *typical* nature of the disorder driven physics in comparison to the TMDCA scheme (shown as black dashed line with squares). Contrary to this, in the low disorder regime (shown in the inset of Fig. 6.8, both the TMDCA (black solid line with

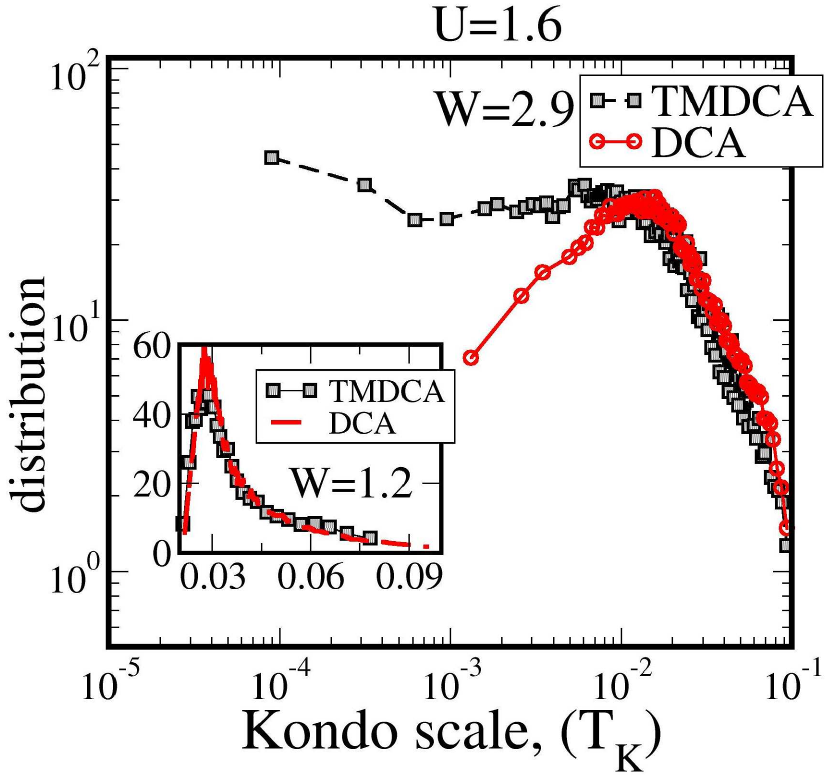

Figure 6.8: **Comparison of $P(T_K)$ obtained from TMDCA and DCA:** This figure illustrates the *dual* importance of employing the correct disorder averaging scheme (TMDCA) and including spatial fluctuations of disorder. (Main) $P(T_K)$ obtained by doing an arithmetic averaging of the DoS, *i.e.* the DCA scheme (red line with open circles) for $W = 2.9$ compared to that obtained by employing the typical medium ansatz (black dashed line with open squares) as in Eq. (6.5) showing dramatic difference in the behaviour of the low-T_K regime. (Inset) The same comparison shown for $W = 1.2$, where the two are are in good agreement. The $U = 1.6$ and $N_c = 38$.

squares) and the DCA scheme (red dashed line) are in excellent agreement both quantitatively and qualitatively. Fig. 6.8 demonstrates the necessity for capturing the mixing of the localized and extended states. This comparison highlights the true success of the current cluster theory for disordered-interacting systems, namely the TMDCA. It shows that with certain further developments (in the direction of multi-orbital interacting systems etc.) it can potentially emerge into a consistent theoretical framework for interacting disordered systems that may be used for a direct comparison of theory and experiment.

6.4 Summary and Conclusions

In this chapter, we developed a cluster theory for looking into short-range correlation effects of quenched disorder in a strongly interacting electronic system. We chose the AHM as a representative for describing the interplay of disorder and interactions. Developing on the TMDCA framework [25], the many-body electron problem was embedded as a *local cluster solver* that was solved self-consistently in real-space to obtain a local hybridization described by site-local effects of electron interactions with non-local effects of random energetic disorder incorporated. With this framework, we subsequently explored the effective Kondo screening physics in the simultaneous presence of disorder and interactions. By analysing the imaginary part of the disorder-averaged self-energy, we predicted the emergence of a unique, disorder dependent FL to nFL crossover energy scale, ω^*. The nFL nature was identified as an $\sim |\omega|^{\alpha(W)}$ dependence of -Im$\Sigma_{ave}(\omega)$ where, $\alpha(W) = 2$ at low disorder describing conventional coherent to incoherent crossover; as the disorder was increased $\alpha(W)$ acquired a value less than 1 and a vanishing low energy scale, ω^* was identified. At moderate disorder strengths, ω^* represented scales lying along the low T_K tails of the respective $P(T_K)$. At higher disorder strengths, these low T_K tails in the distribution of Kondo scales merged with the broad maximum of the distribution, leading to a $P(T_K)$ that tended to acquire a finite weight as $T_K \to 0$. At such disorder strengths, extremely low Kondo scales, $T_K \sim 10^{-6}$, became more and more probable. In this regime ω^* was found to be of the same order as the *most probable* value of the Kondo scale. The identification of a single low energy scale, in the form of ω^* thus helped us establish an energy boundary describing the dynamics of the Mott-Anderson quantum critical point as a function of disorder (or interactions). This boundary separates the physics of the quantum-critical point from the conventional Fermi liquid. Moreover, our results also reflect on a generic scenario of *disorder induced* nFL scattering dynamics that is not confined just to a narrow window close to U dominated Mott-like transitions but can also be realized as a consequence of W driven physics at a moderate U.

Finally, we also highlight the non-self averaging nature of the physics due to disorder and interactions as disorder is increased at a fixed U; more precisely, we emphasize that both the *local* and *non-local* dynamical effects of disorder should be properly incorporated in the disorder averaging.

Bibliography

[1] B. Kramer, A. MacKinnon, T. Ohtsuki, and K. Slevin, International Journal of Modern Physics B **24**, 1841 (2010).

[2] A. MacKinnon and B. Kramer, Zeitschrift für Physik B Condensed Matter **53**, 1 (1983).

[3] P. Markoš, arXiv preprint cond-mat/0609580 (2006).

[4] R. Silver and H. Röder, International Journal of Modern Physics C **5**, 735 (1994).

[5] R. Silver and H. Röder, Phys. Rev. E **56**, 4822 (1997).

[6] A. Weiße, G. Wellein, A. Alvermann, and H. Fehske, Reviews of modern physics **78**, 275 (2006).

[7] G. Schubert, J. Schleede, K. Byczuk, H. Fehske, and D. Vollhardt, Phys. Rev. B **81**, 155106 (2010).

[8] G. Schubert, A. Weiße, and H. Fehske, Phys. Rev. B **71**, 045126 (2005).

[9] E. Domany and S. Sarker, Phys. Rev. B **20**, 4726 (1979).

[10] L. Root and J. Skinner, Phys. Rev. B **33**, 7738 (1986).

[11] V. Dobrosavljević, A. A. Pastor, and B. K. Nikolić, Europhysics Letters **62**, 76 (2003).

[12] A. Georges, G. Kotliar, W. Krauth, and M. J. Rozenberg, Rev. Mod. Phys. **68**, 13 (1996).

[13] K. Byczuk, W. Hofstetter, and D. Vollhardt, Phys. Rev. Lett. **94**, 056404 (2005).

[14] M. C. O. Aguiar, V. Dobrosavljević, E. Abrahams, and G. Kotliar, Phys. Rev. B **73**, 115117 (2006).

[15] M. C. O. Aguiar, V. Dobrosavljević, E. Abrahams, and G. Kotliar, Phys. Rev. Lett. **102**, 156402 (2009).

[16] E. Miranda and V. Dobrosavljevic, ArXiv e-prints (2011), `1112.6184`.

[17] K. Byczuk, W. Hofstetter, U. Yu, and D. Vollhardt, The European Physical Journal Special Topics **180**, 135 (2009), ISSN 1951-6355.

[18] V. Dobrosavljević and G. Kotliar, Philosophical Transactions of the Royal Society of London A: Mathematical, Physical and Engineering Sciences **356**, 57 (1998).

[19] E. Abrahams, *Fifty Years of Anderson Localization* (Singapore: World Scientific, 2010).

[20] M. C. O. Aguiar and V. Dobrosavljević, Phys. Rev. Lett. **110**, 066401 (2013).

[21] D. Semmler, K. Byczuk, and W. Hofstetter, Phys. Rev. B **84**, 115113 (2011).

[22] A. Gonis, *Green functions for ordered and disordered systems* (Elsevier Science Ltd, 1992).

[23] S. Chiesa, P. B. Chakraborty, W. E. Pickett, and R. T. Scalettar, Phys.Rev.Lett **101**, 086401 (2008).

[24] P. Denteneer, R. Scalettar, and N. Trivedi, Phys.Rev.Lett **83**, 4610 (1999).

[25] C. E. Ekuma, H. Terletska, K.-M. Tam, Z.-Y. Meng, J. Moreno, and M. Jarrell, Phys. Rev. B **89**, 081107 (2014).

[26] H. Terletska, C. Ekuma, C. Moore, K.-M. Tam, J. Moreno, and M. Jarrell, Phys. Rev. B **90**, 094208 (2014).

[27] Y. Zhang, H. Terletska, C. Moore, C. Ekuma, K.-M. Tam, T. Berlijn, W. Ku, J. Moreno, and M. Jarrell, Phys. Rev. B **92**, 205111 (2015).

[28] E. Miranda and V. Dobrosavljević, Phys. Rev. Lett. **86**, 264 (2001).

[29] E. C. Andrade, E. Miranda, and V. Dobrosavljević, Phys. Rev. Lett. **102**, 206403 (2009).

[30] P. Coleman, Phys. Rev. B **29**, 3035 (1984).

[31] S. E. Barnes, Journal of Physics F: Metal Physics **6**, 1375 (1976), URL `http://stacks.iop.org/0305-4608/6/i=7/a=018`.

[32] J. Kroha, P. Hirschfeld, K. Muttalib, and P. Wölfle, Solid State Communications **83**, 1003 (1992).

[33] E. Miranda and V. Dobrosavljević, Reports on Progress in Physics **68**, 2337 (2005).

[34] A. Punnoose and A. M. Finkel'stein, Science **310**, 289 (2005).

[35] G. Stewart, Reviews of modern Physics **73**, 797 (2001).

[36] Z. Qu, J. Peng, T. Liu, D. Fobes, V. Dobrosavljević, L. Spinu, and Z. Mao, Phys. Rev. B **86**, 014434 (2012).

[37] B. I. Shklovskii and A. L. Efros, *Electronic properties of doped semiconductors*, vol. 45 (Springer Science & Business Media, 2013).

[38] H. von Löhneysen, Journal of Physics: Condensed Matter **8**, 9689 (1996).

[39] F. Grosche, P. Agarwal, S. Julian, N. Wilson, R. Haselwimmer, S. Lister, N. Mathur, F. Carter, S. Saxena, and G. Lonzarich, Journal of Physics: Condensed Matter **12**, L533 (2000).

[40] T. Moriya, *Spin fluctuations in itinerant electron magnetism*, vol. 56 (Springer Science & Business Media, 2012).

[41] M. A. Continentino, G. M. Japiassu, and A. Troper, Phys. Rev. B **39**, 9734 (1989).

[42] A. Millis, Phys. Rev. B **48**, 7183 (1993).

[43] P. Gegenwart, Q. Si, and F. Steglich, nature physics **4**, 186 (2008).

[44] O. Bernal, D. MacLaughlin, H. Lukefahr, and B. Andraka, Phys.Rev.Lett **75**, 2023 (1995).

[45] C. Booth, D. MacLaughlin, R. Heffner, R. Chau, M. Maple, and G. Kwei, Phys.Rev.Lett **81**, 3960 (1998).

[46] N. Büttgen, W. Trinkl, J.-E. Weber, J. Hemberger, A. Loidl, and S. Kehrein, Phys. Rev. B **62**, 11545 (2000).

[47] D. MacLaughlin, O. Bernal, R. Heffner, G. Nieuwenhuys, M. Rose, J. Sonier, B. Andraka, R. Chau, and M. Maple, Phys.Rev.Lett **87**, 066402 (2001).

[48] C. Booth, E.-W. Scheidt, U. Killer, A. Weber, and S. Kehrein, Phys. Rev. B **66**, 140402 (2002).

[49] A. Chattopadhyay and M. Jarrell, Phys. Rev. B **56**, R2920 (1997).

[50] A. Chattopadhyay, M. Jarrell, H. Krishnamurthy, H. Ng, J. Sarrao, and Z. Fisk, arXiv preprint cond-mat/9805127 (1998).

[51] E. Miranda, V. Dobrosavljevic, and G. Kotliar, Journal of Physics: Condensed Matter **8**, 9871 (1996).

[52] L. Degiorgi and H. Ott, Journal of Physics: Condensed Matter **8**, 9901 (1996).

[53] D. Tanasković, E. Miranda, and V. Dobrosavljević, Phys. Rev. B **70**, 205108 (2004).

[54] M. Aguiar, E. Miranda, and V. Dobrosavljević, Phys. Rev. B **68**, 125104 (2003).

[55] M. Guo, R. Bhatt, and D. A. Huse, Phys. Rev. B **54**, 3336 (1996).

[56] H. Rieger and A. Young, Phys. Rev. B **54**, 3328 (1996).

[57] A. H. Castro Neto, G. Castilla, and B. A. Jones, Phys. Rev. Lett. **81**, 3531 (1998), URL `http://link.aps.org/doi/10.1103/PhysRevLett.81.3531`.

[58] N. Read and D. Newns, Journal of Physics C: Solid State Physics **16**, L1055 (1983).

[59] P. Coleman, Phys. Rev. B **35**, 5072 (1987).

[60] V. Dobrosavljević and G. Kotliar, Phys. Rev. Lett. **78**, 3943 (1997).

[61] M. Hettler, A. Tahvildar-Zadeh, M. Jarrell, T. Pruschke, and H. Krishnamurthy, Phys. Rev. B **58**, R7475 (1998).

[62] T. Maier, M. Jarrell, T. Pruschke, and M. H. Hettler, Reviews of Modern Physics **77**, 1027 (2005).

[63] A. C. Hewson, *The Kondo problem to heavy fermions*, vol. 2 (Cambridge university press, 1997).

[64] P. W. Anderson, Phys. Rev. **124**, 41 (1961).

[65] N. S. Vidhyadhiraja and D. E. Logan, European Physical Journal B **39**, 313 (2004).

[66] D. E. Logan and M. R. Galpin, Journal of Physics: Condensed Matter **28**, 025601 (2016).

[67] J. Bonča, T. Pruschke, et al., Phys. Rev. B **80**, 245112 (2009).

[68] C. E. Ekuma, H. Terletska, Z. Y. Meng, J. Moreno, M. Jarrell, S. Mahmoudian, and V. Dobrosavljević, Journal of Physics: Condensed Matter **26**, 274209 (2014).

Chapter 7

Summary and Future Outlook

In this chapter, we summarize the main results presented in this thesis. Additionally we also mention some future directions that this thesis open up. In our study we have focused on *emergent* physics in (1) spatially inhomogeneous geometries where translational invariance is broken in one direction and (2) energetically disordered electronic systems where translational invariance is broken in all directions.

In the study of the proximity effects of *interfacial* disorder in **Chapter 3**, we investigated the effect of substitutional disorder on the dynamical spectrum of layered f-electron systems. In particular, we looked at the interface of a single Kondo hole substituted Kondo insulator with several clean layers that could be interacting or non-interacting. The first step involved in this work was the proposal and implementation of a self-consistent scheme that could be used to explore some aspects of the considered geometries. We combined simple analytical expressions with full numerical calculations to obtain self-consistent many body solutions for the considered systems.

We observed that the presence of disorder induced spectral weight transfer over all energy scales, from the high energy Hubbard bands to the low energy Kondo scaling regime. The disorder-induced spectral weight transfer, used here for quantification of the proximity effect, decayed algebraically with distance from the boundary layer. Further, we showed that the spectral weight transfer was highly dependent on the frequency range considered as well as the presence of interactions in the clean adjacent layers. The changes in the low frequency spectrum were very similar when the adjacent layers were either metallic or Kondo insulating, and hence were independent of interactions. In stark contrast, a distinct picture emerged for the spectral weight transfers across large energy scales. The spectral weight transfer over all energy scales was much higher when the adjacent layers were non-interacting as compared to when they were strongly interacting Kondo insulators. Thus, over all scales, interactions were found to screen the disorder effects significantly.

Some of the open directions may involve the investigation of transport across such disordered interfaces within the above framework. Additionally, the proposed self-consistent scheme may also be utilized for other model scenarios like disordered interfaces of Hubbard layers. An extension to superlattice geometries should lead to a pronounced proximity effect of substitutional disorder. The above study may well be extended to asymmetric situations and analyses similar to that reported in PRB **88**, 195120 (2013) may be performed. Here, even at the mean field level, we expect to observe a Fermi-liquid to non-Fermi liquid crossover by increasing the ratio of the clean heavy-fermion layers to the disordered interfaces.

In **Chapter 4** we looked into a specific case of the (more general) model explored in **Chapter 3**, namely a bilayer heterojunction of a Kondo insulator and a non-interacting metal. The focus in this work was the investigation of an *unconventional* Mott metal insulator transition in such a model, that to the best of our knowledge has not been explored before. Employing the framework of dynamical mean field theory (DMFT), we indeed predicted such an *emergent* scenario where the otherwise localized f-electrons in the Kondo insulator layer become itinerant due to an implicit coupling with the metallic layer. Based on the behaviour of low energy scales, namely the Kondo scale in the Fermi liquid phase and the Mott gap in the Mott insulator phase and the spectral features, we demonstrated the existence of a *surface* of continuous Mott transitions in this model as a function of the interlayer coupling or the Hubbard-type interaction or the conduction and f orbital hybridization.

One important open direction is to explore the finite temperature properties of the system, especially, investigations such as finite temperature critical scaling of the transport and thermodynamic properties of the model. We are currently investigating the effects of non-local dynamical correlations by going beyond DMFT and through determinant quantum Monte Carlo simulations of finite systems.

In **Chapters 5** and **6** we explored energetically disordered systems within the paradigm of the Anderson-Hubbard model. In **Chapter 5** we employ a non-perturbative but local framework for treating the electron-electron interactions and the disorder. In particular, we rely on the use of the DMFT with a *typical* host, also known as the TMT-DMFT framework. Our primary focus was on the implementation of the local moment approach within this mean-field framework for a 3-dimensional cubic density of states and compare the results obtained with known results on the Bethe lattice density of states. Additionally, we also explored the impurity scattering rate and spectral dynamics to obtain universal scaling regimes close to the metal insulator transition boundaries. The universal scale in this regard was predicted to be the most probable value of the Kondo scale obtained from the respective distribution of the Kondo scales.

In **Chapter 6** we developed a *statistical-DMFT* type cluster solver for incorporating electron-electron interactions within the typical medium dynamical cluster approximation framework. Based on our analysis of the distribution of Kondo scales and the disorder averaged self-energy, we established the existence of a unique low energy scale, ω^*, below which the system could be characterized as a disordered Fermi liquid, but beyond it, the scattering dynamics followed an, $|\omega|^\alpha$ dependence where the exponent α depended on the disorder strength. The scale, ω^* tended to vanish continuously as the Mott-Anderson metal insulator transition was approached, thus acting like a critical boundary that separates the physics of the disorder induced non-Fermi liquid from a conventional Fermi liquid.

An important direction that **Chapters 5** and **6** open up is their extensions to layered geometries. Should we then be able to look at more realistic scenarios of disordered interfaces? Could we then look at a Fermi liquid to non-Fermi liquid crossover in the electron dynamics as the number of layers are tuned? These would require the combination of the concepts/methods developed in this thesis and these are some of the directions left for future work.

Appendices

Appendix A

Supporting information for results pertaining to Chapter 5

This appendix consists of additional information in regard to the Chapter titled “A local theory for the Anderson-Mott localization”. We begin with the clean single band Hubbard model (SBHM) (disorder, $W = 0$) on a 3-dimensional cubic lattice, solved within the framework of dynamical mean field theory (DMFT) using the local moment approach (LMA).

A.1 U_{c2} for the 3-dimensional cubic lattice

As already mentioned in Chapter 2, within LMA, the low energy scale, T_K, is identified by the position of the peak of the transverse spin-polarization propagator. This scale is known to be proportional to the Kondo scale. The Kondo scale, also identified as the Fermi liquid coherence scale, is known to vanish when the Fermi liquid (FL) breaks down. For the SBHM, this breakdown is the onset of a Mott insulating phase. Approaching from the FL, the critical interaction strength where, $T_K = 0$, is denoted as U_{c2}. Similarly, approaching from the Mott insulating side, the critical interaction strength, where the Mott gap, $\Delta_g = 0$ is denoted as U_{c1}. In this appendix we derive U_{c2} for the 3-dimensional cubic lattice with full bandwidth,

$D = 3$. We employ the LMA within the framework of DMFT for solving the SBHM.

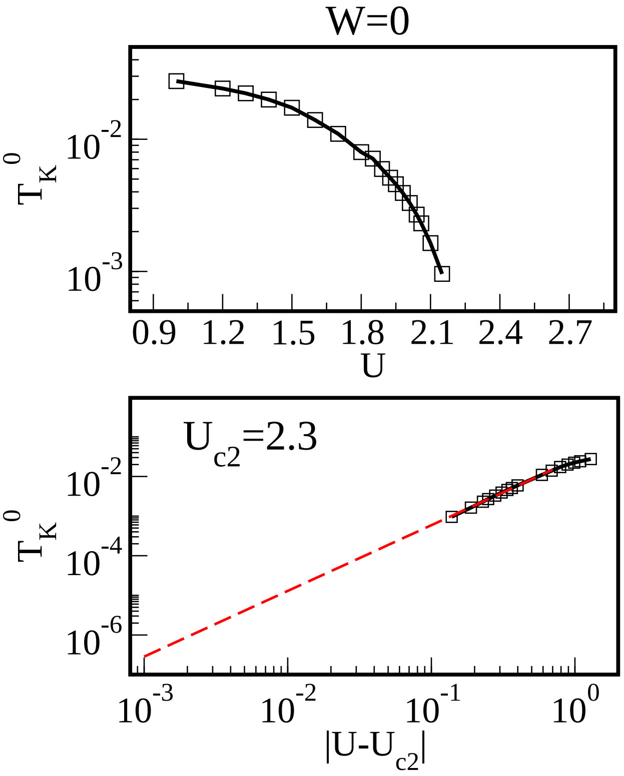

Figure A.1: Approaching the Mott metal-insulator transition from the FL side on a 3-dimensional cubic lattice. (Top panel) The Kondo scale, T_K^0, (at zero disorder) in a SBHM is shown to vanish continuously at a critical interaction strength, $U = U_{c2}$; (bottom panel) the T_K^0 is extrapolated to zero; the data is plotted on a log-log scale and a guess value is initially subtracted. Subsequently, we add/subtract a small number ~ 0.005 until a visually inspected straight line is obtained.

In Fig. A.1 (top panel) we show the behaviour of T_K as a function of increasing U; since this represents the $W = 0$ limit of the Anderson-Hubbard model, we denote T_K as T_K^0 . Within LMA we obtain $U_{c2} \approx 2.3 \approx 0.8D$.

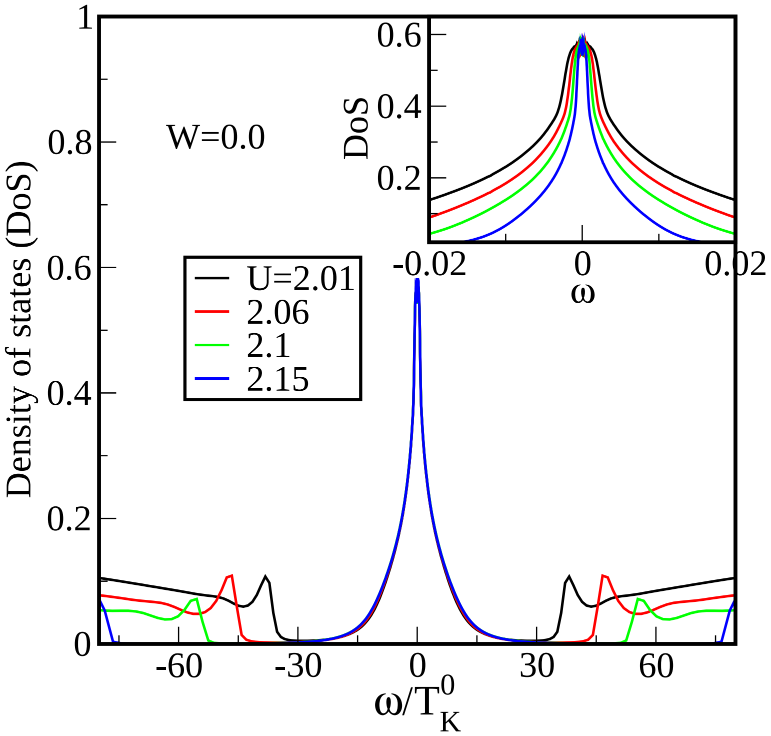

Figure A.2: (Main) Scaling collapse of the spectral density of states close to the U driven metal-insulator transition broundary at $W = 0$. The frequency, ω is rescaled by the respective Kondo scale, T_K^0 a quantity demonstrated in Fig. A.1. (Inset) The same plotted on a bare frequency scale.

A.2 Universal spectral scaling in the interacting disordered lattice scenario

We begin this section by an illustration of the universal scaling spectra of the SBHM close to the Mott transition. This is shown in Fig. A.2 where the main panel represents the spectral density plotted as a function of frequency, ω rescaled by T_K^0. As evident, T_K^0 indeed serves to be *the* underlying lattice coherence scale until energies $\gtrsim 30T_K^0$; also note that the scaling collapse persists for higher and higher energies as one approaches the transition. The inset, demonstrates the spectra for the same U's as in the main panel but on a bare frequency scale. Also, note the prominent preformed gap, in the middle of which the Kondo resonance resides. This serves to be a spectral signature of a first-order Mott transition.

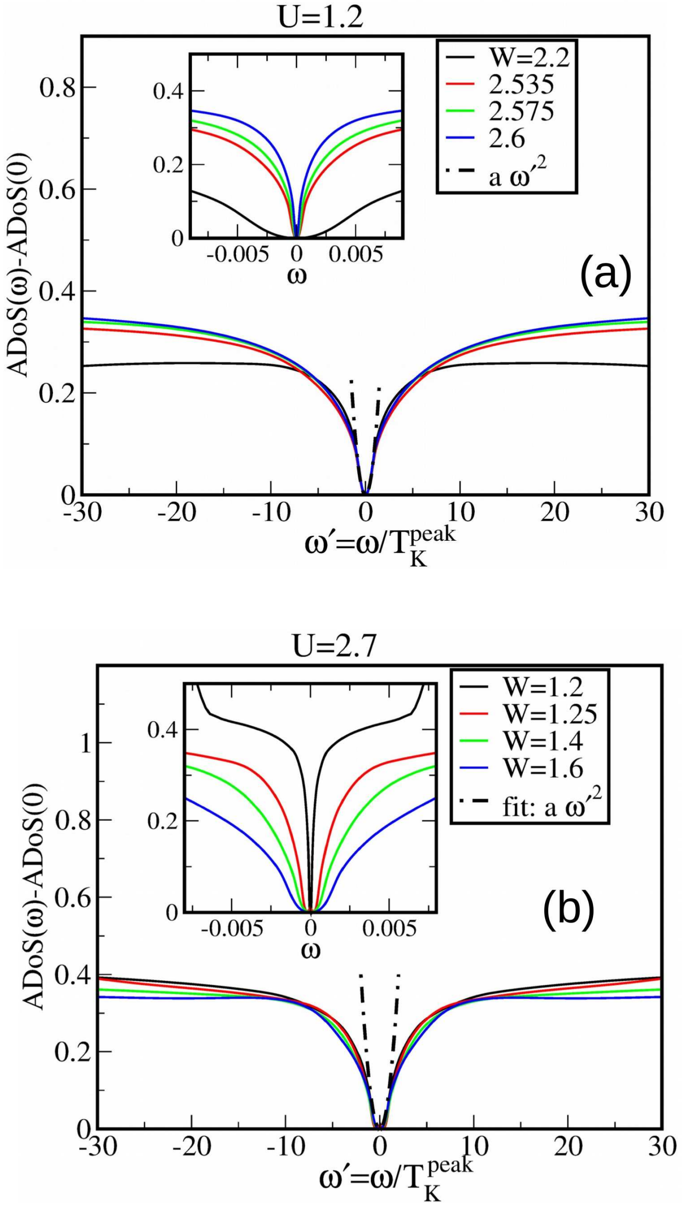

Figure A.3: (a) (Main) Scaling collapse of the arithmetically averaged spectral density of states close to the W driven Anderson-Mott metal-insulator transition boundary at a fixed $U = 1.2$. The frequency, ω is rescaled by the respective T_K^{peak} that corresponds to the peak of the distribution of Kondo scales, a quantity explored in Chapter 5. (Inset) The same plotted on a bare frequency scale. (b) Scaling collapse of the arithmetically averaged spectral density of states close to the W driven Mott metal-insulator transition boundary at a fixed $U = 2.7$. (Inset) The same plotted on a bare frequency scale.

We shall now look at the spectral scaling with respect to T_K^{peak} in presence of a non-zero W. We use the arithmetically averaged density of states (ADoS) for demonstrating this. We illustrate this in Fig. A.3 where we demonstrate spectral scaling with respect to T_K^{peak} for $U = 1.2$ and $U = 2.7$. Note that the respective scaling of the imaginary part of the disorder averaged self-energy for $U = 1.2$ and $U = 2.7$ was illustrated in Chapter 5 (Fig. 5.16 and Fig. 5.17 respectively). The density of states close to the metal-insulator transition appeared to be very noisy; thus the precision to which such a scaling can be observed over a wide range of U's and W's would depend on various numerical factors, like, the frequency grid resolution, number of disorder realizations etc.. In order to be numerically consistent, we therefore, optimally chose the same energy grid parameters for these results wherever possible and kept the same number of disorder realizations, which was ~ 20000.

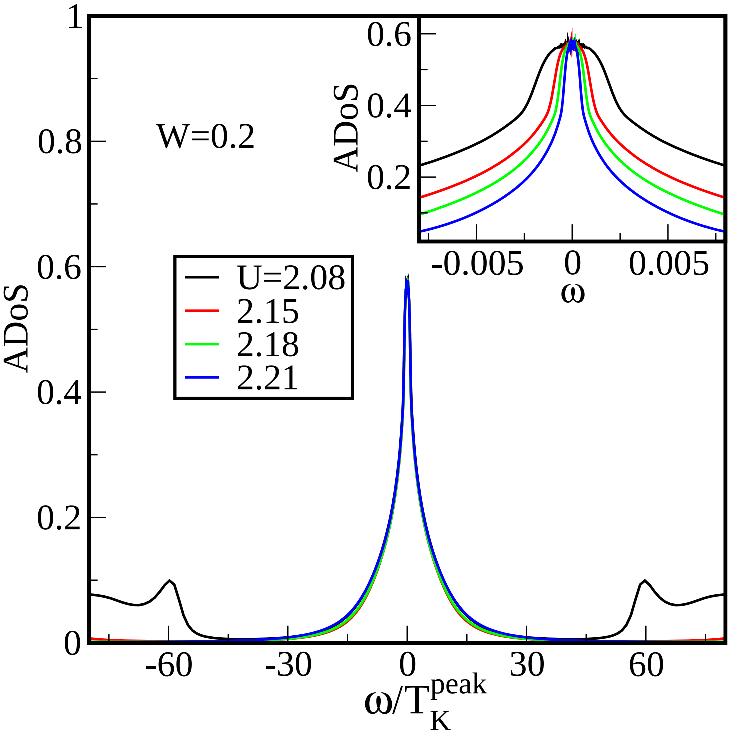

Figure A.4: (Main) Scaling collapse of the arithmetically averaged spectral density of states close to the U driven metal-insulator transition broundary at a fixed $W = 0.2$, with $W \ll U$. The frequency, ω is rescaled by the respective T_K^{peak} that corresponds to the peak of the distribution of Kondo scales, a quantity explored in Chapter 5. (Inset) The same plotted on a bare frequency scale.

In Fig. A.4 we do a similar spectral scaling analysis close to U driven transition, in presence of (low) disorder ($W = 0.2$). In the main panel of Fig. A.4, frequency is rescaled by the respective T_K^{peak} obtained from the distribution of Kondo scales. Of course, at $W = 0.2$ the distribution would be very narrow. The W being fixed, the ADoS is pinned at $\omega = 0$. The perfect collapse observed for the spectra at different U, indicates that the universality is observed irrespective of the direction of approach. The scaling collapse may be observed close to either W or U driven metal-insulator transition. This corroborates our prediction that at least within a local theory for a disordered interacting electron system, a universal lattice-coherence scale still persists. This single-scale picture for a disordered lattice establishes that within a mean-field theory, the effects of interactions are renormalized by disorder such that an effectively renormalized Kondo impurity physics takes charge.

Appendix B

Supporting information for results pertaining to Chapter 6

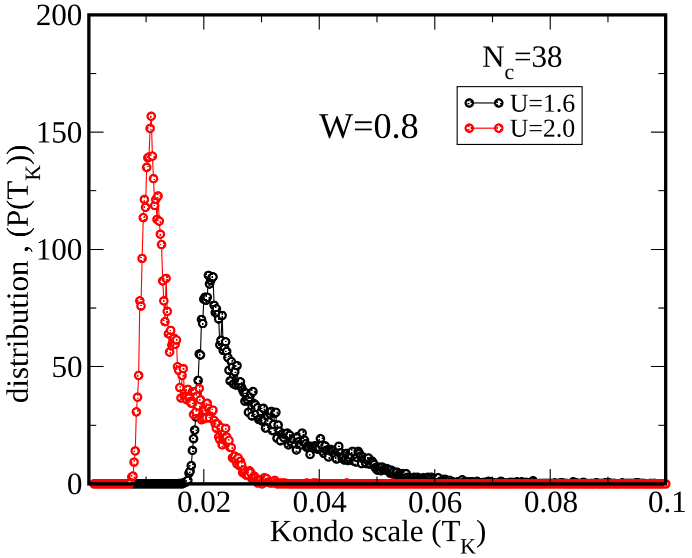

Figure B.1: $P(T_K)$ for $U = 1.6$ and 2.0 at a fixed $W = 0.8$. The distribution corresponding to $U = 2.0$ is narrower and peaked at a lower $T_K \approx 0.01$ compared to that of $U = 1.6$ with the peak at $T_K \approx 0.02$.

This appendix consists of additional information in regard to Chapter 6. We first begin with a comparison of the the distribution of Kondo scales $P(T_K)$ for two different interaction strengths, $U = 1.6$ and $U = 2.0$, at a sufficiently low fixed disorder strength, $W = 0.8$. Such an analysis would help us demonstrate how the $P(T_K)$ would evolve when the U is varied, a condition that was not explored extensively in Chapter 6.

In Fig. B.1 we observe that at $W = 0.8$, the interaction effects are still dominant and behaves similarly as $W = 0$ (clean) limit, where, the T_K scale decreases with an increase of U.

B.1 Tails of $P(T_K)$

In a disordered interacting system, disorder (W) renormalizes interactions, U, in such a way, that while some sites are weakly hybridized with the local medium others may be moderately or strongly hybridized with the same. Such a spatially fluctuating hybridizing medium would naturally lead to a broad distribution of T_K's. Moreover, the respective $P(T_K)$ can vary strongly depending on how far we are from the localization transition. The stochastic nature of the problem would lead to scales that may span $5-6$ orders of magnitude from $\sim 10^{-6}$ to $\sim 10^{-1}$; a uniform binning procedure would require a bin width resolution of this order to be able to represent such low energy scales, which in turn would require a huge number of data points for very broad distributions. Instead, we may adopt an adaptive binning procedure for plotting the distributions. We adopt the following procedure:

1. Let us consider that we have N number of points, where each point represents a T_K. Typical values of N used in our calculation were $\gtrsim 10^4$. We sort these data points from smallest to largest and put the first, N_1 points in the first bin, the second N_1 points in the second bin and so on. So we end up with $nbins = N/N_1$, where $nbins$ represent the number of histogram bins.

2. We accordingly find out the i-th bin-width, $\Delta_{bin}^{(i)}$ as the difference between the highest T_K of the $(i-1)$-th bin and the highest T_K of the (i)-th bin.

3. The distribution function would be given by $N_1/\Delta_{bin}^{(i)}$ for an average T_K within the respective bin.

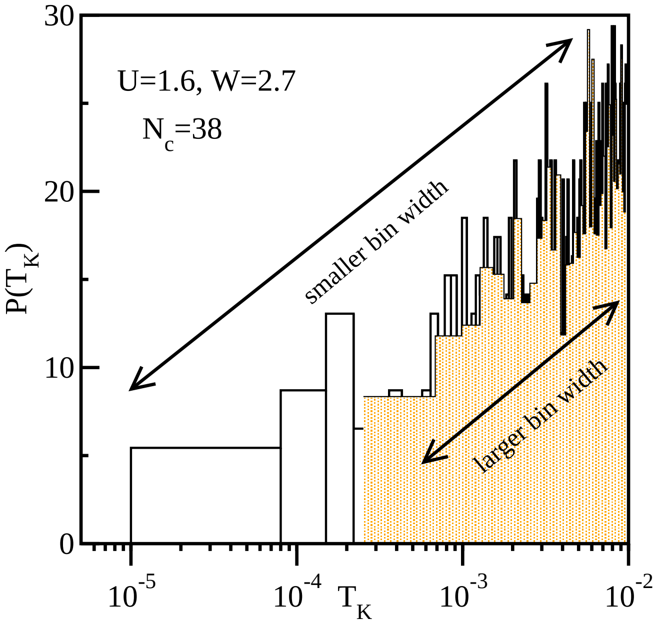

Figure B.2: $P(T_K)$ for $U = 1.6$ and $W = 2.7$ using two different bin width resolutions, Δ_{bin}. $\Delta_{bin} = 7 \times 10^{-5}$ for black-unshaded histogram and Δ_{bin} is adaptive for the orange shaded histogram, and for which the lowest $\Delta_{bin} \approx 10^{-4}$. Thus the data obtained using the latter loses out on representing $T_K < 10^{-4}$.

We realized that the systematic inclusion of short range correlation effects of disorder resulted in low T_K tails that were completely absent in a local theory. In Chapter 6, we identified a low energy scale, ω^* from the dynamics of the disorder averaged single-particle self-energy, -Im$\Sigma_{ave}(\omega)$. The low energy scale, namely, ω^* determines the energy scale at which we should expect a crossover from coherent, ω^2 Fermi liquid (FL) scattering to an incoherent non-FL scattering dynamics. If we now try to locate ω^* in the respective $P(T_K)$, we realize that for certain W's this scale might correspond to an *outlier* value residing in the low T_K tails. In order to identify these in $P(T_K)$, we would require very finely spaced bins for plotting the histogram. In this regard, the plots presented in Chapter 6 were obtained using optimal bin widths, such that, it could capture the qualitative picture. In Fig. B.2 we demonstrate a comparison between two such distributions for a fixed (U, W) pair, namely, $U = 1.6$ and $W = 2.7$. We note that $\omega^* \approx 5 \times 10^{-5}$ for $W = 2.7$ as obtained from the analysis of -Im$\Sigma_{ave}(\omega)$. The (a) black-unshaded distribution is obtained with a uniform binning procedure with bin width, $\Delta_{bin} = 7 \times 10^{-5}$ and (b) the orange shaded distribution is obtained using the adaptive binning procedure described earlier. As seen from Fig. B.2 indeed, the $\omega^* \approx 5 \times 10^{-5}$ for $W = 2.7$ at $U = 1.6$ lie in the tail of $P(T_K)$ and scales of this order or lower show up only when the $\Delta_{bin}^{(i)}$ is of this order. The adaptive binning procedure that was used for the plots presented in Chapter 6 loses out on the precise determination of this tail; nevertheless it successfully captures the correct trend and thus provides a qualitative understanding of the underlying physics. Also, note that while this value can certainly be captured by the same adaptive binning procedure, with a finer resolution, it will render the distribution extremely noisy.